

Severe Accident Investigations for VVER-Reactors including Radiological Impact and Quantification of Uncertainties

Zur Erlangung des akademischen Grades eines
Doktors der Ingenieurwissenschaften (Dr.-Ing.)
von der KIT-Fakultät für Maschinenbau des
Karlsruher Instituts für Technologie (KIT)

angenommene

Dissertation

von

M.Sc. Ahmet Kağan Mercan

geboren in Konak

Tag der mündlichen Prüfung:	26.09.2023
Referent:	Prof. Dr.-Ing. Robert Stieglitz Karlsruher Institut für Technologie
Korreferent:	Prof. Dr.-Phys. César Qeral Universidad Politécnica de Madrid

2024

Acknowledgements

Firstly, I would like to express my gratitude to the Republic of Türkiye Ministry of National Education for funding my doctoral work. Even in the hardest times of Covid-19 pandemic, their support of them never waned.

Secondly, I would like to thank every member of my group of RPD – Reactor Physics and Dynamics- for accepting to coordinate, review, supervise and evaluate this work. From starting my supervisor Prof. Dr. -Ing. Robert Stieglitz, I want to share my gratitude to this marvelous group. I must special thanks to my dearest friend and guide Dr. Fabrizio Gabrielli who made the path clearer, durable and exciting.

My deepest gratitude for my special group member and my friends soon-to-be-Dr-Ing Onur Murat and soon-to-be-Dr.-Ing Nuri Beydoğan whose mental and technical support opened the pathway of this approved work. Also, I want to express my acknowledgments for our group secretaries of Frau Petra Klug and Birgit Zagolla for their immeasurable and unvaluable support during this period.

Son olarak her zaman benim yanımda olan, bana sonsuz sabır gösteren ve benim en büyük yardımcım ve hayat ortağım olan değerli eşim Nida Yağmur Mercan'a kalbimin en derinlerinden bir teşekkürü borç bilirim. Aynı zamanda bu süreçte benim yanımda olan değerli ailem Ali Mercan, Melek Mercan, Sema Nur Yalçın, Mustafa Yalçın ve Aylanur Yalçın'a katkıları nedeniyle teşekkür ederim.

Karlsruhe, 2023

Abstract

Safety concern on mitigating potential impact of a possible release of Source Term (ST) to the environment largely increased after the major severe accidents of Chernobyl and Fukushima. Severe accident studies are conducted by regulators using deterministic integral tools to predict the accident progression and the resulting ST including the radiological impact. Based on such analysis, emergency response teams develop emergency management plans considering the best-possible, reliable and available information just after the accident happens. In this dissertation, a simulation platform is established consisting of the integral severe accident code ASTEC, the atmospheric dispersion and decision support tool JRODOS to predict the transport and release of the ST during a severe accident, and the radiological consequences of the released ST-inventory to the environment. It also includes the codes for the Fission Product inventory of realistic VVER-1000 core loadings such as KORIGEN, and ORIGEN. In addition, uncertainty quantification and sensitivity analysis (U&S) of the ASTEC and JRODOS codes is performed by using UQ-tool named KATUSA.

With this aim, physical models of ASTEC code to simulate in-vessel phase of a severe accident are validated by using VVER-specific test data such as the QUENCH-12 experiment. The prediction capability of the ASTEC code simulating VVER-specific in-vessel severe accident phenomena is evaluated by comparing the calculation results with the experimental data related to physical models describing main key phenomena of accident progression such as oxidation, heat transfer and oxide scale growth. Based on the validation work, it can be stated that the ASTEC-code is able to predict most relevant in-vessel severe accident phenomena e.g., oxidation, hydrogen generation, oxide layers of the fuel rods for LOCA-conditions including the quenching phase. The underestimation of hydrogen production during quenching phase is caused by missing models for oxidation of VVER related material.

The VVER-1000 plant is modelled by ASTEC including all the primary and secondary circuit components, containment rooms, and active and passive safety systems to be able to simulate progression of severe accident scenarios and release of FPs to the environment. Risk-relevant scenarios that lead to core damage and ST release were identified. The Large Break Loss of Coolant Accident (LBLOCA) on cold and hot leg coincident with the Station Blackout (SBO) were selected and this scenario was simulated until the rupture of the reactor cavity. Following ASTEC simulation, JRODOS analysis is performed for selected sites with selected season to predict the dispersion of the radiological inventory to the environment. Finally, KATUSA tool is used to quantify uncertainties and determine the most sensitive variables within the selected

parameters impacting the source term prediction. Based on the severe accident results obtained with ASTEC, following findings are highlighted:

- The generated hydrogen mass is about 790 kg when the break is located on cold leg. The highest hydrogen mass of about 1270 kg is predicted in case of a LBLOCA on the hot leg due to slower progression of severe accident.
- The activity released to the environment is about 1.2×10^{18} Bq at the end of simulation in case of LBLOCA on cold leg. The retention levels are significantly high due to retention on the walls of steam generators.
- On contrary, 7.0×10^{18} Bq activity is released when break is located on hot leg since the pathway to the containment is significantly shorter than the one break on the cold leg.

Based on the subsequent prediction of the radiological impact using the JRODOS code, the following statements can be made:

- Analysis shows that the contamination reaches about 22.9 MBq/km^2 , resulting with 1.38×10^3 mSv annual effective dose for an adult from all pathways with the predicted ST for the case of LBLOCA on cold leg.

Higher ST prediction in case of LBLOCA on hot leg results with 11.5 GBq/km^2 aerosol deposition and 1.75×10^5 mSv annual effective dose for an adult. Based on the performed quantification of the Uncertainties of JRODOS using KATUSA it can be stated that the maximum dose prediction is about 2.9×10^{18} Bq for cold leg break and 1.30×10^{19} Bq for hot leg break. In both cases, the shape factor relative to Stokes velocity is the dominating factor on the results which the change of this parameter impacts the gravitational settling of aerosols.

- Finally, the difference on the contamination of Cs-137 isotope is about 3.2 MBq/km^2 for the cold leg break scenario whereas this difference is about 0.5 TBq/km^2 in case of hot leg break based on the radiological impact analysis using best-estimate and worst-case ST inventories.

The established simulation platform consisting of the tools such as ORIGEN, ASTEC, JRODOS and KATUSA was essential to predict accurate, reliable and fast information about the progress of a severe accident, the potential radiological consequences and the range of radiological dispersion for any nuclear site, any accident scenario and any meteorological condition. That kind of information are of paramount importance for regulators and early response teams in order to develop plans to minimize the radiological consequences of severe accidents and for the implementation of effective and efficient measures to protect the people

and environment. In addition, this dissertation demonstrates the unique and extended capability of the simulation platform capable to evaluate the consequences of a severe accident from the early in-vessel core degradation phase to the dispersion of ST around the nuclear power plant considering a realistic nuclide inventory of any burnt core loading.

Kurzfassung

Sicherheitsbedenken hinsichtlich der Minderung potenzieller Auswirkungen einer möglichen Freisetzung von Source Term (ST) auf die Bevölkerung und die Umwelt werden nach den Folgen des Unfalls von Tschernobyl und Fukushima verstärkt. Studien zu schweren Unfällen werden von Aufsichtsbehörden unter Verwendung deterministischer und integraler Tools durchgeführt, um den Unfallverlauf und ST vorherzusagen sowie die radiologischen Auswirkungen einer solchen Freisetzung zu bewerten, um Notfallmanagementpläne zu entwickeln und Notfallteams mit der bestmöglichen, zuverlässigen und zuverlässigen Unterstützung zu unterstützen schnelle Auskunft. In dieser Dissertation wird eine Plattform des integralen Schwere-Unfall-Tools ASTEC-Atmosphären dispersions- und Entscheidungsunterstützungssystem JRODOs verwendet, um den Transport und die Freisetzung des ST während eines schweren Unfalls sowie die möglichen Folgen eines solchen ST-Inventars für die Umwelt vorherzusagen, ausgehend von der Berechnung des Spaltproduktinventars unter Verwendung von KORIGEN in VVER-1000. Außerdem werden die Unsicherheitsquantifizierung und Sensitivitätsanalyse (U&S) mit dem KATUSA-Tool durchgeführt.

Mit diesem Ziel werden physikalische Modelle des ASTEC-Codes zur Simulation der Schiffsphase eines schweren Unfalls validiert, indem eine VVER-ähnliche Geometrie von QUENCH-12-Experimentdaten verwendet wird. Die Vorhersagen des ASTEC-Codes werden mit Versuchsergebnissen verglichen, und physikalische Modelle, die die wichtigsten Schlüsselphänomene des Unfallverlaufs wie Oxidation, Wärmeübertragung und Wachstum von Oxidablagerungen beschreiben, sind gut geeignet, um den Unfallverlauf zu demonstrieren. Obwohl das Wasserstoffherstellungsprofil vollständig von ASTEC erfasst wird, sind die Modelle in der Lage, eine ähnliche Wasserstoffmenge bis zur Abschreckphase vorherzusagen. Die Unterschätzung der Wasserstoffproduktion während der Abschreckphase wird durch fehlende thermische Eigenschaften von VVER-verwandtem Material verursacht.

Das umfangreiche Modell von VVER-1000 wird von ASTEC modelliert, einschließlich aller primären und sekundären Kreislaufkomponenten, Sicherheitsräume und aktiven und passiven Sicherheitssysteme nach der Validierung, um den Verlauf schwerer Unfallszenarien und die Freisetzung von FPs in die Umwelt simulieren zu können. Risikorelevante Szenarien, die zu Kernschäden und ST-Freisetzung führen, werden

ermittelt und Large Break Loss of Coolant Accident (LBLOCA) auf Cold- und Hot-Leg zeitgleich mit Station Blackout (SBO) bis zum Reißen der Kavität simuliert. Nach der ASTEC-Simulation wird eine JRODOS-Analyse für ausgewählte Standorte mit ausgewählter Jahreszeit durchgeführt, um die Ausbreitung des radiologischen Inventars in die Umwelt zu beobachten. Schließlich wird das KATUSA-Tool verwendet, um Unsicherheiten zu quantifizieren und die empfindlichsten Variablen innerhalb der ausgewählten Parameter zu bestimmen. Nach den Ergebnissen der genannten schweren Unfallfolgen lassen sich folgende Befunde auflisten:

- Die erzeugte Wasserstoffmasse beträgt etwa 790 kg, wenn sich die Unterbrechung auf dem kalten Abschnitt befindet. Die höhere Wasserstoffmasse, 1270 kg, entsteht im Bruchfall auf dem heißen Strang aufgrund des langsameren Fortschreitens des schweren Unfalls.
- Die an die Umgebung abgegebene Aktivität beträgt etwa 1.2×10^{18} Bq am Ende der Simulation im Fall von LBLOCA auf der kalten Strecke. Die Retentionswerte sind aufgrund der Retention an den Wänden von Dampferzeugern signifikant hoch.
- Im Gegensatz dazu werden 7.0×10^{18} Bq Aktivität freigesetzt, wenn sich der Bruch auf dem heißen Bein befindet, da der Weg zum Containment deutlich kürzer ist als der eine Bruch auf dem Fall des kalten Beins.
- Die JRODOS-Analyse zeigt, dass die Kontamination etwa 22.9 MBq/km^2 erreicht, was zu einer jährlichen effektiven Dosis von 1.38×10^3 mSv für einen Erwachsenen aus allen Pfaden mit der vorhergesagten ST für den Fall von LBLOCA auf kaltem Bein führt.
- Höhere ST-Vorhersage im Fall von LBLOCA auf Hot Leg-Ergebnissen mit 11.5 GBq/km^2 Aerosolablagerung und 1.75×10^5 mSv jährlicher effektiver Dosis für einen Erwachsenen
- Die durchgeführte KATUSA-Analyse zeigt, dass die maximale Dosisvorhersage etwa 2.9×10^{18} Bq für kalte Beinbrüche und 1.30×10^{19} Bq für heiße Beinbrüche beträgt. In beiden Fällen ist der Formfaktor relativ zur Stokes-Geschwindigkeit der dominierende Faktor für die Ergebnisse, dass die Änderung das gravitative Absetzen von Aerosolen beeinflusst.
- Schließlich beträgt der Unterschied bei der Kontamination mit Cs-137-Isotopen etwa 3.2 MBq/km^2 für das Kaltbeinbruchszenario, während dieser Unterschied im Falle eines Heißbeinbruchs etwa 0.5 TBq/km^2 beträgt, basierend auf der radiologischen Auswirkungsanalyse unter Verwendung Beste-Schätzung- und Schlimmsten-Fall-ST-Lagerbestände.

Die Ergebnisse der Arbeit und der ASTEC-JRODOS-KATUSA-Plattform sind unerlässlich, um genaue, zuverlässige und schnelle Informationen über den Verlauf eines schweren Unfalls, mögliche radiologische Folgen und den Bereich der radiologischen Ausbreitung für jeden nuklearen Standort, jedes Unfallszenario und jede meteorologische Bedingung zu erhalten an die Aufsichtsbehörden und Teams für frühzeitige Reaktion, um Pläne für schwere Unfälle sowie effektive und effiziente Reaktionen auf die Unfälle zu entwickeln. Außerdem erweitert diese Dissertation die Fähigkeit, Folgen eines schweren Unfalls von der Einleitung des Ereignisses bis zur Ausbreitung von ST zu bewerten.

Publications related to this thesis

Gabrielli, Fabrizio, Victor Hugo Sanchez-Espinoza, Onur Murat, Ahmet Kagan Mercan, and Walter Tromm. 2021. "Employment of the ASTEC code in the Severe Accidents Research Activities at KIT." Nuclear Energy for New Europa (NENE). Ljubljana, ISBN: 978-961-6207-51-5, COBISS.SI-ID: 86400771. doi:10.5445/IR/1000140014.

Mercan, Ahmet Kağan, Fabrizio Gabrielli, and Victor Hugo Sanchez-Espinoza. 18-20 March 2019. "Validation of ASTEC2.1 Using QUENCH-12 for VVER-Reactors." 9th Conference of Severe Accident Research. Prague. 106-126. doi:ISBN 978-80-270-5809-9.

Mercan, Ahmet Kağan, Fabrizio Gabrielli, and Victor Hugo Sanchez-Espinoza. 16-19 May 2022. "Source Term Estimation and Dispersion Analysis of VVER-1000 Reactor in case of LBLOCA Along with SBO." The 10th European Review Meeting on Severe Accident Research (ERMSAR2022). Karlsruhe: KIT. 296, ID:287. doi:10.5445/IR/1000151444.

Mercan, Ahmet Kağan, Fabrizio Gabrielli, and Victor Hugo Sanchez-Espinoza. 2022. "Validation of Astec2.1 using Quench-12 for VVER-Reactors." Nuclear Engineering and Design 395 (ISSN 0029-5493): 111840.

—. 13-15 November 2018. "Validation of ASTEC2.1 using QUENCH-12 for VVER-reactors." 24th International QUENCH Workshop. Karlsruhe: Karlsruher Institut für Technologie (KIT). 376. doi:10.5445/IR/1000088229.

Mercan, Ahmet Kağan, Fabrizio Gabrielli, Victor Hugo Sanchez-Espinoza, and Wolfgang Raskob. 2022. "Analysis of the consequences of a LBLOCA with SBO severe accident in a generic VVER-1000 by means of ASTEC and JRODOS codes." Nuclear Engineering and Design 400 (ISSN 0029-5493): 112078.

Sanchez-Espinoza, V. H., F. Gabrielli, U. Imke, K. Zhang, L. Mercatali, G. Huacco, J. Duran, et al. 2023. "KIT reactor safety research for LWRs: Research lines, numerical tools, and prospects." Nuclear Engineering and Design 112573, Vol. 414, ISSN 0029-5493, <https://doi.org/10.1016/j.nucengdes.2023.112573>.

Contents

	List of figures.....	xviii
	List of tables.....	xxv
1	INTRODUCTION	1
1.1	MOTIVATION	1
1.2	PROBLEM FORMULATION & CHALLENGES	3
1.3	GOALS OF THE THESIS.....	7
1.4	STRUCTURE OF THE THESIS	7
2	BRIEF DESCRIPTION OF THE VVER-1000 NUCLEAR POWER PLANT	9
2.1	CORE CHARACTERISTICS.....	9
2.2	PRIMARY /SECONDARY CIRCUITS	13
2.3	CONTAINMENT	17
2.4	SAFETY SYSTEMS	19
3	SEVERE ACCIDENT PHENOMENA IN VVER-1000 NUCLEAR POWER PLANTS.....	21
3.1	CHANGE OF MATERIAL COMPOSITION OF THE CORE DURING THE OPERATION	22
3.2	KEY PHENOMENA DURING THE IN-VESSEL PHASE.....	23
3.2.1	Oxidation of core materials.....	24
3.2.2	Cladding ballooning and burst	25
3.2.3	Formation of the molten pool and relocation to the lower plenum.....	26
3.2.4	Failure of lower plenum of the vessel	26
3.3	KEY PHENOMENA DURING THE EX-VESSEL PHASE.....	27
3.3.1	Early containment failure	28
3.3.2	Late containment failure	29
3.4	FISSION PRODUCTS RELEASE AND TRANSPORT INTO THE CONTAINMENT.....	30
3.5	DISPERSION OF RADIOACTIVE ISOTOPES AND RADIOLOGICAL IMPACT.....	32
4	DEVELOPED CALCULATION PLATFORM	35
4.1.1	The KORIGEN code for depletion analysis of the core	37
4.1.2	Integral severe accident code ASTEC	37
4.1.3	Radiological dispersion and impact analysis code JRODOS.....	39
4.1.4	Uncertainty Quantification with The Karlsruher Tool for Uncertainty Quantification and Sensitivity Analysis (KATUSA)	39
5	VALIDATION OF ASTECV2.1 CODE WITH QUENCH-12 TEST	41

Severe accident investigations for VVER-Reactors including Radiological Impact and the Quantification of Uncertainties

5.1	DESCRIPTION OF THE QUENCH-12 EXPERIMENT	41
5.2	DEVELOPMENT OF ASTEC MODEL QUENCH-12 TEST	45
5.2.1	Modelling of the test section of QUENCH-12 ASTEC model	45
5.2.2	Initial and boundary conditions of QUENCH-12 ASTEC model.....	47
5.2.3	Chemical and physical models considered in ASTEC model.....	50
5.3	COMPARISON OF ASTEC-PREDICTIONS WITH EXPERIMENTAL DATA.....	51
5.4	DISCUSSION OF THE RESULTS	60
5.5	SUMMARY	62
6	PREDICTION OF THE RADIOLOGICAL SOURCE TERM FOR A VVER-1000 SEVERE ACCIDENT WITH ASTEC.....	63
6.1	FISSION PRODUCT INVENTORY INVESTIGATION BY KORIGEN TOOL	63
6.2	INTEGRAL MODEL OF THE VVER-1000 NPP	65
6.2.1	Reactor Pressure Vessel model	65
6.2.2	Primary and secondary circuit model.....	66
6.2.3	Cavity and Containment models	68
6.2.4	Control and safety system models	70
6.2.5	Verification of the integral ASTEC-model.....	71
6.3	SOURCE TERM PREDICTION FOR LBLOCA SEVERE ACCIDENT SEQUENCE OF THE VVER-1000.....	73
6.3.1	Source Term Transport and Release during a LBLOCA on cold leg of the pressurizer along with the SBO	74
6.3.2	Source Term Transport and Release during a LBLOCA on hot leg of the pressurizer loop along with the SBO	79
6.4	SUMMARY	83
7	ESTIMATION OF THE RADIOLOGICAL IMPACT AFTER A SEVERE ACCIDENT IN A VVER-1000 NPP USING JRODOS	85
7.1	JRODOS ANALYSIS OF THE VVER-1000 AT THE KOZLODUY NPP SITE AFTER A HYPOTHETICAL LBLOCA ON THE COLD LEG OF WITH SBO	85
7.2	JRODOS ANALYSIS OF VVER-1000 AT THE AKKUYU NPP SITE AFTER A HYPOTHETICAL LBLOCA ON THE HOT LEG WITH SBO	89
7.3	COMPARISON WITH OTHER STUDIES AND DISCUSSION	93
7.4	SUMMARY	94
8	UNCERTAINTY AND SENSITIVITY ANALYSIS OF ASTEC FOR THE PREDICTION OF THE RADIOLOGICAL SOURCE TERM WITH KATUSA	95
8.1	DETERMINATION OF UNCERTAIN PARAMETERS	95
8.2	U&S- ANALYSIS OF ASTEC FOR THE LBLOCA ON THE COLD LEG WITH SBO	96

8.3	U&S ANALYSIS OF ASTEC FOR A LBLOCA ON THE HOT LEG WITH SBO	104
8.4	SUMMARY	111
9	CONCLUSIONS AND PERSPECTIVES	113
	BIBLIOGRAPHY.....	117
Appendix A	Further results of the ASTECV2.1 validation on the QUENCH-12 experiment.....	127
A.1	Temperature comparison at several elevation.....	127
A.2	Oxide scale growth on fuel rods	129
Appendix B	Further results of the performed sequences in a VVER-1000 using ASTEC V2.2	132
B.1	Further results of LBLOCA on the cold with SBO accident	132
B.2	Further results of LBLOCA on the hot leg with SBO accident	138
Appendix C	Further results of radiological consequence analysis by JRODOS.....	143
C.1	Further results of the radiological consequence analysis in Kozloduy NNP with the ST estimations of the break on the cold leg with SBO	143
C.2	Further results of the radiological consequence analysis in Akkuyu NNP with the ST estimations of the break on the hot leg with SBO.....	150
Appendix D	Further results of the uncertainty quantification and sensitivity analysis by KATUSA and comparison of radiological consequences.....	160
D.1	Further results of the uncertainty quantification and sensitivity analysis of the break on the cold leg with SBO	160
D.2	Further results of the uncertainty quantification and sensitivity analysis of the break on the cold leg with SBO	169

List of figures

Figure 1-1: Sketch of typical loop with pressurizer of VVER-1000 plant modified from (Nuclear Regulatory Authority of the Slovak Republic, 2010)	3
Figure 2-1: The radial layout of the VVER-1000 assemblies modified (Hadad, Mirvakili, Safaei, & Nematollahi, 2009)	11
Figure 2-2: The layout of the lower plenum of the generic VVER-1000 core modified from (Ivanov, Ivanov, Groudev, Pavlova, & Hadjiev, 2002)	12
Figure 2-3: The layout of the vessel of the generic VVER-1000 modified from (NEA-OECD, 2004)	12
Figure 2-4: The layout of the steam generator of the generic VVER-1000 modified from (Ivanov, Ivanov, Groudev, Pavlova, & Hadjiev, 2002)	13
Figure 2-5: Geometric arrangement of the steam generators and coolant loops modified from (Ivanov, Ivanov, Groudev, Pavlova, & Hadjiev, 2002)	14
Figure 2-6: The layout of the pressurizer of the generic VVER-1000 modified from (Ivanov, Ivanov, Groudev, Pavlova, & Hadjiev, 2002)	15
Figure 2-7: The generic containment of the VVER-1000 plant modified from (Ryzhov, et al., 2010)	17
Figure 2-8: The sketch of the lower end of the reactor and cavity hall of VVER-1000 reactor modified from (Stefanova, Gencheva, & Groudev, 2011)	18
Figure 2-9: The schematical arrangement of the ECCS system in the VVER-1000 plant modified from (Queral, et al., 2021)	20
Figure 3-1: The physical phenomena occur during a severe accident modified from (Van Dorsselaere, Albiol, & Micaelli, 2011)	22
Figure 3-2: The melting points of several nuclear core materials as a function of temperature [°C] (left) and phases of the accident progression assigned to the temperature level from (Schanz, Hagen, Hofmann, Schumacher, & Sepold, 1992)	24
Figure 3-3: Measured change of burst pressure against the burst temperature of E110 and Zircaloy-4 claddings from (Hózer, et al., 2005)	26
Figure 3-4: The debris configuration in the lower plenum and focusing effect modified from (IRSN, 2021)	27
Figure 3-5: Evaluated detonation and burn limits for volumetric fractions of hydrogen-air-steam mixtures in the Shapiro diagram modified from (Shapiro & Moffette, 1957)	29
Figure 3-6: Scheme of a Gaussian plume model from (IAEA, 2020) indicatory spread of radionuclides as function of distance from release of plant site	32

Figure 3-7: Transfer chain options of the activity concentration from radionuclides to foodstuff from (Raskob, Trybushnyi, Ievdin, & Zheleznyak, 2012)	34
Figure 4-1: ASTEC-JRODOS-KATUSA calculation route	36
Figure 4-2: General structure of ASTEC integral code and its modules from (Chatelard & Laborde, 2022)	38
Figure 4-3: Schematic illustration of atmospheric transport of the isotopes and deposition with terrestrial exposure pathways from (Karlsruhe Institute of Technology (KIT), 2017) covered by JRODOS software	39
Figure 4-4: KATUSA calculation structure for U&S analysis modified from (Stakhanova A. , Gabrielli, Sanchez-Espinoza, Hoefler, & Pauli, 2022)	40
Figure 5-1: Sketch of the test bundle of the QUENCH-12 experiment (right) and test section of the QUENCH-12 experiment with flow lines modified from (Stuckert, et al., 2008)	42
Figure 5-2: Section of the heated fuel rods (HFRs) used in the experiment (left) and section of the unheated fuel rods (UFR) used in the experiment (right) modified from (Stuckert, et al., 2008)	43
Figure 5-3: Cross-section view of the fuel bundle used in QUENCH-12 experiment (left) and axial positions of thermocouples and spacer grids used in the experiment modified from (Stuckert, et al., 2008)	44
Figure 5-4: Temperature, flow and power conditions implemented in the experiment modified from (Stuckert, et al., 2008)	45
Figure 5-5: Radial meshing of the QUENCH-12 test bundle in ASTEC code	46
Figure 5-6: Axial meshing of the QUENCH-12 test bundle in ASTEC code	47
Figure 5-7: Employed steam, argon and quenching water flow rate during the simulation in ASTEC	49
Figure 5-8: Considered power supply temporal evolution of inner and outer rods of the ASTEC- QUENCH-12 simulation	50
Figure 5-9: Comparison of the predicted and experimental temperature data as a function of time at an axial height of 950 mm for heated rods	53
Figure 5-10: Comparison of the predicted and experimental temperature data as a function of time at an axial height of 950 mm for unheated rods and shroud	53
Figure 5-11: Axial temperature profile comparison between predicted and experimental results at several axial positions for heated rods at the beginning of transient phase (6000 s)	54
Figure 5-12: Axial temperature profile comparison between predicted and experimental results at several axial positions for heated rods at the quenching onset (7160 s)	55
Figure 5-13: Axial temperature profile comparison between predicted and experimental results at several axial positions for unheated rods and shroud at the beginning of transient phase (6000 s)	55

Figure 5-14: Axial temperature profile comparison between predicted and experimental results at several axial positions for unheated rods and shroud at the quenching onset (7160 s)	56
Figure 5-15: Axial oxidation profile comparison between predicted and experimental results at several axial positions for ejected control rod at the beginning of transient phase (6000 s)	57
Figure 5-16: Axial oxidation profile comparison between predicted and experimental results at several axial positions for ejected control rod before quenching (7160 s)	57
Figure 5-17: Axial view of the test bundle with material composition at the end of the experiment	58
Figure 5-18: Comparison of predicted and experimental hydrogen generation mass	59
Figure 5-19: Comparison of predicted and experimental hydrogen generation mass rate	60
Figure 5-20: Comparison of hydrogen generation by different oxidation models and experimental results	61
Figure 6-1: Considered irradiation history with downtimes of a VVER-1000 used as input to the KORIGEN to obtain FP inventory	64
Figure 6-2: Computed activity levels generated for one tHM and 0.3-ton cladding material of a generic VVER-1000 core at the end of irradiation history	65
Figure 6-3: Sketch of the reactor vessel for a generic VVER-1000 as modelled in ASTEC	66
Figure 6-4: Sketch of the primary and secondary circuit model of ASTEC for a generic VVER-1000 reactor; here loop 1 with the PZR	67
Figure 6-5: Sketch of the containment model for a generic VVER-1000 by ASTEC	69
Figure 6-6: The core damage frequency according to the initiator event for Kalinin VVER-1000 NPP (U.S. Nuclear Regulatory Commission (NRC), 2005)	73
Figure 6-7: Computed generation of hydrogen mass as a function of time during the transient of LBLOCA on cold leg of the pressurizer loop along with the simultaneous SBO of a VVER-1000 reactor	76
Figure 6-8: Computed temporal evolution of the activity transported from vessel to primary circuit, containment and environment cold leg of the pressurizer loop along with the simultaneous SBO of a VVER-1000 reactor	78
Figure 6-9: Computed activity level after a LBLOCA on the cold leg of pressurizer loop along with a SBO in the containment and in the environment at the end of transient for selected isotopes	78
Figure 6-10: Computed generation of hydrogen mass as a function of time during the transient of LBLOCA on hot leg of the pressurizer loop along with the simultaneous SBO of a VVER-1000 reactor	81

Figure 6-11: Computed temporal evolution of the activity transported from vessel to primary circuit, containment and environment hot leg of the pressurizer loop along with the simultaneous SBO of a VVER-1000 reactor	82
Figure 6-12: Computed activity level after a LBLOCA on the hot leg of pressurizer loop along with a SBO in the containment and in the environment at the end of transient for selected isotopes	83
Figure 7-1: Calculated total aerosol contamination over the calculation site at the end of the 10-day of radiological dispersion of ST calculated for LBLOCA on the the cold leg accident case with SBO	87
Figure 7-2: Simulated effective dose on adults by all pathways 1 year after 10-day of radiological distribution of ST calculated for LBLOCA on the the cold leg accident case with SBO	88
Figure 7-3: Simulated maximum activity of cesium isotopes in the cow's milk at the end of 10th day of radiological dispersion for the LBLOCA on the cold leg accident case with SBO	89
Figure 7-4: Simulated total aerosol contamination over the calculation site at the end of the 10-day of radiological dispersion of ST calculated for the hot leg accident	90
Figure 7-5: Simulated effective dose on adults by all pathways 1 year after 10-day of radiological distribution of ST calculated for a hot leg accident	91
Figure 7-6: Simulated maximum activity of cesium isotopes in the cow's milk at the end of 10th day of radiological dispersion for the hot leg accident case	91
Figure 8-1: Evaluated most probable time window for the onset of FP release in case of LBLOCA on the cold leg of the pressurizer loop along with the SBO	98
Figure 8-2: Evaluated most probable time window for the core uncovering in case of LBLOCA on the cold leg of the pressurizer loop along with the SBO	98
Figure 8-3: Evaluated most probable time window for the onset of RPV failure in case of LBLOCA on the cold leg of the pressurizer loop along with the SBO	99
Figure 8-4: Evaluated most probable time window for basemat rupture in case of LBLOCA on the cold leg of the pressurizer loop along with the SBO	99
Figure 8-5: Evaluated minimum, maximum, mean and most probable values of activity released to the environment in case of LBLOCA on the cold leg of the pressurizer loop along with the SBO	100
Figure 8-6: Pearson correlation coefficient between the activity released to the environment and uncertain parameters at 22461.7 s (left) and at 65852.6 s (right).	101
Figure 8-7: Pearson correlation coefficient between I-131 activity (left) and Cs-137 activity (right) released to the environment and shape factor relative to Stokes velocity in case of LBLOCA on the cold leg of the pressurizer loop along with the SBO	101
Figure 8-8: Released isotope activity in the best-estimate, optimistic and worst case at the end of the uncertainty quantification calculation by KATUSA in case of LBLOCA on the cold leg of the pressurizer loop along with the SBO	102

Figure 8-9: Simulated deposition of the aerosols from the Zaporizhzhia NPP in selected time period for best-estimate ST obtained in LBLOCA on the cold leg with SBO	103
Figure 8-10: Simulated deposition of the aerosols from the Zaporizhzhia NPP in selected time period for worst-case ST obtained in LBLOCA on the cold leg with SBO	103
Figure 8-11: Most probable time window for the onset of FP release in case of LBLOCA on the hot leg of the pressurizer loop along with the SBO	105
Figure 8-12: Most probable time window for uncovering of the core in case of LBLOCA on the hot leg of the pressurizer loop along with the SBO	105
Figure 8-13: Most probable time window for the onset of RPV failure in case of LBLOCA on the hot leg of the pressurizer loop along with the SBO	106
Figure 8-14: Most probable time window for basemat rupture in case of LBLOCA on the hot leg of the pressurizer loop along with the SBO	106
Figure 8-15: Minimum, maximum, mean and most probable values of activity released to the environment in case of LBLOCA on the hot leg of the pressurizer loop along with the SBO	107
Figure 8-16: Pearson correlation coefficient between the activity released to the environment and uncertain parameters during in-vessel phase (left) and ex-vessel phase (right)	108
Figure 8-17: Pearson correlation coefficient between I-131 activity (left) and Cs-137 activity (right) released to the environment and shape factor relative to Stokes velocity in case of LBLOCA on the hot leg of the pressurizer loop along with the SBO	108
Figure 8-18: Calculated released isotope activity in the best-estimate, optimistic and worst case at the end of the uncertainty quantification calculation by KATUSA in case of LBLOCA on the hot leg of the pressurizer loop along with the SBO	109
Figure 8-19: Simulated deposition of the aerosols from the Zaporizhzhia NPP in selected time period for best-estimate ST obtained in LBLOCA on the hot leg with SBO	110
Figure 8-20: Simulated deposition of the aerosols from the Zaporizhzhia NPP in selected time period for worst-case ST obtained in LBLOCA on the hot leg with SBO	110

List of tables

Table 2.1: The fuel and clad dimensions of a generic VVER1000/V320 core from (Murphy, et al., 2000)	10
Table 2.2: The material composition of VVER1000/V320 clad and equivalent masses for 1tHM from (Murphy, et al., 2000)	10
Table 2.3: Dimensions areas and volumes of the primary and secondary circuit components of the generic VVER-1000 modified from (Ivanov, Ivanov, Groudev, Pavlova, & Hadjiev, 2002)	16
Table 2.4: The chemical composition of the concrete used in VVER-1000 cavity modified (Stefanova, Gencheva, & Groudev, 2011)	18
Table 2.5: The technical specification of ECCS components from (NEA, 2001)	19
Table 3.1: The half-life and volatility of the main fission products	31
Table 5.1: Employed mass flow rate, temperature and pressure of the flows in time	48
Table 5.2: Total hydrogen generation comparison at different phases of the test	60
Table 6.1: Comparison of the key plant parameters of the VVER-1000 between ASTEC predictions and the literature (Ivanov, Ivanov, Groudev, Pavlova, & Hadjiev, 2002)	72
Table 6.2: Computed sequence of the major events during the transient of LBLOCA on cold leg of the pressurizer loop along with the SBO	75
Table 6.3: Calculated sequence of the major events during the transient of LBLOCA on hot leg of the pressurizer loop along with the SBO	80
Table 8.1: Impactful uncertain parameters with reference values, variation range and probabilistic distribution function used in the ASTEC VVER-1000 model	96

List of Abbreviations:

Abbreviations	Description
ADM	Atmospheric Dispersion Model
AM	Accident Management
ARVI	Assessment of Reactor Vessel Integrity
ASCOM	ASTEC Community
ASTEC	Accident Source Term Evaluation Code
ATHLET	Analysis of Thermal hydraulics of Leaks and Transients
BARC	Bhabha Atomic Research Centre
BOC	Beginning of Cycle
BULATOM	Bulgaria Atomic Agency
BWR	Boiling Water Reactor
CC	Cold Collector
CD	Core Degradation
CDF	Core Damage Frequency
CESAM	Codes for European Severe Accident Management
CL	Cold Leg
CORINE	Coordination of Information on the Environment
CRP	Coordinated Research Activities
CSNI	Committee on the Safety of Nuclear Installations
DCH	Direct Containment Heating
ECCS	Emergency Core Cooling System
EMERSIM	Early Countermeasure Module
EOC	End of Cycle
EPR	European Pressurized Reactor
EU	European Union
FMDT	Food Chain and Dose Module for Terrestrial Pathways
FOM	Figure-of-Merit
FP	Fission Product
FSTC	Fast Source Term Calculation
FZKA	Forschungszentrum Karlsruhe
GRS	Gesellschaft für Anlagen-und Reaktorsicherheit
HC	Hot Collector
HFR	Heated Fuel Rod
HM	Heavy Metal
HPIS	High Pressure Injection System
HZDR	Helmholtz Zentrum Dresden-Rossendorf
IAEA	International Atomic Energy Agency
ICRP	International Commission on Radiological Protection
INES	International Nuclear and Radiological Event Scale
INRNE	Institute of Nuclear Research and Nuclear Energy
IRSN	Institute de Radioprotection et Surète Nucléaire
JRODOS	Java based Real-time On-line Decision Support
KATUSA	Karlsruher Tool for Uncertainty and Sensitivity Assessment
KFK	Kernforschungszentrum Karlsruhe

KIT	Karlsruher Institute of Technology
LBLOCA	Large Break Loss of Coolant Accident
LEU	Low Enriched Uranium
LHS	Latin-Hypercube Sampling
LOCA	Loss of Coolant Accident
LP	Lower Plenum
LPIS	Low Pressure Injection System
LWR	Light Water Reactor
MBLOCA	Medium Break Loss of Coolant Accident
MCCI	Molten Core Concrete Interaction
MCNP	Monte Carlo N-Particle
MCP	Main Coolant Pump
MOCABA	Monte Carlo-Bayes Procedure
MSH	Main Steam Head
MSL	Main Steam Line
MUSA	Management and Uncertainties of Severe Accidents
NEA	Nuclear Energy Agency
NPP	Nuclear Power Plant
NPS	Nuclear Power Station
NRC	Nuclear Regulatory Commission
NUGENIA	The Nuclear Generation II & III Alliance
OECD	Organization for Economic Cooperation and Development
PAR	Passive Autocatalytic Recombiners
PDF	Probabilistic Distribution Function
PRA	Probabilistic Risk Assessment
PSA	Probabilistic Safety Assessment
PZR	Pressurizer
PWR	Pressurized Water Reactor
RCS	Reactor Cooling System
RHWG	Reproductive Health Working Group
RIA	Reactivity Insertion Accident
ROSATOM	State Atomic Energy Corporation Rosatom
RPV	Reactor Pressure Vessel
SA	Severe Accident
SAM	Severe Accident Management
SBO	Station Blackout
SG	Steam Generator
SGTR	Steam Generator Tube Rupture
ST	Source Term
TC	Thermocouple
TFS	Temperature of Fuel Surface
TMI	Three Mile Island
TSO	Technical Support Organization
TUM	Technical University of Munich
UFR	Unheated Fuel Rod

VVER	Water-Water Energetic Reactor
WWER	Water-Water Energetic Reactor

1 Introduction

1.1 Motivation

The Water-Water Energetic Reactor (VVER) was designed by the former Soviet Union and several variations of this pressurized water reactor is operational in 15 countries with 67 nuclear power plants (NPPs). VVER-1000 is the most common Generation II design inside these variations with 31 NPPs and new VVER-1200 reactors of generation III+ under construction in different countries including Turkey, Bangladesh and Hungary.

Despite progress on reactor technology and safety culture, major severe accident occurred in the world in 1979 in USA (TMI-2), 1989 in Russia (Chernobyl) and 2011 in Japan (Fukushima Daichi). In case of severe accidents with core meltdown and significant release of fission products into the environment, the Emergency teams of a Nuclear Power Plant (NPP) site have promptly to undertake countermeasures to minimize the radiological consequences of such an accident for the public and environment. To the take most appropriate decisions, the Emergency Teams need reliable information about the timing, amount, and type of radioactive materials being released into the environment from the NPP. This information is provided by Technical Support Organizations (TSOs), research centers, regulators or any other qualified organization that have expertise in the following computational tools:

- a) Radioactive inventory in the core of the NPPs,
- b) radiological source term to be potentially released from the containment into the environment, and
- c) radiological impact caused by the released radiological source term from a meltdown core.

It is worth mentioning that the core of a commercial NPP of 1000 MW electrical power is loaded with about 100 tons of UO_2 enriched with around 4 % U-235 of the fuel. The nuclide inventory changes drastically during the operation period due to burn-up and decay process of the fission products (FPs). Hence, it is important to consider the most representative nuclide inventory in a core different from the one in the beginning of cycle i.e., middle or end of cycle for the estimation of the radiological source term. Depending on the cycle, the amount of the FPs as well as the power generated by decay of FPs changes and this situation can create different scenarios on accident progression and released activity inventory into to environment. Dedicated tools that describe the fission process and the subsequent radioactive decay in a

reactor core –called depletion codes e.g., ORIGEN-S (Meiyin, et al., 2014), APOLLO (Hoffmann, Jeanpierre, Kavenoky, Livolant, & Lorain, 1973), FISPIN (Burstall, 1979), MONTEBURNS (Trellue, 1998), KORIGEN (Wies & H.W., 1998) etc.- are needed for a reliable prediction of the nuclide inventory at any point of the operation and standby.

The radiological source term under b) is typically predicted with integral severe accident codes such as ASTEC (Chatelard, et al., 2014), MAAP (EPRI, 2013) and MELCOR (Humpries & Gauntt, 2018). ASTEC is the European reference severe accident code being developed by IRSN. It is being validated and improved within different European projects such as the EU CESAM (Nowack, et al., 2018) and NUGENIA ASCOM (Chatelard P. , ASCOM project overview and description of work, 2018) (Chatelard, et al., 2014) (Chatelard & Laborde, 2022). Integral severe accident codes are mainly used for the prediction of safety-relevant phenomena such as the timing of the failure of safety barriers during postulated severe accident sequences, which will initiate the fission products release from the core, and their subsequent transport into the containment. They play a very important role in the development of appropriate severe accident management measures.

In addition, these codes allow the prediction of the timing, amount and species of fission products after the containment failure or by venting as severe accident management (SAM) measure into the containment that is needed for the follow-up estimation of the radiological impact. Despite the high level of maturity reached by the current integral codes, the mechanistic nature of the severe accident as well as the physical models employed are still affected by significant uncertainties, e.g., core degradation, corium relocation, fission product behavior. Hence, there is an increased interest of the scientific community to quantify the uncertainty and sensitivity of the tools that predict the source term and the radiological consequences for the environment. Such additional information is very valuable for the Emergency team and for the development of SAM-measures. The importance of such evaluations is reflected by international activities of the IAEA [Coordinated Research Project “Advancing the State-of-Practice in Uncertainty and Sensitivity Methodologies for Severe Accident Analysis in Water Cooled Reactors”] and the European project named MUSA (Herranz & Paci, 2020)

Finally, dedicated tools are under development, validation and improvement for the prediction of the radiological impact such as JRODOS (Karlsruhe Institute of Technology (KIT), 2017) at KIT, AUSTAL of the German Environment Agency (BMU, 2002) etc. A new trend is the quantification of the uncertainty and sensitivity of such tools provided that the radiological source term and uncertainty bands for the species are provided, which can be calculated in a previous step.

After Fukushima accident, Technical Support Organizations (TSOs) and regulators re-evaluated the accident management (AM) strategies of each European NPP to identify improvements considering lessons-learnt (BfS, 2015) (WENRA, 2013) (Lankin, 2014) (Laaksonen, 2013). Because of it, the improvement of accident management strategies was implemented in many countries (NEA-OECD, 2013) (Mizokami, 2022) (Manara, et al., 2018). Finally, a re-evaluation of the emergency plans for all NPP-types started aiming to increase the protection of citizens and environment against hazardous release of the fission products (IAEA, 2012).

Finally, since many reactors of VVER-type are in East and West Europe and other of newer design (VVER-1200) are under construction outside Russia, it is crucial and necessary to develop and establish simulation platforms that describes the full plant behavior under core melt-down accidents with the most appropriate and validated tools including the radiological impact.

On the above-mentioned issues, the main motivation of this thesis is the development of a platform to calculate radiological impact of a severe accident in VVER reactors starting from the initiation of the event including uncertainties and realistic fission product inventory.

1.2 Problem formulation & challenges

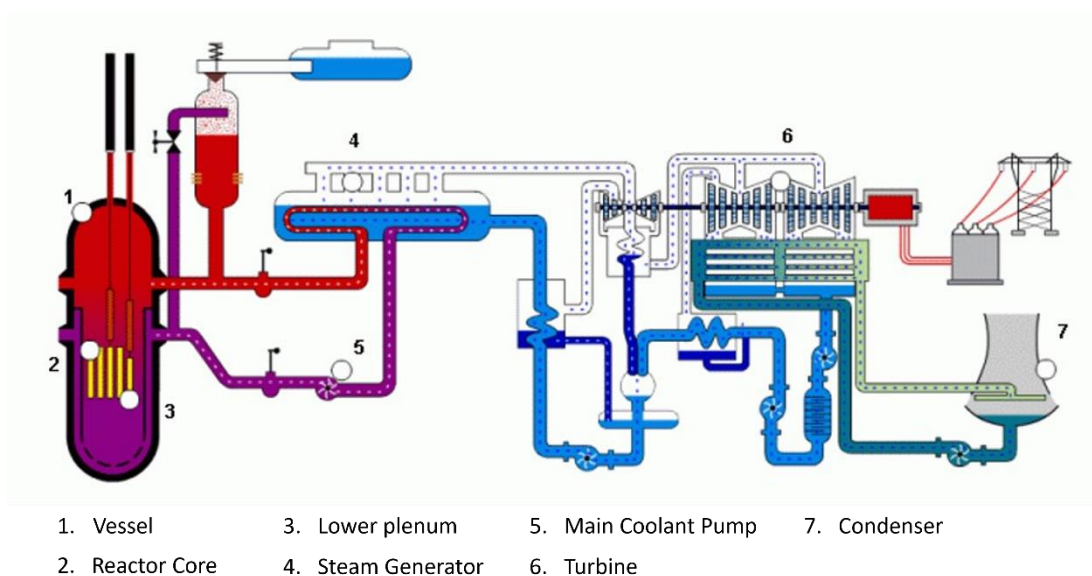


Figure 1-1: Sketch of typical loop with pressurizer of VVER-1000 plant modified from (Nuclear Regulatory Authority of the Slovak Republic, 2010)

Figure 1-1 illustrates the sketch of typical VVER-1000 plant. In the core region, the fresh fuel composition of the VVER-1000 includes only enriched U and burnable poisons.

However, the concentrations of the isotopes change during the operation of the NPP. Within several days, fission products start to be created due to fission reactions and natural radioactive decay. While some of these fission products like Xenon starts decay soon due to its short half-life, they also have large absorption cross-sections altering the core inventory (Cacuci, 2010) and multiplication factor. In addition, cladding and structural materials are also activated due to the interaction with neutrons and different radiation types (α , β , γ). Naturally, the core inventory becomes more complex since it depends on the burn-up level of the core and effective power operation day including downtimes and recycling of the core inventory. Under accidental conditions, the reactor is shut down so that the nominal power falls to a residual power (fission products, actinides, store energy in structures, of around 7 % of the nominal power) which decays with time. In addition, the initial mass inventory of fission products can be transported to the containment and to the environment in case of an integrity loss of the fuel rods and the vessel. It can also be discharged from the primary and secondary circuit in case of a Loss of Coolant Accident (LOCA), or Steam Generator Tube Rupture (SGTR) accident. Therefore, accurate prediction of the nuclide inventory is significantly important to provide reliable information to the regulators and emergency teams soon after the occurrence of a severe accident. Finally, the status of the core in terms of beginning of cycle (BOC) or end of cycle (EOC) is also an essential information to support the related bodies since it may drastically impact the source term and radiological impact due to dispersion of the released inventory (Gabrielli, et al., 2022). To achieve reliable information about the initial inventory, depletion calculation based on Monte Carlo methods (Garcia, et al., 2020) (Lötsch, 2014) (Meiyin, et al., 2014) coupled with depletion codes as well as standard deterministic burn-up calculation with pre-generated cross-sections can be performed. However, the irradiation history of the reactor and specific power as well as core material composition and dimensions are needed for the calculation. In the end, the mass or the molar concentration of the light elements, fission products and actinides are provided to the system and integral codes from dedicated depletion code simulations.

The release of the radiological inventory from the nuclear installations is the initial pillar for the assessment of the potential radiological risk (Sehgal B. R., 2012). The fission product inventory because of fission reaction, irradiation and depletion can be released due to integrity loss of the fuel rods in case of a severe accident. These fission products are carried on the aerosols and steam to the primary circuit. In the end, these products are transported to containment depending on the accident scenario. Accurate simulation of accident progression during a severe accident is essential to predict the transportation of such source term and several severe accident tools such as mechanistic code of RELAP/SCDAP (Cheng, Berna, Allison, Wagner, & Hagrman, 1986) or integral codes like ASTEC (Chatelard, et al., 2016), MELCOR

(Humpries & Gauntt, 2018) are used to simulate whole process chain of severe accidents. While integral codes are composed of several submodules that deal with different thermo-physical processes, mechanistic code calculates the progression of accident simultaneously. For the realistic simulation of the transportation of the fission products to the environment, the first step is the elaboration of the comprehensive model of the vessel, the circuits and the containment of the VVER-1000 as well as the safety systems. By this way, precise initial conditions for the accident can be considered, the progression of the transient can be evaluated accurately and physical surfaces with which the FPs may interact can be properly identified. In addition to that, models to calculate several physical and chemical phenomena of a severe accident inside of the vessel until the vessel failure (in-vessel phase) and inside of the containment after vessel failure (ex-vessel phase) must be applied since they affect the prediction of the source term potentially to be released into the environment. Moreover, the decay of the fission product during the simulation has to be calculated as well as chemical power from the steam oxidation of core and vessel such as Zr, stainless steel the B₄C, and heat generated by the interaction of the FPs with the surfaces of the vessel and primary circuit since it also affects the isotope mass.

In case of potential release of radiological Source Term during severe accidents, these can be carried by the winds over the certain geography and can be deposited to the soil and water sources. The radiological dispersion analysis becomes essential to predict the possible consequence of these Source Term inventory. During the release, acute doses to the population can be reached by the exposure by the radiation due to isotopes in the cloud (cloud shining) and radioisotopes reach to the ground by rainfall and gravity (ground shining). After that, these isotopes can be integrated to the food chain to be transferred to the foodstuff and feedstuff. Gaseous isotopes and noble gases are potential for cloud shining and skin doses whereas Cs, Sr and I isotopes are more hazardous in case of deposition to the foodstuff and feedstuff creating certain doses, depending on half-life of the isotope, in case of consumption of these products. Hence, the primary step of the radiological consequence analysis is providing isotope-wise activity to the atmospheric dispersion tools to predict potential impact. To predict the dispersion of the radioactive material and the radiological impact, atmospheric dispersion and decision support systems like JRODOS (Raskob, Trybushnyi, Ievdin, & Zheleznyak, 2012) and PAVAN (Bander, 1982) are developed. When considering the release of the activity of the isotopes, atmospheric conditions and geopotential status of the land is critical information to determine the impact to the population. This information is used by atmospheric dispersion models and depending on the wind speed, wind direction, and rainfall rate, the impacted area and contamination will change. Therefore, accurate weather history is essential information for these studies. In addition, geopotential information gives clues about terrain structure, agricultural and commercial activity of selected structure as well as population of the area, which are important

to evaluate potential and long-term dose projections. Finally, each country generates their regulations and limits for these hypothetical events and this information can be applied for emergency planning and coordination of the emergency teams. Early emergency plans depending of the regulations of related countries are used to assess the effectiveness of these activities over the radiological dose estimations.

The severe accident progression in NPPs involves numerous physical and chemical phenomena occurring simultaneously. Indeed, the knowledge behind the progress of the events is based on the existing nuclear accidents and experiments dedicated to specific phenomena happening during an event. Hence, the models that have been used in integral and mechanistic codes are based on these experiences and experiments. Because of this situation, many models dedicated on particular physical and chemical phenomena may have uncertainties by themselves or when it happens together with other phenomena. When all the progress of severe accident from the initiation of the event to the radiological dispersion, cumulative impact of the uncertainties become more influential over the results. Therefore, determination of the uncertainties is essential to sustain best-possible information to the regulators and early emergency teams. By this way, efficient and applicable plans on the intervention of the possible consequences of a severe accident can be developed considering the uncertainty bands about e.g., time of release, amount of release of fission products, and level of dose. In addition, sensitivity studies permit us to identify the most influential parameter for a specific figure of merit. Then research priorities can be focused on these parameters and less on other not so important ones. The prediction accuracy of e.g., severe accident tools is determined by the initial and boundary conditions, and by the extensive number of model parameters included in the codes for the mathematical/physical description of all severe accident phenomena of a specific nuclear power plant. Since the design of any nuclear system has complex structure and lack of experimental data, and limited information on severe accidents, numerous uncertain factors need to be considered. However, consideration of all these uncertainties creates expensive computations. Therefore, the initial step of the uncertainty quantification and sensitivity analysis is determining the Figure-of-Merits (FOMs). FOMs can determine which parameter requires a focus of investigation. Quantification of uncertainties can be done with both deterministic methods and sampling based. Deterministic methods have low cost in terms of computation and the contribution of each parameter can be determined but require much information such as sensitivity between input and output, covariance of the parameters. Even though sampling methods require high computational effort due to high number of samples for accuracy, linear and non-linear models can be applied (McKay, Beckman, & Conover, 1979). The most used method for uncertainty quantification i.e. the propagation of the uncertainty of the input done by the use of Monte Carlo or Latin Hypercube sampling in tools like SUSANA

(GRS, 2021), URANIE (Gaudier, 2010), SUNSET (NEA, 2007), DAKOTA (Adams & Hooper, 2020), RAVEN (D'onorio, Giannetti, Mascari, & Caruso, 2018), KATUSA (Stakhanova A. , Gabrielli, Sanchez-Espinoza, Pauli, & Hofer, 2022). After this point, determination of necessary sample size must be performed for supporting certain confidence level (Wilks, 1941). Finally, sensitivity analysis method should be applied to find out the most contributing variables over selected results (Saltelli, Chan, & Scott, 2009).

1.3 Goals of the thesis

Considering the motivation, the doctoral thesis is focused on the development and application of a complete and novel computational framework that allow the prediction of the radiological impact after a hypothetical severe accident in a NPP as in a VVER-1000 and the assessment of the uncertainties and sensitivities of tools for the prediction of the radiological source term and radiological impact. For this purpose, the following technical goals are addressed:

- Estimation of the realistic nuclide inventory in the core of a VVER-1000 NPP,
- Validation of the integral severe accident code ASTEC regarding the physical and chemical models of the early in-vessel phase of a severe accident in a VVER-1000 reactor using the data of the QUENCH-12 test, and identification of the model deficiencies.
- Development of an integral VVER-1000 plant model for the ASTEC-code for the simulation of severe accident sequences with core meltdown and FP-release into the environment.
- Evaluation of radiological impact on environment and the people after a hypothetical severe accident s in a VVER_1000 NPP using the JRODOS-code
- Quantification of the uncertainties and sensitivities of the ASTEC and JRODOS codes using the KATUSA-code

1.4 Structure of the thesis

The doctoral thesis includes nine chapters to achieve listed goals of the work. The brief description about the VVER-1000 plant are provided in **Chapter 2**. The important physical and chemical phenomena occurring during a severe accident in a generic VVER reactors is described in **Chapter 3**. In-vessel and ex-vessel events are covered, and transportation of the

Fission Products is reviewed in this section. **Chapter 4** covers the tools used for performing the analysis and computational pathway for the KORIGEN-ASTEC-JRODOS-KATUSA platform.

Chapter 5 describes the validation work of the ASTEC code with the QUENCH experiment. The capabilities of the code are evaluated, and deficiencies of the code are illuminated. After the validation work, the simulation of the selected severe accident scenario on the VVER-1000 reactors is presented in **Chapter 6**. The modelling of main components of the primary /secondary circuit, the reactor pressure vessel, containment, and safety systems of VVER-1000 reactor using the ASTEC is shown there. In addition, the severe accident scenarios for the VVER-1000 reactor are identified in this chapter. Radiological dispersion of the Source Terms obtained from selected severe accident scenarios are analyzed with ASTEC and the results are discussed in **Chapter 7**. The assessment of the uncertainties and sensitivities of the ASTEC and JRODOS codes when predicting the radiological source term and its radiological impact are described and discussed in **Chapter 8**.

The key findings of performed doctoral work are summarized in **Chapter 9**. In addition to the main chapters, following Appendixes support the main work:

- **Appendix A** covers further results for the validation of the ASTEC with VVER QUENCH-12 test.
- **Appendix B** includes further results of the selected severe accident cases modelled on ASTEC.
- **Appendix C** contains additional results of the consequence analysis performed with JRODOS with the source terms estimated by ASTEC calculations.
- **Appendix D** shows further analysis results of the U&S analysis and additional findings of the comparative results of the two sets of the source terms.

2 Brief description of the VVER-1000 Nuclear Power Plant

In order to simulate the severe accident progression in a NPP, information about the internal and external structures of the plant as well as safety systems are required. Therefore, this chapter is devoted to the description of the structures of the VVER-1000 plant unit.

2.1 Core characteristics

The VVER-1000 core has 163 hexagonal fuel assemblies which contain 312 fuel rods and 18 control rods. The total mass of the fuel is about 77 tons. The dimensions of the generic VVER-1000/V320 fuel and clad are shown in **Table 2.1**. The material composition of the VVER-1000/V320 cladding and equivalent mass for 1 tHM is shared in **Table 2.2**. Finally, **Figure 2-1** demonstrates the layout of the generic VVER-1000 assemblies.

Table 2.1: The fuel and clad dimensions of a generic VVER1000/V320 core from (Murphy, et al., 2000)

Parameter	Value
Clad inner diameter	0.772 cm
Clad thickness	0.07220 cm
Fuel pellet diameter	0.755 cm
Central hole diameter	0.15 cm
Height of the column	355 cm

Table 2.2: The material composition of VVER1000/V320 clad and equivalent masses for 1tHM from (Murphy, et al., 2000)

Material	Weight %	Mass in 1 tHM (g)
Zr	94.21849	281348.31
Nb	0.95199	2849.37
Hf	0.02856	85.48
Fe	3.35491	10041.47
Ni	0.50410	1508.81
Cr	0.88818	2659.38
Ti	0.04801	143.70
C	0.00576	17.24

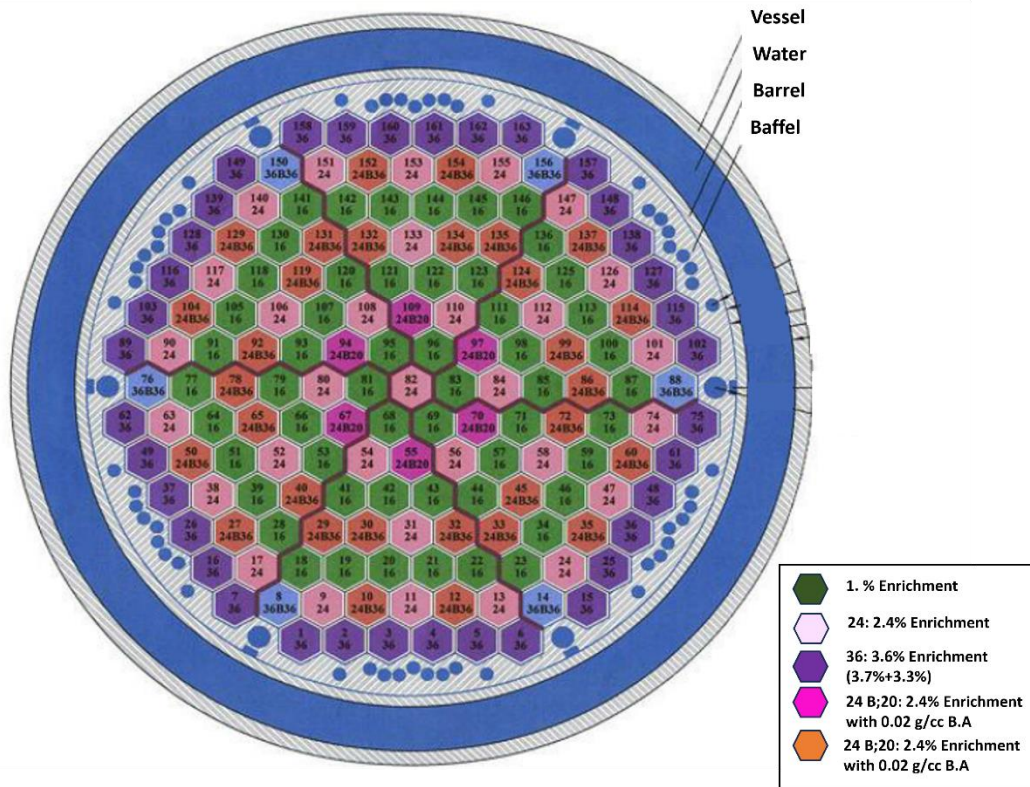


Figure 2-1:The radial layout of the VVER-1000 assemblies modified (Hadad, Mirvakili, Safaei, & Nematollahi, 2009)

During the irradiation process of the core of VVER-1000, the nuclide composition of the fuel rods changes significantly. Because of this situation, the inventory at the BOC and EOC may create significantly different impacts in case of severe accident. The inventory of the actinides and fission products are about 13.6 kg/t initial inventory at the low burnups whereas it can reach up to 66.16 kg/t initial inventory (Murphy, et al., 2000) which means additional decay heat during the severe accident and increase of the potential source term inventory and radiological impact. **Figure 2-2** illustrates the lower plenum (LP) of the VVER-1000 reactor and dimensions in mm. Fuel assemblies are in the core by the help of 163 support columns inside of the lower plenum. While these columns create mixing effect for the coolant, additional heat surface might affect the heat transfer between reactor pressure vessel (RPV) walls and the corium during a meltdown. Finally, the layout of the vessel is given in **Figure 2-3**.

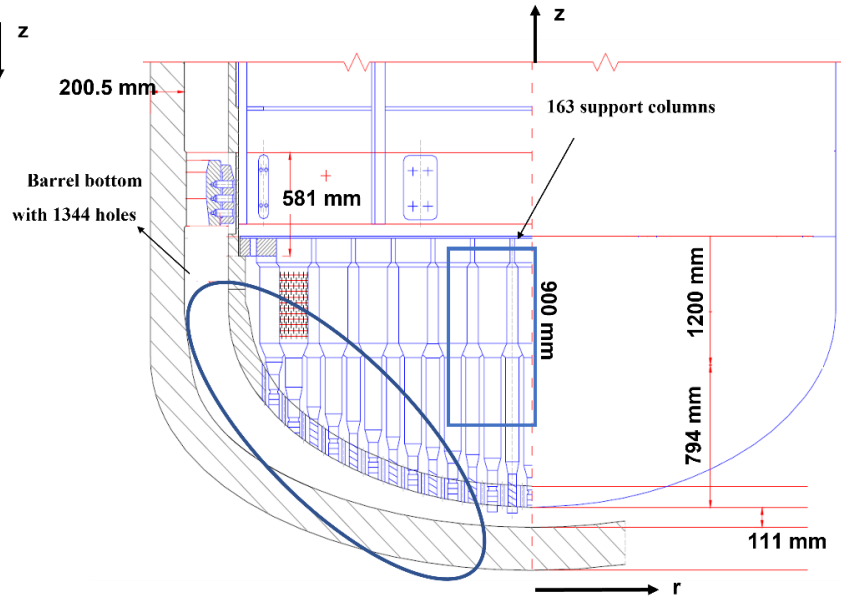


Figure 2-2: The layout of the lower plenum of the generic VVER-1000 core modified from (Ivanov, Ivanov, Groudev, Pavlova, & Hadjiev, 2002)

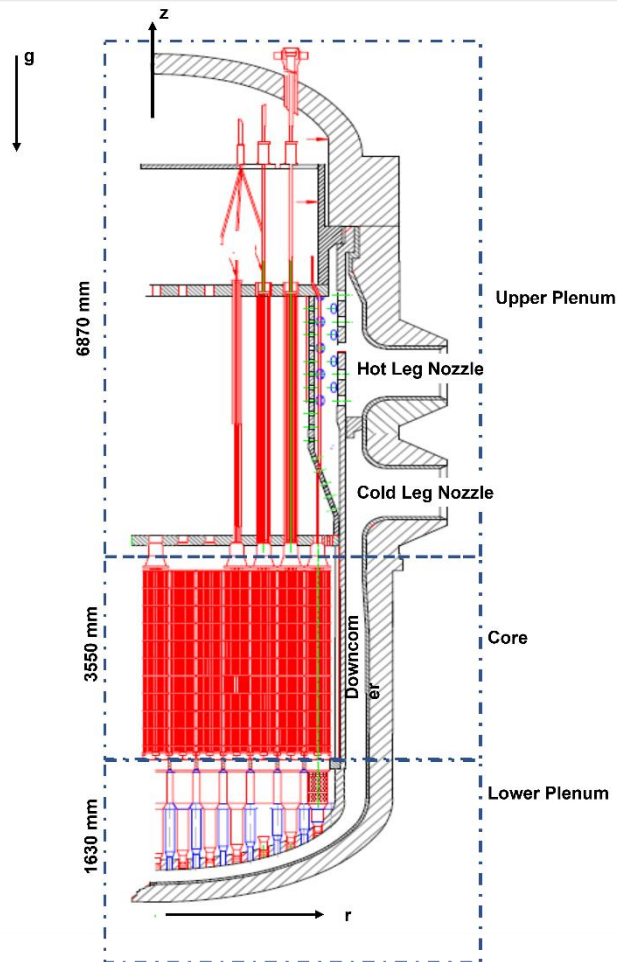


Figure 2-3: The layout of the vessel of the generic VVER-1000 modified from (NEA-OECD, 2004)

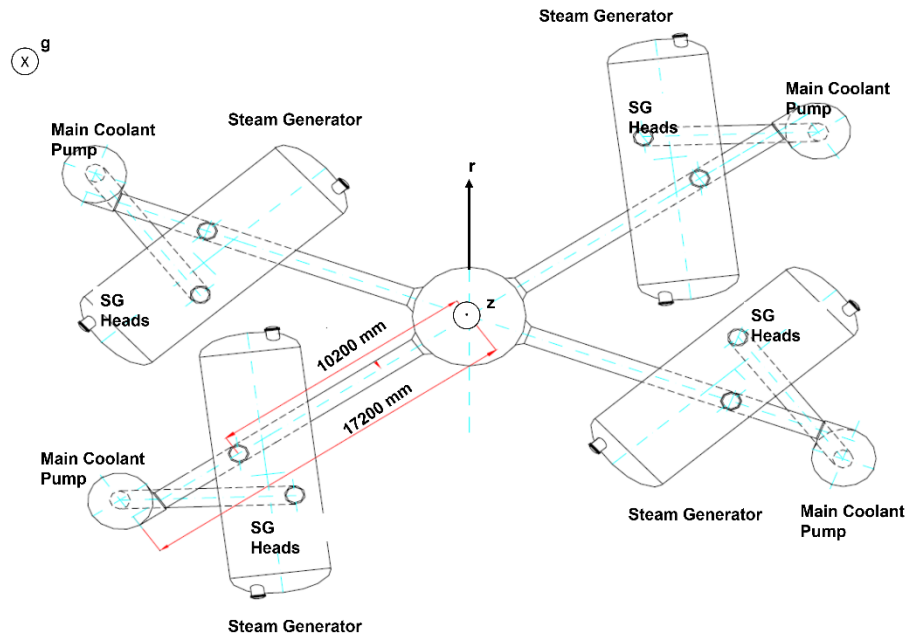


Figure 2-5: Geometric arrangement of the steam generators and coolant loops modified from (Ivanov, Ivanov, Groudev, Pavlova, & Hadjiev, 2002)

The pressurizer is responsible for adjusting pressure inside of the system. It includes heaters and spray system to help adjust the pressure. While spray system activates when pressure increases, the heaters generate additional steam in case of pressure decrease. This system is connected to the hot leg by surge line. The layout of the pressurizer is demonstrated in **Figure 2-6**. The physical properties of the SGs, pressurizer and other elements of the reactor coolant system (RCS) are listed in **Table 2.3**.

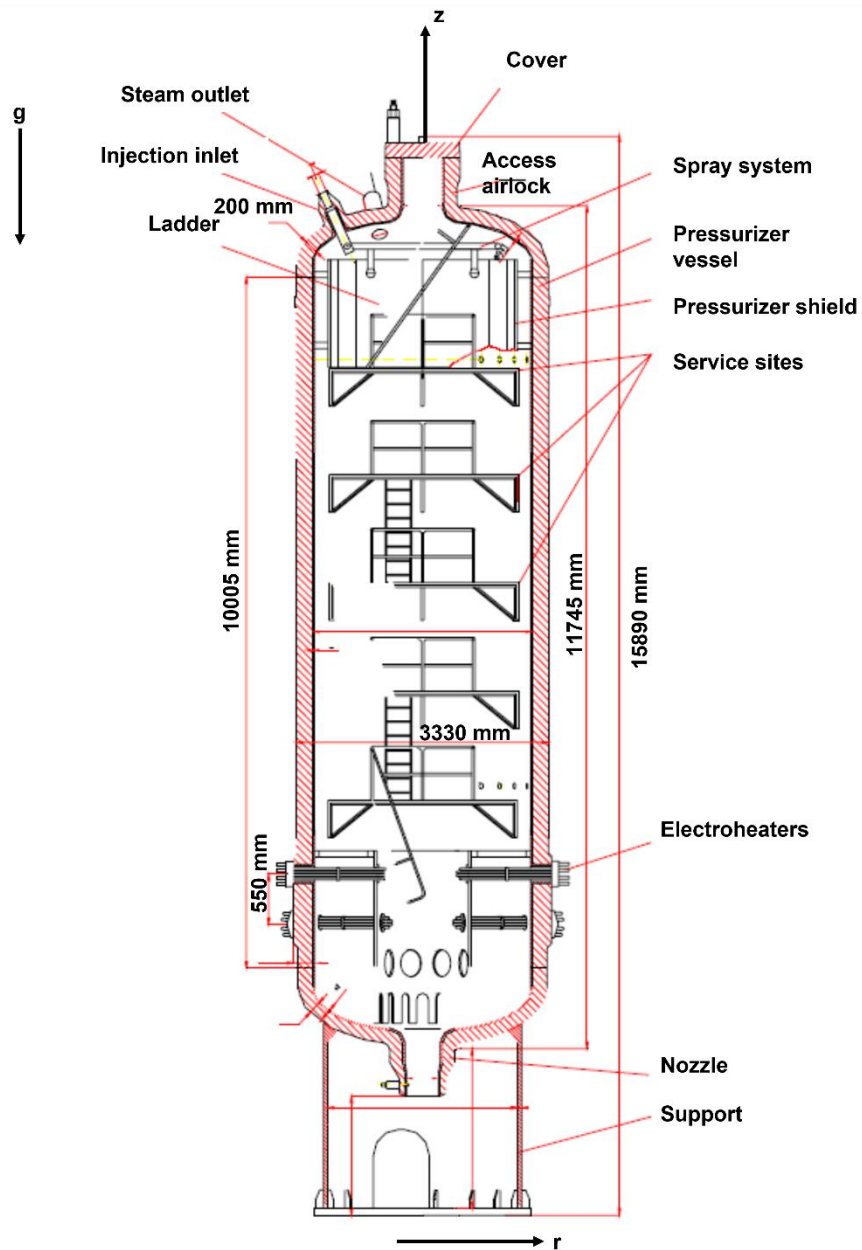


Figure 2-6: The layout of the pressurizer of the generic VVER-1000 modified from (Ivanov, Ivanov, Groudev, Pavlova, & Hadjiev, 2002)

Table 2.3: Dimensions areas and volumes of the primary and secondary circuit components of the generic VVER-1000 modified from (Ivanov, Ivanov, Groudev, Pavlova, & Hadjiev, 2002)

Description of SGs	Value	Description of Pressurizer	Value	Description RCS	Value
Length of the tubes (m)	11.1	Nominal Pressure (MPa)	16	Hot Leg Length (m)	10.12
Number of tubes	11000	Height(m)	12.7	Cold Leg Length (m)	26.6
Primary Side Volume (m^3)	20.5	Water Level (m)	8.77	Coolant Volume in one cold leg (m^3)	15.07
Volume of SG head (m^3)	2.4	Water Volume (m^3)	55	Coolant Volume in one Hot Leg (m^3)	5.74
Inner Diameter of the tube (mm)	13	Steam Volume (m^3)	24	Hot Leg Diameter (m)	0.85
Outer Diameter of the tube (mm)	16	Total Volume (m^3)	79	Cold Leg Diameter (m)	0.85
Total Heat Transfer Area of the Tubes (m^2)	1.46	Internal Diameter (m)	3	Coolant Flow Rate (kg/s)	17611
Heat Transfer Area of Secondary Side (m^2)	6115	Spray Line Length (m)	219	Surge Line Diameter (m^3)	0.346
Hydraulic Diameter of Secondary Side (m)	0.174	Spray Line Inner Diameter (m)	0.181	Coolant volume in Surge Line (m^3)	1.69
Total Volume of MSL (m^3)	162	Spray Line Outer Diameter (m)	0.219	Volume of MCPs (m^3)	3
Feedwater Temperature (K)	551.65	Relief Valve Steam Flow (l/hr)	50	Nominal Flow of MCPs (m^3/s)	5.555
Feedwater Flow (kg/s)	437	Relief Valve Diameter (m)	0.2	Nominal Rotor of MCPs (rad/s)	104.2

2.3 Containment

A typical VVER-1000 reactor consists of 3 main building structures. These are reactor building, auxiliary building and turbine building. The reactor building has two layers of containment and covers all the circuits of the NPP and vessel. Also, safety buildings and steam cells are in the reactor building. Auxiliary building is used for the storage of fresh fuel and solid radioactive waste and service building whereas turbine building includes the turbine and generator. The view of the generic VVER-1000 containment is shown in **Figure 2-7**.

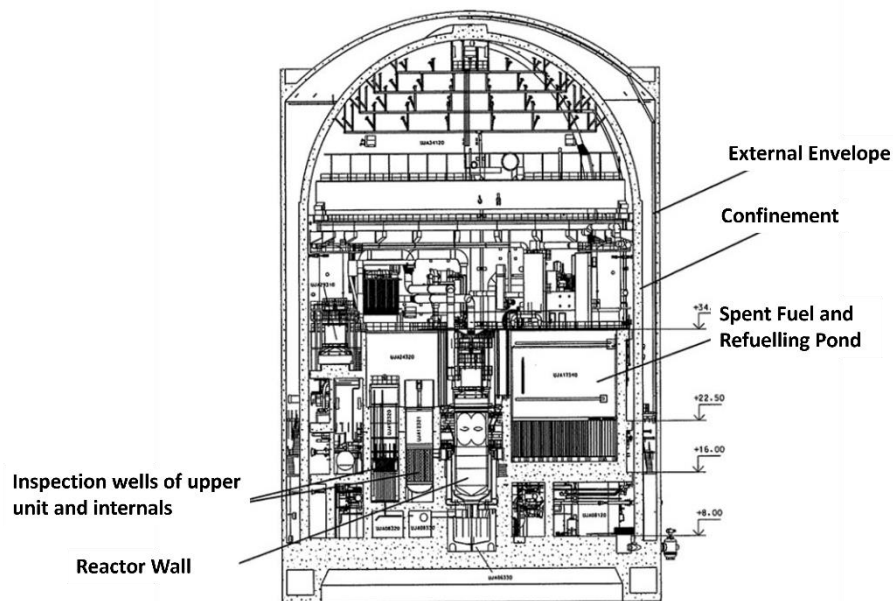


Figure 2-7: The generic containment of the VVER-1000 plant modified from (Ryzhov, et al., 2010)

The cavity of the VVER-1000 consists of siliceous type of concrete with lower gas content and higher iron fraction compared to regular PWR. Total height of the cavity is 2.35 m, and cavity floor area is 31.47 m^2 which cylindrical parts is 26.53 m^2 (Stefanova, Gencheva, & Groudev, 2011). The scheme of the lower end of the reactor and cavity section of the VVER-1000 is illustrated in **Figure 2-8**. Also, the chemical composition of the VVER-1000 cavity concrete with concentration of the species is given in **Table 2.4**.

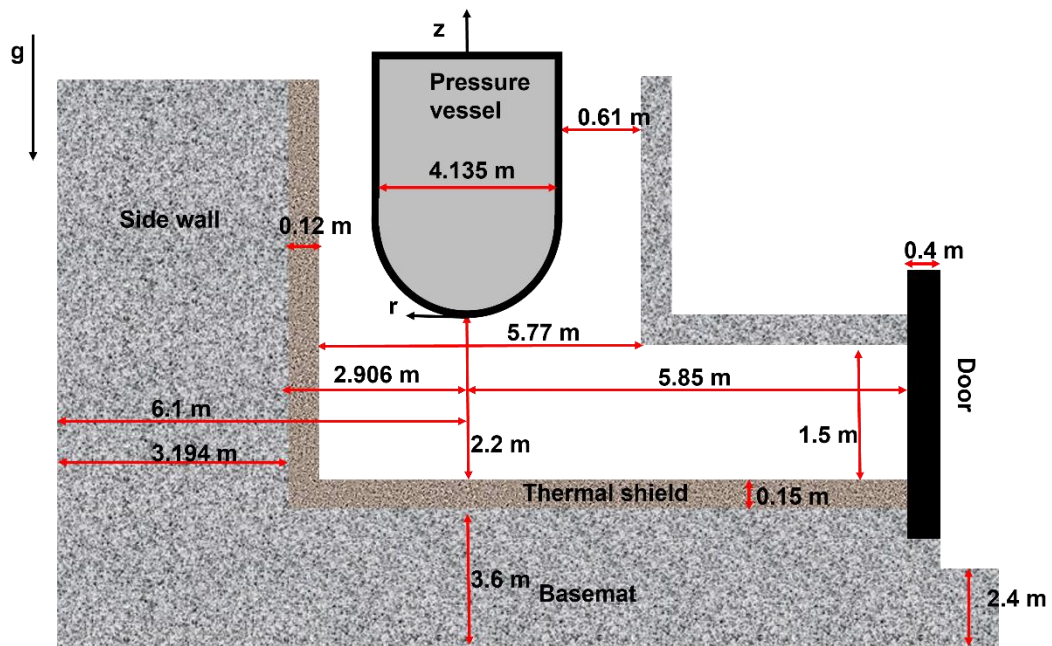


Figure 2-8: The sketch of the lower end of the reactor and cavity hall of VVER-1000 reactor modified from (Stefanova, Gencheva, & Groudev, 2011)

Table 2.4: The chemical composition of the concrete used in VVER-1000 cavity modified (Stefanova, Gencheva, & Groudev, 2011)

Species	Concentration (%)
H_2O_{chem}	1.775
H_2O_{evap}	3
Fe	16.17
CaO	20.3
MgO	1.135
CO_2	6.761
SiO_2	47.36
Fe_2O_3	2.01
Al_2O_3	1.775

2.4 Safety systems

Various mitigation and preventative safety systems are designed for the VVER-1000 plants. Emergency Core Cooling System (ECCS) is the main protective system for the loss-of-coolant cases (LOCA). High-Pressure Injection System (HPIS) is intended to inject borated water to the primary circuit at high pressures. Similarly, Low Pressure Injection System (LPIS) is designed with same purpose, though it is equipped with higher water inventory than HPIS. In addition to that, hydro-accumulators (HAs) consist of four tanks to inject water from downcomer and from upper plenum passively in certain conditions. The specification of each system is shared in **Table 2.5**. Also, the layout of the ECCS system is shown in **Figure 2-9**.

Table 2.5: The technical specification of ECCS components from (NEA, 2001)

HPIS Specifications	Value	LPIS Specifications	Value	Hydro-accumulator specifications	Value
Number of Trains	3	Number of Trains	3	Number of Tanks	4
Actuation Pressure (MPa)	8.8	Actuation Pressure (MPa)	2.2	Actuation Pressure (MPa)	5.9
Boron Concentration (g/kg)	40	Boron Concentration (g/kg)	16	Boron Concentration (g/kg)	16
Total inventory (m^3)	45	Total inventory (m^3)	630	Total inventory (m^3)	50

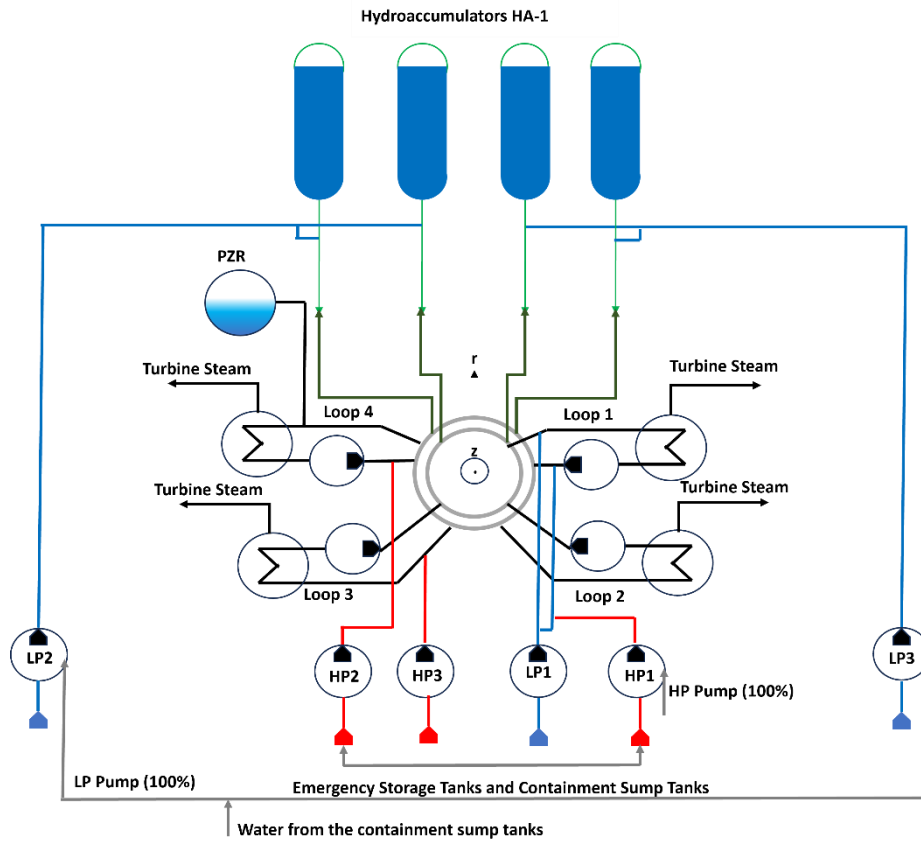


Figure 2-9: The schematical arrangement of the ECCS system in the VVER-1000 plant modified from (Queral, et al., 2021)

Several relief and safety valves are designed in the primary and secondary circuit to relieve steam from the system in case of pressure increase. This accident management systems are actively used as depressurization strategy to mitigate accident progression (Tusheva, 2012). In the pressurizer, three sets of SEMPELL type electromagnetic relief valve are located. While the control valve actuates at 18.11 MPa and closes at 16.67 MPa, the other two groups of safety valves open at 18.60 MPa and close at 17.07 MPa. These SEMPELL type valves function passively when the pressure of the primary circuit rises. Like these systems, the secondary side has four valves to dump the steam to the condenser (BRU-K), four valves to dump the steam to the atmosphere (BRU-A) and eight steam generator relief valves to decrease pressure in the secondary system in case of over pressurization. However, only BRU-A valves can function in case of blackout.

In the containment, spray systems are used to localize the accident by injecting $700 \text{ m}^3/\text{h}$ water by three trains from the dome of the containment. This system allows to pressure decrease in the containment as well as condensation of the fission products in the containment. Finally, Passive Autocatalytic Recombiners (PARs) are located inside of the containment to recombine generated hydrogen inventory.

3 Severe accident phenomena in VVER-1000 Nuclear Power Plants

An accident results with loss of partial or total loss of core geometry and loss of decay heat removal capability is defined as severe accident, and sequence of accident is divided into in-vessel and ex-vessel phase. Events from the initiating until the failure of the vessel cover oxidation of core materials, cladding failure and FP release and transport, formation of molten pool and relocation into the LP and vessel failure. After vessel integrity failure, events such as MCCI and hydrogen combustion are considered in the ex-vessel phase of an accident. The temporal phases of a Large Break Loss of Coolant Accident (LBLOCA) with Station Blackout (SBO) in a VVER-1000 is listed below:

- Initiating an event and rapid pressure drop,
- Actuation of passive safety systems,
- Core degradation due to uncover of the core structures (in-vessel phase),
- Relocation of molten material to the lower plenum,
- Reactor pressure vessel (RPV) failure and spread to the containment (ex-vessel phase),
- Release to the ambient with spread of Source Term by boundary conditions (wind speed, precipitation, wind direction etc.).

Each phase of the accident requires extensive research to understand progression of accident and determine thermal-physical phenomena involved.

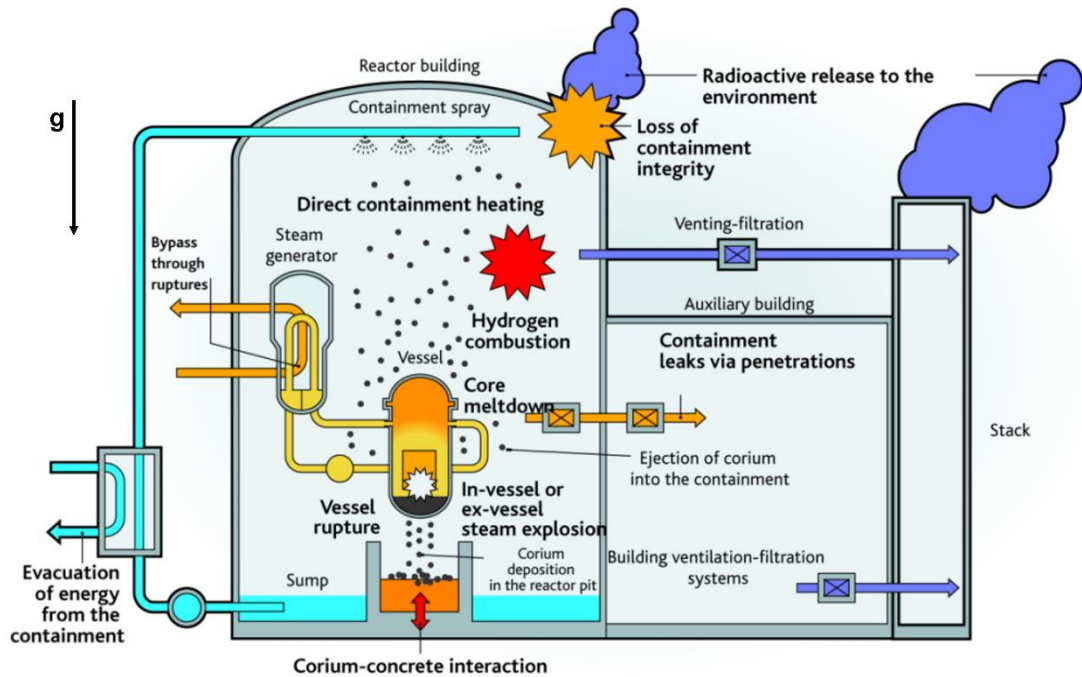


Figure 3-1: The physical phenomena occur during a severe accident modified from (Van Dorsselaere, Albiol, & Micaelli, 2011)

This chapter covers a general overview on the important phenomena occurs during in-vessel and ex-vessel phase of a hypothetical low pressure severe accidents in a VVER-1000 reactor (Sehgal B. R., 2012). Additional insights for both low- and high-pressure sequence of an accidents on PWRs and VVERs can be found in (GRS, Assessment of the Accidental Risk of Advanced Pressurized Water Reactors in Germany) (Tusheva, 2012). Fission product release from the fuel rods, physical and chemical phenomena impact the transport of fission products to the containment is also covered in this section. Finally, the chapter ends with radiological dispersion of the fission products and calculation of dose from all pathways.

3.1 Change of material composition of the core during the operation

During the operation of the NPPs, the radioisotope inventory inside of the fuel changes depending on the initial fuel composition and burn-up. Due to depletion of the fuel, fission products are generated as well as actinides. These products generate decay heat and decay heat becomes dominant power source after the insertion of control rod. Therefore, the accurate evaluation of the progress of the transient in the NPP lies within accurate estimation of the power that comes from the decay process.

The inventory of the fission products is not stable during the transients. Since the inventory alters depending on the burn-up level, decay heat can be different which results with dissimilar progression of the severe accident. Also, the amount of the fission product inventory

critically impacts the activity of the released inventory. This versatile process can be calculated by using the Bateman equations. This equation considers the generation of heavy nuclei by fission, generation of parent isotope by neutron capture or by the decay and disappearance of the isotopes by decay and neutronic capture (Bateman, 1910). The Bateman equation for the change of a single isotope during the transient is given by **Equation 3.1** where ϕ is neutron flux, σ_f^{hn} is microscopic fission cross-section each heavy nucleus (hn), σ_c^n indicates the microscopic capture cross-section of the parent (P_k), σ_a^i is the microscopic capture cross-section of the FP, N_{hm} , N_{Pj} and N_{Pk} is the concentration of each hn and parents that coming from branching ratios of α_i^j and β_i^k , y_n^i is the fission yield of each hn, and radioactive decay constants of FPs and parents are represented as λ_i and λ_{Pk} respectively (Sehgal B. R., 2012).

$$\frac{dN_i}{dt} = \underbrace{\phi \sum \sigma_f^{hn} y_{hn}^i N_{hn}}_{\text{Heavy nuclei creation due to fission}} + \underbrace{\sum \alpha_i^f \lambda_n^i N_{Pj}}_{\text{Generation of parent by decay}} + \underbrace{\sum \beta_i^k \sigma_c^{Pk} \phi N_{Pj}}_{\text{Generation of parent by neutron capture}} - \underbrace{\sigma_a^i \phi N_i}_{\text{Neutron capture of the FP}} - \underbrace{\lambda_i N_i}_{\text{Radioactive decay of the FP}} \quad \text{Equation 3.1}$$

3.2 Key phenomena during the in-vessel phase

The summary key phenomena of the in-vessel of a severe accident are summarized in this part of the section. Lessons learnt from the TMI-2 accident enlightens many phenomena in this stage but several experiments on LWR also extend the research. CORA (Schanz, Hagen, Hofmann, Schumacher, & Sepold, 1992) experiment investigates the early phase of in-vessel phase, oxidation of claddings and interaction of the fuel and clad. Also, QUENCH (Steinbrück, Große, Sepold, & Stuckert, 2010) (Stuckert, Steinbrück, & Große, Experimental program QUENCH at KIT on core degradation during reflooding under LOCA conditions and in the early phase of a severe accident, 2015) experiments help the investigation of oxidation as well as reflooding of the degraded core. For the core degradation, molten material behavior and vessel failure mode, CODEX (Hózer Z. , Summary of the Core Degradation Experiments CODEX, 2002), FARO (Magallon, 2006), MASCA (Asmolov & Tsurikov, 2004), and FOREVER (Sehgal, et al., 2005) test was carried out, and PEARL (Repetto, Garcin, Eymery, & Fichot, 2013) and LIVE (Gaus-Liu, Miassoedov, Cron, & Wenz, 2010) experiment are being resumed.

In case of severe accident, the coolability of the core is not sustained due to unavailability of necessary safety systems. Coolant starts to boil off and core starts to uncover from starting of the top part of the core. The steam environment in the uncovered part of the core reduces the heat transfer compared to liquid phase, thus core heats-up by decay heat the prevalent of approximately a rate of 100 K/s (NEA, 2009) and tests the limits of the barriers. Additionally, exothermic reaction of oxidation of core materials such as Zr in cladding, stainless steel in structural components and B_4C inside of control rods by steam provides additional heat-up of the core. The phases of core degradation in a LWR fuel rod and melting points of the materials inside of the core are shown in **Figure 3-2**. Core degradation process of VVER-1000 is quite similar with the typical VVER cases. Slight material differences in VVER claddings and structural materials can lead early deterioration of the cladding (Hózer, et al., 2005), and having boron-carbide for control rods, and stainless steel for the control rod cladding can lead additional hydrogen production and gaseous carbon species similar to the BWR case (Hózer, et al., 2006).

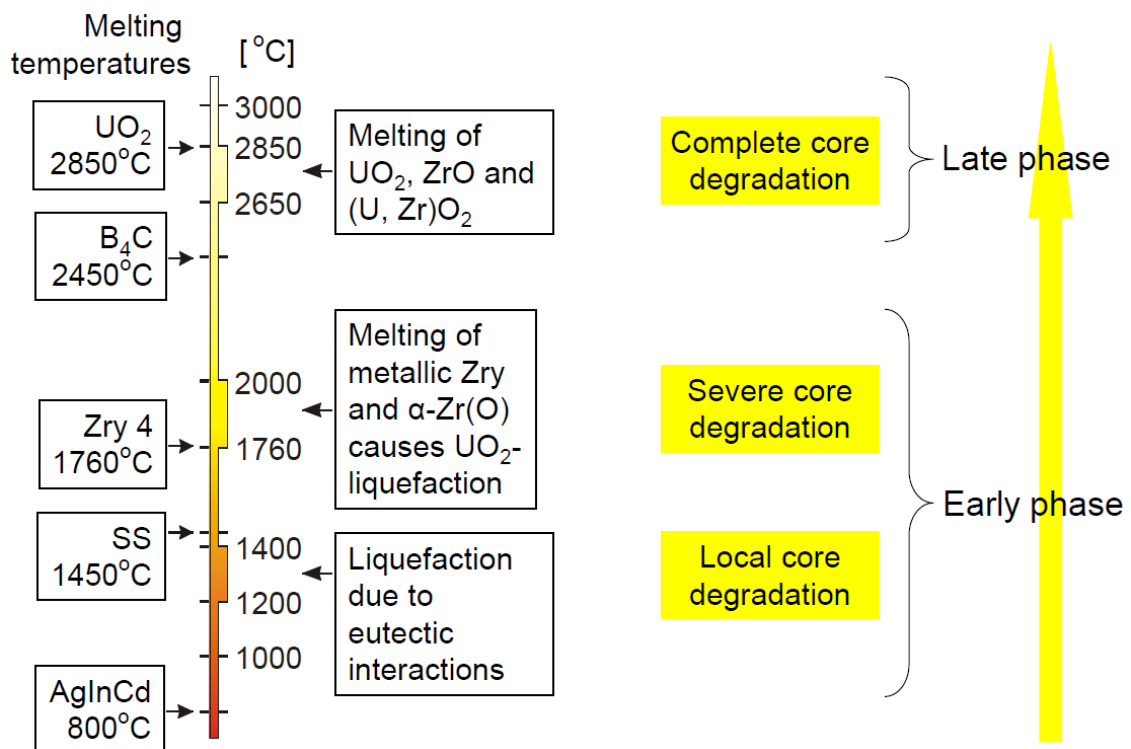


Figure 3-2: The melting points of several nuclear core materials as a function of temperature [°C] (left) and phases of the accident progression assigned to the temperature level from (Schanz, Hagen, Hofmann, Schumacher, & Sepold, 1992)

3.2.1 Oxidation of core materials

VVER core includes large amount of Zr-1%Nb (namely E110) used in cladding, B_4C used in control rods and several steel compositions like 15XHMΦA, 08X18H10T, 12X18H10T

10ГН2МΦА (IAEA, 1994), and uncover of the core leads to oxidation of these material. Zircaloy oxidation is the most vital for the VVER reactors since the core includes a large mass of Zr related materials. The additional energy produced due to Zr oxidation (585 kJ/mol) contributes to the melting of the core, as well as the weakening in mechanical integrity of the cladding material in phase transformation and the production of combustible hydrogen forces the integrity of the reactor. Stainless steel oxidation also forms on the metallic surfaces and contributes total hydrogen production (Powers, 1981). Additionally, influence of alloying elements such as Cr and Ni and supporting elements such as Mo, Ti, V and Nb adds unique complexity for the estimation of oxide layers.

Oxidation experiments on Zircaloy based claddings has defined that diffusion of oxygen anions through zirconia structures that has not sufficient anion is the dominating process of oxidation (Urbanic & Heidrich, 1978) (Prater & Courtright, 1985) (Sokolov & Andreeva-Andrievskaya, 1993), and mass gain and layer growth can be modelled by parabolic laws. However, specific conditions such as the breakaway process and steam starvation are not defined by parabolic laws. For the Zr-1%Nb materials, three oxidation regimes are defined according to (Sokolov & Andreeva-Andrievskaya, 1993);

- Field of effective tetragonal $\beta\text{-ZrO}_2$ ($T < 1798$ K)
- Transition region between $\beta\text{-ZrO}_2$ and $\alpha\text{-ZrO}_2$ (1798 K $< T \leq 1900$ K)
- Field of existence of ZrO_2 ($T > 1900$ K)

3.2.2 Cladding ballooning and burst

Insufficient cooling in case of severe accident can lead to increase of the internal pressure of the rod to the point and system pressure can be smaller than the internal pressure. This situation leads to ballooning of the clad and eventually cladding burst. Between 1100 and 1300 K, plastic deformation of the E110 cladding takes place which is almost 100 K lower than the one in Zircaloy cladding (Hózer, et al., 2005). In the end, not only additional oxidation due to oxidation of internal surface of cladding will produce further hydrogen but also radiological inventory will be transported to the primary circuit (Nagase, Konings, & Stoller, 2020). **Figure 3-3** shows the burst pressure against temperature comparison of E110 used in VVERs and Zircaloy-4.

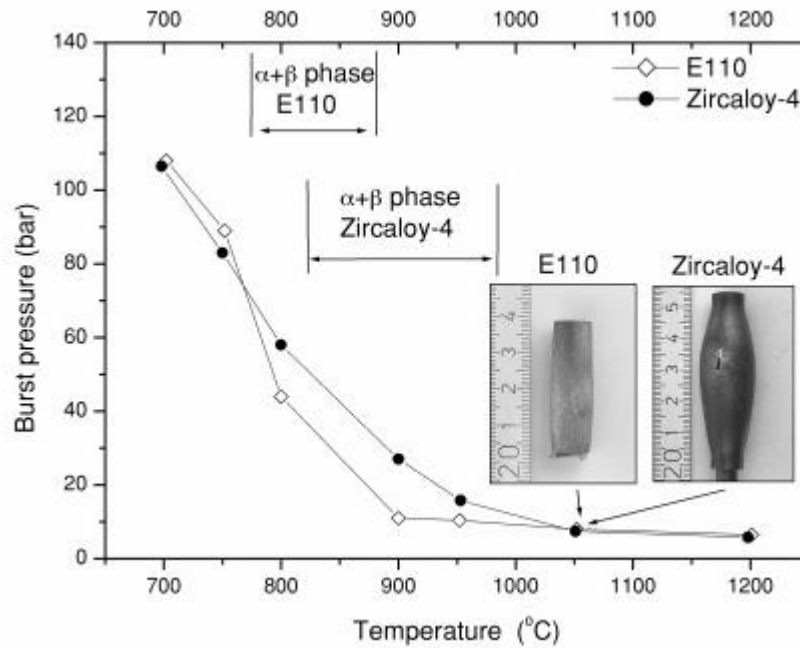


Figure 3-3: Measured change of burst pressure against the burst temperature of E110 and Zircaloy-4 claddings from (Hózer, et al., 2005)

3.2.3 Formation of the molten pool and relocation to the lower plenum

Meltdown of the cladding leads to relocation of U-Zr-O mixtures to move downwards of the core region. Relocation to the lower sections of the core may result in the freezing of this molten mixture creating blockages inside of the channels. Molten pools inside of the core are generated with remelting of these frozen crust structures in case of insufficient cooling (Sehgal B. R., 2012). The molten pool spreads radially and axially inside of the core until the baffle on the sides and lower plenum support plates at the bottom. Relocation to the lower plenum can lead to the failure of this structure leading to the relocation to the lower plenum. Also, relocation to the lower plenum can occur due to melting through the baffle.

3.2.4 Failure of lower plenum of the vessel

The in-vessel accident progression ends with the breach of the lower head during a severe accident. After molten material relocation to the lower plenum, immense thermal and physical load start to challenge the lower head. The molten material composition inside of the lower plenum is dispersed according to their densities. UO_2 and ZrO_2 like oxidic materials create a dense layer which relocates the bottom of the pool. Heavy metallic structures relocate to the bottom of the pool whereas light ones can create a layer at the top of the oxidic pool. Since the radiative heat transfer is effective, these light metallic layers can melt during the process. Lower radiative heat transfer to the upper part of the metallic layer, most of the heat is transferred

radially at the points in contact with the metallic layer on the reactor protection vessel walls which creates ``focusing effect``. The spallation of the layers and focusing effect is shown in **Figure 3-4**.

Temperature of the molten materials, the mechanical pressure due to load, corrosion inside of the lower plenum (LP) can lead to failure of the walls. Even though internal pressure of the molten material and the mechanical stress are the primary sources of the load, temperature creates creeps and plastic deformations on the walls. The location of the failure can be located where the temperature is the highest and the danger of the event increases at higher elevations of the LP since stress in the cylinder part of the vessel higher than in those in the sphere part (Sehgal B. R., 2012).

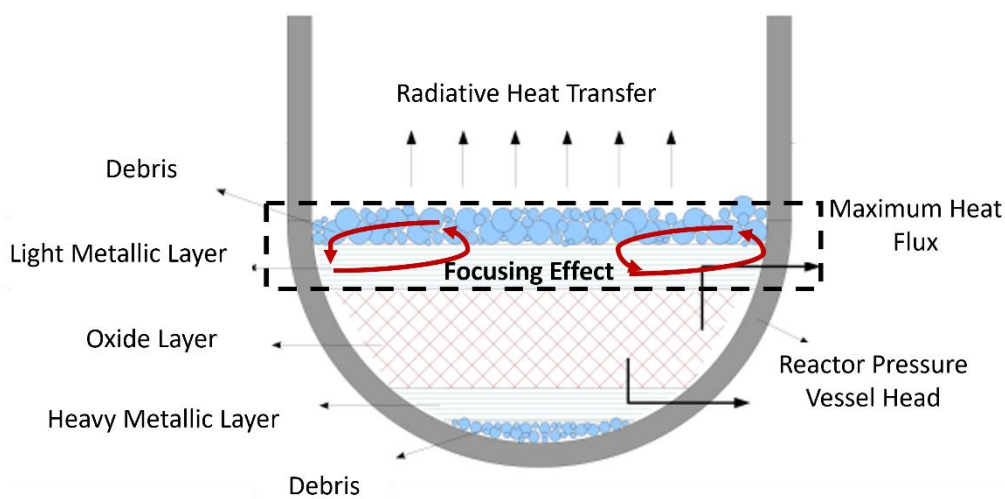


Figure 3-4: The debris configuration in the lower plenum and focusing effect modified from (IRSN, 2021)

3.3 Key phenomena during the ex-vessel phase

The phase of ex-vessel accident progression covers the process that may result with failure of the containment. During this stage, direct containment heating (DCH) and hydrogen detonation create additional pressure load on the containment and challenge the integrity of the structure at an early stage. Molten Core-Concrete Interaction (MCCI) process also threatens the integrity of the containment due to ablation inside of the cavity at later phases. Furthermore, gas generation during the MCCI process not only pressurizes the containment but also contributes burnable gas inventory inside of the containment. For the evaluation of hydrogen behavior during a severe accident case, experiments such as THAI (NEA/CSNI/NEA, 2007), TOSQAN (Malet, Porcheron, & Vendel, 2010) and MISTRA (Studer, Magnaud, Dabbane, & Tkatschenko, 2006) has been employed. Similarly, many major experiments like MOCKA

(NEA/OECD, 2017), CORINE (Veteau & Wittmaack, 1996), KATS (Engel, Fieg, Massier, Stiegmaier, & Schütz, 2000), BETA (NEA/OECD, 2017) and VULCANO (NEA/OECD, 2017) are dedicated to observe ex-vessel cooling, spreading of corium and corium-concrete interaction under various conditions.

3.3.1 Early containment failure

During a severe accident in an NPP, containment integrity is challenged by pressure in early phase. The design of the containment covers the pressure load of a typical LOCA accident. However, there are several physical phenomena that create local pressure peaks inside of the containment. These are (Sehgal B. R., 2012):

- Hydrogen burning and detonation,
- Direct containment heating (DCH),
- Steam explosions.

Hydrogen is produced during the severe accident case from many sources such as zirconium-steam oxidation, boron carbide-steam reaction, oxidation of steel by steam, molten core-concrete interaction (MCCI), corrosion of metallic structures inside of the containment etc. Most dominant factor to the hydrogen production is zirconium oxidation. Indeed, cladding of fuels consists of the composition of zirconium and sometimes other structural materials like grid spacers, and guide tubes in VVER and control rod claddings in BWR contributes total zirconium inventory. Oxidation starts after the uncover of the core liquid inventory and it can accelerate when the cladding loses integrity and steam ingress in the rod to react with the inner surfaces of cladding. Additionally, reflooding of the hot core provided by the accumulators increases the steam inventory inside the vessel and favors further hydrogen production. Finally, the MCCI process increases additionally the hydrogen inventory inside of the containment due to ablation of the cavity, and CO and CO₂ are also generated because of this phenomenon which are also non-condensable gases similar as hydrogen. In certain conditions, hydrogen and CO might burn and even detonate inside the containment. Explosions inside of the containment might create pressure spikes and challenge the integrity like in Fukushima. **Figure 3-5** shows the Shapiro diagram that represents burning and detonation limits of air-steam-hydrogen volumetric concentrations (Shapiro & Moffette, 1957).

When the lower head of the pressure vessel loses its integrity due to thermal and physical loads of molten materials, these materials are transferred to the cavity. The transfer can be driven by gravity when the pressure difference level between RPV and the containment is small or none. In case of larger pressure differences, rapid ejection of the molten materials transfers materials to the cavity. Heat exchange between the molten materials and the cavity not only

produces additional hydrogen and CO but also increases the temperature and pressure inside of the containment due to entrainment onto cavity walls. Even though containment spray system could be used to decrease temperature inside of the containment and diminish the FP inventory by condensation, this application has potential of increasing hydrogen production. Therefore, systems such as passive recombiners in VVERs are used to neglect reaching critical concentrations during a severe accident (Queral, et al., 2021).

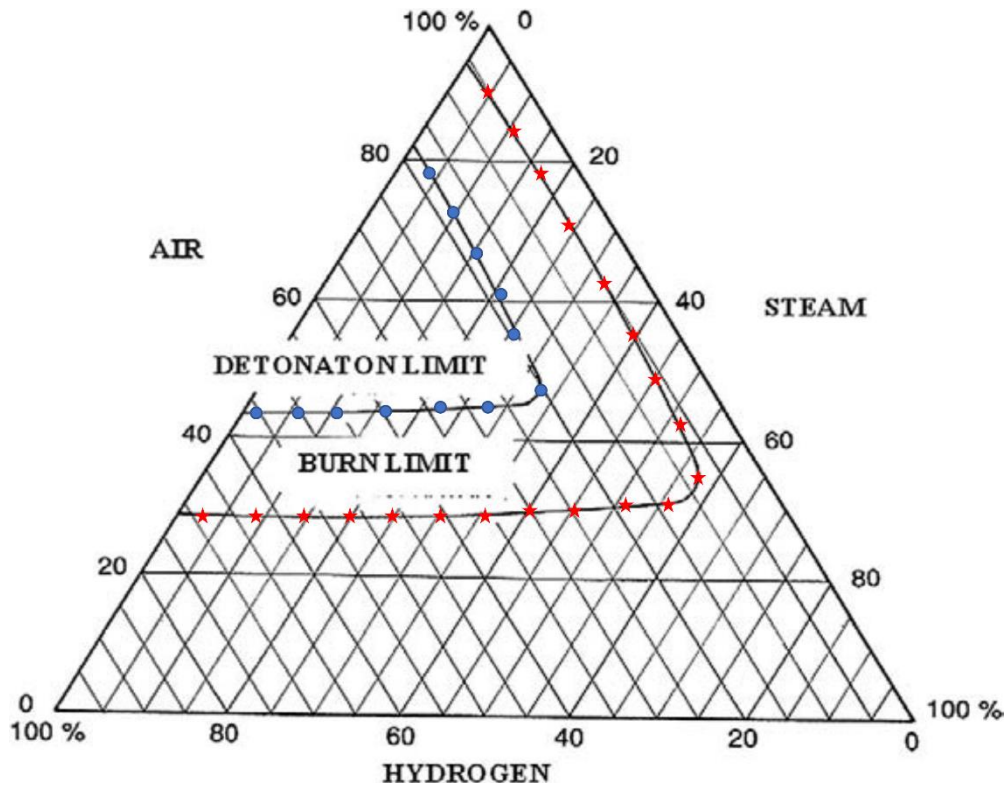


Figure 3-5: Evaluated detonation and burn limits for volumetric fractions of hydrogen-air-steam mixtures in the Shapiro diagram modified from (Shapiro & Moffette, 1957)

Steam explosions during severe accidents are observed when molten materials contact the coolant and critical contact temperature is exceeded. Fragmentations of the corium materials creates unstable mixtures inside of the water and results with explosions. These explosions can escalate to supersonic velocities that may challenge RPV walls as chemical explosions. Similarly, this phenomenon can be seen inside of the cavity, and it can challenge cavity walls as well.

3.3.2 Late containment failure

As described in the previous section, molten materials either relocate to the cavity by gravity or melt ejection. In this stage, the consideration of having water pools or not inside of the cavity alters the progression of the accident. The stabilization of the corium is essential not

only the keeping integrity of the cavity to avoid late containment failure but also for avoiding radiation release to the environment.

In dry cavity conditions like in VVER-1000, the corium starts to ablate adjacent walls between 1200 °C and 1400 °C depending on the cavity structure. In the early phase of the ablation, high heat flux is transferred to the cavity wall and intense gas generation can be observed. In medium-term phase, concrete oxide mass increases and oxidation of remaining zirconium and steel contributes high heat flux. VVER-1000 has typical limestone-sand concrete with higher iron fraction and lower gas content (Stefanova, Gencheva, & Groudev, 2011).

Wet cavity conditions, either deep pools in Nordic BWRs or pools with small depths (Sehgal B. R., 2012), have potential of steam explosions and steam generation when water and molten materials contact. This situation can lead to DCH and rise of containment temperature and pressure but coolability of the corium can be sustained.

3.4 Fission products release and transport into the containment

The process starts with the fission product release to the environment leading to radiological dispersion of the source term (ST). Estimation of the ST is the starting point of the risk assessment, therefore, accurate prediction of the inventory by including chemical and physical processes inside of the primary circuit and inside of the containment is essential for the assessment of the distribution of the hazardous materials in the environment. The fission product release starts after the integrity loss of the cladding. While the noble gases are transported to the containment without any retention, volatile and low-volatile isotopes go under retention depending on their volatility. The PHEBUS test are dedicated to understanding these phenomena occurs during this stage (Clement & Zeyen, 2013). Additionally, failure of the vessel results with transport of the fission products to the containment. After this stage, MCCI process further increases the fission product release due to ablation. Finally, depletion of the isotopes due to decay process impacts the inventory released to the environment. The important fission products and their half-lives are given in **Table 3.1**. The noble gases are indicated as red, and the volatile isotopes are written in orange. Also, semi-volatile and low volatile isotopes are represented with green and blue. Finally, the non-volatile isotopes are black on the table. While noble gases such as Xe and Kr isotopes can be source of internal exposure, long half-lived isotopes of Cs and Sr can remain in the soil and impact the foodstuff and feedstuff in certain regions.

Table 3.1: The half-life and volatility of the main fission products

Short half-lived isotopes		Medium half-lived isotopes		Long half-lived isotopes	
Fission product	Half-life	Fission product	Half-life	Fission product	Half-life
Xe-135	9.1 h	Xe-133	5.2 d	Kr-85	10.7 y
Kr-88	2.8 h	Xe-133m	2.2 d	Cs-137	30.1 y
I-132	2.3 h	Mo-99	2.8 d	Sb-125	2.8 y
I133	20.8 h	I-131	8 d	Cs-134	2.1 y
I134	0.9 h	Zr-95	64 d	Sr-90	28.6 y
I135	6.6 h	Te-132	3.2 d	Ce-144	284 d
Ba-137m	2.55 min	Ba-140	12.8 d	Ru-106	1 y
Rb-88	17.77 min	La-140	1.7 d	Eu-144	8.6 y
Zr-97	1.2 h	Np-239	2.43	Ag-110m	0.7 y

Aerosol particles are formed in the reactor coolant system (RCS) due to condensation of the fission products in the coolant and these are carried by the steam flow. These aerosols may interact with each other or with the wall surfaces of the coolant system which resolves fusing of particles or built ups and inclusion of chemical interactions are essential since all phenomena are dependent to the temperature. The main effective physical and chemical phenomena in the RCS are listed in (Sehgal B. R., 2012):

- Homogenous nucleation of vapors,
- Agglomeration by sedimentation, Brownian diffusion, and turbulence,
- Deposition by thermophoresis, electrophoresis, sedimentation, inertial impactation, turbulence, pool scrubbing, and diffusiophoresis,
- Revaporization,
- Mechanical resuspension,
- Reaction with deposits and/or the gas phases,
- Condensation on aerosols and surfaces,
- Chemical reactions between other gases, aerosols, vapors and structural surfaces.

3.5 Dispersion of radioactive isotopes and radiological impact

Dispersion of the radioactive inventory to the environment requires information of meteorology and hydrological data definition. Inventory distribution and activity concentration in the food are highly influenced by seasonal and daily changes of meteorological data. Therefore, site specific meteorological and hydrological data are essential for the characteristic of the dispersion (IAEA, 2002). The dispersion of the released material in the atmosphere and deposition into the soil due to this dispersion requires numerous calculations to estimate doses to the population, health effects and costs as well as to develop protective actions. While wind and turbulence influence the transport of these materials, radioactive decay of these isotopes as well as wet and dry contamination alters the whole process. Therefore, Gaussian puff model (Zannetti, 1990) or trajectory models are used. The basic scheme of a Gaussian plume model is shown in **Figure 3-6**. These models require constant rate of release, constant atmospheric conditions, uniform geometry and altitude. However, different turbulence conditions, different stability classes defined by Pasquill-Gifford class (Kernforschungszentrum Karlsruhe (KFK), 1984) or velocity fluctuations computed from eddy diffusivities using Monin-Obukhov theory (Sun, Takle, & Acevedo, 2020), result with different horizontal and vertical crosswind diffusion parameters. Therefore, Gaussian based puff models are generated to be able to introduce change in atmospheric conditions. Also, Lagrangian particle models are the next step improvement of dispersion modelling by large number of independent particles move along individual trajectories.

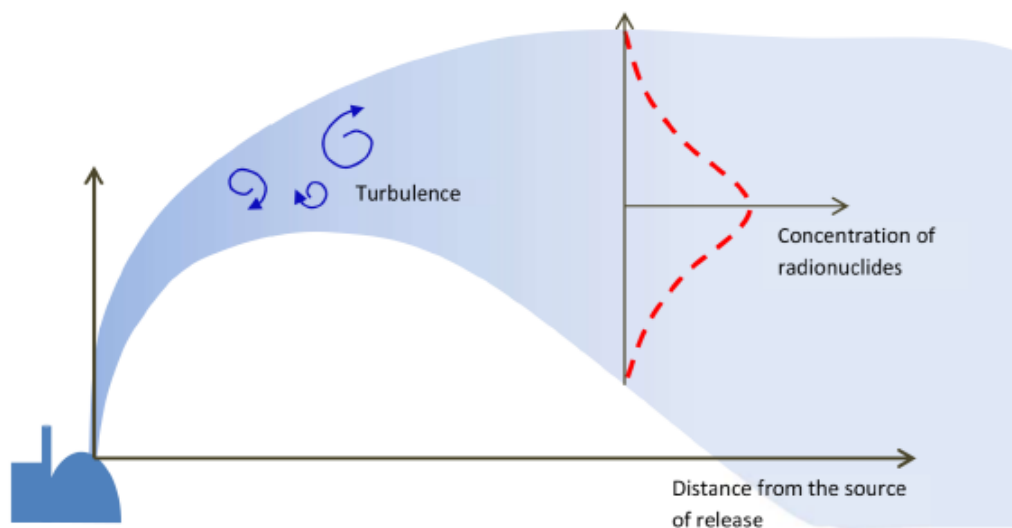


Figure 3-6: Scheme of a Gaussian plume model from (IAEA, 2020) indicative spread of radionuclides as function of distance from release of plant site

The description of the basic Gaussian plume dispersion model is given by **Equation 3.2** modified from (Sehgal B. R., 2012) where Q, released material activity in Bq, h is the height of plume centerline in m, u is wind speed in the direction of x in m/s, z and y is the coordinates in a puff directions and θ_z and θ_y represents diffusion coefficients direction of the downwind z and y. These diffusion coefficients can be determined differently in all around world but most owned method is Pasquill parameters (Pasquill, 1961) which is calculated based on the relation of turbulent types to the weather conditions (Slade, 1968).

$$C(x, y, z) = \frac{Q}{2\pi\theta_y\theta_z u} \left\{ \exp\left(-\frac{(z-h)^2}{2\theta_z^2}\right) + \exp\left(-\frac{(z+h)^2}{2\theta_z^2}\right) \right\} \left\{ \exp\left(-\frac{(y)^2}{2\theta_y^2}\right) \right\}$$

Equation 3.2

The deposition of the radioisotopes can be either dry deposition due to adsorption, impaction or sedimentation and wet deposition because of washout by rains. These depositions have risk of exposure to the population and soil, and different ways of the exposure depending of the scenario impact the population. External radiation exposure can be from the source and plume by cloud shining whereas deposition on the skin and ground can be created by ground shining. Inhalation of the plume of resuspend material can create risk of internal exposure. Also, the ingestion of radionuclides from processed food and water can be a source of the exposure by internally. The transfer of the isotopes to the foodstuff and feedstuff is shown in **Figure 3-7**. To prevent and mitigate the exposure, countermeasures such as evacuation of the population from the area of dispersion, sheltering of the people by using barriers like buildings, potassium iodide distribution to avoid radioactive iodine uptake by supporting stable iodine and relocation of the population are considered. Each country develops their emergency planning according to their regulations and ICRP recommendations in according to principles of justification, optimization and application of dose constraints to avoid stochastic and deterministic effects of the events.

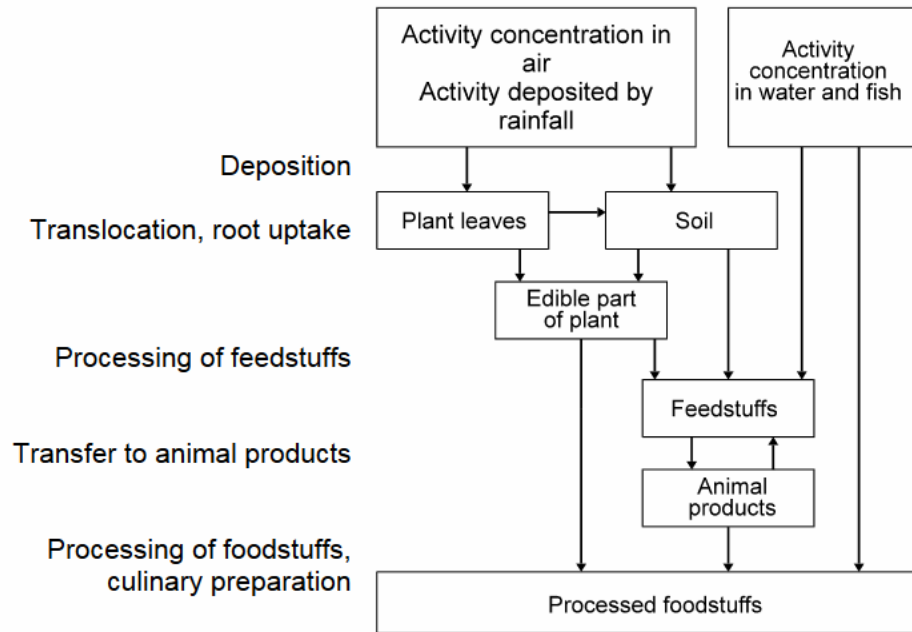


Figure 3-7: Transfer chain options of the activity concentration from radionuclides to foodstuff from (Raskob, Trybushnyi, Ievdin, & Zheleznyak, 2012)

4 Developed Calculation Platform

This chapter describes the numerical tools that form part of the computational route for the prediction of the dispersion of fission products and the subsequent radiological impact after a hypothetical severe accident with release of fission products in a VVER-1000 NPP located in different sites. It requires numerical tools to describe the many models to calculate physical and chemical phenomena happening during an event within each part of the reactor. Therefore, integral code of ASTEC is used to simulate entire SA accident sequences using nuclide inventory calculated by the KORIGEN. The radiological dispersion and dose projection analysis is performed by means of JRODOS. The KATUSA tool is selected for uncertainty and sensitivity study, and again JRODOS is used to analyze the impact of these uncertainties on the radiological dispersion distribution. The calculation route is demonstrated in **Figure 4-1**.

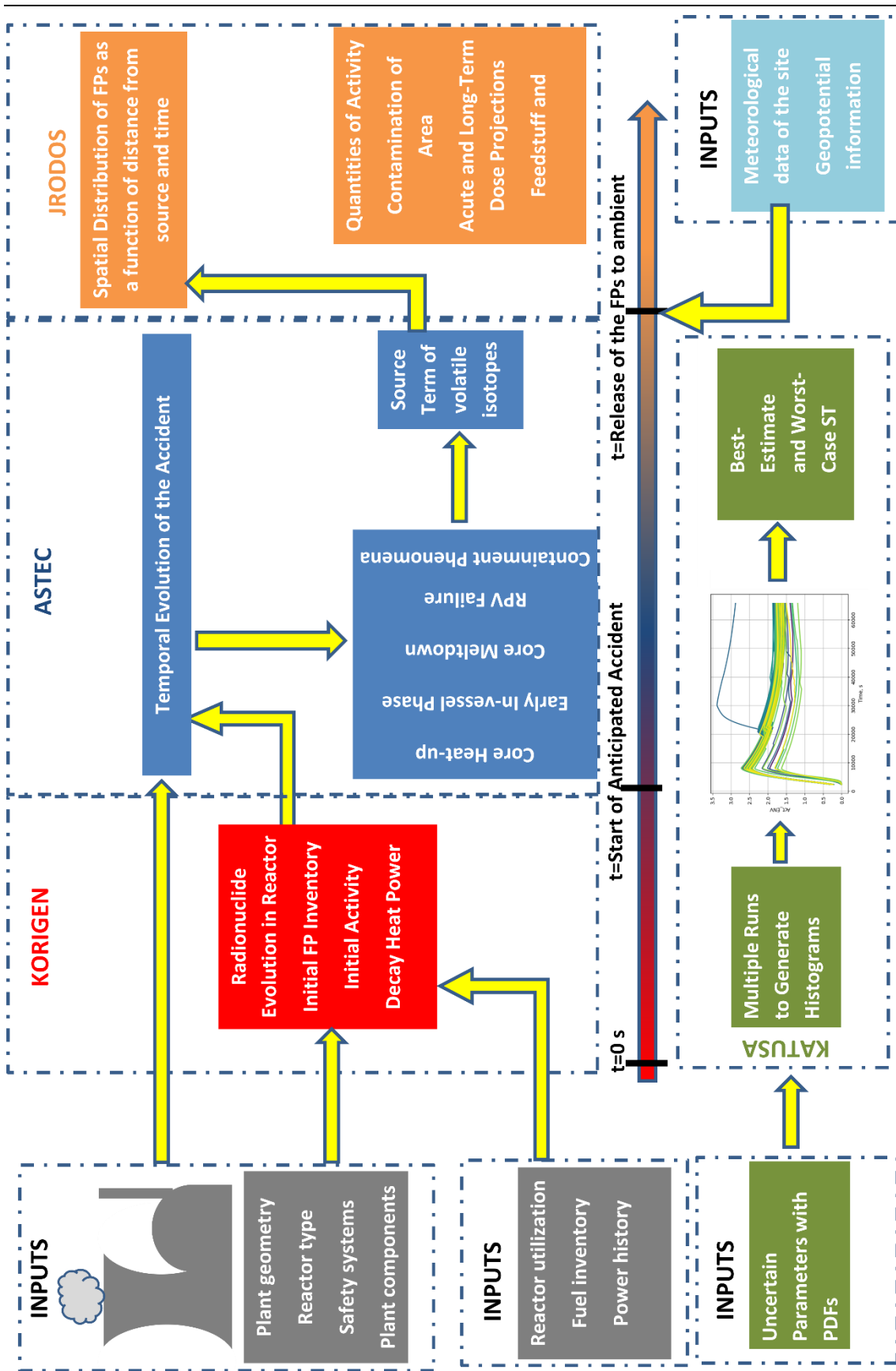


Figure 4-1: ASTEC-JRODOS-KATUSA calculation route

4.1.1 The KORIGEN code for depletion analysis of the core

To calculate the inventory of the fission product after depletion and burn-up of the VVER-1000 core, KORIGEN analysis is performed. This tool is developed by KIT to perform depletion calculations by using pre-generated cross-section databank and material information. KORIGEN also includes the decay data for isotopes as well as ground and metastable state information to support accurate isotope mass, isotope activity, and isotope-wise decay energy. Estimation of these parameters is calculated by using the initial material composition of the fuel and clad along with fuel irradiation history. In addition to that, Refueling and reshuffling of the core can be considered and inventory evaluation for the spent fuels can be performed (Wies & H.W., 1998).

4.1.2 Integral severe accident code ASTEC

The ASTEC was developed by IRSN to simulate entire severe accident sequences in water-cooled reactors from initiating event to the release of the radioactive elements from the containment for PWRs, BWRs, SMRs and spent fuel pools. Modular structure of the ASTEC includes models and parameters required to simulate thermal and physical processes during a severe accident as well as FP decay, transport and release (Chatelard, et al., 2016) and the structure of the code is shown in **Figure 4-2**. ASTEC reference code is widely used for probabilistic safety assessments as well as interpretation of experiments. Validation of the code has been performed with Phebus FP, QUENCH and MCCI experiments (Chatelard & Laborde, 2022).

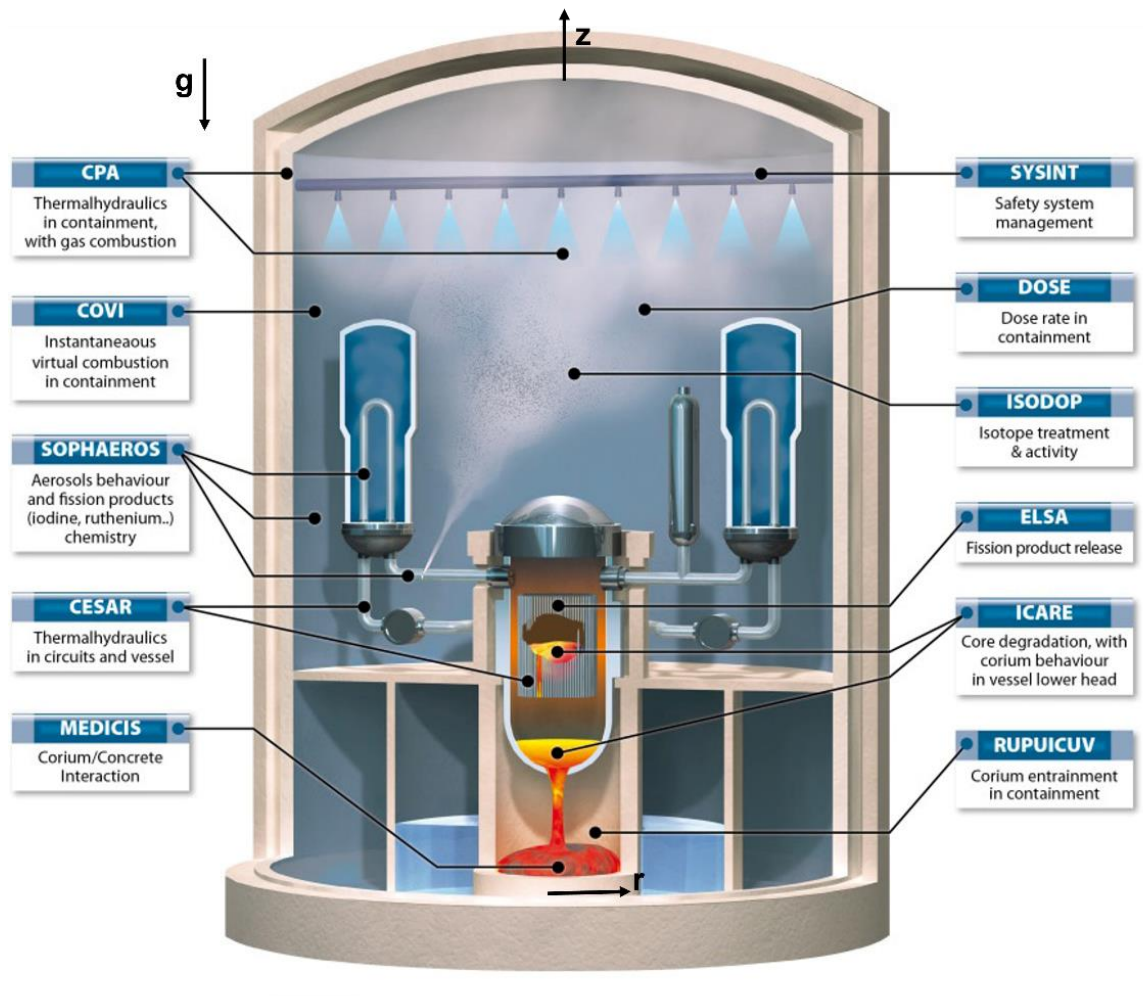


Figure 4-2: General structure of ASTEC integral code and its modules from (Chatelard & Laborde, 2022)

The ICARE module of ASTEC calculates in-vessel phenomena such as oxidation, molten material relocation, vessel failure. The ISODOP module is used for initial fission product inventory whereas the ELSA module deals with release of the FPs from the fuels and the SOPHAEROS simulates aerosol behavior and chemistry of the FPs as well as transport and release of them. CESAR module is responsible for thermal-hydraulic calculation inside of the reactor coolant system of the ASTEC. The CPA module covers the thermal-hydraulic behavior inside of the containment, but MEDICIS and RUPUICUV modules are required to simulate ex-vessel phenomena like Direct Containment Heating (DCH) and Molten Material-Concrete Interaction (MCCI). SYSINT includes active safety systems and COVI is the module for virtual hydrogen deflagration.

4.1.3 Radiological dispersion and impact analysis code JRODOS

Real-time On-line Decision Support (JRODOS) system is developed for decision support on nuclear emergency management. The models of the code allow to calculate atmospheric dispersion and hydrological dispersion as well as dose calculation and dose transfer from soil to feedstuff and foodstuff (Karlsruhe Institute of Technology (KIT), 2017).

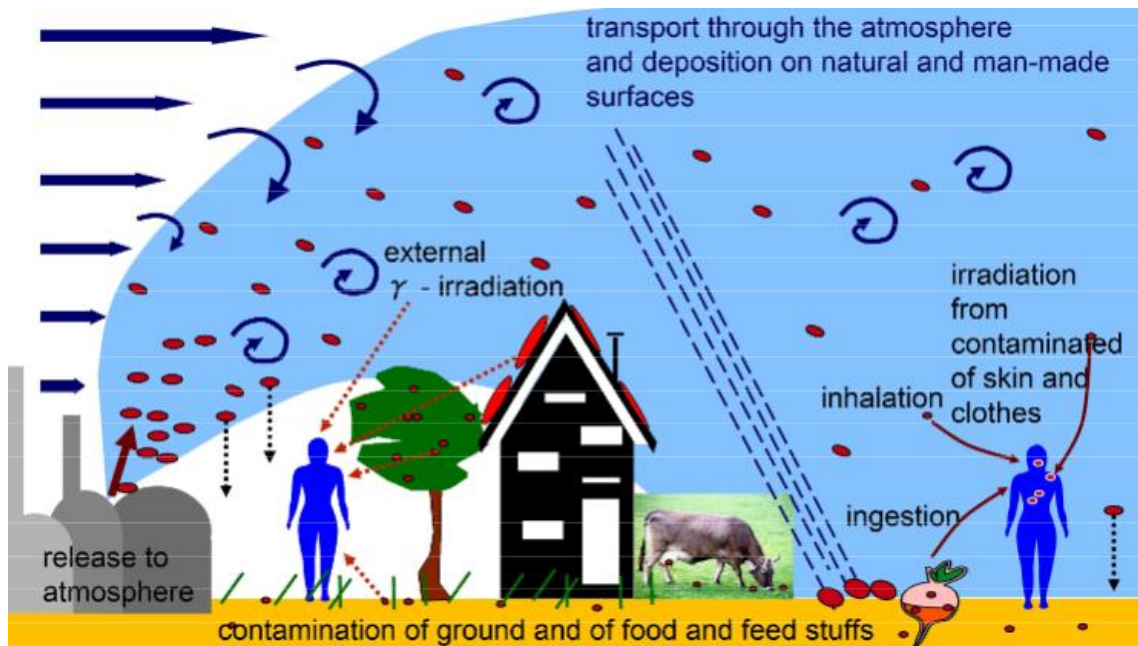


Figure 4-3: Schematic illustration of atmospheric transport of the isotopes and deposition with terrestrial exposure pathways from (Karlsruhe Institute of Technology (KIT), 2017) covered by JRODOS software

JRODOS includes several Atmospheric Dispersion Models (ADM) like ATSTEP (Päsler-Sauer, 2000), RIMPUFF (Thykier-Nielsen, Deme, & Mikkelsen, 1999), DIPCOT (Andronopoulos, Davakis, & Bartzis, 2009) etc. to simulate dispersion in different ranges. Food Chain and Dose Module for Terrestrial Pathways (FDMT) package is used for simulating radioactive material transfer following food chains by inhalation, ingestion, cloud shining and ground shining. Finally, Early Countermeasure Module (EMERSIM) predicts individual doses as well as acute and long-term doses on the population including early emergency action.

4.1.4 Uncertainty Quantification with The Karlsruher Tool for Uncertainty Quantification and Sensitivity Analysis (KATUSA)

FSTC tool is developed by KIT in frame of WAME project to be able to quantify uncertainties and analysis of sensitivities (U&S) and MOCABA implementation (Stakhanova A. , Gabrielli, Sanchez-Espinoza, Pauli, & Hofer, 2022) (Gabrielli, et al., 2022) (Stakhanova A. , Gabrielli, Sanchez-Espinoza, Hofer, & Pauli, 2022). The KATUSA is generated from FSTC to

perform U&S analysis which allows creating samples over selected uncertain parameters in defined probabilistic distribution function (PDFs), running ASTEC simultaneously and calculation of the uncertainties by filtering the results. **Figure 4-4** shows the flowchart of the KATUSA.

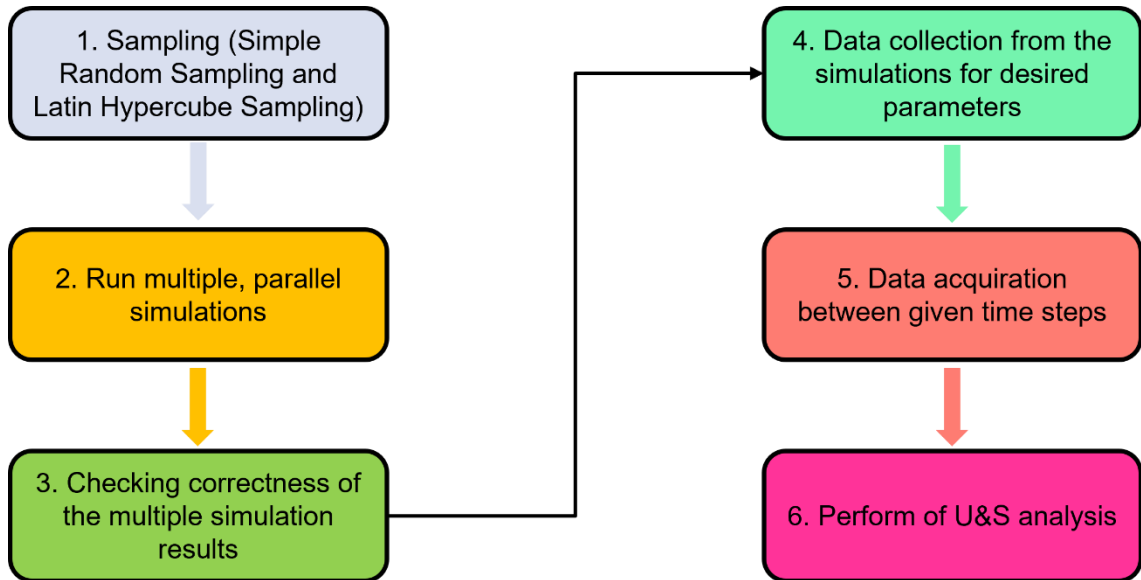


Figure 4-4: KATUSA calculation structure for U&S analysis modified from (Stakhanova A. , Gabrielli, Sanchez-Espinoza, Hofer, & Pauli, 2022)

5 Validation of ASTECV2.1 code with QUENCH-12 Test

5.1 Description of the QUENCH-12 Experiment

The objective of the QUENCH experiments with VVER-fuel rod simulators is to investigate the behavior of overheated core when quenched with cold water as a severe accident management measure to stop the accident progression and to prevent or delay the failure of the safety barriers i.e., of the reactor pressure vessel. However, injection of cold water into an overheated the core can lead to a rapid rise in temperature, due to an increased oxidation and hydrogen generation (Sehgal B. R., 2012). The heat generated due to reactions together with nuclear power may cause the formation of debris and molten pools within the core. The amount of molten material relocated to the lower plenum may be influenced by the cold-water injection.

Since the cladding material of the VVER fuel rods has different thermal properties than the typical Western type PWRs, another purpose of the experiment is to test the VVER-specific materials against Western type PWRs. Particularly, the QUENCH-06 experiment which was dedicated to investigating the effects of quenching PWR fuel rod simulators and the findings of QUENCH-12 experiment is also compared the one in the QUENCH-06 experiment (Stuckert, et al., 2008).

Figure 5-1 shows the sketch of the test bundle and test section of the QUENCH-12 experiment with flow lines (Stuckert, et al., 2008). The steam and argon used for the experiment enter the bottom section of the bundle and leave the bundle in the upper part which is equipped with hydrogen spectrometers to measure the mass of the generated hydrogen during the experiment. The pipes for the quenching are also located in the bottom section of the bundle which is equipped with a flowmeter to measure the water flow rate. The cooling jacket is located at the outermost part of the bundle and consists of two sections that form a flow area for cooling the inner cooling jacket. Argon flows through these cooling jacket sections, and water is also used for cooling in the upper elevations additionally.

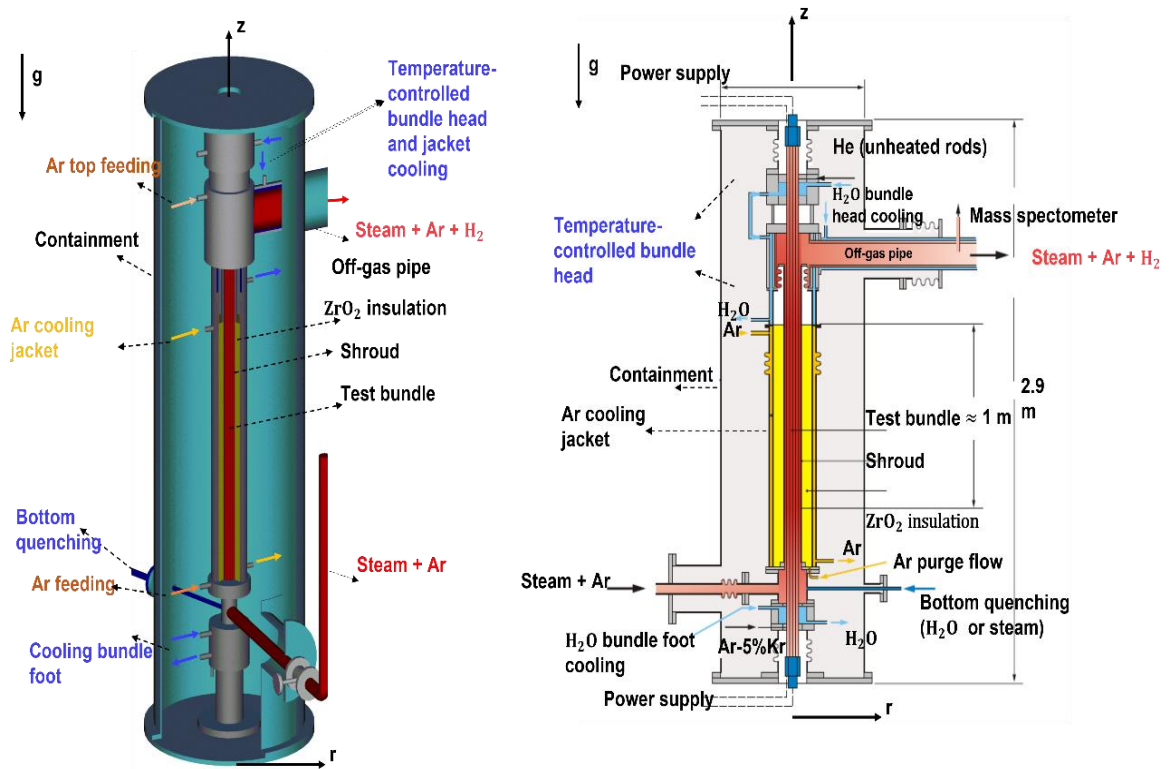


Figure 5-1: Sketch of the test bundle of the QUENCH-12 experiment (right) and test section of the QUENCH-12 experiment with flow lines modified from (Stuckert, et al., 2008)

Figure 5-2 illustrates section of the heated and unheated rods used for the experiment (Stuckert, et al., 2008). The length of the heated section is 1024 mm, and this section includes four different materials at different axial levels. Copper (Cu) electrodes are connected to molybdenum (Mo) at the below section and tungsten (W) heating elements are connected to the Mo electrodes from both upper and lower sections. The thickness of the W heating elements is 4 mm, and the thickness of Cu and Mo layers is 7 mm in heated rods. Unheated rods do not contain Cu, Mo and W regions and are filled with pellets with a hole of 2.5 mm in diameter. These layers are surrounded with insulating material (ZrO_2) and Zr-1%Nb (E110) covers the insulating material with a thickness of 0.7 mm.

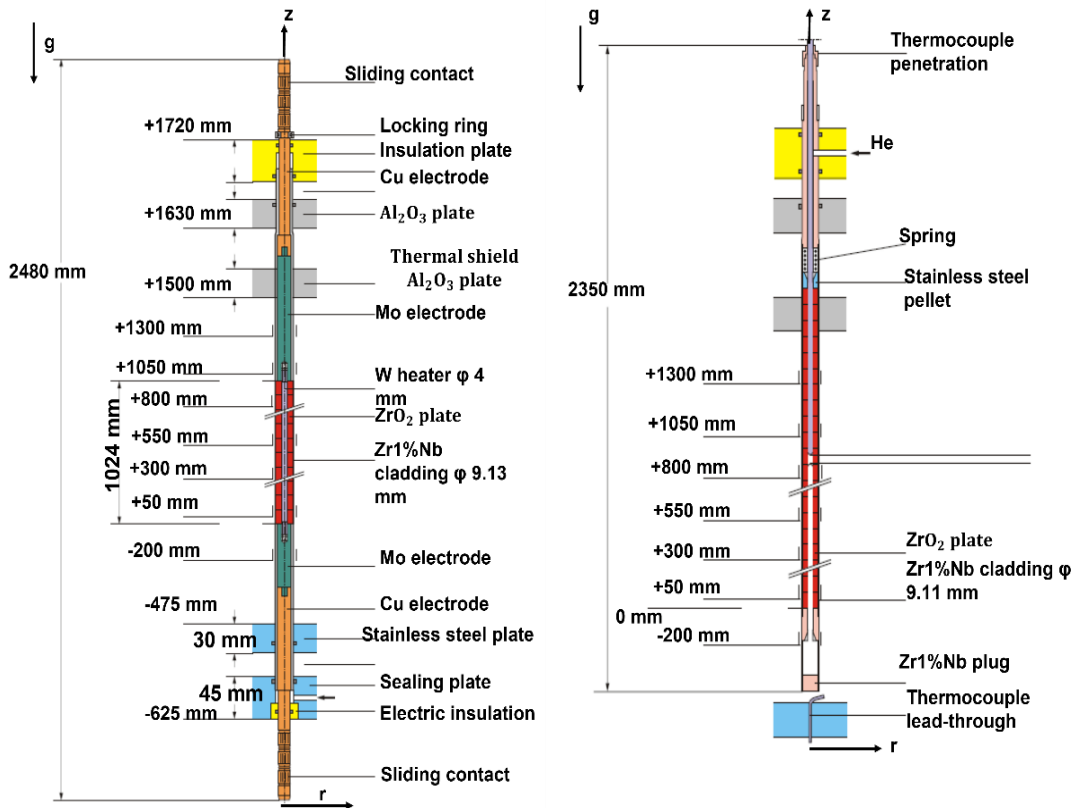


Figure 5-2: Section of the heated fuel rods (HFRs) used in the experiment (left) and section of the unheated fuel rods (UFR) used in the experiment (right) modified from (Stuckert, et al., 2008)

Figure 5-3 shows the cross-section of the fuel bundle (Stuckert, et al., 2008). In the experiment, 13 unheated rods and 18 heated rods are used, and 6 corner rods are located to sustain flow area of typical VVER-core and for oxide scale calculations. Unheated rod groups are separated as 1 in the center (Group 1) and 12 between heated rods (Group 3 and Group 4). Inner heated rods (Group 2) consist of 6 rods and outer heated rods (Group 5) have 12 rods. The pitch is 12.75 millimeters. Shroud surrounds fuel bundle and Zr-2.5%Nb (E250) is used as material. Axial location of the thermocouple (TC) groups and spacer grids are also shown on **Figure 5-3** (Stuckert, et al., 2008). Seven spacer grids are used in the system and all spacer grids are made of Zr1%-Nb (E110). Data of each thermocouple recorded as their pin number, their group and elevation number. The thermocouples measures temperature of attached clad structure and additionally further thermocouples are placed inside the clad to measure central temperature. Even though there is minimum one thermocouple in every elevation, there can be clads that has no thermocouple and due to this situation, there is no data for some clad structure at every elevation.

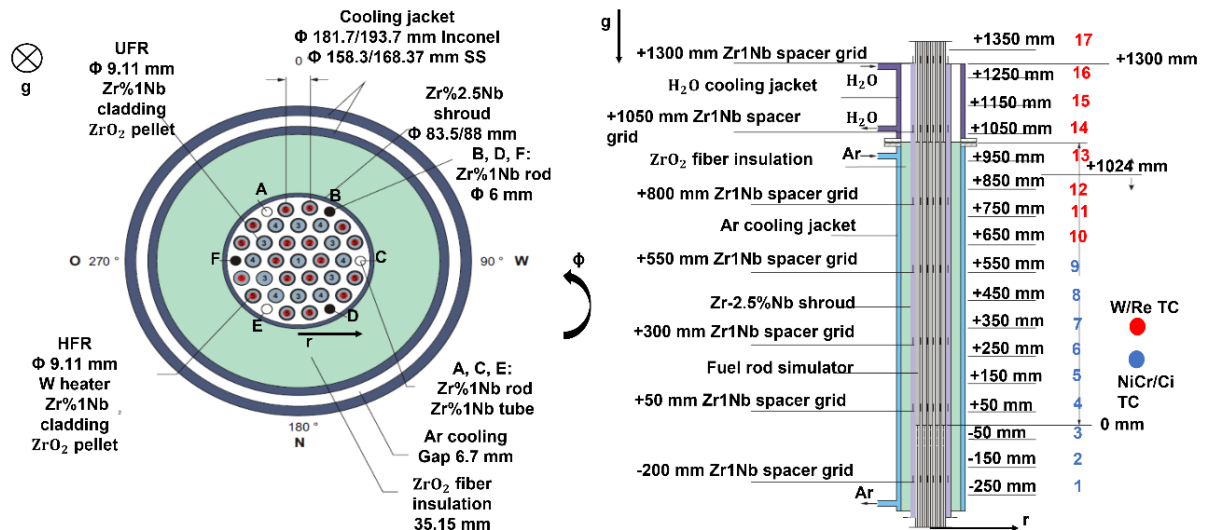


Figure 5-3: Cross-section view of the fuel bundle used in QUENCH-12 experiment (left) and axial positions of thermocouples and spacer grids used in the experiment modified from (Stuckert, et al., 2008)

Figure 5-4 shows temperature, flow and power history at every phase of the experiment (Stuckert, et al., 2008). The power history is like the QUENCH-06 experiment in order to compare the behavior between VVER and PWR fuel rod bundles. However, the mass flow rate of the quenching water is higher than the QUENCH-06 to sustain a similar flow rate during this phase. Corner rod D was ejected about 6000 s. and corner rod F was taken from the bundle before quenching. Performed QUENCH-12 experiment performed has five phases listed below.

- **Phase I: Stabilization:** The system was heated up to 600°C and was stabilized at that temperature approximately 1 hour.
- **Phase II: Heat-up:** The system was heated up to reach to 1470 °C step by step and this period took approximately 2620 s.
- **Phase III: Pre-oxidation:** The temperature was kept at 1470 °C for 3400 s. to reach maximum oxide thickness of 200 μm.
- **Phase IV: Transient:** The temperature was increased to a maximum temperature of ~2050 K for 1250 s with steps of 0.3 K/s (from 1500 K to 1750 K) and 1.3 K/s (from 1750 K to 1950 K).
- **Phase V: Quenching:** The bundle quenched with 48 g/s of water at 7270 s. and power was decreased.

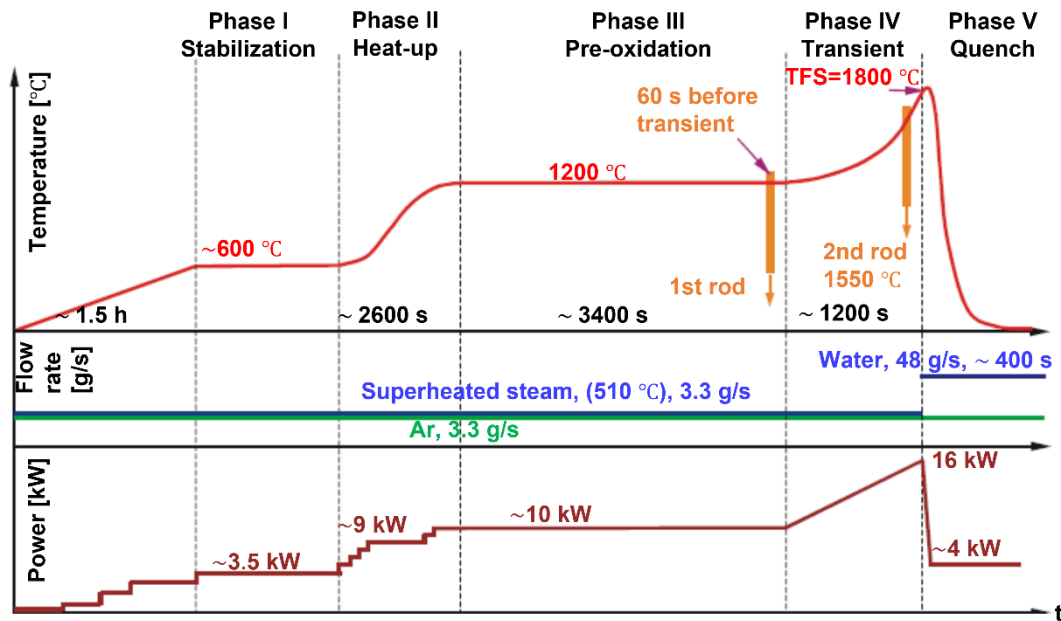


Figure 5-4: Temperature, flow and power conditions implemented in the experiment modified from (Stuckert, et al., 2008)

5.2 Development of ASTEC model QUENCH-12 Test

5.2.1 Modelling of the test section of QUENCH-12 ASTEC model

The modeling of the test section consists of the representation of the fluid domain and of the solid structures e.g. heated and unheated fuel rod simulators, corner rods, shroud in ASTEC. The fluid domain of the test section is represented by three channels: the central, the middle and the outer channel, which are characterized by the flow area and the heated and wetted diameter. Radial arrangement of the rods of QUENCH-12 set-up is depicted in ASTEC by cylindrical domains according to distance to the center. **Figure 5-5** illustrates the radial mesh modelling of the test bundle cross-section and fuel rods located inside of each channel. According to the distance of each rod group, the flow area is calculated, and each rod group is modelled inside of the bundle.

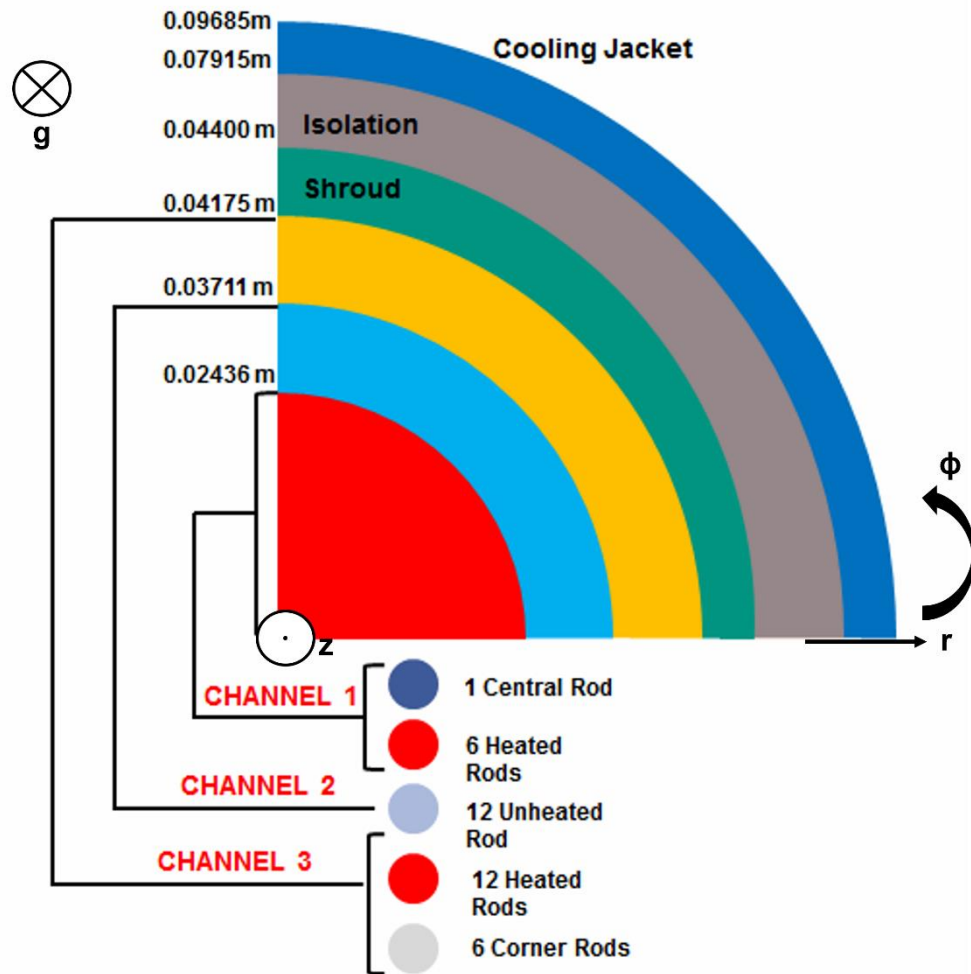


Figure 5-5: Radial meshing of the QUENCH-12 test bundle in ASTEC code

Figure 5-6 illustrates the axial meshing model of the QUENCH-12 test bundle on ASTEC with material compositions. The heated section (between 0 m and 1.024 m) is divided into 24 equidistant axial nodes. The region under the heated section (between -0.325 m to 0 m) is separated into 9 axial meshes which Mo zone had 5 meshes and Cu zone had 4 meshes, and upper part of the heated section (between 1.024 m to 1.5 m) is divided into 10 axial nodes. The material for the cladding, control rods, spacer grids and shroud have been as Zr-4 since thermo-physical data for VVER-related materials are not available on ASTEC. Although the thermal properties of each material are quite similar (Stuckert, et al., 2008), hydrogen uptake and break-away phenomena creates differences on hydrogen generation (Hózer, Gyóri, Matus, & Horváth, 2008). The shroud section between 1.024 m to 1.3 m is surrounded by argon cooling and insulator (ZOFR) covers the rest of the shroud section. Finally, the inner cooling jacket is modelled as Ni to represent Inconel material.

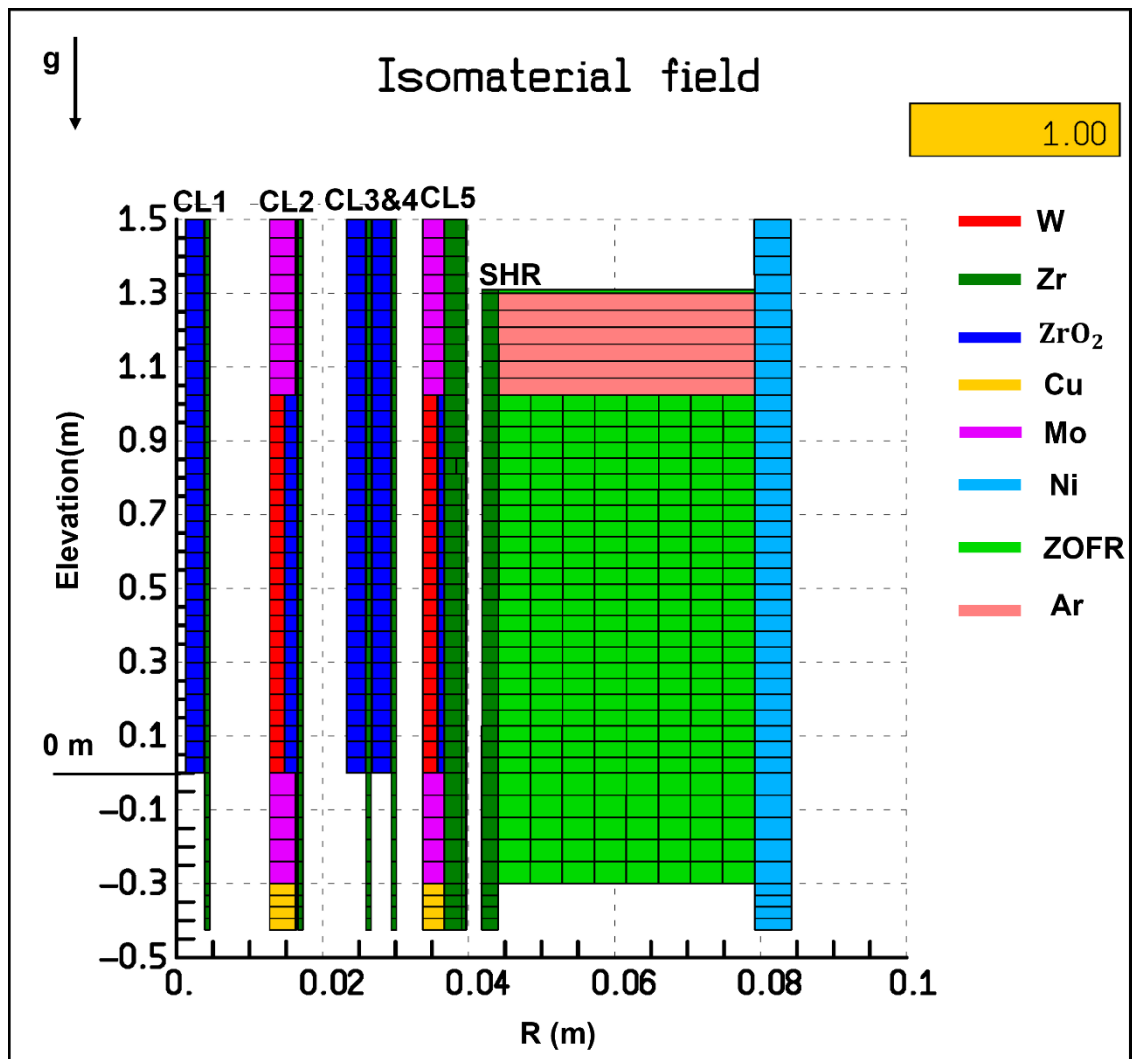


Figure 5-6: Axial meshing of the QUENCH-12 test bundle in ASTEC code

5.2.2 Initial and boundary conditions of QUENCH-12 ASTEC model

Initial conditions such as temperature, pressure and flow to be defined for ASTEC model were supported from the experimental reports and was applied to the model according to the axial and radial discretization of the structures and channels. The injection times and physical properties are shown in **Table 5.1**. The flow rate during the ASTEC simulation is given in **Figure 5-7**.

Table 5.1: Employed mass flow rate, temperature and pressure of the flows in time

Coolant	Time (s)	Mass Flow Rate (g/s)	Temperature (K)	Pressure (bar)
Argon	0	3.3	607.70	2.2
	7270	3.3	642.0	2.2
	10000	3.3	298	2.2
Steam	0	3.3	607.70	2.2
	7270	3.3	642.0	2.2
	10000	3.3	298	2.2
Quench	0	0.421	298	2.2
	7269	0.421	298	2.2
	7270	48	298	2.2
	7695	0.421	298	2.2
	10000	0.421	298	2.2

The boundary conditions of mass flow rate of steam, argon and quenching water were taken from the reports of the experiments. The flow rate, temperature and pressure values are given in **Figure 5-7**. Additionally, pre-injection is modelled to sustain accurate quench flow and total pre-injected mass is 4 kg during the quenching phase (Stuckert, et al., 2008).

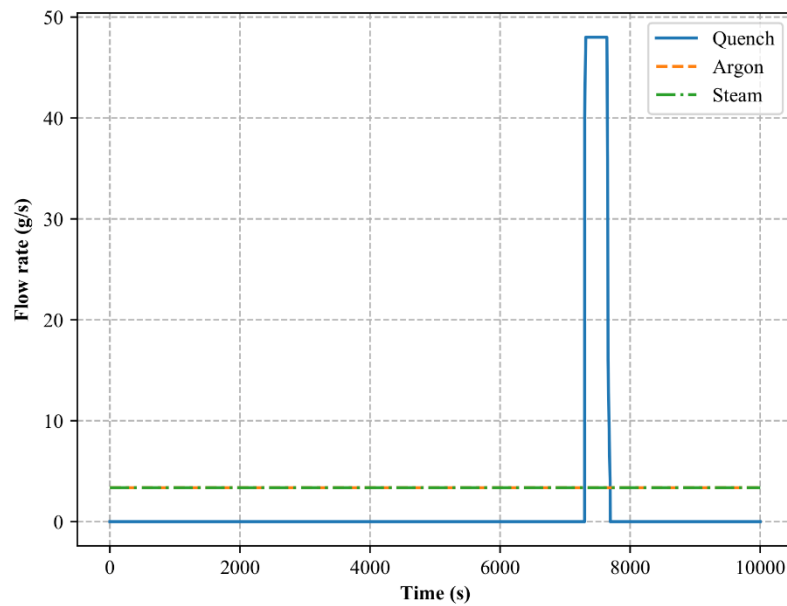


Figure 5-7: Employed steam, argon and quenching water flow rate during the simulation in ASTEC

Figure 5-8 shows the power profile of the inner and outer heated rods during the simulation (Mercan, Gabrielli, & Sanchez-Espinoza, Validation of Astec2.1 using Quench-12 for VVER-Reactors, 2022). Heat data for inner heated rods and outer heated rods are provided also from experimental data. Electrical resistance of the inner rods is calculated to $3.87 \text{ m}\Omega$ after stabilization phase and external electrical resistance of inner rods are $2.1 \text{ m}\Omega$ which is $1/6$ the corresponding to each inner rod (Stuckert, et al., 2008). Outer rods' resistance was $1.84 \text{ m}\Omega$ after stabilization phase and $3 \text{ m}\Omega$ is external electrical resistance which $1/12$ corresponding to each rod (Stuckert, et al., 2008). Like the experiment, supported heat to the outer rod group is almost twice of the inner rod group heat.

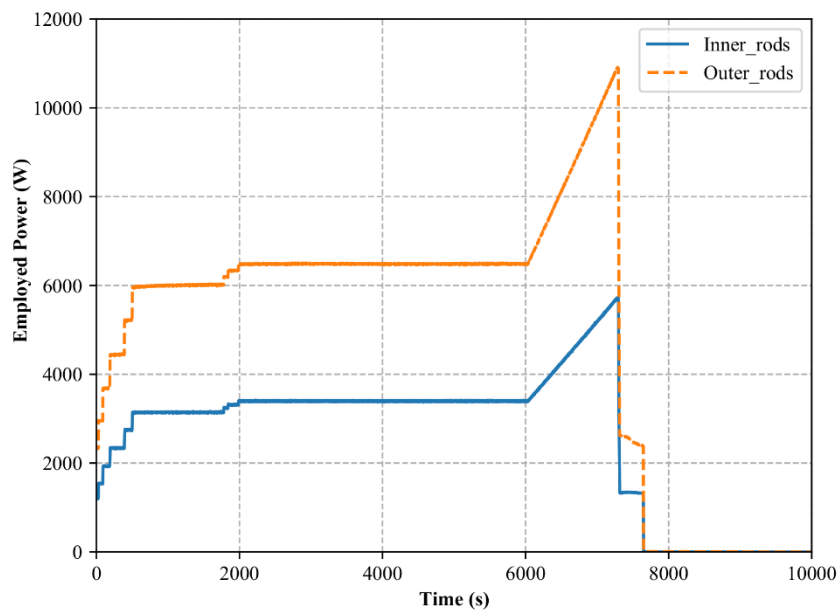


Figure 5-8: Considered power supply temporal evolution of inner and outer rods of the ASTEC-QUENCH-12 simulation

5.2.3 Chemical and physical models considered in ASTEC model

Several physical and chemical phenomena e.g., the models for the heat transfers, oxidation, chemical interactions and the criteria for the rod failure, start of the material relocation were activated to properly simulate progression of experiment with ASTEC.

Radial heat conduction is defined for every adjacent structure inside clad. Also, grid spacers are modelled considering heat conduction with adjacent clad structure. Gaps between pellets and clads transfer heat only by conduction. Axial heat conduction is also defined for the system. Convection between clads, corner rods, shroud and grids to domain are defined. Radial and axial conduction between structures is defined including shrouds internal surface and gaseous channel. Also, convection between argon gap and shroud and argon gap and inner surface of cooling jacket is defined by considering argon gap as solid material with same heat transfer parameters with argon due to ASTEC modelling problems. The radiation heat transfer between regions that have the same elevation is considered. Radiation heat transfer between clad structures, shroud, corner rods and cooling jacket is considered in model. To do so, the system is divided two elevations which are between 0 to 1.3 m and 1.3 to 1.5 m. Region between 0 to 1.3 m elevations radiative heat transfer is between rods, corner rods and shroud. Region between 1.3 m to 1.5 m radiative heat transfer includes transfer between shrouds to inner cooling jacket additionally.

Oxidation of solid Zr-4 material and molten structure of Zr-4 (α -Zr-4, ZrO₂) by steam is accounted in the system. Oxidation of clad materials, corner rods, grids and shroud are also considered for chemical interactions. These materials start to oxidize when the temperature exceeds 600 K. Best-Fit correlation is used to calculate oxidation of structures. Additionally, oxidation of the molten material (UZOXMAG) is considered to simulate oxidation of these materials (Chatelard, et al., 2014).

The integrity of clads corner rods, shroud and spacer grids are defined in ASTEC as compact. This compact structure is arranged to dislocate under the following conditions. Also, cracked structures are also dislocated in calculation domain.

- If temperature of the compact structure gets over 2300 K or thickness of compact structure decreases less than 300 μ m
- If temperature of cracked structure gets over 2300 K or thickness of cracked structure decreases less than 300 μ m
- If temperature of compact structure gets over 2500 K.
- If temperature of cracked structure gets over 2500 K.

Structures that come to dislocation criteria start to relocate and move in bundle. ZrO₂ pellets, clads, grids and corners rods dislocate in ASTEC and create molten material composition (MAGMA) in bundle. MAGMA 2-D model can calculate relocation of molten materials (decanting) and dripping of the melt to the lower elevations (candling) of magma structure by solving momentum and energy conservation equations in porous media (Chatelard, et al., 2014).

5.3 Comparison of ASTEC-predictions with experimental data

The ASTEC predictions over the temperature for heated rods, unheated rod and shroud at 950 mm, temperature profile at 6000 s and 7160 s for heated rods, unheated rod and shroud and oxide thickness on the control rods at different phases have been acquired and these predictions have been compared with experimental results. Further temperature evaluations at several elevations and oxide thickness are presented in **Appendix A**.

Within the figures, inner heated rod group is referred as **CL2** and it is represented with **red, solid lines**. **CL5** is used for outer heated rod groups and **orange, solid line** is defined to represent this group. Inner unheated rod group and outer heated rod group are named **CL3** and **CL4** respectively, and **blue, solid line** is selected to refer **CL3** and **purple, solid line** is used for

CL4 representations. Finally, shroud structure is visualized by **green, solid lines** and is named as **SHR**. For the experimental results, dashed line is used.

Figure 5-9 and **Figure 5-10** show the temperature comparison at 950 mm for rod groups and shroud. It can be observed that ASTEC is able to capture the trend of temperature change during the simulation at every elevation which can be seen in **Figure A.1- 1**, **Figure A.1- 2** and **Figure A.1- 3**. Despite the good agreement, some discrepancies are observed during the transient:

- Higher temperature predictions at 950 mm compared to the experiment have been observed until the quenching phase. The calculated temperatures vary within a range about 80 K. The temperature deviation is smaller for the unheated rod groups and the shroud.
- It can be said that after the quenching phase, there is no major discrepancy between the calculated temperatures and the experimental results. Lower temperature predictions can be observed which can be resulted due to uncertainty in the properties of the materials such may create differences on the results (Stuckert & Gerogiev, Analysis of the QUENCH-12 bundle experiment with the ATHLET-CD2.2A code, 2012). However, some of the thermocouples such as the one on the inner rod group and inner unheated group failed during the test at about 7492 s and about 7500 s respectively. Hence, comparison after this point is not possible.
- A possible explanation for deviations before quenching phase is the estimated values of the thermal resistance used in the inner heated rods and outer heated rods. In the test, thermal resistance parameters were reported at each phase of the experiment (Stuckert, et al., 2008), nevertheless, the change of the thermal resistance cannot be sustained in ASTEC.

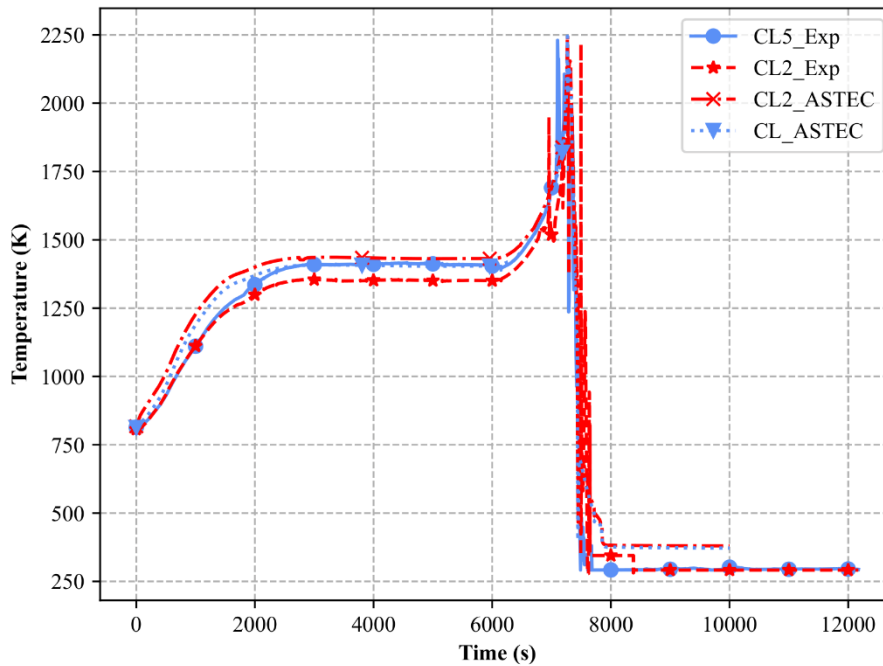


Figure 5-9: Comparison of the predicted and experimental temperature data as a function of time at an axial height of 950 mm for heated rods

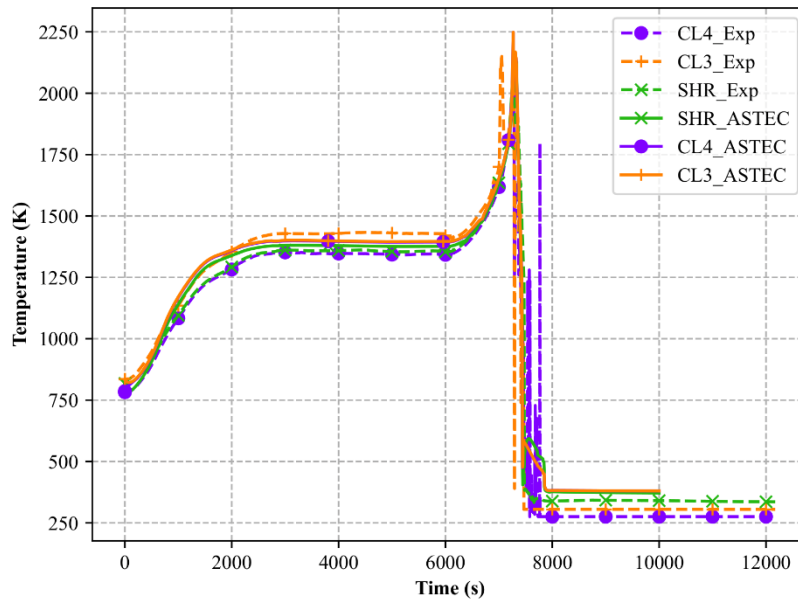


Figure 5-10: Comparison of the predicted and experimental temperature data as a function of time at an axial height of 950 mm for unheated rods and shroud

Figure 5-11 and **Figure 5-12** illustrate axial temperature change in the experiment and during the simulation at the beginning of the transient phase and at the quenching onset for the heated rods. Similarly, **Figure 5-13** and **Figure 5-14** show the axial temperature change at the

beginning of the transient and at the beginning of quenching phase for unheated rods and the shroud. ASTEC can estimate temperature profile at each rod group and the shroud in both phases of experiment. Overestimation of temperature at elevations below 950 mm can be observed but temperature differences are in the range of 100 K. The deviations might be occurred due to missing thermal properties of E110 and E250 material. On the other hand, the developed argon gap model at an elevation higher than 1024 mm can reproduce the heat transfer that the shroud temperature prediction is in great coherence with the experiment.

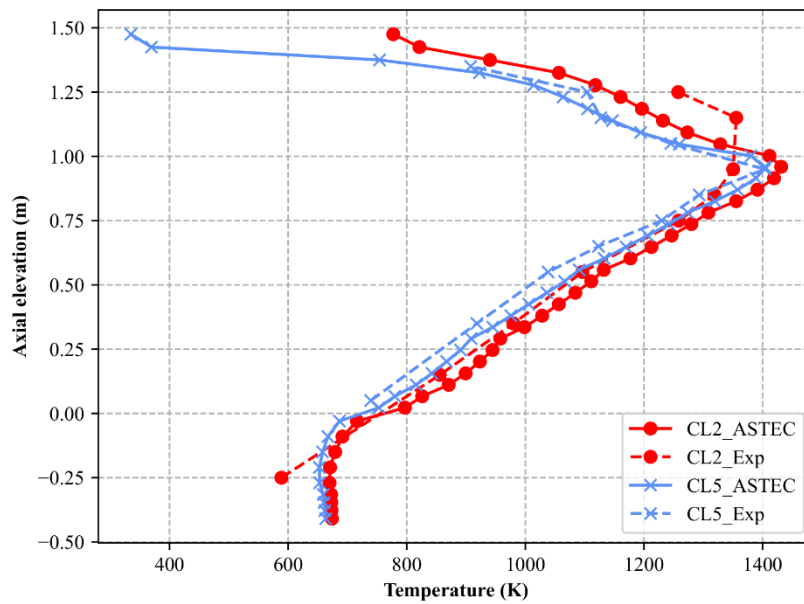


Figure 5-11: Axial temperature profile comparison between predicted and experimental results at several axial positions for heated rods at the beginning of transient phase (6000 s)

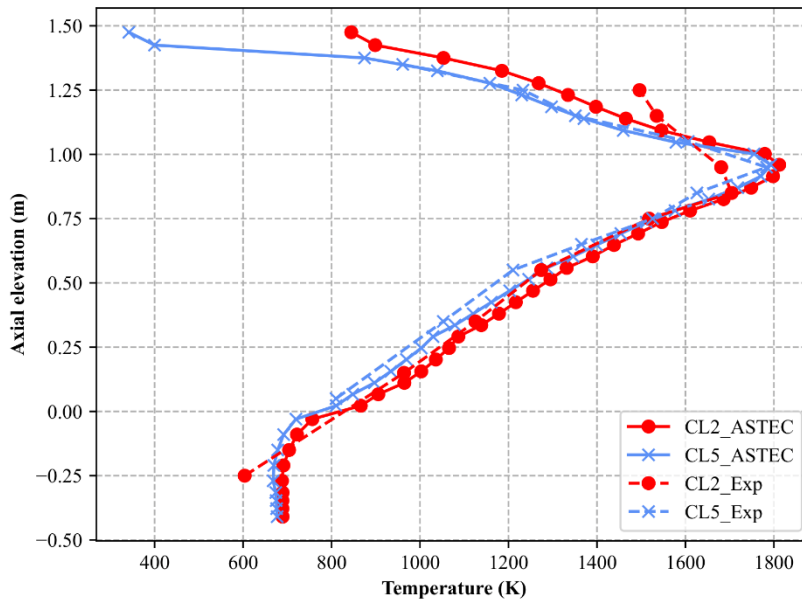


Figure 5-12: Axial temperature profile comparison between predicted and experimental results at several axial positions for heated rods at the quenching onset (7160 s)

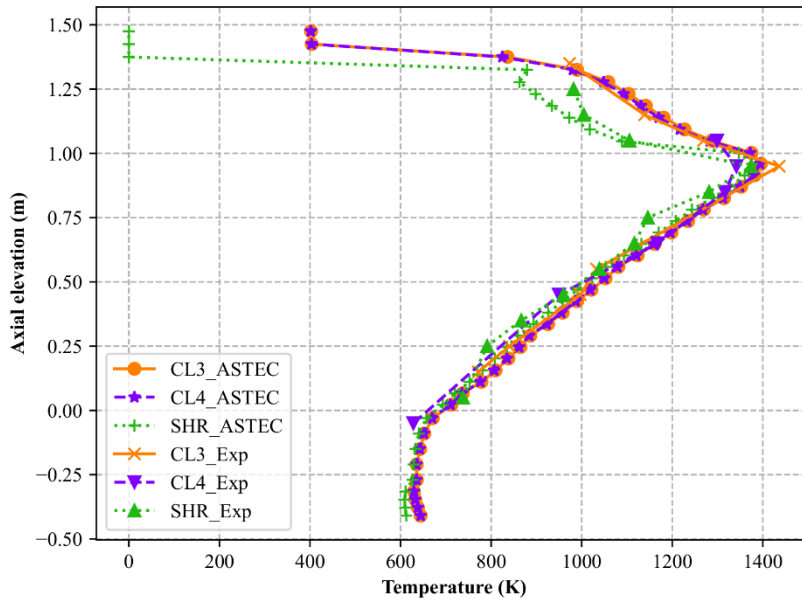


Figure 5-13: Axial temperature profile comparison between predicted and experimental results at several axial positions for unheated rods and shroud at the beginning of transient phase (6000 s)

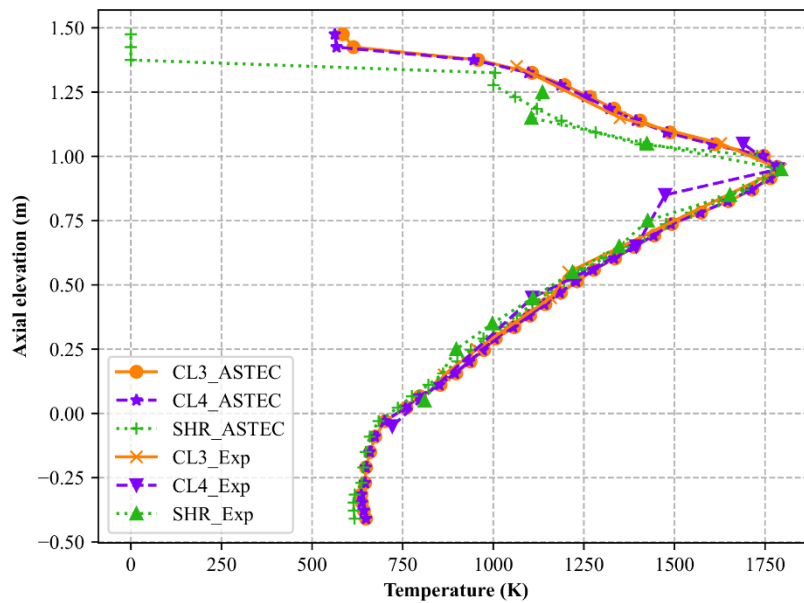


Figure 5-14: Axial temperature profile comparison between predicted and experimental results at several axial positions for unheated rods and shroud at the quenching onset (7160 s)

Figure 5-15 and **Figure 5-16** represent oxide layer forming on the control rods and comparison with the experimental results at the beginning of the transient phase (control rod B) and before quenching phase approximately at 7160 s (control rod D). As seen from the left side of the figure, oxide scale growth is underestimated at most of the elevations at this phase and the difference is higher at upper elevations. On the other hand, the predictions for oxide scale before quenching are almost similar except the elevations below 750 mm. Nevertheless, the trend of oxide formation is captured by ASTEC. It should be noted that these rods were ejected from the test bundle and the test was preceded without these rods. Therefore, the flow area increased due to this ejection and this physical phenomenon cannot be represented during simulation since ASTEC code cannot allow physical alterations during calculation. The ejection of the rod would result as more heat transfer and lower temperatures and oxide scales on the rods.

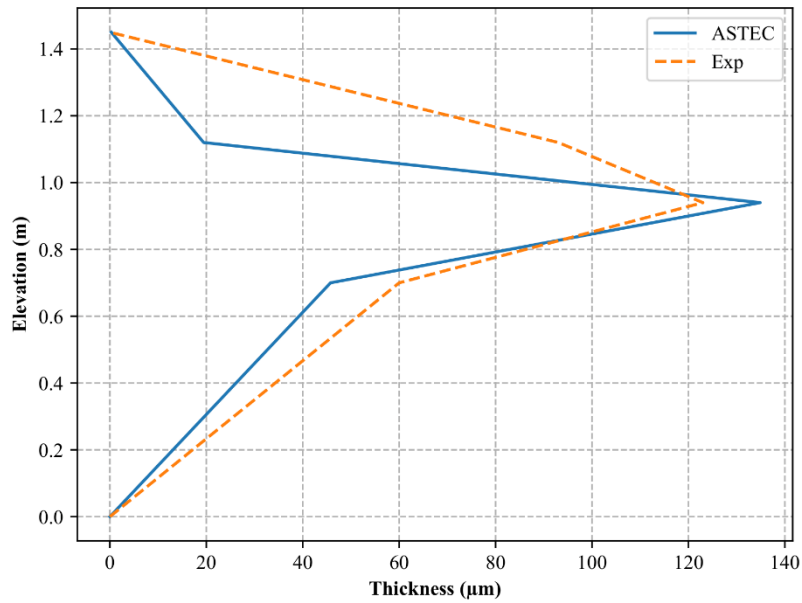


Figure 5-15: Axial oxidation profile comparison between predicted and experimental results at several axial positions for ejected control rod at the beginning of transient phase (6000 s)

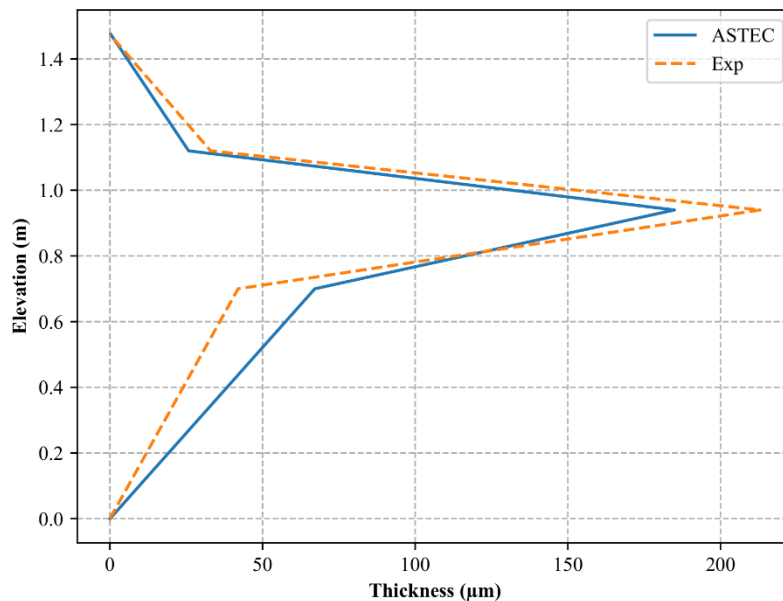


Figure 5-16: Axial oxidation profile comparison between predicted and experimental results at several axial positions for ejected control rod before quenching (7160 s)

Figure 5-17 demonstrates axial representation of the test bundle at the end of the simulation. Integrity loss of the materials can be observed at elevation of 950 mm as in the experiment. The meltdown of material is more observable at shroud, but meltdown is also observable at each rod surface. Estimation of lower meltdown leads to lower oxidation increase

due to break-away phenomena at quenching phase. The oxide scale profile on the inner heated rods and outer heater rods at the end of ASTEC calculation can be seen in **Figure A.2- 1** and **Figure A.2- 4** respectively. Similarly, oxide scale growth predictions on unheated rods as well as shroud are depicted in **Figure A.2- 2**, **Figure A.2- 3** and **Figure A.2- 5**.

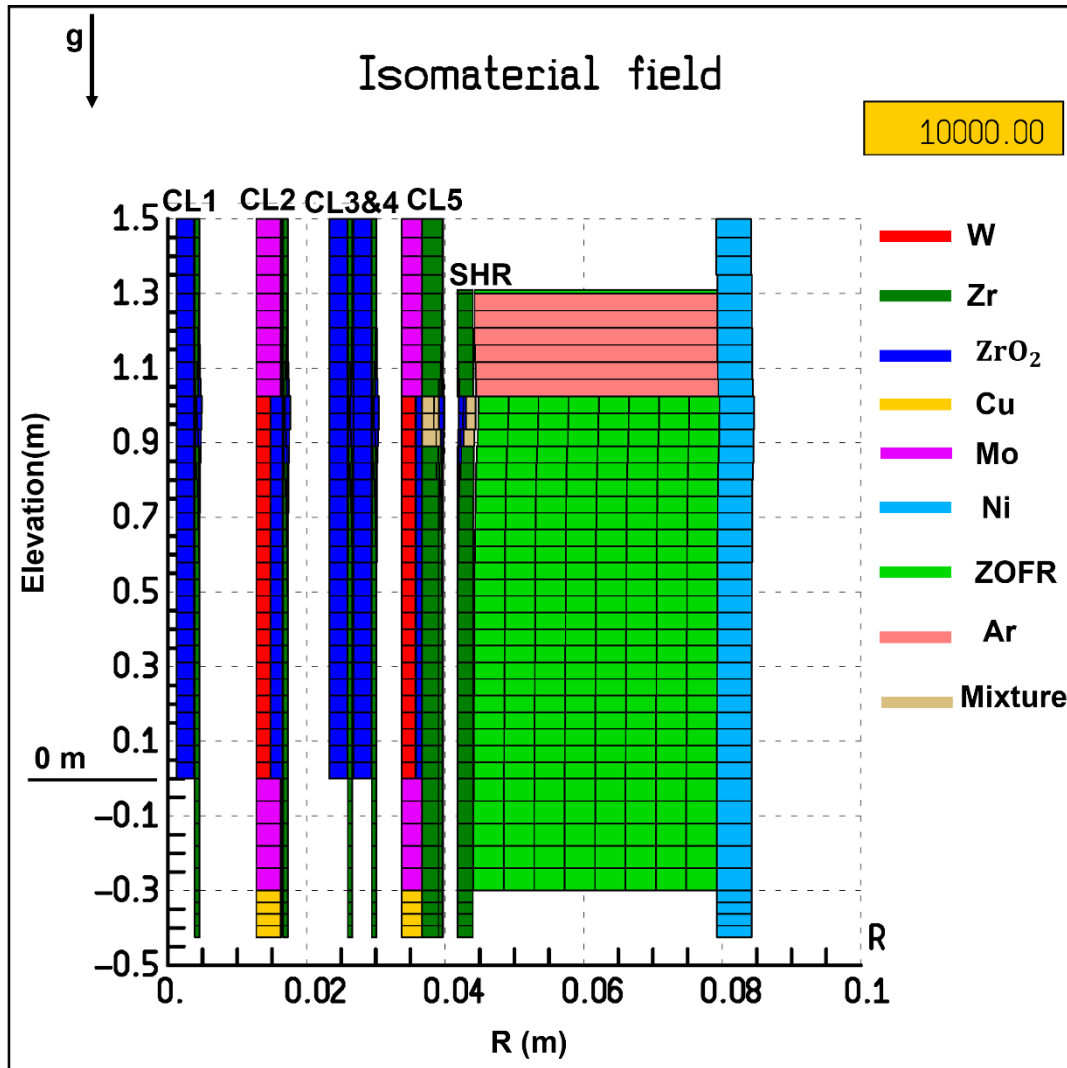


Figure 5-17: Axial view of the test bundle with material composition at the end of the experiment

Figure 5-18 and **Figure 5-19** show the generated hydrogen mass and hydrogen generation rate compared with the experimental results respectively. As seen **Figure 5-18**, ASTEC prediction over hydrogen generation is similar with the experiment until the reflooding phase. The higher temperatures during this phase, especially at lower elevations, generate more hydrogen but the break-away phenomenon was observed in the test, and it accelerated the hydrogen generation. Hence, the produced hydrogen mass is almost like the experiment at this phase. Though, developed model could not capture immense hydrogen generation during

quenching phase, see **Figure 5-20**. Therefore, total generated hydrogen mass is underestimated than the experimental value at the end of the calculation. The comparison of the total mass of generated hydrogen is given at **Table 5.2**.

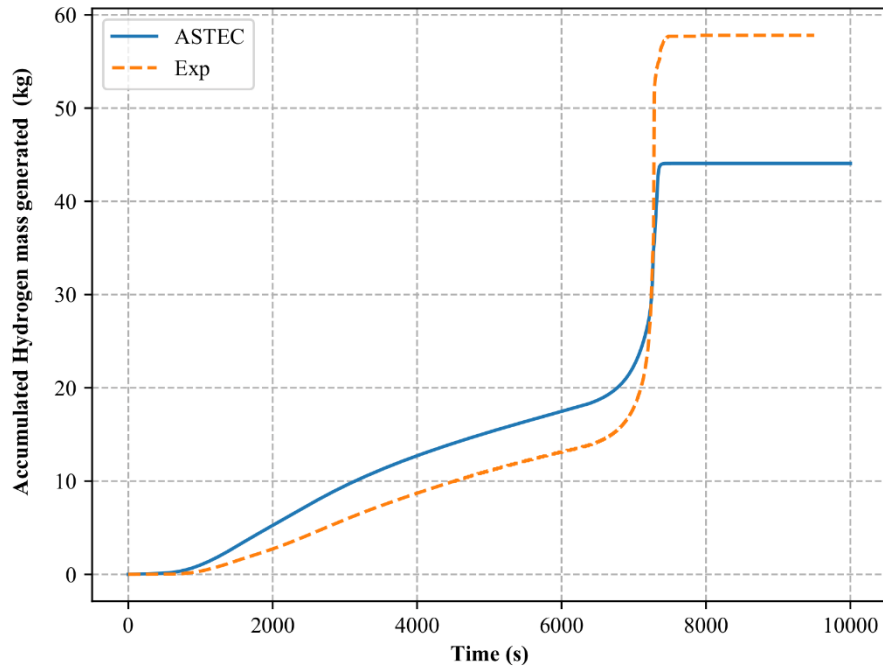


Figure 5-18: Comparison of predicted and experimental hydrogen generation mass

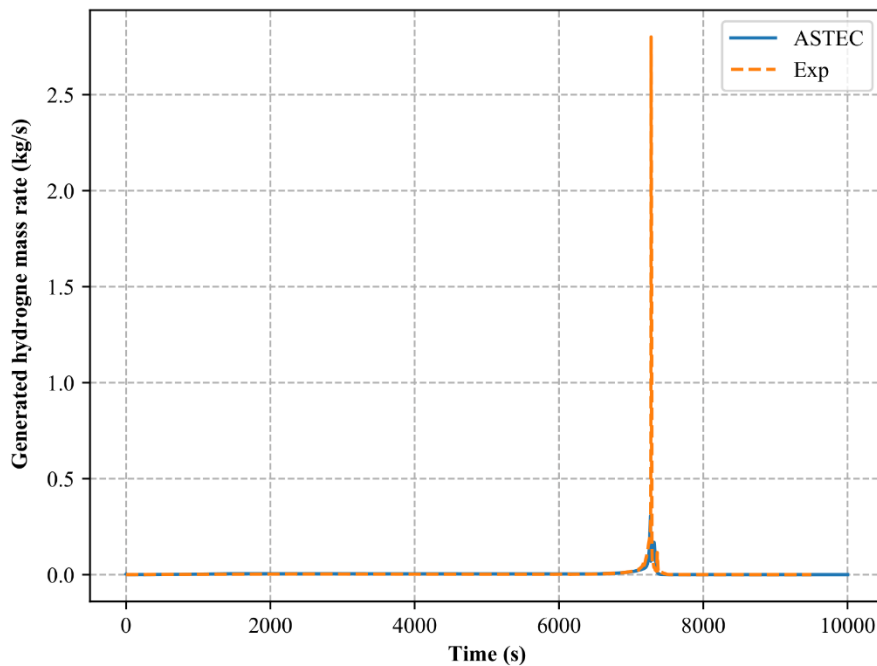


Figure 5-19: Comparison of predicted and experimental hydrogen generation mass rate

Table 5.2: Total hydrogen generation comparison at different phases of the test

Total H_2 generation (g)		Before reflooding (g)		After reflooding (g)	
Experiment	ASTEC	Experiment	ASTEC	Experiment	ASTEC
57.8	44.07	34.7	34.21	23.1	9.86

5.4 Discussion of the results

The presented calculations have shown that ASTEC V2.1 is able to predict temperature profile with slight differences. However, some deviations over hydrogen generation and temperature profiles are observable in both before and during reflooding phases. These are material differences and requirement of oxidation materials based on VVER-materials. As concerns of the material differences, Zr had to be used instead of E110 of E250 in the test bundle. Although similar thermal conductivity values were reported before (Stuckert, et al., 2008; Peletsky, 1999), the heat capacity difference was observable at the temperature around 1200 K (Stuckert, et al., 2008; Petrova, Peletsky, & Samsonov, 1999). When the temperature difference until the transient phase was considered, it seems the main reason of the deviation can be due to thermal

parameters. For the case of hydrogen generation E110 based cladding materials can uptake more hydrogen than Zr based materials and more hydrogen can be generated during break-away phenomena due to higher uptake of hydrogen (Hózer, Gyóri, Matus, & Horváth, 2008). Therefore, oxidation models developed for Zr-4 cannot represent oxidation of E110 and E250 materials.

Figure 5-20 illustrates hydrogen generation estimations by three different oxidation models and comparison of these estimations with experimental results. It can be observed that all three models estimate higher hydrogen generation profile even though the generated hydrogen mass is similar until the quenching phase. However, the rapid increase of oxidation cannot be captured by all three models and predictions remain underestimated at the end of the calculation. Similar behavior was also observed the QUENCH-12 analysis modelled by ATHLET-CD2.2A which uses Sokolov oxidation model developed for VVER-related materials (Stuckert & Gerogiev, Analysis of the QUENCH-12 bundle experiment with the ATHLET-CD2.2A code, 2012), and QUENCH-12 analysis with the model of SVECHA/QUENCH (Palagin & Stuckert, 2007)

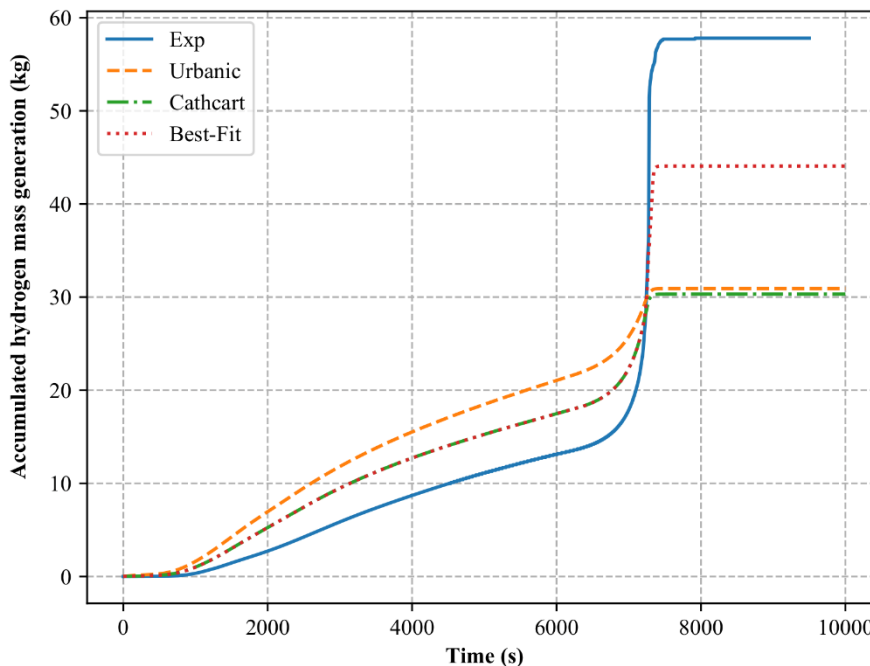


Figure 5-20: Comparison of hydrogen generation by different oxidation models and experimental results

5.5 Summary

In this chapter, an early in-phase experiment of QUENCH-12 has been modelled by ASTECV2.1 to demonstrate capability of the physical models inside of the code. After short description of the test facility and ASTEC model devoted to this experiment, the comparison of key predictions has been done with experimental results to confirm ASTEC code is able to represent important phenomena ongoing during a severe accident event on VVER bundles.

Despite higher temperature estimations during pre-oxidation phase, ASTEC is able to capture temperature profile in the experiment. Discrepancies over material information are resulted with underestimation of hydrogen generation during reflooding. The generated hydrogen before quenching phase seems higher but underestimation during transient phase is concluded similar hydrogen generation. Also, deviations due to employing different oxidation models and different axial meshing are also identified.

According to the findings of the validation work and identified differences between ASTEC estimations and experimental results, the results for further calculations may be affected this difference in terms of hydrogen production. However, the difference is not severe when considering reactor scale calculation.

After the validation of ASTEC code with QUENCH-12 experiment and identification of discrepancies, adequate ASTEC model to represent VVER-1000 reactor is required to detect not only the phenomena occurred during in-vessel but also during ex-vessel phase.

6 Prediction of the radiological source term for a VVER-1000 severe accident with ASTEC

To investigate of the FP transport from the vessel to the primary circuit and then to the containment and a release to the environment of the ST, a detailed model of the plant is essential. A generic ASTEC model of the VVER-1000 reactor has been generated at 2017 for the ASTEC V2.0 and studies have been undertaken by INRNE and BARC (Chatterjee B. , et al., 2010; Gencheva, Stefanova, & Groudev, 2015; Stefanova, Gencheva, & Groudev, 2011) until the version of V2.1.3. The improvement work of new model concerns the core and lower plenum (LP) modelling and integration of newer physical and chemical models in ASTEC, remodeling of the primary circuit components, mainly the steam generators (SGs), in order to sustain steady-state parameters, evaluation of the containment and the cavity model for molten core-concrete interaction (MCCI) process and gas generation, application of latest modules into to model and FP inventory calculation by in-house KORIGEN at the beginning of the transient to estimate accurate ST release to the environment.

6.1 Fission product inventory investigation by KORIGEN tool

To obtain accurate predictions for the ST, the determination of the initial fission product inventory is essential. Indeed, the inventory at the end of effective cycle is significantly different from that at in the beginning of the cycle. Hence, fission transport and release as well as several phenomena during the transient progression such as the release of FP are directly dependent on the initial FP inventory (Gabielli, et al., 2022).

In-house KORIGEN tool is used to maintain initial FP loading for a generic core of the VVER-1000/V320 and to support inventory to the ASTEC's ISODOP module calculates FP transmutation and decay during a transient. The generic VVER 1000/V320 consists of 163 hexagonal fuel assemblies with 312 fuel rods. The fuel enrichment is 4.4 wt. % and the burn-up is assumed in between 42 to 47.3 GWd/tHM with the cycle length of 413 days (Murphy, et al., 2000). The dimensions of the VVER-1000 reactor components are given in **Table 2.1** and element-by-element material composition of the VVER cladding material, known as E110, and the mass of each element in the cladding for 1 t heavy metal (HM) are given in

Table 2.2 (Murphy, et al., 2000). According to the given dimensions and composition, the material information is taken as input to the KORIGEN. Also, the duration of each cycle with

downtimes to achieve 42.23 MWd/kg is shown in **Figure 6-1** (Mercan, Gabrielli, & Sanchez-Espinoza, Validation of Astec2.1 using Quench-12 for VVER-Reactors, 2022) which is required for depletion calculation.

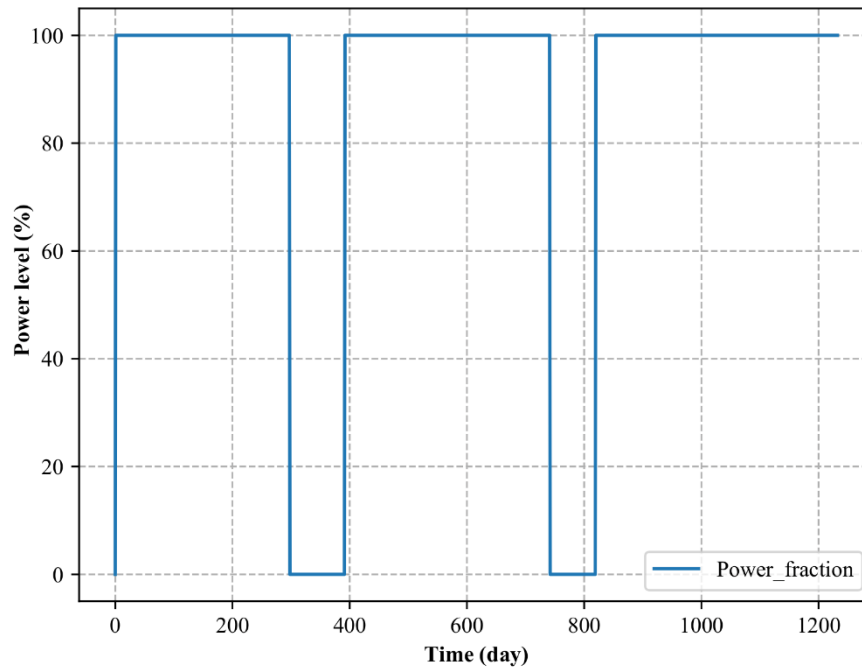


Figure 6-1: Considered irradiation history with downtimes of a VVER-1000 used as input to the KORIGEN to obtain FP inventory

At the end of the calculation, the activity and mass of the isotopes of the light elements, actinides and fission products have been determined for 1 tHM and 0.3 t of cladding material.

Figure 6-2 shows the activity level of the main FP elements in the core. At the beginning of the transients, the total activity at the vessel is 730.2 PBq, of which 15.02 PBq activity is the iodine isotopes. Additionally, the activity of the Pu, Np and total of all actinides are 3.49 PBq, 19.19 PBq and 31.91 PBq respectively. Finally, the activity of the FPs covers about 693 PBq of the total activity in the vessel.

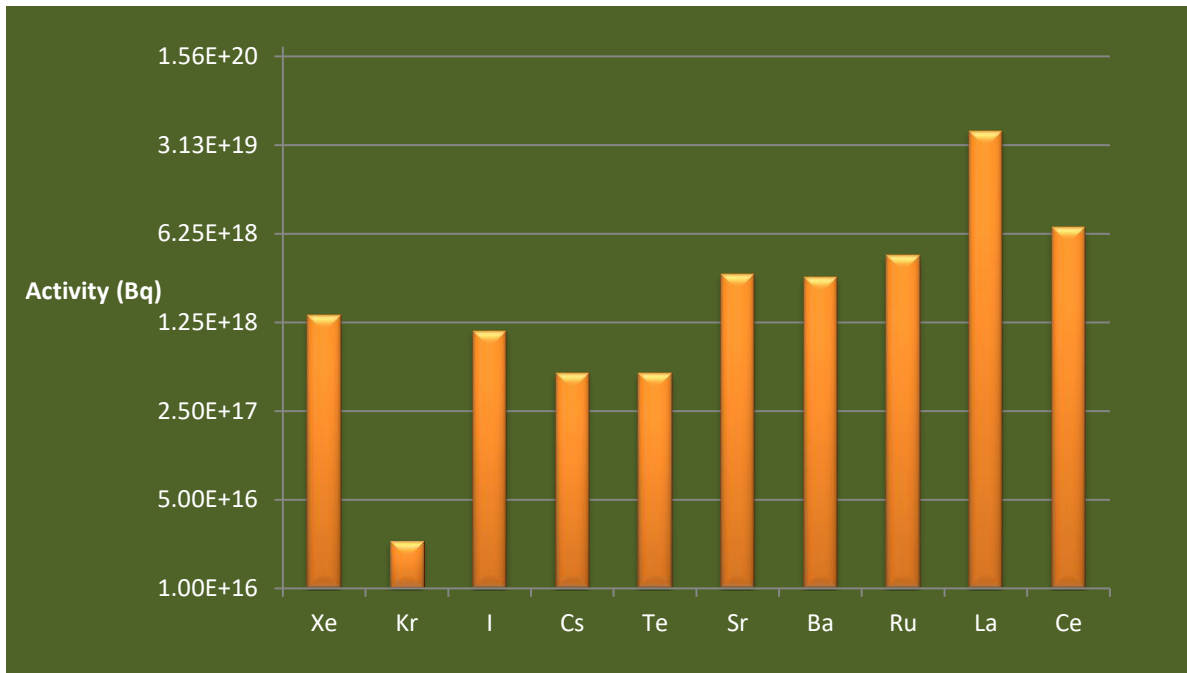


Figure 6-2: Computed activity levels generated for one tHM and 0.3-ton cladding material of a generic VVER-1000 core at the end of irradiation history

6.2 Integral model of the VVER-1000 NPP

6.2.1 Reactor Pressure Vessel model

The ICARE module inside ASTEC is used for the representation of the fluid channels and physical structures and it deals with the thermo-physical phenomena such as heat transfer, oxidation, molten material relocation and interaction with other materials as well as in the lower plenum (LP).

With the developed model, the core region is represented in a simplified manner five radial thermal-hydraulic channels. Additionally, two channels are modelled to represent bypass and downcomer channels inside of the core section. Each channel includes fuel rods, claddings, control rods, control rod claddings, guide tubes, spacer grids and lower plenum plate according to the weightings. **Figure 6-3** illustrates the sketch of modelled VVER-1000 vessel in ASTEC code.

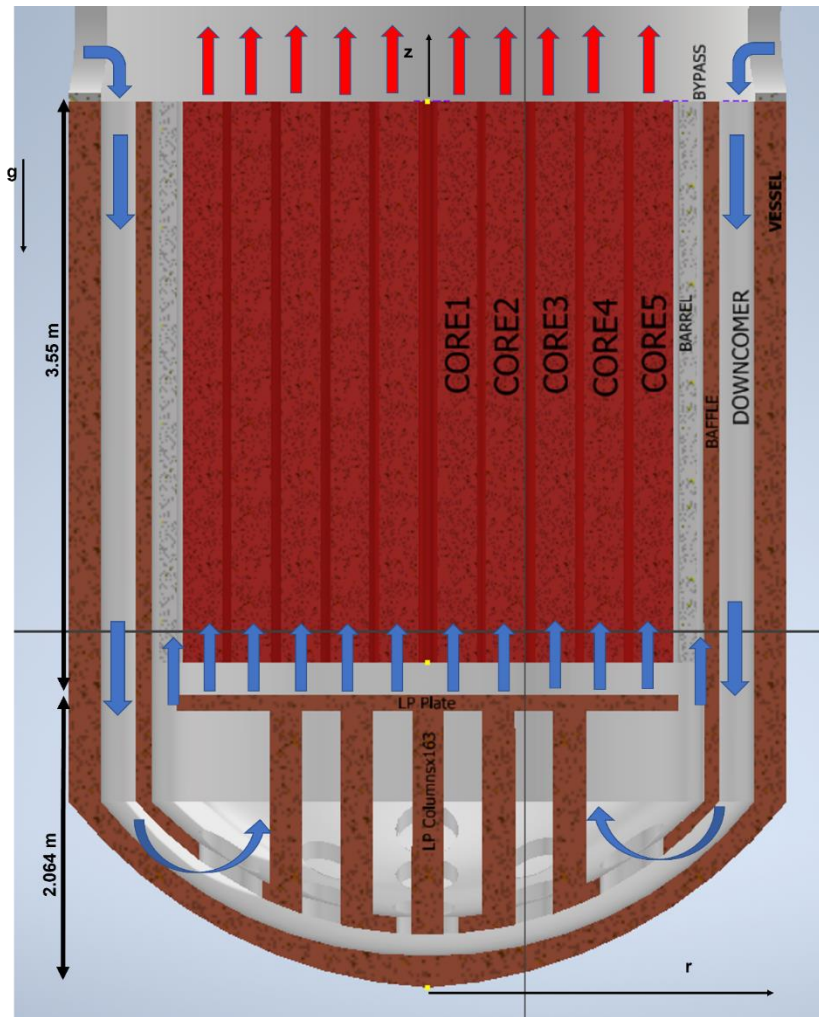


Figure 6-3: Sketch of the reactor vessel for a generic VVER-1000 as modelled in ASTEC

The fuel rods of VVER-1000 consist of UO_2 pellets with a central hole which is unique for VVER fuels. As cladding material, niobium based zircaloy E110 (or Zr-1%Nb) material is used in the plant. However, Zr-4 material is used to represent cladding in the developed ASTEC model since the thermal properties and oxidation models developed for E110 is not available in ASTEC databank. Absorber rods made of B_4C are used as control rod materials and stainless steel is used in the cladding. Like fuel rod claddings, Zr-4 is used to represent grid spacer and guide tubes. The baffle separates the bypass channel from these thermal channels and barrel is located between the bypass and downcomer. Finally, the vessel wall consists of stainless steel, containing the core region.

6.2.2 Primary and secondary circuit model

The CESAR module of ASTEC allows modelling of the primary and secondary coolant circuit components by using control volumes, junctions and walls. In the developed ASTEC model, a four-loop plant is represented by two loops, in which loop 1 includes the pressurizer

(PRZ) and loop 2 consist of the other three loops. The ASTEC representation of the primary and secondary circuit for the loop with pressurizer is illustrated in **Figure 6-4**.

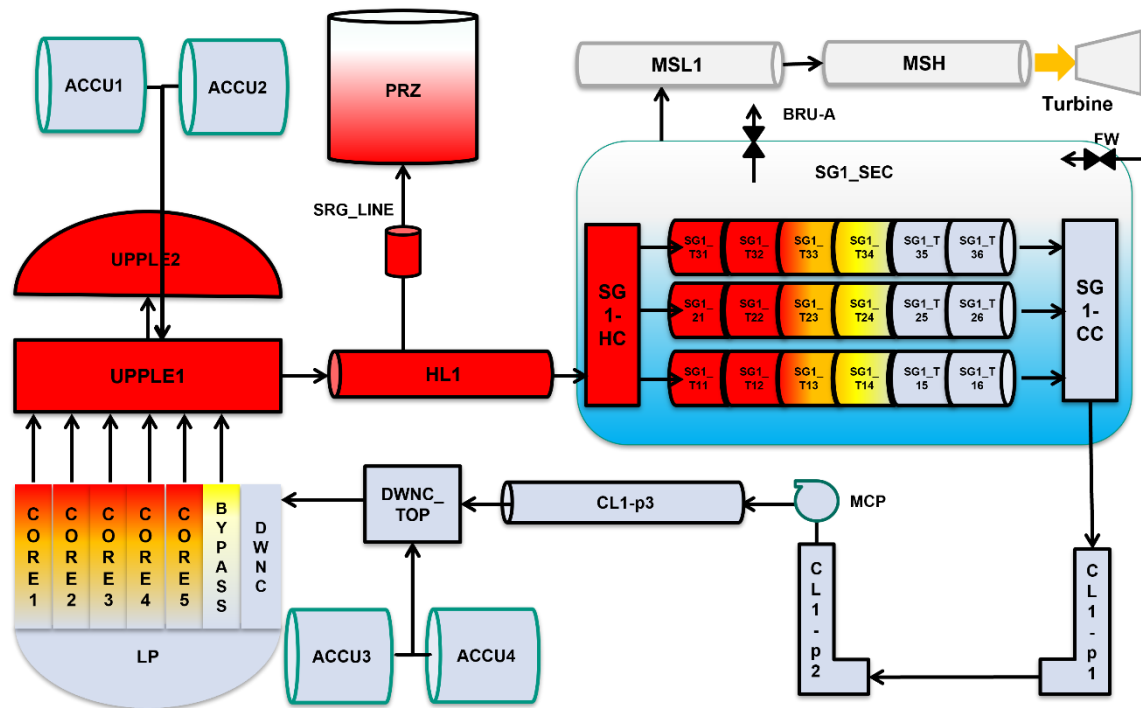


Figure 6-4: Sketch of the primary and secondary circuit model of ASTEC for a generic VVER-1000 reactor; here loop 1 with the PZR

The vessel section is connected to the upper plenum and the coolant moves to the hot legs and upper head. Coolant moves to the steam generator (SG) hot collector head through hot legs. Pressurizer is connected to the hot leg through surge line and pressure is regulated with heaters. Unique to a VVER reactor is the horizontal design of the SG requiring six control volumes at three different elevations to accurately capture heat transfer from the primary circuit to the secondary side. Additionally, hot collectors (HC) and cold collectors (CC) are separated into three axial volumes to calculate accurate thermal properties at different elevations. The cold collector is collected to the cold leg and the cold leg is discretized into three volumes. Recirculation of the coolant is sustained by the modelling of the Main Coolant Pumps (MCPs) between two volumes of the cold legs.

Secondary side of the SG is modelled as a single volume with injection of the 408 kg/s of feedwater at 220 °C. The water level of the SG is 2.55 m and regulation of the flow of the injection is modelled in order to keep the level. Steam moves to the corresponding Main Steam Line (MSL) where the pressure boundary condition is set to 6.27 MPa. Each MSL is connected to Main Steam Head (MSH) to be passed to the turbine.

6.2.3 Cavity and Containment models

The containment modelling is established by the CPA module of the ASTEC, and the module calculates heat and mass transfer between zones inside of the containment during transient. The model of the containment is depicted in **Figure 6-5**.

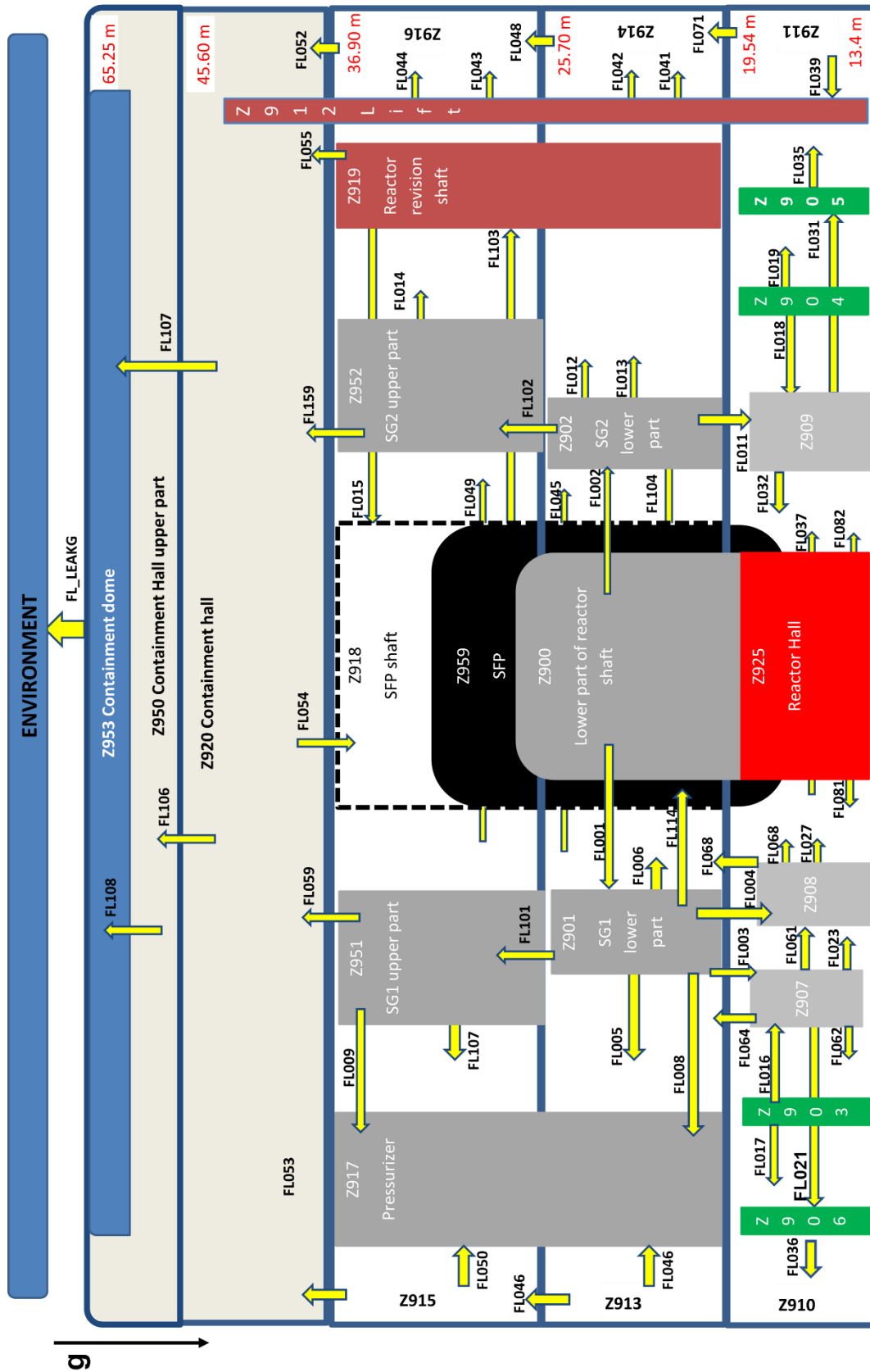


Figure 6-5: Sketch of the containment model for a generic VVER-1000 by ASTEC

The VVER-1000 containment is separated into 27 control zones. Also, the environment is modelled by a large volume. The rooms for essential components that are considered in the model listed below.

- The lower part of the reactor shaft (Z900) and reactor hall (Z925)
- Upper, and lower parts of the SGs (Z909 and Z952 for SG, and Z901 and Z951 for SG2), sections below the SGs (Z907, Z908 and Z909), pressurizer and surge line (Z917) as in grey
- Spent fuel pool and SFP shaft (Z959 and Z918)
- Reactor revision shaft and lift (Z919 and Z912)
- Reactor halls at the dome (Z920, Z950 and Z953)
- Upper, middle and lower sections and ladders of the containment (Z910, Z911, Z913, Z914, Z915 and Z916)
- Steam valve operation filters (Z903, Z906, Z904 and Z905)

Atmospheric junction has been established for the connection between zones which allows heat and mass exchange between zones. The leakage to the environment is sustained between Z953 to the ENVIRON zones and the leakage is sustained after the pressure of the dome exceeds 4.1 bar. Walls of the containment are also modelled to be used as surfaces that aerosols can interact with. The filtering operation as well as containment spray systems are not considered.

6.2.4 Control and safety system models

In the ASTEC model of VVER-1000, convergence of the steady state parameters has been obtained by modelling several control systems. These control systems allow obtaining expected value of a selected parameters at the end of the calculation by adjusting the effective parameter on the expected value. Also, the heaters in the pressurizer are adjusted by regulations in which they are switched off after the steady-state conditions are fulfilled. The regulations in the model have been listed below:

- Heating power in the pressurizer is regulated by the pressure inside of the pressurizer.
- A water flow rate of 4400 kg/s at is expected at each loop of the reactor cooling system. A regulation on the torque of the MCP is modelled to sustain expected value of the flow rate.
- Pressurizer liquid water volume is 55 m³ at nominal conditions for a VVER-1000 reactor. For this purpose, regulation depending on the liquid water volume has been modelled and flow rate of the pump on pressurizer is adjusted.

- Similar to the pressurizer water volume, steam generators have a regulation to optimize water level. Feedwater flow is modified according to the liquid water volume of the steam generators to sustain 2.55 m level.
- Pressure value at the exit of steam generators is also established by a regulation which adjusts the pressure drop coefficient on the junction between steam generators and MSL.
- The flow rate of feedwater is expected to be 408 kg/s. Hence, a regulation on the pumps of main feedwater has been defined to sustain this value by deviation on the flow of these pumps.
- Pressure drops along the RCS is also set by means of several regulations. These regulations sustain the pressure drop values by adjusting the pressure drop coefficient defined for the junction. Pressure drop on the downcomer has been set to 193 kPa, pressure losses on the upper plenum is adjusted as 60 kPa and pressure drops on the cold legs is modelled to be 10.1 kPa.

6.2.5 Verification of the integral ASTEC-model

ASTEC results for the key system parameters are verified by comparing with the reference data at full power conditions (Ivanov, Ivanov, Groudev, Pavlova, & Hadjiev, 2002) in order to demonstrate that the generated model can represent the steady-state conditions. For this aim, the predictions of the ASTEC, the reference values and relative error between them are compared in **Table 6.1**.

Pressurizer regulations exhibit almost identical RCS pressure with the reference value and mass flow rate of the RCS is same with the literature. A slightly lower pressure drop is observed on the core. A possible reason can be the radial modelling of the channels.

The core inlet temperature is overestimated by the developed model of ASTEC; however, the core heat-up compensates for lower inlet temperature and sustains accurate core exit temperature. The reason for the difference could be the physical effect, particularly the effect of momentum transfer, of lower plenum structures and plate modelling.

When all the relative errors are examined, the differences are smaller than 5%. Further studies on the system are required to determine possible reasons for deviation of core inlet temperatures and lower plenum pressure. Still, the whole picture of the inlet conditions shows a capable and operational model to move transient.

Table 6.1: Comparison of the key plant parameters of the VVER-1000 between ASTEC predictions and the literature (Ivanov, Ivanov, Groudev, Pavlova, & Hadjiev, 2002)

Name of the parameter	Unit	Reference	ASTEC	Rel. Error (%)
Core power	MW	3000	3000	0
Lower plenum pressure	MPa	15.842	15.82	0.11
Pressure above the core	MPa	15.70	15.699	0.13
Core inlet temperature (Loop 1)	K	560.15	561.76	0.29
Core inlet temperature (Loop 2)	K	560.15	561.79	0.29
Core exit temperature (Loop 1)	K	592.05	592.053	0.009
Core exit temperature (Loop 2)	K	592.05	592.1	0.009
Core inlet mass flow rate (Loop 1)	kg/s	4400	4400	0
Core inlet mass flow rate (Loop 1)	kg/s	13200	13200	0
SG exit pressure (Loop 1)	MPa	6.27	6.27	0
SG exit pressure (Loop 2)	MPa	6.27	6.27	0
SG exit temperature (Loop 1)	K	551.65	551.37	-0.05
SG exit temperature (Loop 2)	K	551.65	551.37	-0.05
Feedwater flow	kg/s	409	409	0
Feedwater temperature	K	493.15	493.15	0
SG water level (Loop 1)	m	2.55	2.55	0
SG water level (Loop 1)	m	2.55	2.55	0
SG power transfer (Loop 1)	MW	750	748.81	-0.16
SG power transfer (Loop 2)	MW	2250	2254.5	0.2

6.3 Source term prediction for LBLOCA severe accident sequence of the VVER-1000

For predicting transported and released ST, a hypothetical severe accident is modelled ASTEC. According to the Probabilistic Risk Analysis (PRA) of a VVER-1000 and the core damage frequencies revealed by the PRA, the severe accident case is selected.

The outcomes of the PRA on the example of the Kalinin VVER-1000 plant are shown in **Figure 6-6** (U.S. Nuclear Regulatory Commission (NRC), 2005). According to the analysis, primary LOCAS inside of the containment are the predominant phenomenon in the incident (U.S. Nuclear Regulatory Commission (NRC), 2005). Additionally, the double ended guillotine break LOCA (D=850 mm) has the highest frequency on the Core Damage Frequency (CDF). However, there is no indication over the location of the LOCA. Transients which include station blackout, reactivity insertion accidents (RIA) have the second most frequent contribution to the CDF and the loss of offsite power for more than 0.5 hours has the highest frequency within the transient cases. (U.S. Nuclear Regulatory Commission (NRC), 2005).

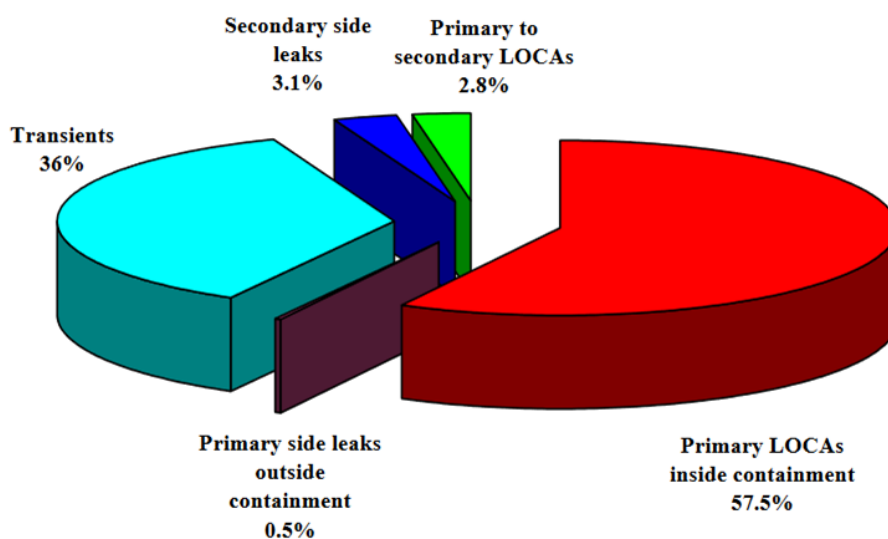


Figure 6-6: The core damage frequency according to the initiator event for Kalinin VVER-1000 NPP (U.S. Nuclear Regulatory Commission (NRC), 2005)

When the PRA is taken into the account, the following accident sequences in a VVER-1000 using ASTECV2.2b have been studied:

- Large Break LOCA (LBLOCA) of 850 mm diameter on the cold leg between pump and downcomer of pressurizer loop

- Large Break LOCA (LBLOCA) of 850 mm diameter on the hot leg of pressurizer loop

For each sequence of events, SBO without any diesel generator supply has been considered. Hence, all active systems are not functioning, only passive systems can be operational. The following assumptions have been made for both accident cases:

- MCPs are stopped at 0 s.
- Reactor SCRAM signal is given at 0 s.
- Turbine trips at 1.6 s after reactor SCRAM.
- Feedwater flow ends 5 s from the initiation of the event.

For each selected scenario, ASTEC predictions for both in-vessel and ex-vessel phenomena have been analyzed, and FP transport and release to the containment and to the environment have been calculated. During the severe accident, the FPs are carried by aerosols to the containment through the break. During this transportation, the aerosols interact with the several surfaces and the radionuclide inventory leaked to the containment significantly decreases. However, the location of the break may highly impact this transportation since a smaller amount of surface of the primary circuit involved through the pathway. Therefore, the consequence of the severe accident may significantly change. Therefore, two different locations of break are selected as severe accident sequences.

6.3.1 Source Term Transport and Release during a LBLOCA on cold leg of the pressurizer along with the SBO

In this section, a LBLOCA (850 mm) in the cold leg of the pressurizer loop is analyzed. The break occurs at 0.0 s at the volume of CL1_p3 which can be seen in **Figure 6-4**. Consideration of SBO results in the loss of every active safety system like HPIS and LPIS. In the section, progression of the accident is identified and estimation of fission product transport and release to the environment during the transient is demonstrated. Heat profile during the event is shown in **Figure B.1- 1**.

The progression of accident as well as the sequence of major events during the transient are listed in **Table 6.2**. The computed generation of hydrogen mass is shown in **Figure 6-7**. The activity distribution because of FP release from the vessel with the activity of isotopes transported to containment and released to the environment is demonstrated in **Figure 6-8**. Also, isotope-wise activity in the containment and in the environment is compared in **Figure 6-9**. The selected further key results of the analysis have been shared in **Appendix B**. According to the analysis, following observations and evaluations can be done:

Table 6.2: Computed sequence of the major events during the transient of LBLOCA on cold leg of the pressurizer loop along with the SBO

Event	Time (s)
Break Opening on the Cold Leg	0
Reactor Scram	0
Coast-down of the MCPs	0
Turbine Trip	1.6
Closing of Feedwater Connections	5
Start of Accumulators' Injection	12
Depletion of Accumulators' Inventory	101
Beginning of Core Uncover	215
Start of FP Release from the Fuel Pellets	2124
Start of Structural Material Release	2213
Total Uncover of the Core	2534
First Material Slumps in the LP	3216
Lower Head Vessel Failure	16294
End of Corium Slumping to the Cavity	16304
Cavity Rupture	79214

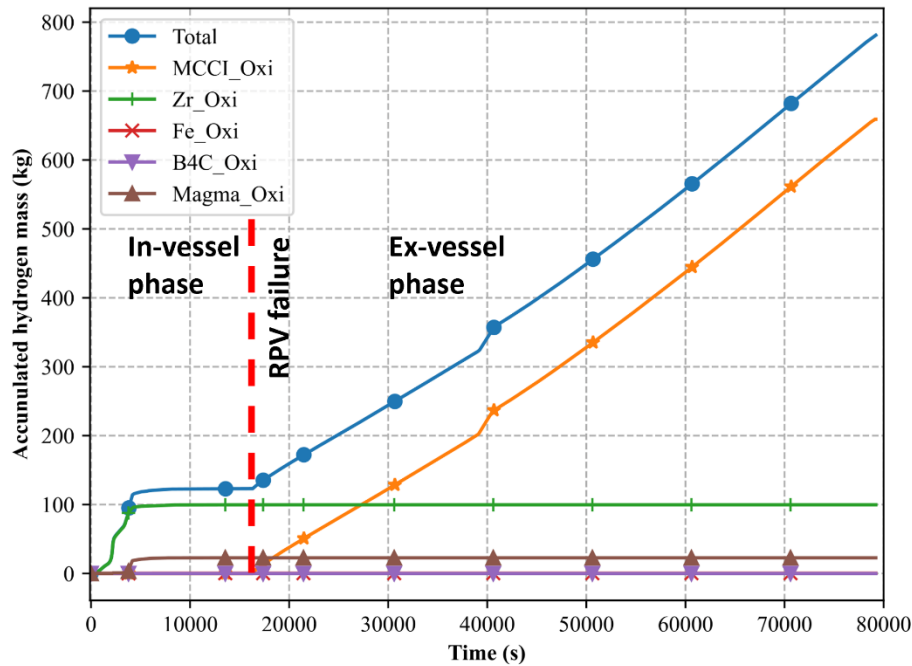


Figure 6-7: Computed generation of hydrogen mass as a function of time during the transient of LBLOCA on cold leg of the pressurizer loop along with the simultaneous SBO of a VVER-1000 reactor

The initiation of the large break results in an immense pressure drop in the primary circuit, and the pressure inside the containment rises above the design pressure but below than the maximum allowable containment pressure due to significant steam discharge to the zones, see **Figure B.1- 2**, **Figure B.1- 3**, **Figure B.1- 4** and **Figure B.1- 5**. Even though the injection by the accumulators is passively activated when the pressure is falls below 5.9 MPa which can be seen in **Figure B.1- 6**, the water inventory inside the RPV cannot be maintained during the transient, the injection only delays the uncover of the core and timely shifts the lower plenum failure. The reduction in liquid coolant inventory contributes to the heating up of the core due to the lower heat transfer coefficient of the steam. Moreover, the heating due to the chemical reactions, especially exothermic cladding oxidation during this phase, is considerable and sometimes even exceeds the decay heat. When the peak temperature of cladding rises above 2500 K, the generated oxide layer begins to reach the melting point. The core is uncovered 42 minutes after the opening of the break, but the lower plenum still contains liquid water until the end of the in-vessel phase.

Molten materials start to relocate downwards through channels and partially freezes by the interaction with water. Yet, rapid decrease in the core levels results with remelting of these frozen structures and these materials potentially reaches to the LP. The first material slumps in the LP have been observed at 3216 s. after the initiation of the event. Inside of the lower

plenum, metallic layer and oxide layer are formed, see **Figure B.1- 7**. Oxide layer consists of UO_2 and ZrO_2 whereas metallic layer includes structural elements such as Fe, Zr and Ni. Formation of these layers ignites decay heat transfer to the walls of the RPV. Eventually, the RPV fails after the total temperature reaches above 1473 K on the mesh that 1.4 m higher than the bottom of the RPV because of the focusing effect. After this point, strong ejection of molten materials to the cavity is observed which triggers the MCCI process, and vertical and horizontal erosion begins to ablate the cavity. Since the cavity is dry, the rupture of the cavity is observed approximately 22 h. after the beginning of the transient which can be seen in **Figure B.1- 8**. Although axial erosion creates strong erosion caused by ejection of the molten materials is effective at the first stage of ablation, radial erosion influences the cavity more and rupture is observed on the walls of the cavity because of siliceous structure of VVER-1000 cavity.

When the fuel rods are uncovered, the oxidation by steam starts on claddings, spacer grids and guide tubes as well as stainless steel oxidation. Additionally, the oxidation of molten materials contributes to the generation of the hydrogen and relocation to the lower sections of the vessel and meeting with the coolant inside of the covered part of the vessel and the LP triggers strong oxidation. At the end of the in-vessel phase of transient, the oxidation of Zr material is dominant over the total generation. The reactor pressure vessel failure results with ejection of molten materials to the cavity and additional hydrogen and other gases release. The MCCI process generates 660 kg hydrogen which is almost six times greater than the whole in-vessel phase. Additionally, the CO generation during the MCCI process reaches 1600 kg in which contributes to the total inventory of burnable gas in the dome, see **Figure B.1- 10**.

After the fuel rods start to release FPs, these elements relocate to the primary circuit through the transport by hydrogen and steam. Primarily, the noble gases reach the containment through the break without any retention and create most of the activity inside of the containment. On the other hand, other isotopes interact with the walls of the primary circuit wall and transfers heat and mass. The highest retention is observed on the walls of steam generators because of sharp directional change between collectors and the steam generator tubes. Additionally, the upper plenum is another important retention location inside of the circuit especially for low volatile isotopes. At the end of the calculation, almost 99% of the isotope mass remained inside of the primary circuit. Despite this high retention, the release to the environment reaches about $1.20E18$ Bq levels. The activity distribution during the transient is illustrated in **Figure 6-8** and isotope-wise activity in the containment and in the environment is shown in **Figure 6-9**.

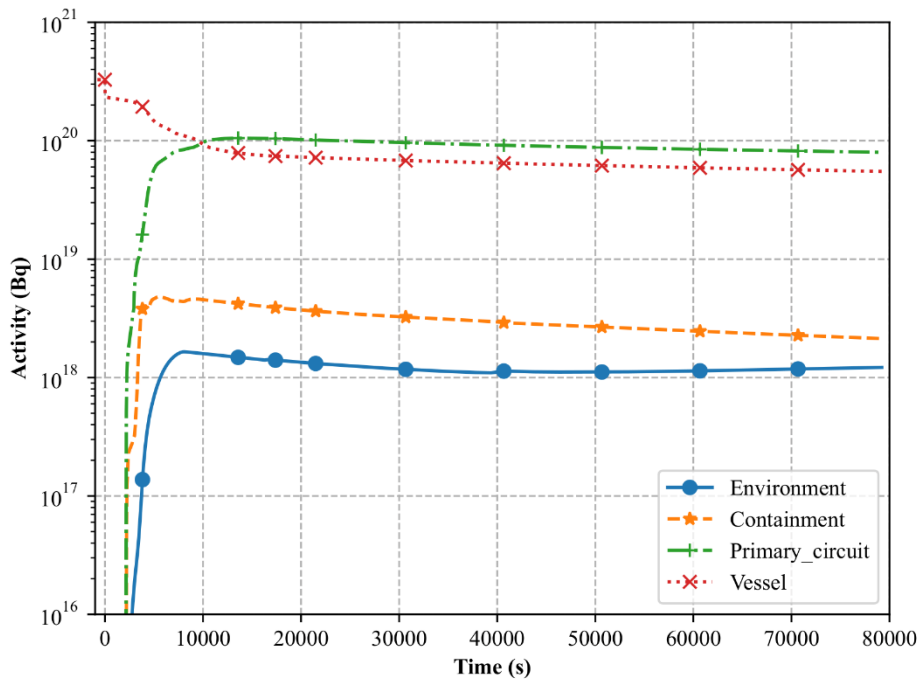


Figure 6-8: Computed temporal evolution of the activity transported from vessel to primary circuit, containment and environment cold leg of the pressurizer loop along with the simultaneous SBO of a VVER-1000 reactor

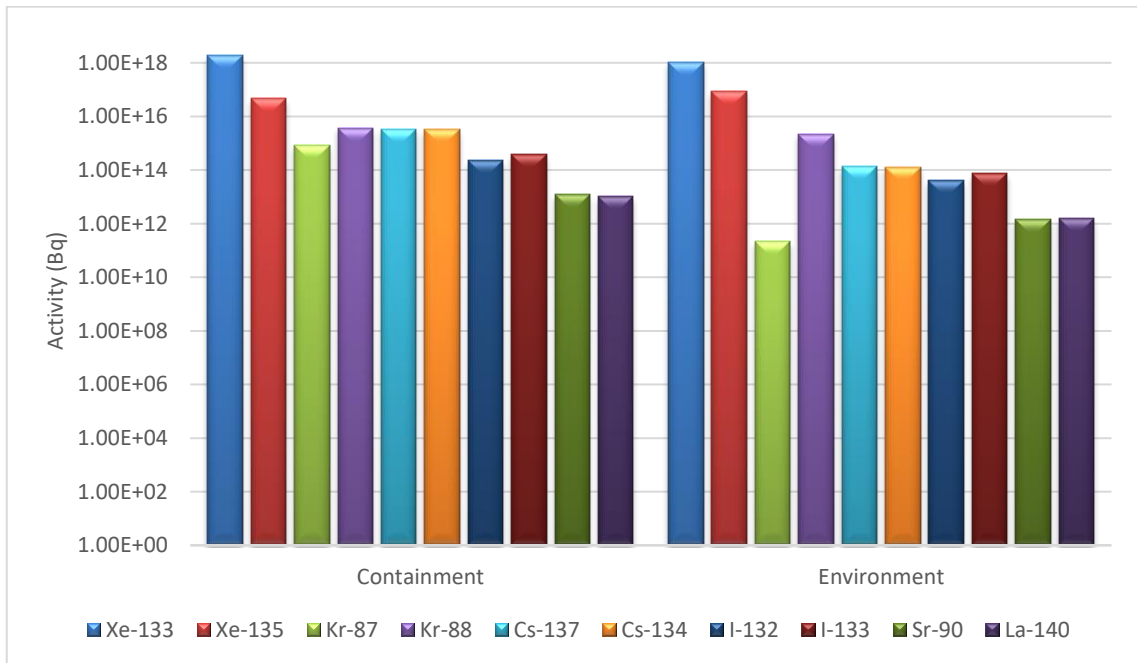


Figure 6-9: Computed activity level after a LBLOCA on the cold leg of pressurizer loop along with a SBO in the containment and in the environment at the end of transient for selected isotopes

6.3.2 Source Term Transport and Release during a LBLOCA on hot leg of the pressurizer loop along with the SBO

This section is dedicated to LBLOCA (850 mm) on the hot leg of the pressurizer loop with SBO case analysis. As can be seen of **Figure 6-4**, the 850 mm break is located on the HL1 volume in the model. Similar to the prior section, the progression of the accident is analyzed and predictions over FP release and transport have been shown in this part.

The sequence of the major events occurring is listed on **Table 6.3** and hydrogen generation during the transient is shown in **Figure 6-10**. The FP release from the vessel, transport of FPs to the containment and release of FPs to the environment are shown in **Figure 6-11** and the comparison between the activity transported to the containment and to the environment is illustrated in. Additional results of the analysis are presented in **Appendix B**.

Table 6.3: Calculated sequence of the major events during the transient of LBLOCA on hot leg of the pressurizer loop along with the SBO

Event	Time (s)
Break Opening on the Cold Leg	0
Reactor Scram	0
Coast-down of the MCPs	0
Turbine Trip	1.6
Closing of Feedwater Connections	5
Start of Accumulators' Injection	14
Depletion of Accumulators' Inventory	115
Beginning of Core Uncover	153
Start of FP Release from the Fuel Pellets	1576
Start of Structural Material Release	2621
First Material Slumps in the LP	4286
First Material Slumps with FP in the LP	4556
Uncover of the Core	6426
Lower Head Vessel Failure	33295
End of Corium Slumping to the Cavity	33305
Cavity Rupture	109628

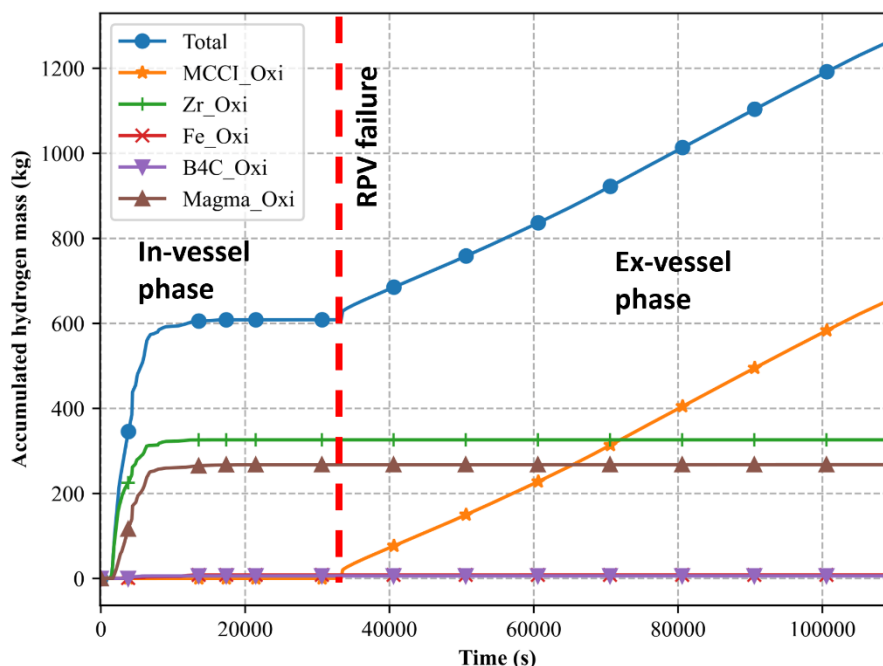


Figure 6-10: Computed generation of hydrogen mass as a function of time during the transient of LBLOCA on hot leg of the pressurizer loop along with the simultaneous SBO of a VVER-1000 reactor

Similar to the previous case, the power source is delayed neutrons and decay heat of the FPs after the shutdown, see **Figure B.2- 1**. The hot leg pressure is lower than the cold leg during steady-state conditions. Indeed, having lower pressure results with slower discharge of steam from the primary circuit to the containment than the discharge in the break on the cold leg case when the break is located on the hot leg. Therefore, the uncovering of the core, the failure of the pressure vessel and rupture of the cavity is observed at later stage than the one for a break in the cold leg. The pressure change in the primary circuit and in the containment are shown in **Figure B.2- 2**, **Figure B.2- 3**, **Figure B.2- 4** and **Figure B.2- 5**. Like the previous case, the pressure is below the maximum acceptable pressure of the containment. Slower discharge is also visible in the **Figure B.2- 6** which shows the accumulator inventory change in time.

When considering hydrogen production, a higher total mass of hydrogen is generated in both the in-vessel phase and the ex-vessel than the case of break on the cold leg. This difference is due to the subsequent exposure of the core and the increasing oxidation of the molten material. Molten materials which relocate to the lower sections of the RPV interact with the uncovered part of the core earlier than in the cold leg case. This situation leads to freezing of this molten material before it reaches the lower plenum. However, oxidation of Zr materials still dominates the total generation, but the contribution of oxidation of molten material increases share inside of total hydrogen generation. In contrast to the previous case, hydrogen generation

during in-vessel phase exceeds that during the ex-vessel phase. The main reason for this situation is more amount of material melts during break on the hot leg of the pressurizer loop which leads to more ejection of core mass to the cavity and faster ablation of cavity. The change of the masses of the gases in the containment is shown in **Figure B.2- 10**.

The results of the analysis show that, despite the equal size of the breaks, all important events are observed later than for the case of break on the cold leg. Higher pressure value at the cold leg results in earlier coolant discharge which delays each subsequent event. The most obvious difference between the cases is observed in the FP release and transport results. Since the steam generator is bypassed due to the location of break, more FP can be transported to the containment. The retention on the walls of the upper plenum of the RPV becomes dominant in this case, yet the retention rate for the volatile elements such as Cs and I decreases even to 20% of its original mass. Therefore, the release to the environment reaches at the end of the calculation 7.0×10^{18} Bq which is significantly higher than in case of the cold leg.

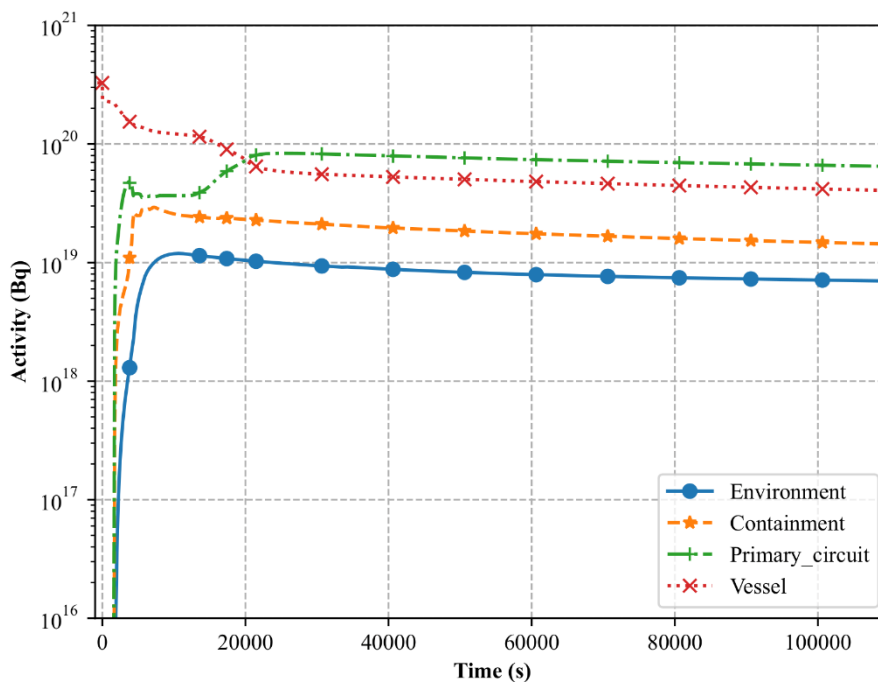


Figure 6-11: Computed temporal evolution of the activity transported from vessel to primary circuit, containment and environment hot leg of the pressurizer loop along with the simultaneous SBO of a VVER-1000 reactor

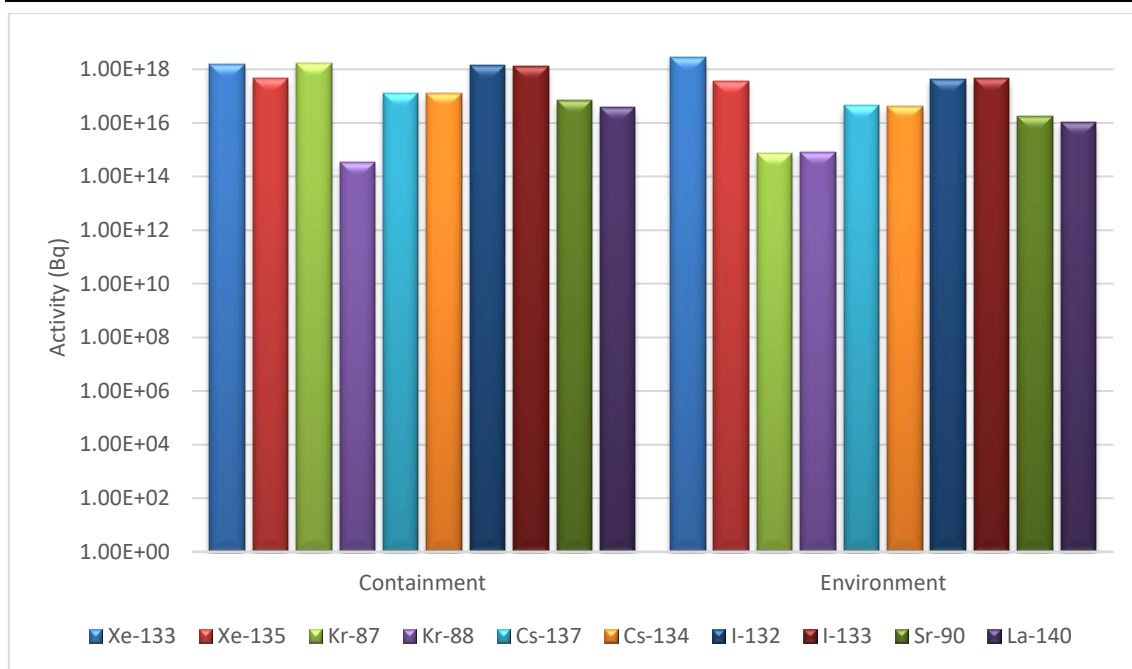


Figure 6-12: Computed activity level after a LBLOCA on the hot leg of pressurizer loop along with a SBO in the containment and in the environment at the end of transient for selected isotopes

6.4 Summary

In this chapter, ASTEC analyses on several cases are performed to predict the radiological source term for a VVER-1000 reactor. The impact of the equal size of breaks at different locations is observed for the case of Large Break Loss of Coolant Accident along with the Station Blackout Accident. According to the results, following elements summarize that:

- Break at the cold leg analysis shows that reactor pressure vessel failure can be observed 4 hours after the initiation of the break. Furthermore, the breach in the cavity takes 22 hours.
- Rupture at the hot leg results in much later failure of the vessel and delayed breach in the cavity, approximately 8.5 hours, than the one in the case of cold leg is observed. Hence, a larger time window for the application of accident management guidelines is possible for this case.
- Even though hydrogen generation in both cases is close to each other, hot leg case reaches these values about 14 hours earlier than in the cold leg case which can lead to early deflagration of the hydrogen in the containment. Unfortunately, pressure peaks created by local hydrogen explosions cannot be estimated by ASTEC.
- Significantly higher Source Term inventory in the environment is observed for the break on the hot leg than in the cold leg case, the difference is about 5.8×10^{18} Bq. Since

the retention in one of the steam generators cannot be possible in the hot leg case, higher inventory can leak to the containment and further to the environment.

It should be noted that no model for the ventilation and filtering systems has been employed in the ASTEC model of the generic VVER-1000 NPP, which lead to a substantial reduction of both the containment pressure and of the fission product release to the environment. Similarly, no SAMs have been considered aiming at mitigating the accident progression and the ST, as shown in, e.g., (Gomez-Garcia-Tarano, 2017) (Tusheva, 2012). Nevertheless, it should be reminded that the goal of the current work is the assessment a novel platform as well as the corresponding proof-of-concept aiming at significantly increase the reliability of the ST prediction and of the estimation of the radiological consequences in the environment.

It can be concluded that release to the environment in both cases is inevitable and it is essential to predict radiological impact due to this release which is conducted in the next step.

7 Estimation of the radiological impact after a severe accident in a VVER-1000 NPP using JRODOS

Following the evolution of different SA scenarios in a VVER-1000, the radiological consequence analysis is conducted by means of the JRODOS using the severe accident data of FP inventory released as Source Term computed by ASTEC and described above. Initially, radiological dispersion and its impact of the leaked source term inventory obtained from the LBLOCA on the cold leg of the pressurizer with SBO is analyzed in **Section 7.1** for the location of Kozloduy NPP at winter weather conditions. **Section 7.2** describes the consequence analysis at the Akkuyu NPP site in summer conditions using the leaked source term inventory of the LBLOCA on the hot leg of the pressurizer loop with SBO. Both locations are VVER reactor sites, though VVER-1200 is being built in Akkuyu site, and they are selected for the JRODOS simulations.

In both calculations, the JRODOS simulation starts with the initiation of the break and continues for 10 days even though the calculation of ASTEC finishes. This assumption means that release to the environment starts when FP reaches the environment.

Note that the novel KORIGEN/ASTEC/JRODOS platform is here employed to predict not only the radiological consequences of the two selected scenarios but also to determine the conditions of the application of emergency response countermeasures. Moreover, the platform is also challenged with a plant site under construction outside of the European region to demonstrate that the novel platform has the potential to be employed in plant locations and meteorological conditions in any region of the world.

7.1 JRODOS analysis of the VVER-1000 at the Kozloduy NPP site after a hypothetical LBLOCA on the cold leg of with SBO

The LBLOCA on the cold leg of the pressurizer circuit along with SBO has shown that despite high retention, the activity released to the environment **Figure 6-9** reaches E18 levels of activity. Therefore, this section investigates possible dispersion of this released source term inventory by JRODOS to predict radiological consequences to the public and to the environment. The assumptions for the dispersion analysis are in the following:

- The calculation area is selected as 1600x1600 km^2 .

- The criteria over sheltering, evacuation and stable iodine distribution determined by Bulgaria is considered for emergency action.
- The sheltering will be active if the effective dose is higher than 10 mSv, and evacuation will start when the effective dose reaches 50 mSv.
- The stable iodine will be distributed when the thyroid dose reaches 100 mSv for adults and 10 mSv for children.

The simulated total deposition of the aerosol at the end of 10 days is shown in **Figure 7-1**. Simulated effective dose on adult after 1 year from cloud shining, ground shining, inhalation and ingestion is depicted in **Figure 7-2**. Finally, dose over cow milk after the contamination is presented in **Figure 7-3**. Further results of dispersion analyses such as acute doses affecting different organ groups, lifetime effective and lifetime thyroid doses on children and adults from all pathways, and dose over grass and milk are shown in **Appendix C**.

The ST is transported to the west-southwest part of the plant on the first day of the calculation, then, the contamination spreads to the southern regions of the selected area over the next 9 days. The cloud arrival and departure are demonstrated in **Figure C.1- 1** and **Figure C.1- 2**. These regions are mostly used for agriculture and contain woodlands; therefore, various feedstuff and foodstuff can be affected. The house types have generally low shielding, and this region has high cloud shine and ground shine location factors which can increase the dose uptake. Clouds move through less mountainous regions; hence, the higher depositions are observed over the valley between these mountains. **Figure 7-1** shows the total deposition of aerosol species at the end of 10 day. Total contamination by aerosols reaches about 22.9 MBq/km² as maximum which the maximum deposition of iodine, **Figure C.1- 4**, is 4.45 MBq/km², and the total deposition decreases to kBq/km² levels at 200 km east or 400 km south from the center of event. Dry and wet ground contamination of Cs-137 is calculated as 1.78 MBq/km² at most which can be seen in **Figure C.1- 3**. Finally, the air concentration near ground is only observed in an area up to 18 km east of the site.

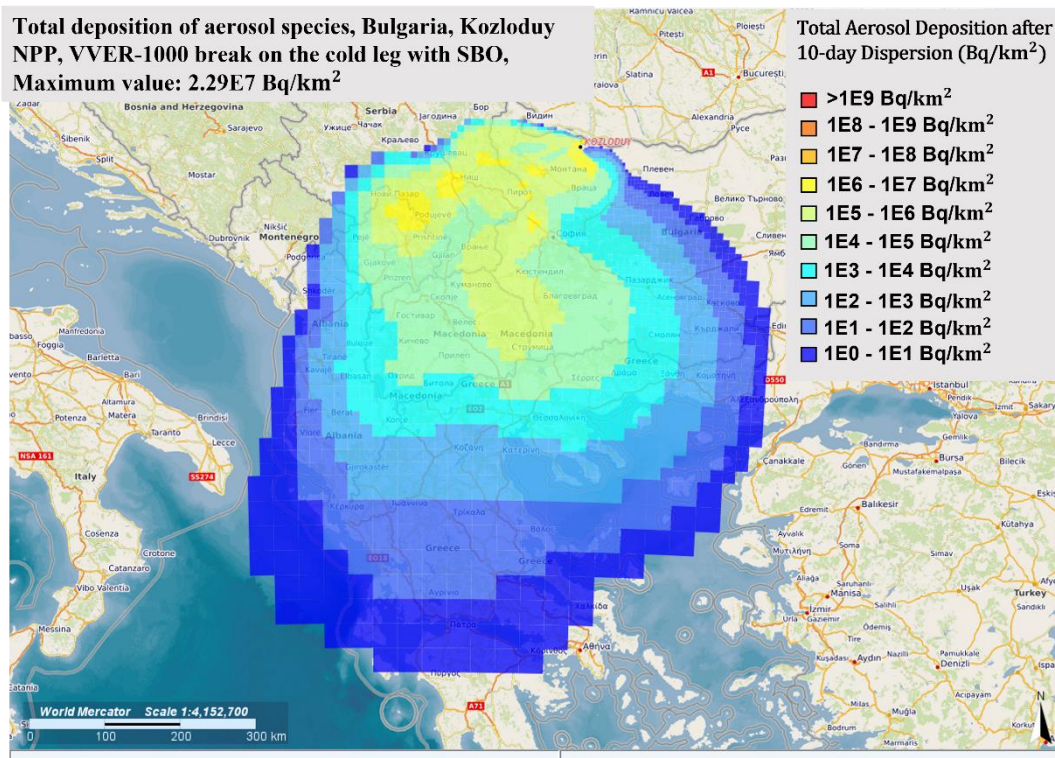


Figure 7-1: Calculated total aerosol contamination over the calculation site at the end of the 10-day of radiological dispersion of ST calculated for LBLOCA on the the cold leg accident case with SBO

The contamination of aerosols influences the people by ground shining, cloud shining and inhalation after the dispersion. The total committed effective dose for normal living can reach 106 mSv as maximum which can only be observed for 4 km² area, and like the spread of the contamination, doses under 1 mSv are observed up to 50 km west of the site due to cloud movement. However, the committed thyroid dose after 1 year reaches 370 mSv as maximum in the first 4 km² area and the doses over 1 mSv can reach up to 200 km southwest of the site. Sheltering decreases the uptake of this dispersion up to 0.147 mSv but temporary and permanent relocation as well as stable iodine pills could help avoid most of the doses. When ingestion is considered together with cloud shining, ground shining and inhalation, the effective dose of all nuclides and all pathways can reach up to 1.38x10³ mSv as maximum at the plant site for an adult in a year if intervention is not supplied, with the contribution of ingestion being approximately 1.187x10³ mSv. During the same screening period and same location, the total effective dose for an infant is a maximum of 5.27x10³ mSv. However, the lifetime doses for adults and infants can only increase up to 2.05x10³ mSv and 5.61x10³ mSv respectively up the 2 km away to the plant, due to the biological and radioactive decay of isotopes that contaminated feedstuff and foodstuff. Effective and organ doses decrease below 100 mSv after 50 km, but effective doses below 100 mSv are calculated at 20 km from the site. Though, more severe radiological effects are observed at thyroid doses. An adult living 2 km from the site can

take 11.7 mSv after one year from I isotopes. An infant at same location may receive a higher thyroid dose, estimated at 90.8 Sv after one year. Since most I isotopes have short half-lives, the long-term doses after one year do not differ significantly. The annual and lifetime effective doses for children and adults are shown in **Figure C.1- 6**, **Figure C.1- 7**, **Figure C.1- 8** and **Figure C.1- 9**.

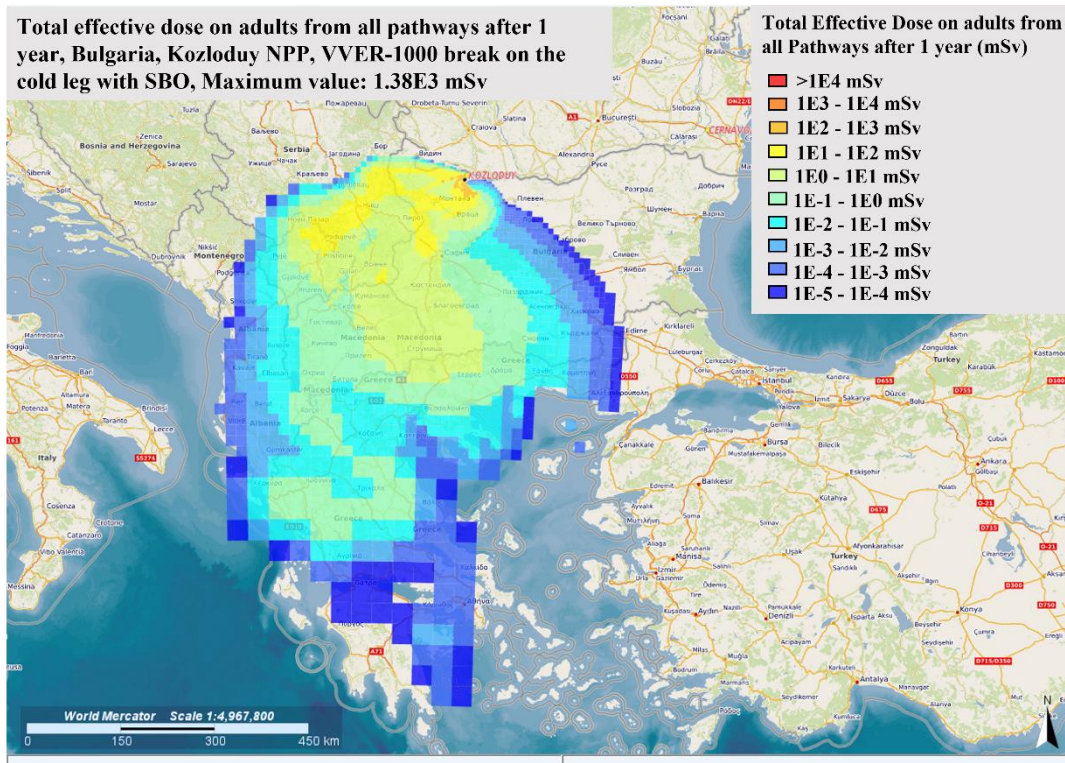


Figure 7-2: Simulated effective dose on adults by all pathways 1 year after 10-day of radiological distribution of ST calculated for LBLOCA on the cold leg accident case with SBO

The results of activity concentration show that cesium isotopes' dose over the grass reaches 16.0 MBq/kg as maximum at the end of the 10 days radiological dispersion at the plant site. However, this dose decreases to the 4.05 kBq/kg level after 400 km. Following the food chain, dose of cesium isotopes over the cow milk is 572 kBq/kg at highest up to 2 km away from the plant as illustrated in **Figure 7-3** and doses lower than 1.00 kBq/kg can be observed after 25 km. Dose of iodine isotopes over the grass is 19.7 MBq/kg and dose over the cow's milk is 2.88 MBq/kg. Nevertheless, the maximum cesium dose over grass decreases to 4.22 kBq/kg due to biological decay of the cesium elements. Similarly, thyroid dose over the grass almost diminishes at the end of 1 year. Furthermore, the impact of cesium isotopes over cows'

milk decreases after one year. However, the activity concentrations can be observed, especially over the grass, even after 100 years.

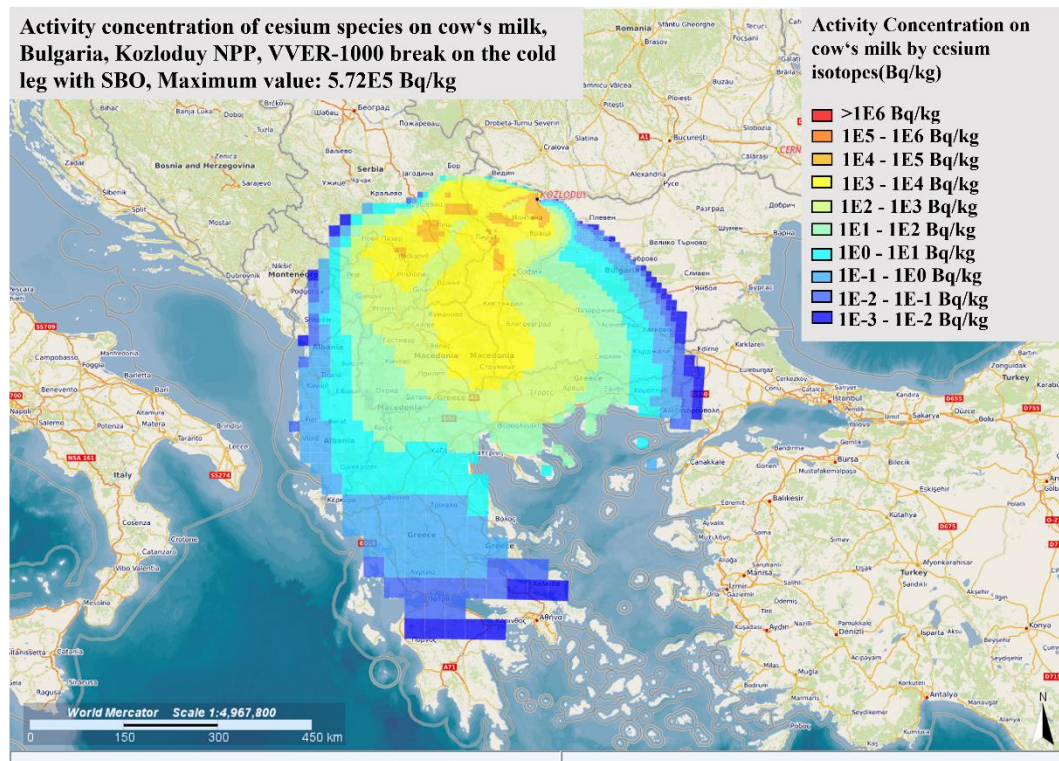


Figure 7-3: Simulated maximum activity of cesium isotopes in the cow's milk at the end of 10th day of radiological dispersion for the LBLOCA on the cold leg accident case with SBO

7.2 JRODOS analysis of VVER-1000 at the Akkuyu NPP site after a hypothetical LBLOCA on the hot leg with SBO

The LBLOCA on the hot leg of the pressurizer circuit along with SBO exhibit that higher amount of activity can reach to the environment which majority of the increase is resulted due to lower retention of volatile and low-volatile isotopes, see **Figure 6-12**. This section aims at investigation possible release of this activity from Akkuyu site. The assumption for the calculation is listed below:

- The calculation area is selected as $1600 \times 1600 \text{ km}^2$.
- The limitations over sheltering, evacuation and stable iodine distribution determined by German regulations are considered for emergency action (Strahlenschutzkommission (SSK), 2019).
- Evacuation will be started after an effective dose of 100 mSv.

- Actions for temporary relocation and permanent relocation will be applied when the effective dose is over 30 mSv and 100 mSv respectively.
- Stable iodine pills will be distributed when the thyroid doses reach 250 mSv for adults and 50 mSv for children.

Similar to the previous section. Total deposition of the aerosol at the end of 10 days, effective dose on adult after one year from cloud shining, ground shining, inhalation and ingestion and dose over cow milk after the contamination are demonstrated in **Figure 7-4**, **Figure 7-5** and **Figure 7-6**, respectively. Additional outcomes of the analysis are presented in **Appendix C**. Based on the results, following comments can be made:

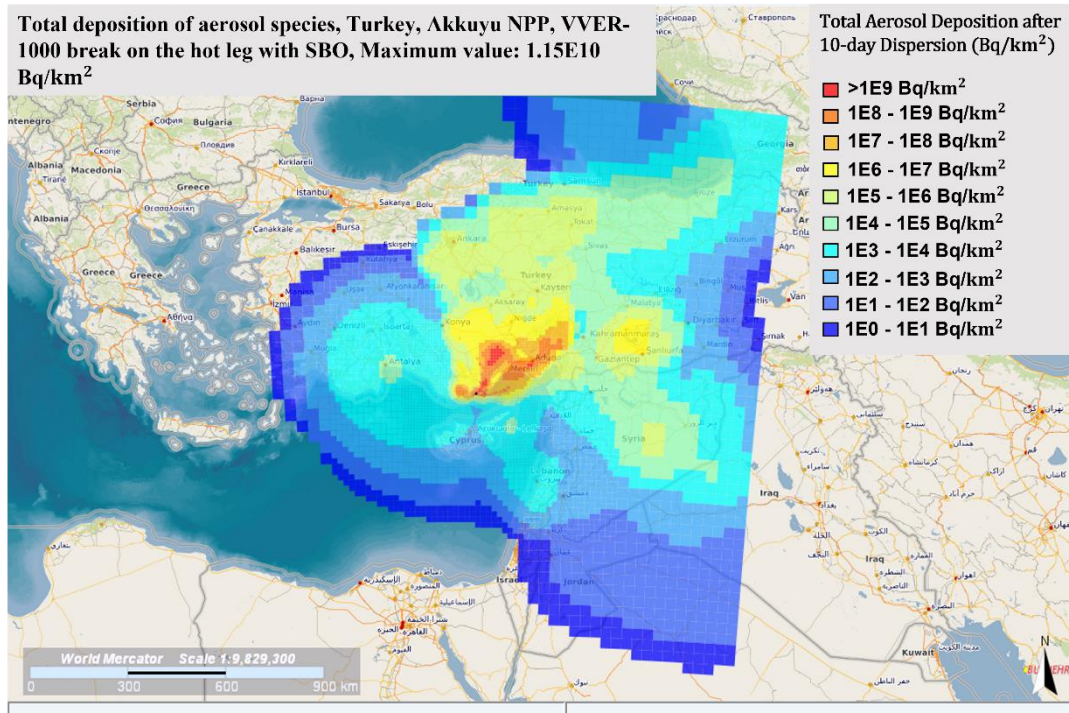


Figure 7-4: Simulated total aerosol contamination over the calculation site at the end of the 10-day of radiological dispersion of ST calculated for the hot leg accident

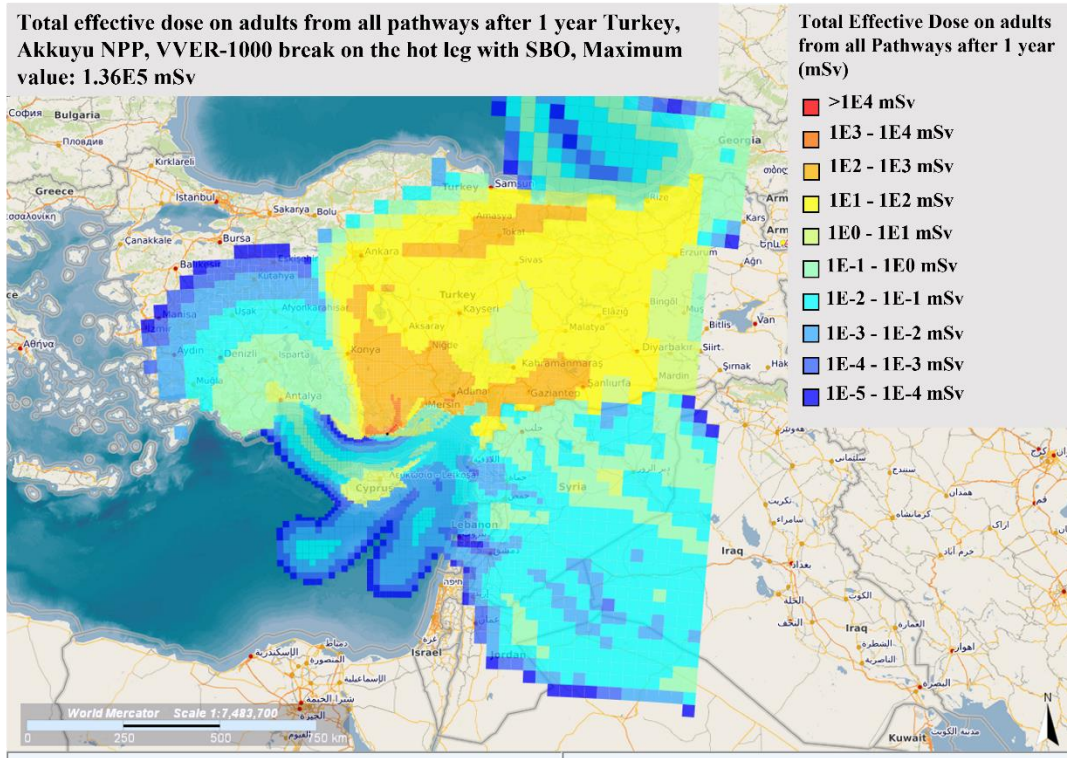


Figure 7-5: Simulated effective dose on adults by all pathways 1 year after 10-day of radiological distribution of ST calculated for a hot leg accident

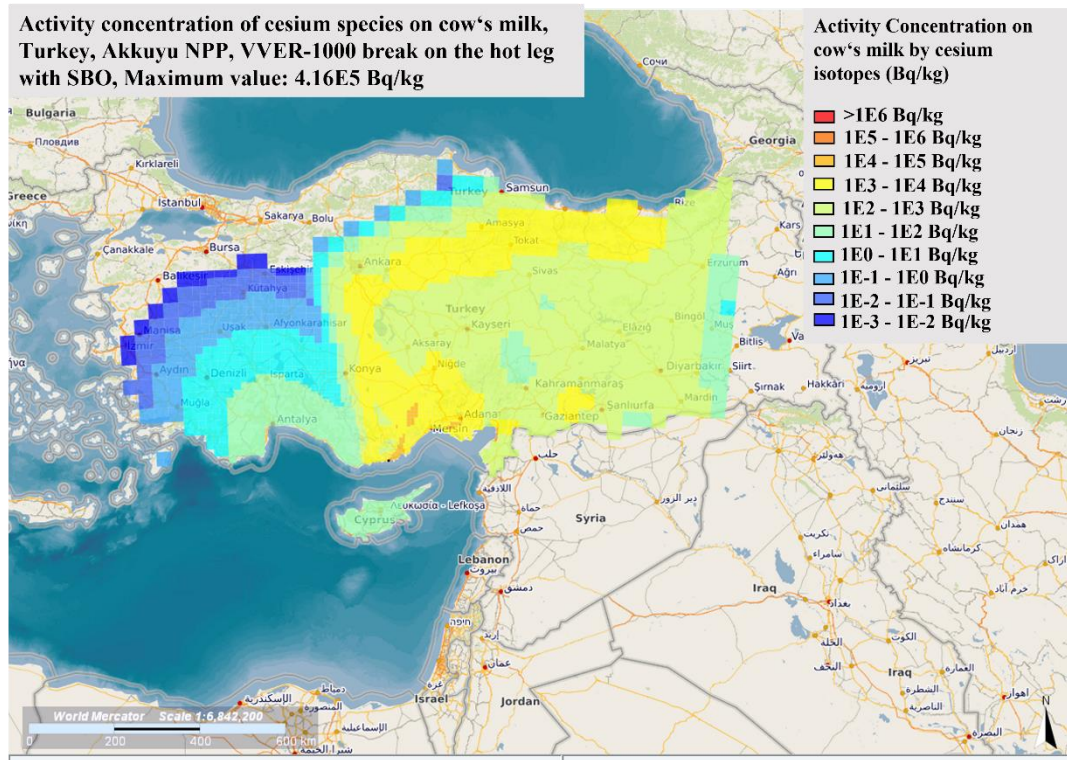


Figure 7-6: Simulated maximum activity of cesium isotopes in the cow's milk at the end of 10th day of radiological dispersion for the hot leg accident case

The deposition of the aerosol results shows that contamination mainly spreads mainly north and north-west part of the site at the first day of dispersion, see **Figure C.2- 1**. Winds carry the aerosol to the Caucasia, up to the edge of 1600x1600 km^2 area. Last day of the dispersion, eastern winds are effective and creates local contamination which can be seen in **Figure C.2- 2**. The maximum value of the aerosol contamination becomes 11.5 GBq/km^2 and depending on the direction, deterministic effects can be observed up to 200 km. In same area, the iodine contamination can reach up to 0.247 GBq/km^2 . The total wet and ground deposition of the Cs-137 is calculated 0.247 GBq/km^2 as maximum at the end of 10 day which the plant site has the highest contamination as demonstrated in **Figure C.2- 3**. Finally, wet deposition is the dominant factor on the total deposition of the aerosols due to high precipitation rate at the first two day of the dispersion.

When the acute doses are investigated during 10 days of dispersion, potential doses are much higher than the case of break on cold leg as expected. Committed effective dose for normal living conditions can encounter 1.13E5 mSv dose as maximum which is the $2 \times 2 km^2$ at the site. Doses under 1000 mSv can be observed after 27 km of the site and can be monitored up to 150 km depending on the direction. At the same $2 \times 2 km^2$ area, the committed thyroid dose is 3.51E5 mSv and committed bone marrow dose is 2.67E5 mSv. During the 10-day dispersion, almost 3.8 million people could be required to be sheltered and 1.3 million people could be evacuated. Furthermore, 2.5 million people are required to relocate one year from 24000 km^2 . Finally, stable iodine pills are distributed to almost 1 million people. The regions that deterministic impact is observed and emergency response efforts applied are shown in from starting **Figure C.2- 14** to the **Figure C.2- 20**.

Activity concentration results shows that most of the products produced in the south-eastern, middle and eastern Anatolia as well as Cyprus are affected by this dispersion. The dose from cesium isotopes on the grass is calculated 4.22 GBq/kg as maximum and the dose from the cesium isotopes on the cow's milk reaches up to 16.6 kBq/kg at the end of 10 days. Cesium dose decreases to 0.417 MBq/kg on the grass, however, dose over the cow's milk increases up to 0.368 MBq/kg since isotopes transferring to the cow's milk during this one year. The maximum dose of iodine isotopes is higher than the one from cesium isotopes for product at the end of 10-day of dispersion. Like the previous case, the impact only remains up to one year due to short half-time of iodine isotopes.

The effective dose from all pathways for an adult can reach maximum of 1.75×10^5 mSv for an adult after 1 year unless the relocation is applied. A child in the same region can take up to 1.27×10^5 mSv at the end of one year, see **Figure C.2- 7**. In addition, the lifetime effective dose from all pathways for an adult and for a child, demonstrated in **Figure C.2- 6** and **Figure**

C.2- 9 can reach 2.57×10^5 mSv and 2.22×10^5 mSv respectively. Also, the thyroid dose from all pathways is almost double the effective dose for each group and for both durations. The dose results after one year also show that doses below 1 mSv are observed only 500 km away from the site depending on the direction.

7.3 Comparison with other studies and Discussion

In previous section, results of radiological consequence analysis after 10-day of dispersion for different sites, different weather conditions and different early emergency application have been presented with ST prediction of the cases of break on the cold leg and break on the hot leg.

ST predictions of break on the cold leg indicates that INES level of 3.8 accident and deterministic effects are very low or none. In addition, the highest Cs-137 contamination recorded is 15.5 MBq/km^2 in Fukushima which indicates that the contamination in this case is far lower than the Fukushima (IAEA, 2020). Similarly, JRODOS calculation shows that 50 km range from the site takes lower doses than the 1 mSv which is the annual public limit for one year (ICRP, 2007). Finally, the cesium dose over the cow's milk is almost five times higher than the determined limit of 1000 Bq/kg for human consumption and international trade (IAEA, 2016). The cesium dose decreases acceptable limits after one year.

The case of break on the hot leg shows more severe consequences than the consequences of break on the cold leg since the INES level of this event is 6.8. As in Chernobyl and Fukushima, deterministic effects on adults and fetuses can be observed during the transient and millions of people can be affected from the possible consequences of this case. Indeed, the deposition of Cs-137 can reach up to 0.247 GBq/km^2 which is higher than the one recorded for Fukushima accident (IAEA, 2020) and Chernobyl (IAEA, 2006). More severe consequences are observed on the activity concentrations for foodstuff and feedstuff. Indeed, the cesium dose over the cow's milk is far over the limit, and concentrations below 1000 Bq/kg can only be observed after 20 years.

When the results were compared with SOARCA analyzes (Kwang-II, Keo-hyoung, & Seok-Won, 2023) (U.S. NRC, 2013) conducted for similar purposes, it was observed that even though the accident scenarios and reactor types were different, the Cs element leaking into the nature as a result of a break in the cold leg was at similar rates.

It should be noted that many safety systems like containment spray system and PARs and severe accident management applications are not considered during the calculations. These

considerations would decrease the potential release of the ST critically and could avoid estimated radiological impact on the population and the environment.

7.4 Summary

In this chapter, radiological consequence analysis is performed using JRODOS with two ST inventories calculated by ASTEC for two different accident scenarios. Radiological dispersion of the aerosols is calculated for selected time interval and for selected regions, potential doses due to this dispersion is estimated for the regions along with the wind path, and action plans determined by countries are applied in order to investigate the effectiveness on possible dose consumption.

The calculations aim to simulate the study of radiological impact of the best-estimated Source Term to test and improve the proposed regulations and action plans, as well as to support emergency response teams with applicable accurate information of dispersion. By this ASTEC-JRODOS platform, the radiological consequence of a hypothetical severe accident can be simulated for any reactor, accident sequence, region and meteorological conditions. It should be noted that any early emergency response applications as well as any change of daily life are not considered, which are the main elements that increase the impact of the radiological dispersion. Since the ingestion pathway covers the main portion of the estimations on the long-term dose projections, the feedstuff and foodstuff that may be contaminated would not be consumed by the population. Also, the population would relocate to safer regions in case of contamination as occurred in the Fukushima accident.

Nevertheless, uncertainties in the selected parameters may affect ST inventory released into the environment and further dispersion. Thus, the quantification of uncertainty studies for selected accident scenarios are next investigated to assist early response teams and regulators with a range of possible source terms.

8 Uncertainty and Sensitivity Analysis of ASTEC for the prediction of the radiological source term with KATUSA

Determination of the uncertainties and analysis of the sensitivities have been considered in this section. Severe accident studies include numerous models to calculate full behavior during the progression of a severe accident. The activity in the containment and the environment as well as FP mass inside of the vessel and in the primary circuit are selected as Figure-of-Merits (FOMs). Based on the FOMs, the related models involved in transport and release of the fission products are considered and the most impactful parameters on the progression of the are investigated based on the reference studies and their findings. Complex structure of accident progression and FP transport and release require understanding of the physical and chemical phenomena occurring during the severe accident. The ASTEC models, created for prediction of the consequences of a possible LBLOCA on the cold leg and hot leg of the pressurizer loop, are simulated with 100 different samples with selected uncertain parameters by the KATUSA tool. Based on Wilks's formula, enough of the samples are calculated as 93 and 100 samples have been created with Latin-Hypercube Sampling method (LHS) to avoid the impact of possible failed runs.

8.1 Determination of uncertain parameters

According to previous studies done on KONVOI plant (Gabrielli, et al., 2022), the selected uncertain parameters and their variation range are in **Table 8.1** (Helton, Iman, Johnson, & Leigh, 1986) (U.S. NRC, 2017) (U. S. NRC, 2016) (Ghosh, et al., 2019) aerosol size, aerosol shape and thermal properties of the aerosol have been investigated mainly to observe FP transport and release behavior during a transient by the SOPHAEROS module. While particle mean density (f_{rho}) and particle mean specific heat (f_{spheat}) can impact the heat transfer between aerosol and the walls of the primary circuit and the containment, particle minimum radius (f_{R_min}) and particle maximum radius (f_{R_max}) alters the aerosol particle dimensions. Shape factor relative to Stokes velocity (f_{v_stks}) heavily impacts the gravitational impact of the aerosols. Additionally, leakage area (f_{leak}) from the containment to the environment have been studied. Also, the effect of the onset temperature of the oxidation (f_{TBEG}) and onset temperature of the ablation in the cavity are investigated since hydrogen is one the carriers of the FPs during the transient.

Table 8.1: Impactful uncertain parameters with reference values, variation range and probabilistic distribution function used in the ASTEC VVER-1000 model

Parameter	Phenomena	Description	Reference Value	Variation Range	PDF
frho	Aerosol size, shape and thermal properties	Particle mean density (kg/m^3)	3000.	Min=2400. Max=3600.	Uniform
fspheat		Particle mean specific heat ($\text{J}/\text{kg K}$)	840.	Min=672. Max=1008.	Uniform
fR_min		Particle minimum radius (m)	1.0E-08	Min=1.E-09 Max=2E-08 Mode=1.1E-08	Triangular
fR_max		Particle maximum radius (m)	2.0E-5	Min=5.E-06 Max=2E-05 Mode=1.99E-05	Triangular
fv_stks		Shape factor relative to Stokes velocity	1.0	Alpha=1.0 Beta=5.0 Min=1.0 Max=3.0	Beta
ftBEG	Gas generation	Temperature of oxidation begins (K)	600.	Min=480. Max=1008.	Uniform
ftABLA		Ablation temperature at cavity (K)	1570.	Min=1256. Max=1884.	Uniform
f_leak	Leakage to the environment	Containment leakage area (m^2)	3.14E-02	Min=3.14E-02 Max=3.14E-01	Uniform

8.2 U&S- Analysis of ASTEC for the LBLOCA on the cold leg with SBO

In this section, uncertainty over the prediction of released isotope inventory in case of LBLOCA on the cold leg of the pressurizer loop with SBO is investigated and sensitivity

analysis over the results is performed by using KATUSA. The time windows for the onset of FP release and uncover of the core window are shown in **Figure 8-1** and **Figure 8-2**. In addition to that, most probable times with 95% of confidence level for the RPV failure and cavity rupture are presented in **Figure 8-3** and **Figure 8-4**. The maximum, minimum, mean and most probable inventory that release to the environment is demonstrated in **Figure 8-5** and Pearson correlation coefficient between this activity and uncertain parameters during early phase and late phase is shown in **Figure 8-6**. The impact of the most effective parameter on the release of I-131 and Cs-137 is illustrated in **Figure 8-7**. Total released activity and activity of selected isotopes at the end of the calculation in best-estimate calculation, optimistic case and worst-scenario is compared in **Figure 8-8**. Finally, JRODOS input decks with best-estimate and worst-scenario for radiological dispersion from Zaporizhzhia NPP are created and deposition of aerosol for both cases are assessed in **Figure 8-9** and **Figure 8-10**. Additional sensitivity result for different stages of the transient and comparison of JRODOS result can be found in Appendix D.

Figure 8-1, Figure 8-2, Figure 8-3 and **Figure 8-4** illustrate the most time window for the major events occurring during a LBLOCA on the cold leg of the pressurizer loop along with the SBO in VVER-1000. Based on the calculation, time window for start of FP release which is the first barrier between FPs and the environment spans between 1200 s and 1400 s depending on the input set. However, some set of the calculations show that this phenomenon can occur around 2000 s. For the uncover of the core ranges between 2000 s and 2400 s. are estimated Failure of RPV, second barrier for the safety, is between 14000 s and 22000 s. Finally, the time window for the cavity rupture is between 80000 s and 140000s.

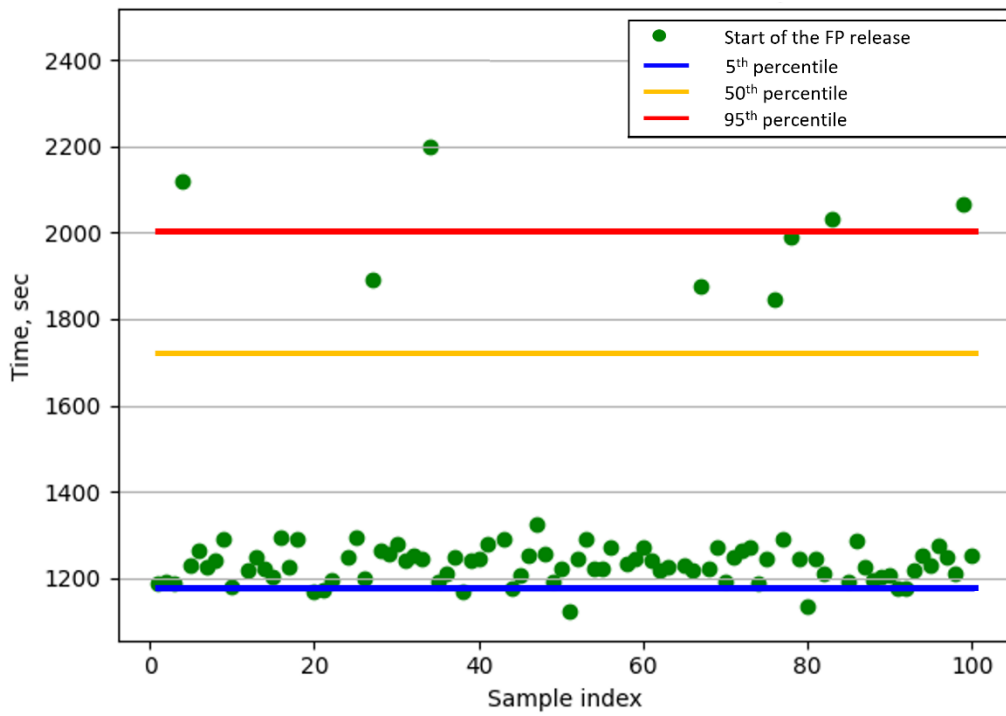


Figure 8-1: Evaluated most probable time window for the onset of FP release in case of LBLOCA on the cold leg of the pressurizer loop along with the SBO

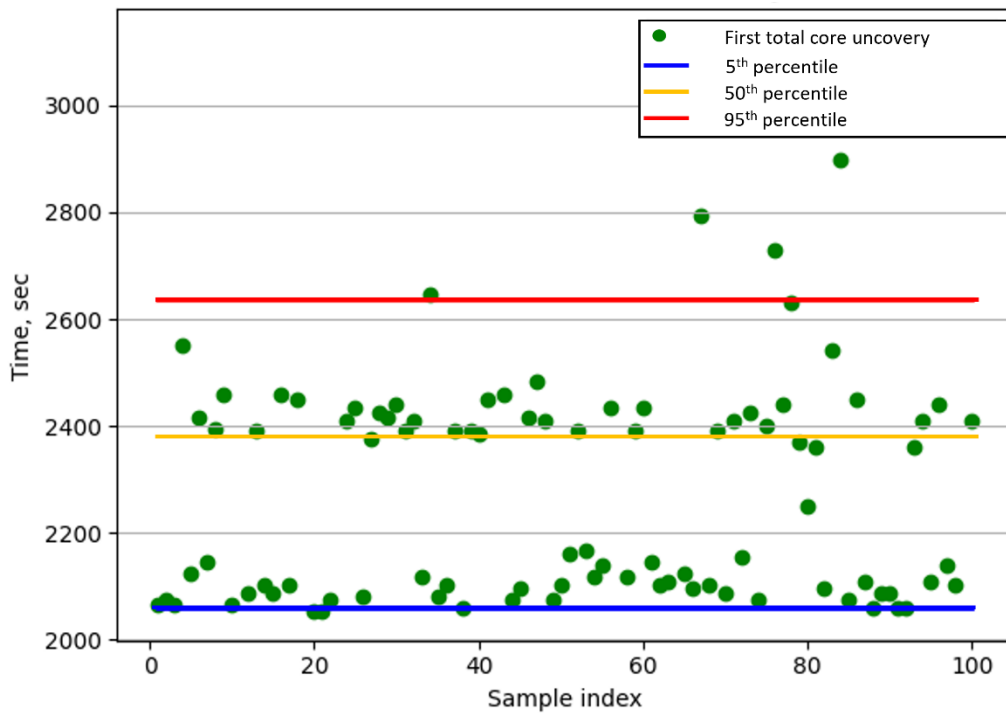


Figure 8-2: Evaluated most probable time window for the core uncover in case of LBLOCA on the cold leg of the pressurizer loop along with the SBO

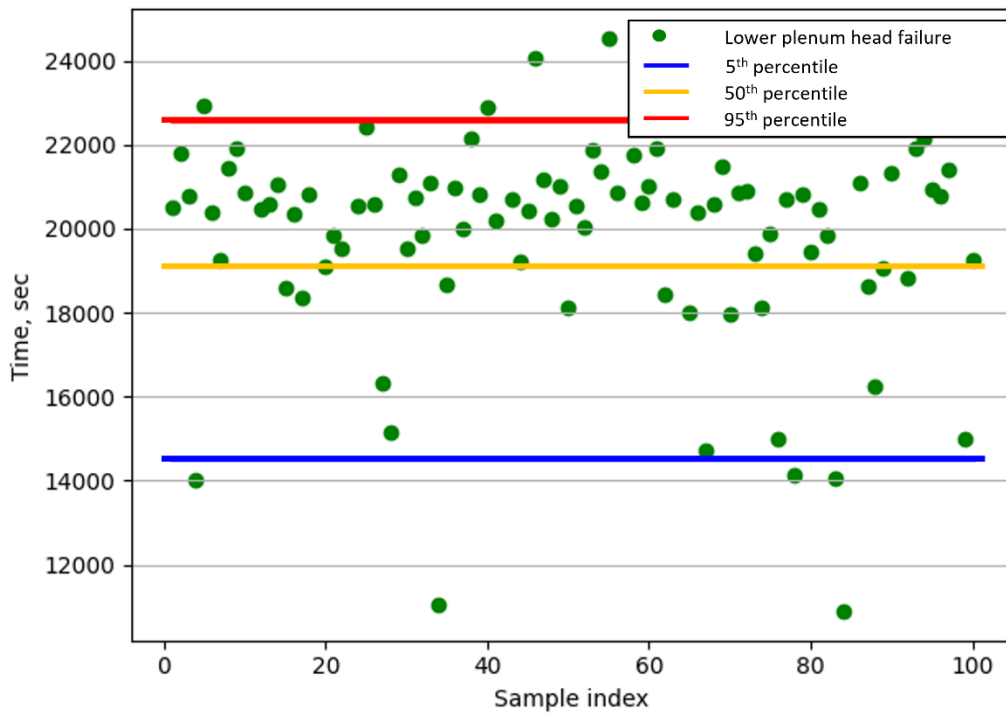


Figure 8-3: Evaluated most probable time window for the onset of RPV failure in case of LBLOCA on the cold leg of the pressurizer loop along with the SBO

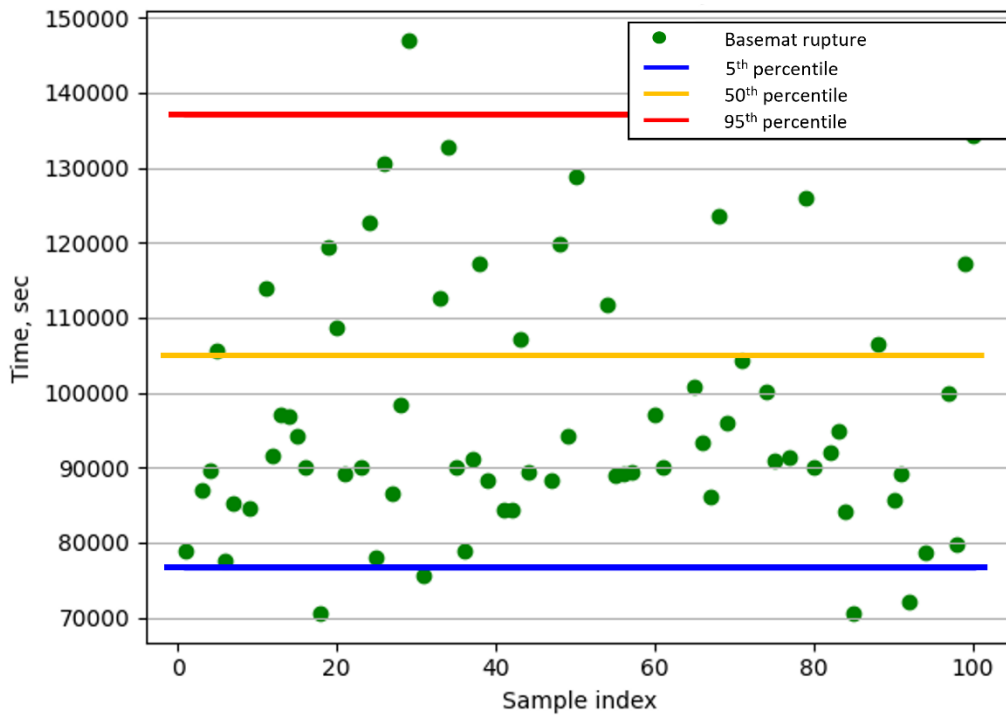


Figure 8-4: Evaluated most probable time window for basemat rupture in case of LBLOCA on the cold leg of the pressurizer loop along with the SBO

When the activity of the released isotopes is investigated, a significant increase from starting the integrity loss of claddings is observed until 10000 s. After this point, the decay mechanism of FPs starts to decrease the inventory. Failure of the RPV creates sharp increase of the released activity since some of the low volatile isotopes are injected to the cavity. After this point, the decay of FPs further decreases the inventory and reaches plateau at the end as shown in **Figure 8-5**. The maximum activity of the released activity can reach 2.9×10^{18} Bq but the most probable release to the environment (percentile 95th) is 1.9×10^{18} Bq at the end of calculation. While 50th percentile is calculated as approximately 1.78×10^{18} Bq which is close to the mean value, the 5th percentile for the released activity is 1.5×10^{18} Bq at end of the simulations. Based on the I-131 activities, 2.19×10^{14} Bq as maximum and 5.06×10^{13} Bq as minimum, the accident is between 2.8 to 3.6 as INES level.

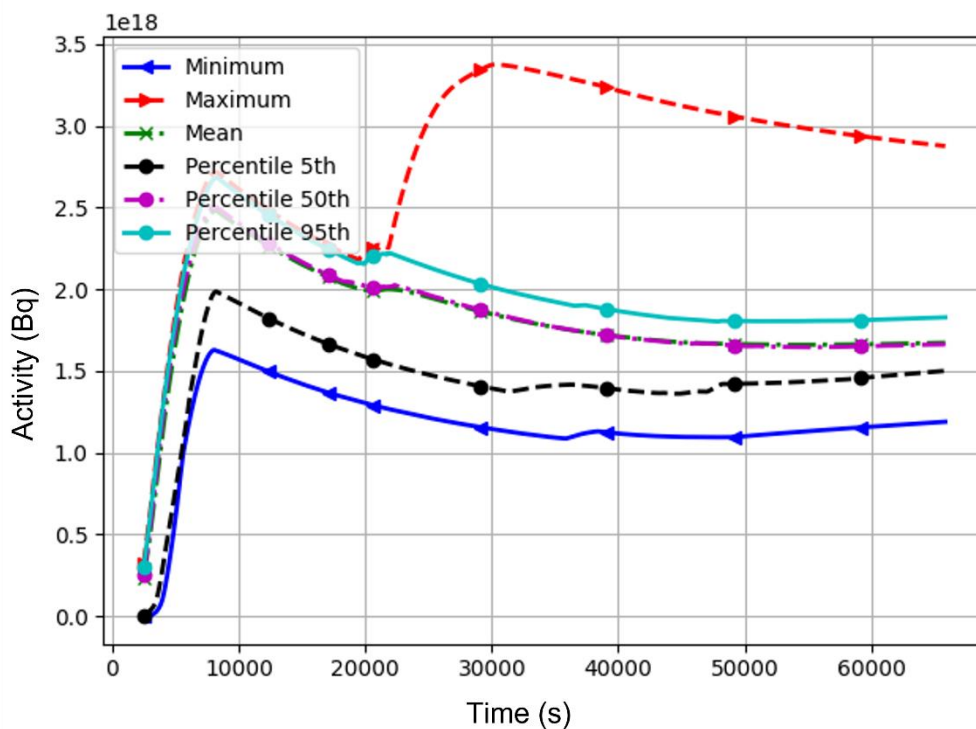


Figure 8-5: Evaluated minimum, maximum, mean and most probable values of activity released to the environment in case of LBLOCA on the cold leg of the pressurizer loop along with the SBO

Figure 8-6 shows Pearson correlation coefficient between activity released to the environment and the selected parameters. The most effective parameter on the released activity is shape factor relative to Stokes velocity (fv_stks) at early stage of the transient. This parameter is used in the SOPHAEROS module of ASTEC to calculate Stokes-velocity correction factor that is used aerosol gravitational settling as well as coagulation models. Therefore, less retention of the isotopes is observed in the primary circuit and the activity difference on low-volatile

isotopes like Ce-144, Sr-90 etc. is greater than the noble gases and high-volatile isotopes such as Xe-133, Xe-135, Cs-137, I-132 etc. At a later stage, specific heat of the aerosols (fspheat) is dominant on the results. Condensation and evaporation of each volatile species and wall is calculated by Chilton-Colburn analogy between heat and mass transfer with this parameter in ASTEC (Çengel, 2014). Even though the relation between shape factor relative to Stokes velocity and total released inventory is about 25%, the impact of this parameter on volatile isotopes such as I isotopes is much higher than the total activity, see **Figure 8-7**. The positive relation between them can impact the results from 45% to over 55%. The main reason of this difference between total released activity and I like isotopes is the main portion of the released activity to the environment is covered by the noble gases which are highly volatile and go under no chemical interaction. However, I species are carried to the containment and the environment by aerosols which are affected settling mechanism.

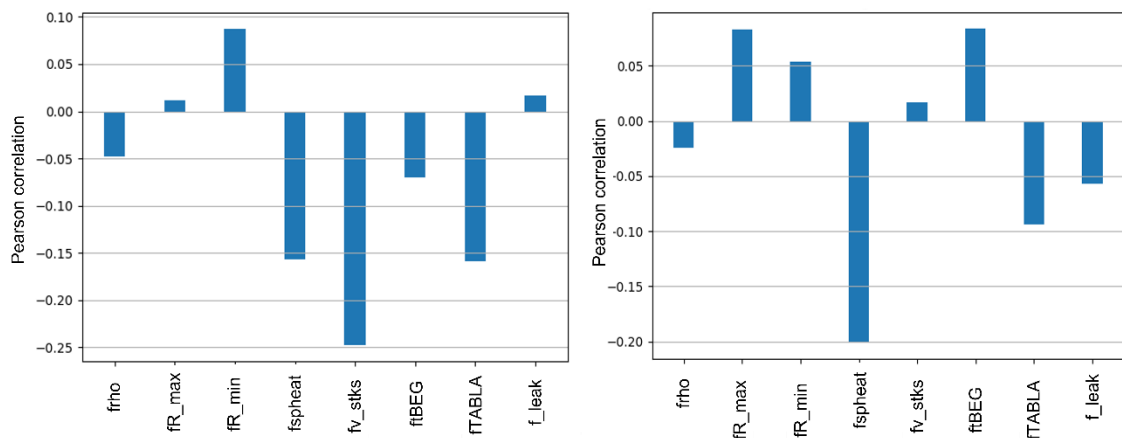


Figure 8-6: Pearson correlation coefficient between the activity released to the environment and uncertain parameters at 22461.7 s (left) and at 65852.6 s (right).

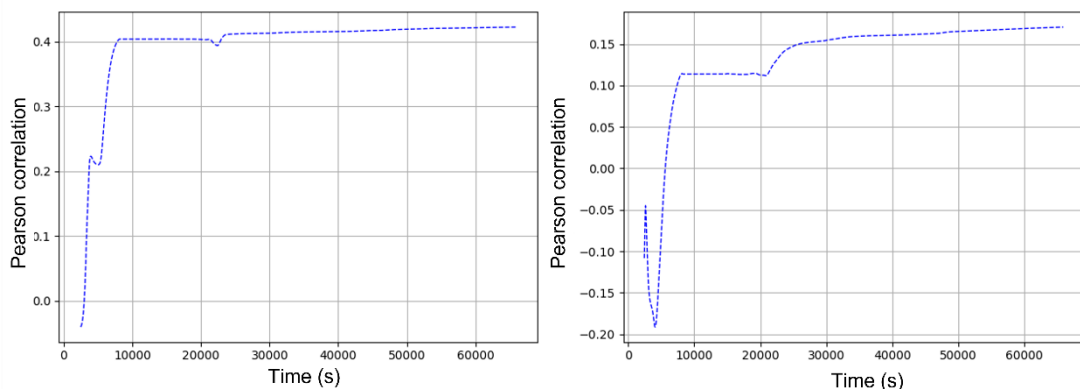


Figure 8-7: Pearson correlation coefficient between I-131 activity (left) and Cs-137 activity (right) released to the environment and shape factor relative to Stokes velocity in case of LBLOCA on the cold leg of the pressurizer loop along with the SBO

The difference on the ST predictions due to uncertain parameters significantly impact the radiological dispersion to the environment. The comparison of calculated minimum, best-estimate and maximum activity for selected isotopes is given in **Figure 8-8**. 10-day radiological dispersion from the Zaporizhzhia in the winter condition with best-estimate and worst-scenario is performed to determine the difference on the contamination, dose and activity concentration. best-estimate case.

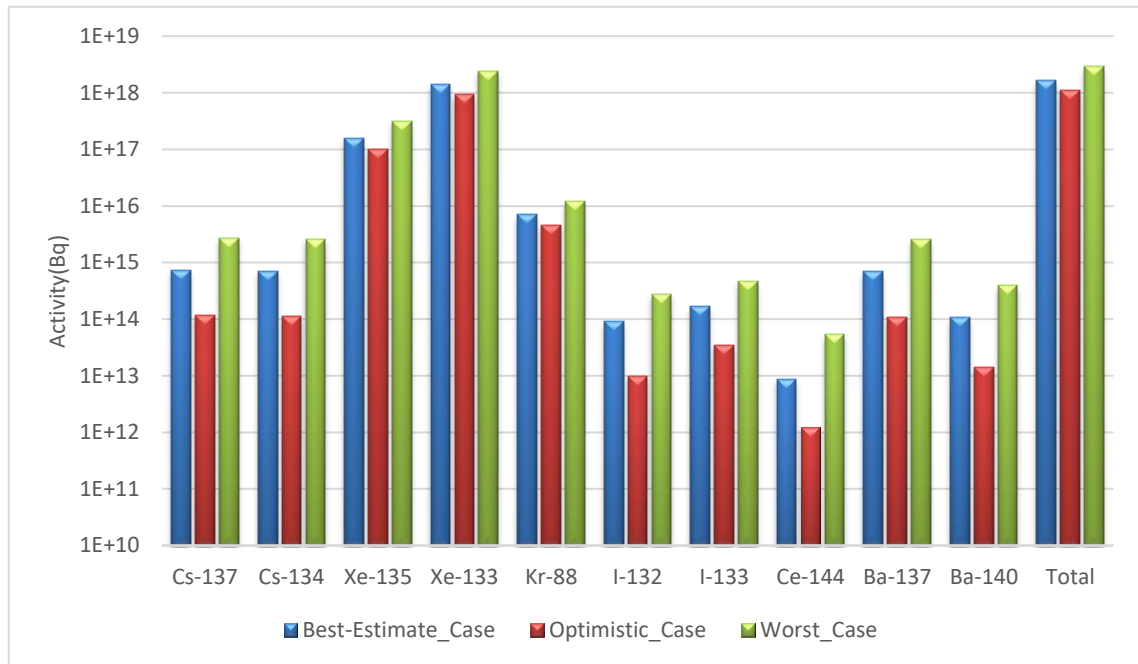


Figure 8-8: Released isotope activity in the best-estimate, optimistic and worst case at the end of the uncertainty quantification calculation by KATUSA in case of LBLOCA on the cold leg of the pressurizer loop along with the SBO

The contamination calculations in **Figure 8-9** and **Figure 8-10** show that the impact with the worst-case ST is 10 times higher than the one with the best-estimate case. In particular, the contamination of Cs-137 isotope is 0.24 MBq/km^2 in the best-estimate case and calculation with the worst-case scenario is 3.86 MBq/km^2 . This major difference in the contamination affects the acute doses as well as long term doses. The acute effective dose is 16.7 mSv and 48.7 mSv as maximum respectively. Similarly, activity concentration on the cow's milk is more than 10 times higher for the worst-estimate case. Finally, the maximum effective dose from all pathways for an adult after 1 year is 308 mSv as maximum for the worst-case scenario and 47.1 mSv for the best-estimate case. The significant difference on activity concentration and acute dose contributes further and yields as increase for the effective dose after 1 year.

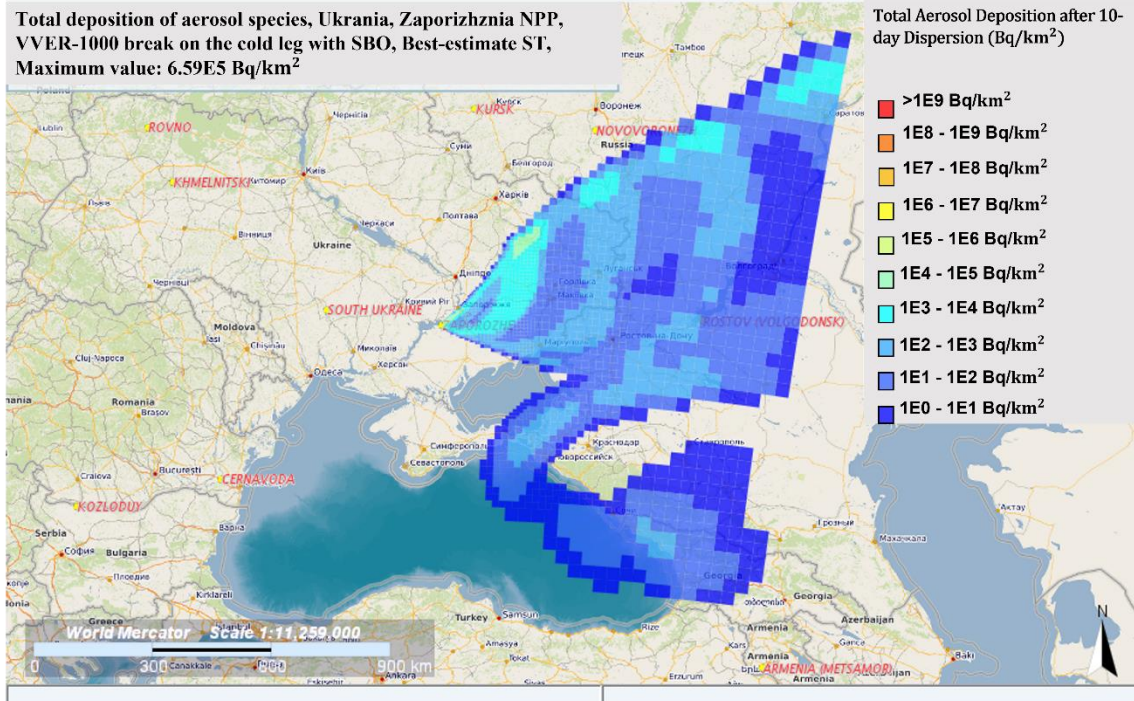


Figure 8-9: Simulated deposition of the aerosols from the Zaporizhzhia NPP in selected time period for best-estimate ST obtained in LBLOCA on the cold leg with SBO

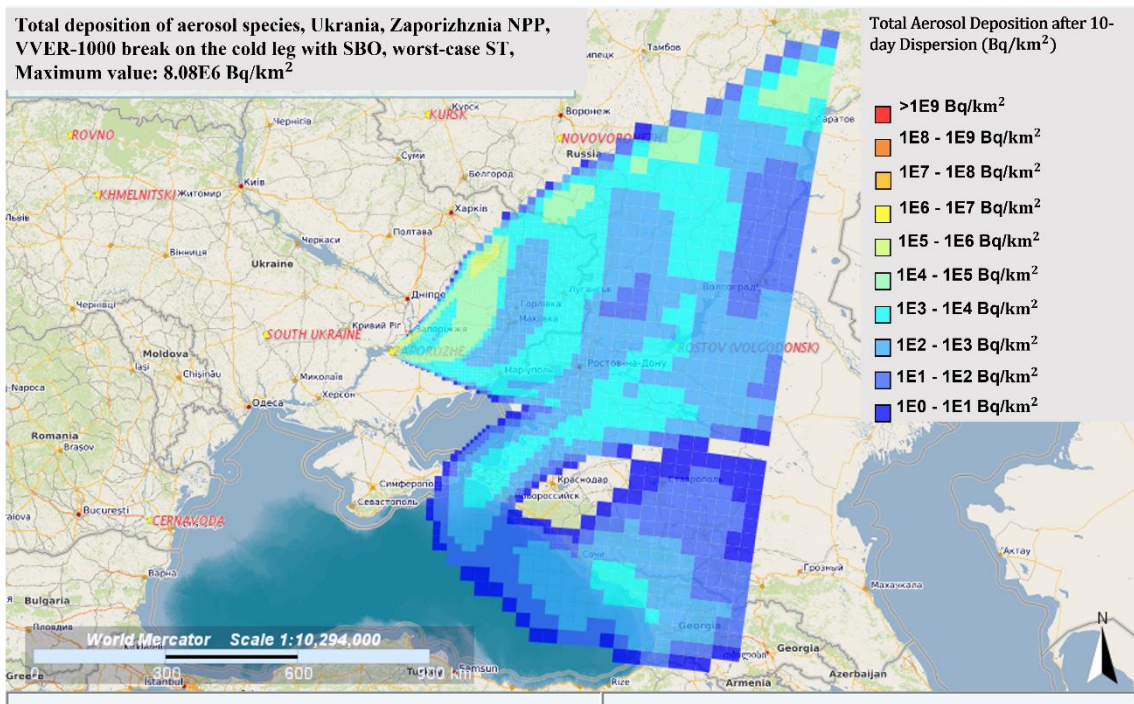


Figure 8-10: Simulated deposition of the aerosols from the Zaporizhzhia NPP in selected time period for worst-case ST obtained in LBLOCA on the cold leg with SBO

8.3 U&S Analysis of ASTEC for a LBLOCA on the hot leg with SBO

This section covers quantification of the uncertainties and sensitivity analysis on the results of LBLOCA on the hot leg of the pressurizer loop with SBO. The uncertain parameters are same with the previous case which can be seen **Table 8.1**. The most probable times for FP release and uncover of the core is given in **Figure 8-11** and **Figure 8-12**. respective **Figure 8-13** and **Figure 8-14** show the time window for RPV failure and rupture of the cavity. According to the assessment of the uncertainties, the activity released to the environment is shown in **Figure 8-15** in worst-scenario, best-estimate and optimistic condition. Pearson coefficient correlation to determine the effective physical phenomena on the released activity in early late stage of the transient is given in **Figure 8-16** and the Pearson correlation between the I-131 and Cs-137 activities and the most sensitive parameter, shape factor relative to Stokes velocity, is shown in **Figure 8-17**. Isotope-wise activity difference in best-estimate, worst and optimistic cases is illustrated **Figure 8-18** and difference in aerosol deposition as a result of radiological dispersion from Zaporizhzhia NPP in selected time period for best-estimate and worst scenario is demonstrated in **Error! Reference source not found..** Additional results on uncertainty and sensitivity study and comparison of the radiological consequences in different scenarios are given in **Appendix D**.

The time window for the starting of FP release from the fuel rods is observed from 1540 s to the 1580 s which is a narrower window than in case of break on the cold leg as illustrated in **Figure 8-11**. Core uncover period is observed between 5600 s and 7500 s which confirms later uncover of the vessel than the one in the cold leg case due to pressure difference on the break locations as shown in **Figure 8-12**. Similarly, the pressure vessel failure, as seen in **Figure 8-13**, is the time window spans between 22000 s. to 39000 s later than the one in the cold leg case and uncertainty results on the cavity rupture shows in **Figure 8-14** that the rupture is between 79000 s to 140000 s. Similar to the break on the cold leg case, the uncertainty band for the cavity rupture is significantly large.

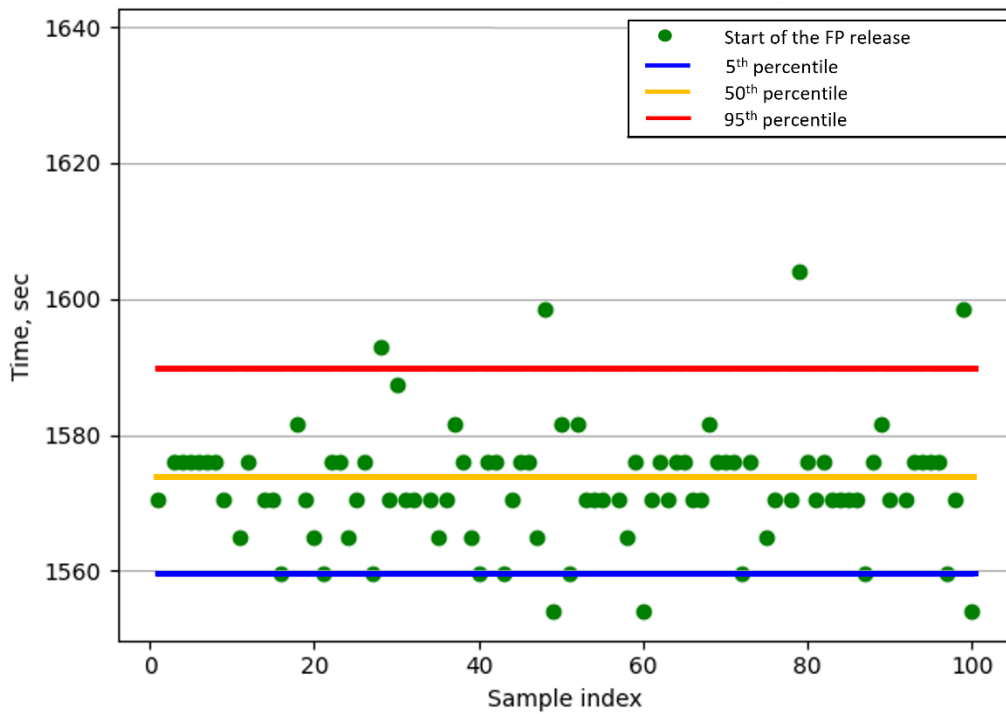


Figure 8-11: Most probable time window for the onset of FP release in case of LBLOCA on the hot leg of the pressurizer loop along with the SBO

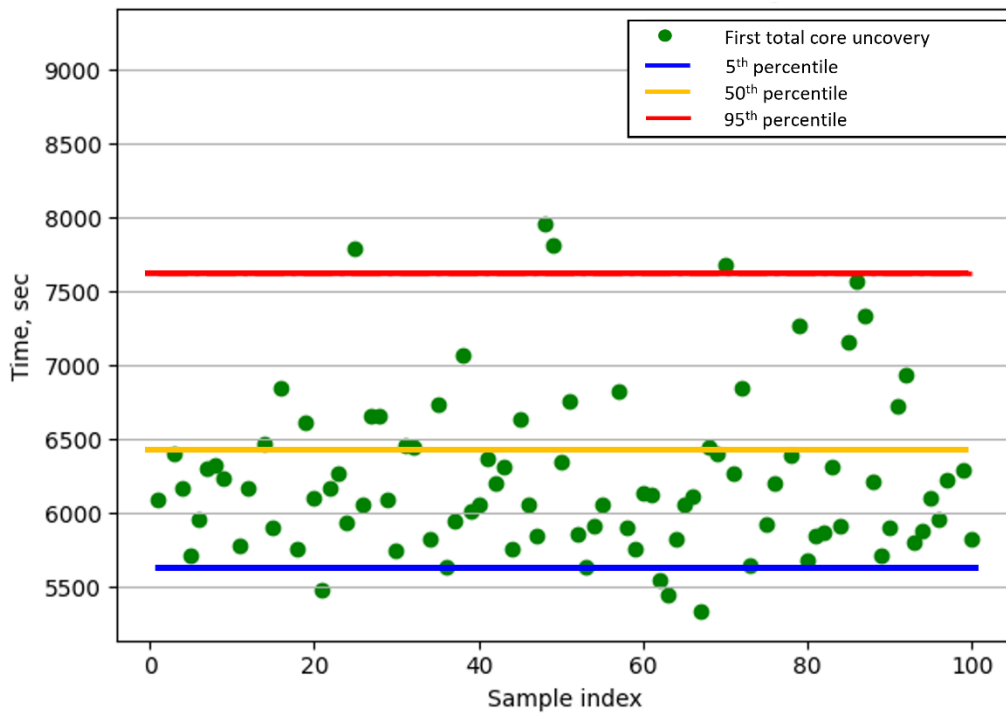


Figure 8-12: Most probable time window for uncovering of the core in case of LBLOCA on the hot leg of the pressurizer loop along with the SBO

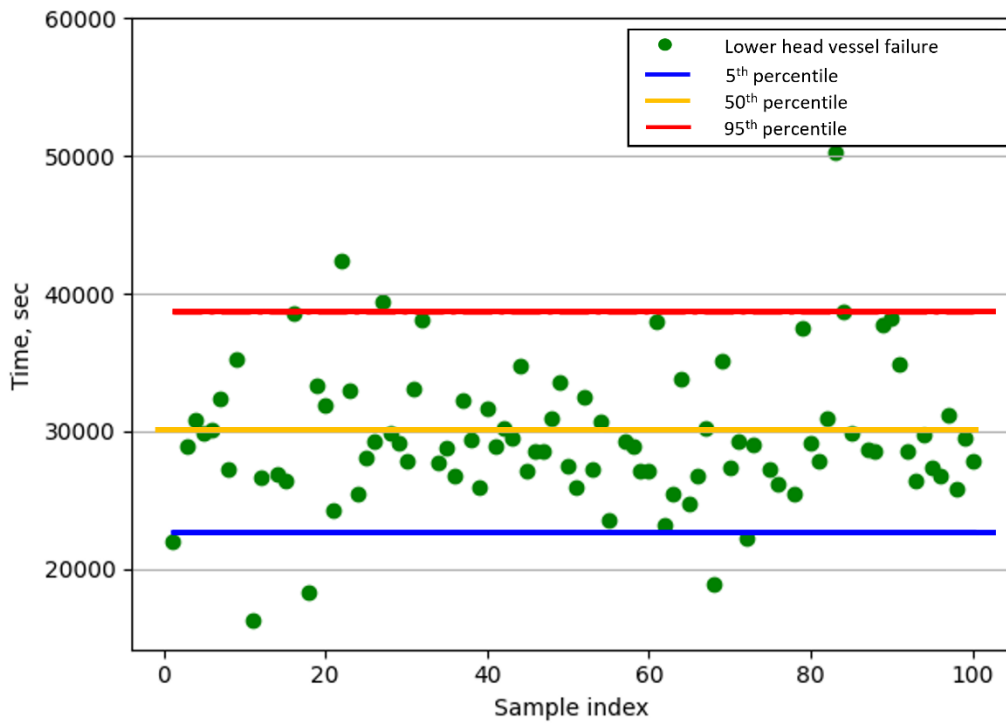


Figure 8-13: Most probable time window for the onset of RPV failure in case of LBLOCA on the hot leg of the pressurizer loop along with the SBO

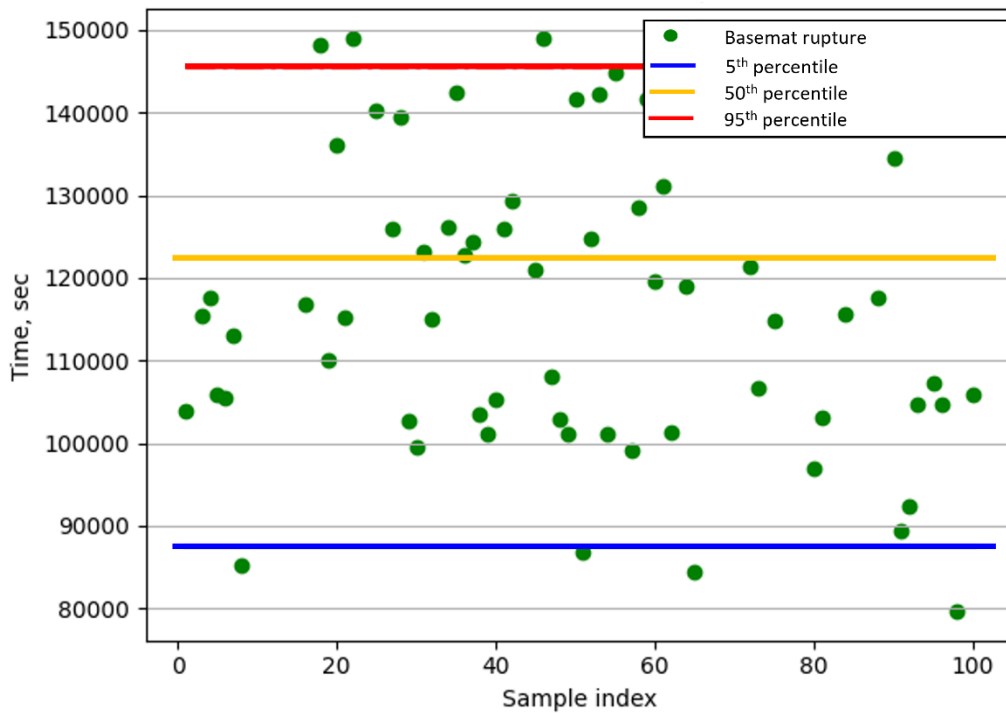


Figure 8-14: Most probable time window for basemat rupture in case of LBLOCA on the hot leg of the pressurizer loop along with the SBO

The uncertainty results on the activity released to the environment shows that the activity can reach to 1.85×10^{19} Bq as maximum at about 11000 s and the decreases to the 1.30×10^{19} Bq at the end of transient. The minimum activity at the end of the transient is calculated as 7.35×10^{18} Bq and the released activity is significantly larger than the one in the cold leg case even in the minimum conditions. The most probable activity is about 8.55×10^{18} Bq at the end of calculation as given in **Figure 8-15** and the 5th percentile is about 7.55×10^{18} Bq. Like the prior analysis, the 50th percentile and mean value are close to each other and are 0.88×10^{18} Bq and 0.91×10^{18} Bq, respectively. The maximum, mean, minimum and most probable activity in the vessel, the containment and the primary circuit are illustrated in **Figure D.1- 1**, **Figure D.1- 2** and **Figure D.1- 3**, respectively

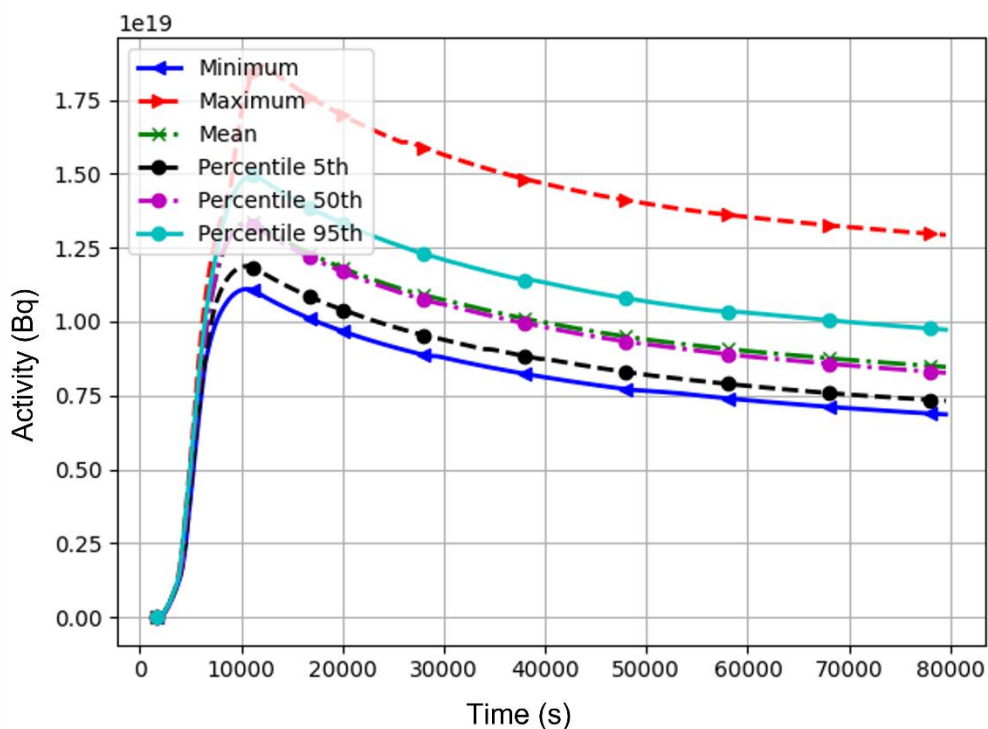


Figure 8-15: Minimum, maximum, mean and most probable values of activity released to the environment in case of LBLOCA on the hot leg of the pressurizer loop along with the SBO

The sensitivity analysis is performed on the case of break on the hot leg of the pressurizer loop which can be seen in **Figure 8-16** and results show that the shape factor relative to Stokes velocity (f_{v_stks}) parameter is the most influencing parameter on the released activity is of the transient. The change of this parameter effectively impacts gravitational settling of radioisotopes in primary circuit and in the containment. This positive relation decreases at the late stage of the transient yet remains the dominating factor. In particular of I and Cs elements, which are more hazardous to the public and the environment due to inhalation

and ingestion, the positive relation is more dominant. The sensitivity to the shape factor relative to Stokes velocity is over 50% as can be seen in **Figure 8-17** and it significantly impacts the deposition to the soil and inhaled dose. The impacts of each selected parameters on the released activity against time are shown between **Figure D.1- 4** and **Figure D.1- 9**.

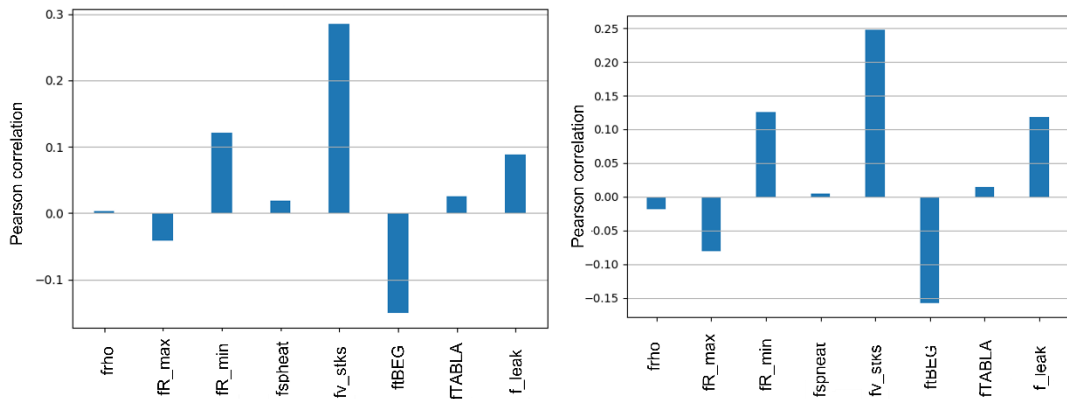


Figure 8-16: Pearson correlation coefficient between the activity released to the environment and uncertain parameters during in-vessel phase (left) and ex-vessel phase (right)

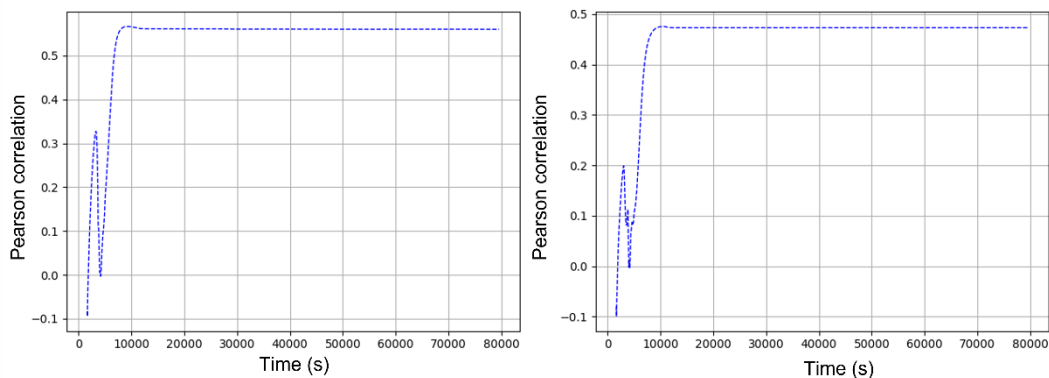


Figure 8-17: Pearson correlation coefficient between I-131 activity (left) and Cs-137 activity (right) released to the environment and shape factor relative to Stokes velocity in case of LBLOCA on the hot leg of the pressurizer loop along with the SBO

Figure 8-18 illustrates comparison of isotope-wise activity of minimum, best-estimate and worst-case released ST inventory. The difference on the inventory of ST is greater for the low-volatile isotopes like Ce-144, Sr-90 and Ba-140 etc. than the volatile fission products. This situation greatly impacts the dose projection for long periods due to ingestion. However, this difference on the released activity inventory is significantly lower than the one in the break on the cold leg case. The analysis on the dispersion of inventories of worst case and best-estimate case indicates that the maximum Cs-137 contamination is 0.15 TBq/km^2 for best-estimate case and 0.20 TBq/km^2 for worst-case in Zaporizhzhia NPP for the winter conditions, see **Figure 8-19** and **Figure 8-20**. The difference on maximum aerosol contamination between best-

estimate and worst-case results reaches to the $2 \text{ TBq}/\text{km}^2$ at the end of 10-day dispersion. The acute effective dose significantly changes due to difference on the contamination and maximum acute effective doses are calculated as 7.96 Sv and 35.1 mSv respectively at the end of calculation which is drastically greater than the annual dose limits. As a result of contamination, the activity concentrations on the feedstuff and foodstuff also are higher than the consumption and international trade levels. Finally, these dose and activity concentration differences cumulatively affects long term projections, and these results show that the maximum effective dose from all pathways after 1 year can be 22.1 Sv with best-estimate results and 168 Sv with worst-case scenario for an adult unless the early emergency activities are involved. Further JRODOS results on the consequence of radiological dispersion is shown in **Figure D.1- 11**, **Figure D.1- 13** and **Figure D.1- 15** for the best estimate case and **Figure D.1- 12**, **Figure D.1- 14** and **Figure D.1- 16** for th worst-case scenario.

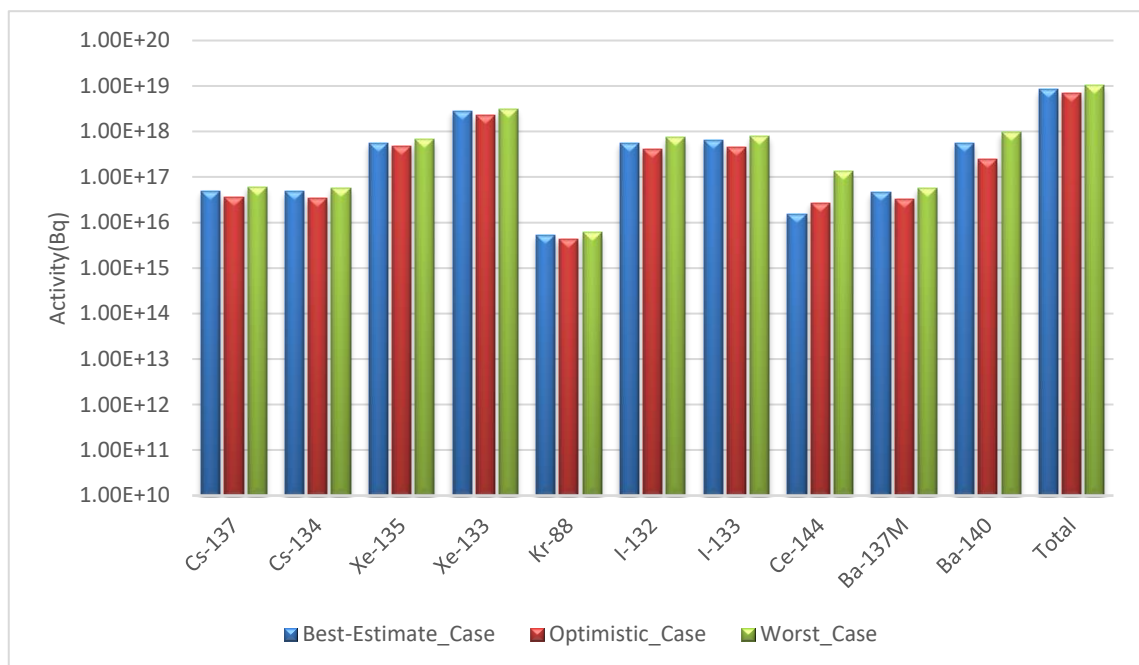


Figure 8-18: Calculated released isotope activity in the best-estimate, optimistic and worst case at the end of the uncertainty quantification calculation by KATUSA in case of LBLOCA on the hot leg of the pressurizer loop along with the SBO

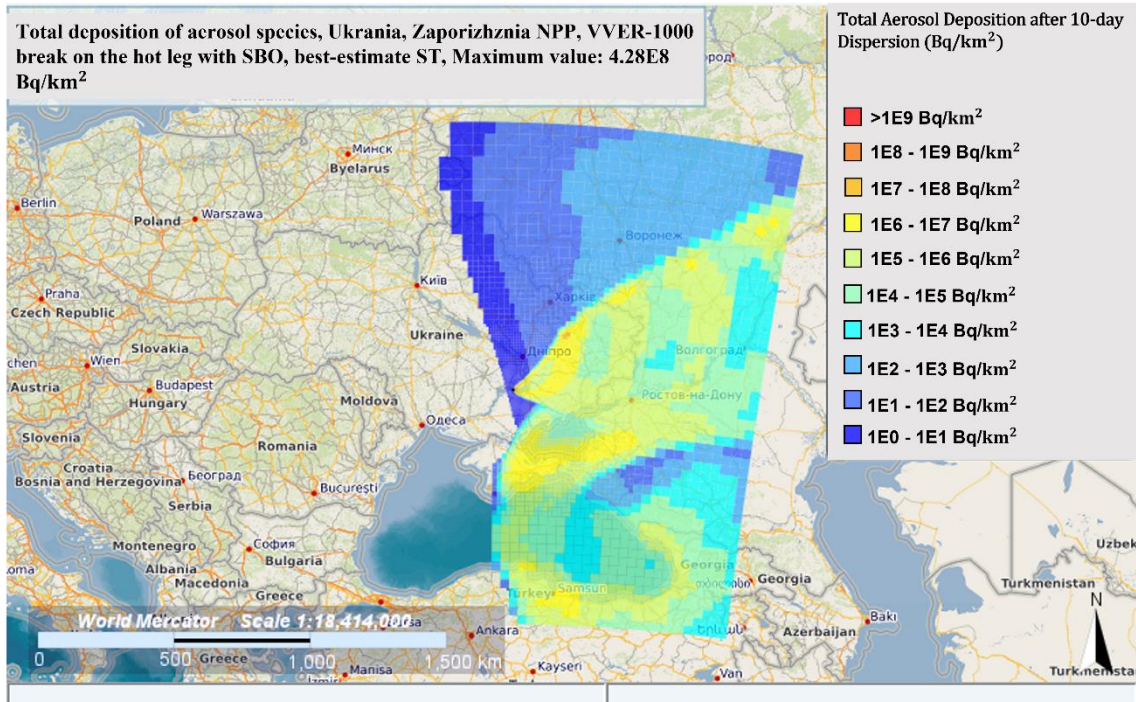


Figure 8-19: Simulated deposition of the aerosols from the Zaporizhzhia NPP in selected time period for best-estimate ST obtained in LBLOCA on the hot leg with SBO

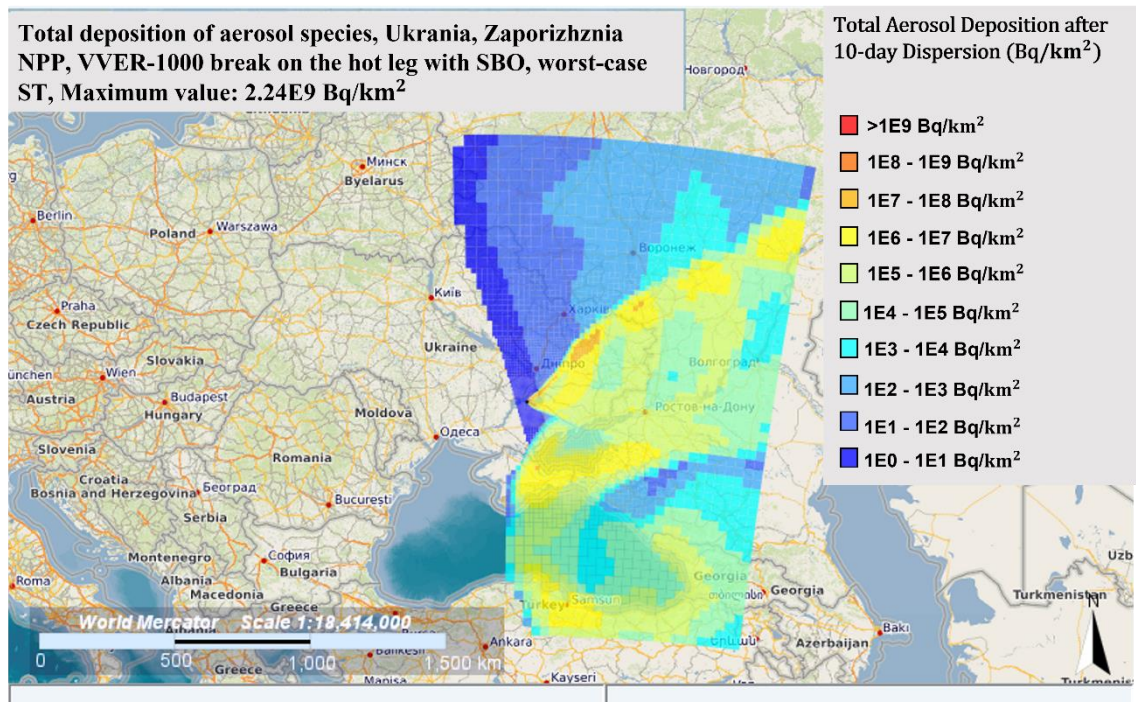


Figure 8-20: Simulated deposition of the aerosols from the Zaporizhzhia NPP in selected time period for worst-case ST obtained in LBLOCA on the hot leg with SBO

8.4 Summary

The uncertainty analysis on ASTEC-JRODOS calculations has been performed by using KATUSA tool to determine uncertainty band on the main events and estimate the sensitivities of these parameters. Additionally, the impact of these uncertainties on the ST inventory and difference on the radiological dispersion and dose estimation at Zaporizhzhia NPP in certain weather condition is calculated.

The most impactful parameters on the activity released to the environment in the cold and scenario is the shape factor relative to Stokes velocity (fv_stks) and the aerosol specific heat ($fspheat$) in the early and late phase of the accident, respectively. In particular, the amount of I isotopes released to the environment show a significant correlation with such parameters (about 45%) Note that the activity of such isotopes is of relevance for the emergency response. For example, the activity of I-131 is employed as reference in the INES scale for evaluating the impact of the ST. At the same time, the results of the U&S analysis show a much lower correlation (about 25%) between the total activity released to the environment and the Stokes velocity and the aerosol specific heat parameters. The main reason for this difference is the weighted portion of the released inventory is based on the the activity of the noble gases and they do not interact with the walls of the circuit and the containment chemically. Since these parameters impact the retention of FPs during the transient, significant difference on the estimation of the released inventory results with totally different radiological consequences which may require different applications during emergency response. On the other hand, the impact of shape factor relative to Stokes velocity is stronger in the hot leg break case. Volatile isotopes like Cs and I isotopes released to the environment show about 45%-55% difference according to the KATUSA analysis. Additionally, less volatile isotopes such as Sr-90, Ce-144 and La-140 inventory significantly changes depending on the selected parameters which alters the radiological impact.

The difference on the activity for the best-estimate and worst-case ST activity results with significant difference on radiological impact. In both cases of break location, the contamination with the worst-case ST inventory is 10 times higher than the one with best-estimate case. As expected, the acute and long-term organ doses as well as activity concentration on feedstuffs and foodstuffs heavily are heavily affected with this difference. Therefore, a different approach on early emergency response planning and management is required which shows the importance of supporting the importance of consequence estimations with uncertainty information.

The severe accident studies include plenty of in-vessel and ex-vessel models to determine physical and chemical phenomena. The developed models are based on previous severe accidents and limited experimental works, therefore, have uncertainties that impact the overall results at the end. Thus, determination of the uncertainties and calculation of sensitivities is essential to obtain the range of key results to sustain the best-possible approach. In the end, having the range contamination and dose estimation may help early emergency management planning and leading emergency teams.

9 Conclusions and Perspectives

Numerous levels of safety are considered in NPPs in order to mitigate hazardous impact of severe accidents to the public and environment. Enhancement of severe accident studies by including radiological consequence analysis to predict radiological impact of a possible severe accident, management and development of the regulations in case of those severe accidents, and application of effective early emergency plans is important sustaining best-possible information to the regulators and to the early response teams.

The work of this thesis aims at investigation of selected severe accident sequences for VVER-1000 NPP using reference code of ASTEC and prediction of radiological impact related with these selected severe accident sequences. Additionally, uncertainty studies on performed severe accident sequences and radiological dispersion are also employed to support emergency teams and regulators with best-possible results including uncertainty range.

Primarily, the validation of the ASTEC physical and chemical models is performed using experimental data from the QUENCH-12 test. The main findings of performed study are:

- ASTEC models dedicated to predicting in-vessel phases of a severe accident in VVER bundles are capable of calculating important physical and chemical phenomena observed in the QUENCH-12 experiment.
- Overestimation of the temperatures on the clad surfaces, particularly at inner heated rods, leads to overprediction of the hydrogen generation until the quenching phase. On contrary, the ASTEC models cannot capture sharp increase during reflooding phase since the break-away phenomena in E110 materials cannot be properly established in ASTEC due to missing thermo-physical models of VVER cladding. Of course, the impact of the argon cooling modelling on the overall results has to be considered.
- The discussed deviations result with reaching higher temperatures earlier than the experiment until the quenching and prediction of break-away on the cladding is later than the experiment. Therefore, hydrogen generation before reflooding is similar with the experimental results but earlier (34.21 g. in ASTEC and 34.7 g. in experiment), and production is underestimated during reflooding phase (9.86 g. in ASTEC and 23.1 g. in experiment).
- The impact of the different oxidation models based on Zr-4 claddings is performed as well as the difference of the axial meshing on the prediction of hydrogen production is identified.

The analysis of VVER-1000 during a severe accident case is established after the validation of the ASTEC code with QUENCH-12 experiment. Two sets of accident scenario are simulated with ASTEC, and sequence of the events, hydrogen production and release to the environment are calculated. Following results are observed according to the simulations:

- The improved ASTECV2.2 model is generated by modelling new steam generator and vessel model as well as inclusion of new containment and cavity models and necessary modules to simulate ex-vessel phenomena. Steady-state conditions are fulfilled and key parameters such as coolant inlet and outlet temperatures, primary and secondary system pressures and coolant flow rate have been verified. Additionally, fission product inventory has been calculated by depletion code of KORIGEN to support the input with realistic inventories.
- The LBLOCA on hot and cold leg of the pressurizer loop along with the SBO accident scenarios are simulated with ASTEC since large break and SBO more than 0.5 h have the highest risk of core damage. The predicted key results are compared with previous ASTEC calculations on VVER-1000 reactor.
- LBLOCA on the cold leg of the pressurizer loop along with the SBO accident results show that the failure of the RPV is observed in 4.5 h. and the rupture of the cavity is observed approximately 22 h. after the initiation of the break. The hydrogen production reaches 800 kg and the hydrogen production due to cavity ablation is the dominant factor on the total hydrogen inventory. Even though most of the fission products go under retention in the primary circuit, mostly inside of the steam generator, the released inventory to the environment reaches an activity of 1.2×10^{18} Bq for unfiltered release.
- When the break is located on the hot leg each phenomenon except FP release from the fuel rods delays due to having lower pressure than the cold leg. Therefore, RPV failure is observed after 9 than the previous case, and cavity rupture occurs at 30 h. after the break opening. Since one of the steam generators is bypassed due to location of the break, significant amount of activity is transported into the containment and from there to the environment. The activity at the end of transient in the environment is 7.0×10^{18} Bq without any filtering activity, almost seven time higher than the one from the break on the cold leg.

The radiological impact analysis of estimated release to the environment is performed by using JRODOS atmospheric dispersion tool. The dispersion of the inventories and potential impact are calculated for the sites of Kozloduy NPP and Akkuyu NPP. Based on the calculation, the most relevant results are:

- First-of-a-kind platform of ASTEC-JRODOS is established to estimate radiological consequence of a hypothetical severe accident scenario. This novel approach allows simulating a severe accident from the initiating event to the dispersion on any type of reactor at any location in the world for selected period of the year.
- According to the dispersion with the outcomes of the LBLOCA on the cold leg of the pressurizer loop along with the SBO, the aerosol contamination can reach 22.9 MBq/km^2 through the cloud movement area. Annual doses under 1 mSv limit can only be observed after 200 km away from the accident site and the maximum effective dose after 1 year from all pathways is more than 100 mSv which appear in the 2km range next to the site. Finally, activity concentration on the cow's milk reduces to the acceptable limits almost after a year.
- Higher inventory from the case of LBLOCA on the hot leg of the pressurizer loop along with the SBO results in higher contamination and higher dose predictions as expected. The contamination is 11.5 GBq/km^2 as maximum which may create deterministic effect on the 20 km range. This time a 500 km range is required to obtain the doses below 1 mSv effective dose and millions of people are affected from the consequences. Therefore, active early emergency applications are required to avoid excess dose considering worst case of unprotected release.

The final step of this study is quantification of the uncertainties and sensitivity analysis by KATUSA tool to determine uncertainties on the key events of the sequence and on the global results of the severe accidents. Additionally, the comparison study of radiological dispersion from Zaporizhzhia NPP is performed with best-estimate and worst-case scenario ST inventories to predict differences on contamination and dose projections. The main outcomes of this study are listed below:

- The findings show that large deviations can be observed especially on the RPV failure predictions and cavity rupture estimations which may impact external intervention of the accident for the case of LBLOCA on the cold leg. These deviations result with different released activity levels at the environment. The most probable activity level is about $1.9 \times 10^{18} \text{ Bq}$ but it may reach to the $2.9 \times 10^{18} \text{ Bq}$ activity in some cases. The main contributors of this deviation are Stokes velocity factor at early stage and specific heat of the aerosols at later stage.
- The dispersion analysis by JRODOS indicates that ten times higher aerosol contamination predictions are seen with the worst-case inventory. The acute effective maximum dose is calculated as about 16.7 mSv with the best-estimate results and 48.7 mSv with the worst-case scenario in the 2 km range of the plant. This dose difference

increases rapidly in a year and approximately ten times higher dose projections are calculated with worst-case scenario. The main difference is resulted from lower retention of volatile and low-volatile isotopes in the primary circuit. Finally, the release with best-estimate inventory does not require significant emergency application, yet, early emergency activities are needed to avoid excess dose.

- On the other hand, impact of determined uncertain parameters in case of break on the hot leg is demonstrated that the uncertainty on the RPV failure is greater but on the FP release and uncover of the core is smaller. The most probable release estimation is about 8.55×10^{18} Bq at the end and maximum activity is approximately 1.30×10^{18} Bq indicating smaller difference than in the one in the cold leg case. The Stokes velocity correction factor is the most influential parameter on the activity results at both stages of the accident.
- Performed JRODOS calculations with best-estimate and with worst-case inventories show that the contamination difference is about 2 TBq/km^2 at the end of dispersion which is relatively smaller than the one with inventories obtained from the break on the cold leg case. The contamination results with 7.96 Sv acute effective dose for the best-estimate inventory and 35.1 Sv with the worst-case scenario. Similar to the previous case, this difference rises in time and annual effective dose difference more than 140 Sv. Significant early emergency activities are required for both cases.

The future work of this study has to focus on the development of material inventory of the ASTEC related to VVER components. An improved ASTEC model of VVER-1000 will increase the capability of assessment of the physical and chemical phenomena occurs during the in-vessel and ex-vessel phase of the severe accident. Also, additional hazardous accident sequences such as SBO, SGTR and different sizes of brakes will be employed to investigate different release radioactive release mechanism to the containment and to the environment. Additionally, this model can be extended to evaluated 3+ Gen of the VVER reactors such as VVER-1200.

The performed work by developed platform proves that any severe accident phenomena on VVER-1000 reactors are effectively modelled from the initiating event to the radiological consequences including uncertainty and sensitivity results. The extension of the technical capability contributes to mitigating potential risk of radiological consequences and decrease economical effort to achieve this mitigation work. Technical measures such as containment venting or scrubbing inside of the containment might reduce the potential Source Term inventory and following radiological impact.

Bibliography

- Adams, B. M., & Hooper, R. W. (2020). Dakota Optimization and Uncertainty Quantification Software: CASL Capabilities and Impact. CASL Symposium at 2020 ANS Winter Meeting. Virtual, SAND2020-2731C.
- Andronopoulos, S., Davakis, E., & Bartzis, J. G. (2009). RODOS-DIPCOT Model Description and Evaluation. RODOS(RA2)-TN(09)-01.
- Asmolov, V., & Tsurikov, D. (2004, June 10-11). MASCA Project: major activities and results. Retrieved from [www.oecd-nea.org: https://www.oecd-nea.org/nsd/workshops/masca2004/oc/papers/Final_Programme_MASCASeminar2004.pdf](https://www.oecd-nea.org/nsd/workshops/masca2004/oc/papers/Final_Programme_MASCASeminar2004.pdf)
- Bander, T. (1982). PAVAN : an atmospheric dispersion program for evaluating design basis accidental releases of radioactive materials from nuclear power stations. Washington, D.C.: Y 3.N 88:25/2858 , Office of Nuclear Reactor Regulation, U.S. Nuclear Regulatory Commission.
- Bateman, H. (1910). Solution of a system of differential equations occurring in the theory of radioactive transformations. Cambridge Philosophical Society, Mathematical and Physical Sciences. 15, pp. 423-427. Cambridge: Cambridge Philosophical Society.
- BfS. (2015). Safety Requirements for Nuclear Power Plants: Translations - Rules and Regulations for Nuclear Safety and Radiation Protection. Edition 03/15, 98 pages, BAnz AT 30.03.2015 B2: BfS.
- BMU. (2002). Erste Allgemeine Verwaltungsvorschrift zum Bundes-Immissionsschutzgesetz (Technische Anleitung zur Reinhaltung der Luft-TA Luft) Vom. GMBL Heft(25-29), 551-605.
- Bonneville, H., Bentaïb, A., & Cousin, F. (2017). Fukushima accident computations with ASTEC: how to match the dose measurements in the environment with the simulations. IAEA Technical Meeting on the Status and Evaluation of Severe Accident Simulation Codes for Water Cooled Reactors. Vienna.
- Burstall, R. F. (1979). FISPIN - a computer code for nuclide inventory calculations. United Kingdom: ND-R--328(R).
- Cacuci, G. D. (2010). Handbook of Nuclear Engineering, Volume 1. Karlsruhe: Pg. 2289-2319, Springer, ISBN:: 978-0-387-98130-7.
- Çengel, Y. A. (2014). Heat and Mass Transfer : Fundamentals and Applications (5th ed.). NY: McGraw-Hill Higher Education. p. 362. ISBN 9780077654764.
- Chatelard, P. (2018). ASCOM project overview and description of work. SARNET-ASCOM-COORDI-P1.

- Chatelard, P., & Laborde, L. (2022). Syntesis of the ASTEC V2.2 Code Validation Against Experimental Data. The 10th European Review Meeting on Severe Accident Research (ERMSAR2022) (pp. 1609-1620). Karlsruhe: ID302, KIT, DOI: 10.5445/IR/1000151444.
- Chatelard, P., Belon, S., Bosland, L., Carénini, L., Coindreau, O., Cousin, F., . . . Chailan, L. (2016). Main modelling features of ASTEC V2.1 major version. *Annals of Nuclear Energy*, 93(doi:101016/janucene201512026), 83-93.
- Chatelard, P., Gabrielli, F., Fichot, F., B. H., C., B., Belon, S., . . . Sanchez, V. (2017). Contribution of ASTEC numerical simulations to the understanding of the Fukushima accidents. IAEA Workshop on advances in understanding the progression of severe accidents in Boiling Water Reactors. Vienna.
- Chatelard, P., Reinke, N., Arndt, S., Belon, S., Cantrel, L., Carenini, L., . . . Piar, L. (2014). ASTEC V2 severe accident integral code main features, current V2.0 modelling status, perspectives. *Nuclear Engineering and Design*, 272(0029-5493), 119-135.
- Chatterjee, B., Mukhopadhyay, D., Lele, H. G., Ghosh, A. K., Kushwaha, H. S., Groudev, P., & Atanasova, B. (2009). Effect of steam environment on severe core damage behaviour for VVER-1000 with the ASTEC V1 code. *Nuclear Engineering and Design*, 239(ISSN 0029-5493), 559-565.
- Chatterjee, B., Mukhopadhyay, D., Lele, H., Ghosh, A., Kushwaha, H., Groudev, P., & Atanasova, B. (2010). Analyses for VVER-1000/320 reactor for spectrum of break sizes along with SBO. *Annals of Nuclear Energy*, 359-370.
- Cheng, T., Berna, G., Allison, C., Wagner, R., & Hagrman, D. (1986). RELAP5/SCDAP - an integrated code for severe accident analysis. NUREG/CP--0072-Vol 6.
- Clement, B., & Zeyen, R. (2013). The Objectives of the Phebus FP Experimental Programme and Main Findings. *Annals of Nuclear Energy*, 61(<https://doi.org/10.1016/j.anucene.2013.03.037>), 4-10.
- D'onorio, M., Giannetti, F., Mascari, F., & Caruso, G. (2018). Uncertainty Analyses using the RAVEN Software Tool Coupled with MELCOR Severe Accident Code. *ANS Best Estimate Plus Uncertainty International Conference (BEPU 2018)*, (p. 282). Lucca, Italy.
- Engel, G., Fieg, G., Massier, H., Stiegmaier, U., & Schütz, W. (2000). KATS experiments to simulate corium spreading in the EPR code catcher concept. *OECD Workshop on Ex-Vessel Debris* (pp. 148-156). Karlsruhe: KITopen-ID: 270047463, KITopen-ID: 270047463.
- EPRI. (2013). *Use of Modular Accident Analysis Program (MAAP) in Support of Post-Fukushima Applications*. Palo Alto, CA, 3002001785: EPRI.
- Gabrielli, F., Stakhanova, A., Sanchez-Espinoza, V., Pauli, E., Hoefler, A., & Feldmann, H. (2022). Impact of Realistic Fuel Inventories on the Radiological Consequences of a Severe Accident Scenario in a Generic KONVOI Plant by means of the ASTEC code. *KERNTECHNIK*. Leipzig.

- Garcia, M., Tuominen, R., Gommlich, A., Ferraro, D., Valtavirta, V., Imke, U., . . . Kliem, S. (2020). A Serpent2-SUBCHANFLOW-TRANSURANUS coupling for pin-by-pin depletion calculations in Light Water Reactors. *Annals of Nuclear Energy*, 139(ISSN 0306-4549), 107213.
- Gaudier, F. (2010). URANIE: The CEA/DEN Uncertainty and Sensitivity platform. *Procedia - Social and Behavioral Sciences*, 2(6, ISSN 1877-0428), 7660-7661.
- Gaus-Liu, X., Miassoedov, A., Cron, T., & Wenz, T. (2010). In-vessel melt pool coolability test- Description and results of LIVE experiments. *Nuclear Engineering and Design*, 240(10.1016/j.nucengdes.2010.09.001), 3898-3903.
- Gencheva, R., Stefanova, A., & Groudev, P. (2015). Plant application of ICARE/ASTECv2.0rev3 computer code for investigation of in vessel retention in VVER-1000 reactor design. *Annals of Nuclear Energy*, 81, 207-212.
- Ghosh, S. T., Esmaili, H., Hattaway III, A. G., Osborn, D., Bixler, N. E., Brooks, D., . . . Wagner, K. C. (2019). State-of-the-Art Reactor Consequence Analyses Project: Uncertainty Analyses for Station Blackout Scenarios. 9th Conference on Severe Accident Research (ERMSAR 2019) (pp. 527-547). Prague: ISBN 978-80-270-5809-9.
- Gomez-Garcia-Tarano, I. (2017). Further development of Severe Accident Management Strategies for a German PWR Konvoi Plant based on the European Severe Accident Code ASTEC. Karlsruhe: Karlsruher Institut für Technologie (KIT), 10.5445/IR/1000073683, 32.02.11; LK 01.
- Gomez-Garcia-Torano, I., Sanchez-Espinoza, V. H., Stieglitz, R., Stuckert, J., Laborde, L., & Belon, S. (2017). Validation of ASTECV2.1 based on the QUENCH-08 experiment. *Nuclear Engineering and Design*, 314(0029-5493), 29-43.
- Groudev, P., Atanasova, B., Chatterjee, B., & Lele, H. G. (2014). ASTEC investigations of severe core damage behaviour of VVER-1000 in case of loss of coolant accident along with Station-Black-Out. *Nuclear Engineering and Design*, 272(ISSN 0029-5493), 237-244.
- GRS. (2021). SUSA: Software for Uncertainty and Sensitivity Analysis. München, ISBN 978-3-949088-20-9: GRS - 631.
- GRS. (Assessment of the Accidental Risk of Advanced Pressurized Water Reactors in Germany). 2002. pg. 177, Germany, ISBN 3-931995-43-7: Grs-184.
- Hadad, K., Mirvakili, S. M., Safaei, S., & Nematollahi, M. R. (2009). REACTIVITY INDUCED ACCIDENT ANALYSIS FOR A VVER-1000. 14th International Conference on Emerging Nuclear Energy Systems. Ericeira, Portugal: ICENES2009.
- Helton, J. C., Iman, R. L., Johnson, J. D., & Leigh, C. D. (1986). Uncertainty and Sensitivity Analysis of a Model for Multicomponent Aerosol Dynamics. *Nuclear Technology*, 73:3(10.13182/NT86-A16075).

- Herranz, L. H., & Paci, S. (2020). The MUSA Project: Management and Uncertainties of Severe Accidents. 9th European Commission Conference on Euratom Research and Training in Safety of Reactor Systems (pp. 97-98). Pitesti, Romania, DOI: 10.2777/83061: Publications Office for the EU, DOI: 10.2777/83061.
- Hoffmann, A., Jeanpierre, F., Kavenoky, A., Livolant, M., & Lorain, H. (1973). APOLLO - A multigroup code for the solution of the transport equation for thermal and fast neutrons. France: CEA-N--1610.
- Hózer, Z. (2002). Summary of the Core Degradation Experiments CODEX. EUROSAFE UROSAFE Forum 2002: convergence of nuclear safety practices in Europe Papers. Berlin: Ref. No: 36065838, INIS Vol: 36, INIS Issue: 30.
- Hózer, Z., Györi, C., Matus, L., & Horváth, M. (2008). Ductile-to brittle transition of oxidised Zircaloy-4 and E110 claddings. *Journal of Nuclear Materials*, 373, 415-423.
- Hózer, Z., Györi, C., Horváth, M., Nagy, I., Maróti, L., Matus, L., . . . Frecska, J. (2005). Ballooning Experiments with VVER Cladding. *Nuclear Technology*, 152(10.13182/NT05-A3676), 273-285.
- Hózer, Z., Maróti, L., Windberg, P., Matus, L., Nagy, I., Gyenes, G., . . . Tóth, B. (2006). Behavior of VVER fuel rods tested under severe accident conditions in the CODEX facility. *Nuclear Technology*, 154(10.13182/NT06-A3735), 302-317.
- Humpries, L., & Gauntt, R. O. (2018). MELCOR 2.2 SEVERE ACCIDENT ANALYSIS CODE – CURRENT STATUS AND PLANS FOR FUTURE. SAND2018-0310C.
- IAEA. (1994). Database for the Kozloduy NSSS for Accident Analysis of WWER-1000 Model 320 Nuclear Plants. Vienna, TC/RER/020: IAEA.
- IAEA. (2002). Dispersion of Radioactive Material in Air and Water and Consideration of Population Distribution in Site Evaluation for Nuclear Power Plants. Vienna: IAEA Safety Standart Series. Safety Guide No. NS-G-3.2.
- IAEA. (2005). WWER-1000 Reactor Simulator: Material for Training Courses and Workshops Second Edition. Vienna: INTERNATIONAL ATOMIC ENERGY AGENCY (IAEA).
- IAEA. (2006). Environmental Consequences of the Chernobyl Accident and Their Remediation: Twenty Years of Experience. Vienna: International Atomic Energy Agency.
- IAEA. (2012). Safety of Nuclear Power Plants: Design. Vienna, IAEA Safety Standards Series No. SSR-2/1 (Rev. 1), Pg. 71, ISBN 978-92-0-109315-8: IAEA.
- IAEA. (2016). Criteria for Radionuclide Activity Concentrations for Food and Drinking Water. Vienna: International Atomic Energy Agency, IAEA-TECDOC-1788.
- IAEA. (2020). Case Study on Assessment of Radiological Environmental Impact from Potential Exposure. Vienna: IAEA-TECDOC-1914.

- IAEA. (2020). Environmental Transfer of RadioNuclides in Japan following the Accident at the Fukushima Daiichi Nuclear Power Plant. Vienna: IAEA, IAEA-TECDOC-1927 | 978-92-0-117920-3.
- ICRP. (2007). The 2007 Recommendations of the International Commission on Radiological Protection. Paris: ICRP Publication 103. Ann. ICRP 37 (2-4).
- IRSN. (2021). ASTEC V2.2: Physical Modelling of the ICARE Module. Aix-en-Provence, Report No: IRSN/2021-00185 BDD-ST SAM-SAM-2021-039: IRSN.
- Ivanov, K., Ivanov, B., Groudev, P., Pavlova, M., & Hadjiev, V. (2002). VVER-1000 Coolant Transient Benchmark-Phase 1 (V1000CT-1) Volume I: Vol. I: Main Coolant Pump (MCP) switching on - Final Specifications. Paris: OECD Publishing, NEA/NSC/DOC(2002)6.
- Karlsruhe Institute of Technology (KIT). (2017). JRodos: An off-site emergency management system for nuclear accidents. Karlsruhe: Karlsruhe Institute of Technology (KIT).
- Kernforschungszentrum Karlsruhe (KfK). (1984). The Meteorological System and the Basic Parameters Required for Predicting the Transfer of Radionuclides Released into the Atmosphere. Karlsruhe: KIT, Kfk 3754.
- Kwang-II, A., Keo-hyoung, L., & Seok-Won, H. (2023). The APR1400 SOARCA study: Insights into the evolution of severe accidents and fission product source term analysis results. *Progress in Nuclear Energy*, 104628, Volume 158, ISSN 0149-1970, <https://doi.org/10.1016/j.pnucene.2023.104628>.
- Laaksonen, J. (2013, September 14). VVER-type nuclear power plants and evolution of their safety. Retrieved from Finnish Nuclear Society: http://ats-fns.fi/images/files/presentations/2013/ATS_jasentilaisuus_2013-3_laaksonen.pdf
- Lankin, M. (2014). Safety Enhancement of the Nuclear Power Plants with WVER-type Reactors in Response to Fukushima Daiichi Accident. Convention on Nuclear Safety : 6th Review Meeting of the Contracting Parties. Vienna: Forum WVER, Conference ID: 46094.
- Lötsch, T. (2014). Fuel assembly burnup calculations for VVER fuel assemblies with the MONTE CARLO code SERPENT. *Kerntechnik*, 79, no. 4(<https://doi.org/10.3139/124.110455>), 295-302.
- Magallon, D. (2006). Characteristics of corium debris bed generated in large-scale fuel-coolant interaction experiments. *Nuclear Engineering and Design*, 236(<https://10.1016/j.nucengdes.2010.09.001>), Volume 236, Issues 19–21, pg. 1998-2009, ISSN 0029-5493.
- Malet, J., Porcheron, E., & Vendel, J. (2010). OECD International Standart Problem ISP-47 on containment thermal-hydraulics- Conclusions of the TOSQAN part. *Nuclear Engineering and Design*, 240(0029-5493, <https://doi.org/10.1016/j.nucengdes.2010.05.061>), 3209-3220.

- Manara, D., Jacquemain, D., Van Dorselaere, J. P., Bottomley, P. D., Adorni, M., Journeau, C., . . . De Jardin, P. (2018). Severe Accident Research Priority Ranking: A New Assessment Eight Years After The Fukushima Daiichi Accident. 9TH Conference on Severe Accident Research (ERMSAR 2019) (pp. 835-860). Prague: ISBN 978-80-270-5809-9.
- McKay, M. D., Beckman, R. J., & Conover, W. J. (1979). A comparison of three methods for selecting values of input variables in the analysis of output from a computer code. *Technometrics*, 21, 239-245.
- Meiyin, Z., Wenxi, T., Hongyang, W., Dalin, Z., Yingwei, W., Suizheng, Q., & Guanghui, S. (2014). Development of a MCNP-ORIGEN Burn-up Calculation Code System and its Accuracy Assessment. *Annals of Nuclear Energy*, 63(ISSN 0306-4549), 491-498.
- Mercan, A. K., Gabrielli, F., & Sanchez-Espinoza, V. H. (16-19 May 2022). Source Term Estimation and Dispersion Analysis of VVER-1000 Reactor in case of LBLOCA Along With SBO. The 10th European Review Meeting on Severe Accident Research (ERMSAR2022) (pp. 296-309). Karlsruhe: DOI: 10.5445/IR/1000151444.
- Mercan, A. K., Gabrielli, F., & Sanchez-Espinoza, V. H. (2022). Validation of Astec2.1 using Quench-12 for VVER-Reactors. *Nuclear Engineering and Design*, 395(111840, ISSN 0029-5493).
- Mercan, A. K., Gabrielli, F., Sanchez-Espinoza, V. H., & Raskob, W. (2022). Analysis of the consequences of a LBLOCA with SBO severe accident in a generic VVER-1000 by means of ASTEC and JRODOS codes. *Nuclear Engineering and Design*, 112078, ISSN 0029-5493, <https://doi.org/10.1016/j.nucengdes.2022.112078>.
- Mizokami, S. (2022). Fukushima: 10 (+1) Years After: Current Sitation of the Site- Facts & Future of Fukushima Daichi NPS. 10th European Review Meeting on Severe Accidents Research (ERMSAR 2022) (pp. 438-469). Karlsruhe: KIT, KITopen-ID: 1000151444, DOI: 10.5445/IR/1000151444.
- Murphy, B., Kravchenko, J., Lazarenko, A., Pavlovitchev, A., Sidorenko, V., & Chetverikov, A. (2000). Simulation of Low-Enriched Uranium (LEU) Burnup in Russian VVER Reactors with the HELIOS Code Package. Tennessee, ORNL/TM-1999/168: Oak Ridge National Laboratory.
- Nagase, F., Konings, R. J., & Stoller, R. E. (2020). *Comprehensive Nuclear Materials (Second Edition)*. In Behavior of LWR Fuel During Loss-of-Coolant Accidents (pp. 307-321). Oxford: Elsevier, DOI: 978-0-08-102866-7.
- NEA. (2001). Validation Matrix for the Assessment of Thermal-Hydraulic Codes for VVER LOCA and Transients. Paris, NEA/CSNI/R(2001)4: OECD Publishing.
- NEA. (2007). BEMUSE Phase 3 Report: Uncertainty and sensitivity analysis on the LOFT L2-5 test. NEA/CSNI/R(2007).
- NEA. (2009). Nuclear Fuel Behaviour in Loss-of-coolant Accident (LOCA) Conditions. Paris: OECD Publishing, ISBN 978-92-64-99091-3.

- NEA/CSNI/NEA. (2007). International Standard Problem ISP-47 on Containment Thermal Hydraulics. NEA.
- NEA/OECD. (2017). State-of-the-art Report on Molten Corium Concrete Interaction and Ex-Vessel Molten Core Coolability. Vienna: NEA No. 7392.
- NEA-OECD. (2004). VVER-1000 Coolant Transient Benchmark (V1000CT) Volume II: Specification of the VVER-1000 Vessel Mixing Problems. Paris: NEA COMMITTEE ON SAFETY OF NUCLEAR INSTALLATIONS.
- NEA-OECD. (2013). The Fukushima Daiichi Nuclear Power Plant Accident: Nuclear Safety Response and Lessons Learnt. Paris: NEA Report No:7161.
- Nowack, H., Chatelard, P., Chailan, L., Hermsmeyer, S., Sanchez, V., & Herranz, L. (2018). CESAM – Code for European severe accident management, EURATOM project on ASTEC improvement. *Annals of Nuclear Energy*(doi:10.1016/j.anucene.2018.02.021), 128-136.
- Nuclear Regulatory Authority of the Slovak Republic. (2010). National Report of Slovak Republic Compiled in terms of the Convention on Nuclear Safety. Bratislava: Nuclear Regulatory Authority of the Slovak Republic.
- Palagin, A., & Stuckert, J. (2007). Application of the SVECHA/QUENCH Code to the Simulation of the Bundle Tests QUENCH-06 and QUENCH-12. Karlsruhe: Forschungszentrum Karlsruhe GmbH, Scientific Report FZKA-7353.
- Päsler-Sauer, J. (2000). Description of the Atmospheric Dispersion Model ATSTEP. RODOS(WG2)-TN(97)-01.
- Pasquill, F. (1961). The estimation of the dispersion of windborne material. *The Meteorological Magazine* 90 (1063), 33-49.
- Peletsky, V. E. (1999). High-temperature thermal conductivity of zirconium based alloys. *High Temperatures- High Pressures*, 31, 627-632.
- Petrova, I., Peletsky, E., & Samsonov, B. N. (1999). Thermophysical Properties of the Zr-O.01Nb Alloy at Various Heating Rates and Repeated Cycles of Heating-Cooling. Fifth International Workshop on Subsecond Thermophysics. 20 No:4, pp. 1117-1127, Vol. 20, Issue 4. *International Journal of Thermophysics*.
- Powers, D. A. (1981). Review of steam oxidation of steels: the forgotten source of hydrogen. Albuquerque: NUREG/CR-2017-Vol.2 p.83-116.
- Prater, J., & Courtright, E. (1985). Oxidation of Zircaloy-4 in steam at 1300 to 2400 °C. Zirconium in the Nuclear Industry: Seventh International Symposium (pp. 489-502). Strasbourg: ASTM Special Technical Publication 939, ASTM Publication Code Number (PCN).

- Queral, C., Sanchez-Espinoza, V., Egelkraut, D., Fernandez-Cosials, M., Redondo-Valero, E., & Garcia-Morillo, A. (2021). Safety systems of Gen-III/Gen-III+ VVER reactors. Madrid: Nuclear Espania.
- Raskob, W., Trybushnyi, D., Ievdin, I., & Zheleznyak, M. (2012). JRODOS: Platform for improved long term countermeasures modelling and management. *Radioprotection*, 46(6), 731-736.
- Repetto, G., Garcin, T., Eymery, S., & Fichot, F. (2013). Experimental Program on Debris Reflooding (PEARL)- Results on PRELUDE Facility. *Nuclear Engineering and Design*, 264(10.1016/j.nucengdes.2012.11.024), 176-186.
- Ryzhov, S., Mokhov, V. A., Nikitenko, M. P., Bessalov, G. G., Podshibyakin, A. K., Anufriev, D. A., . . . Rohde, U. (2010). VVER-Type Reactors of Russian Design. In D. Cacuci, *Handbook of Nuclear Engineering* (pp. 2250-2319). Boston: Springer, .
- Saltelli, A., Chan, K., & Scott, E. M. (2009). *Sensitivity Analysis*. Wiley: ISBN: 978-0-470-74382-9.
- Schanz, G., Hagen, S., Hofmann, P., Schumacher, G., & Sepold, G. (1992). Information on the evolution of severe LWR fuel element damage obtained in the CORA program. *Journal of Nuclear Materials*, 188([https://doi.org/10.1016/0022-3115\(92\)90462-T](https://doi.org/10.1016/0022-3115(92)90462-T)), 131-145.
- Sehgal, B. R. (2012). *Light Water Reactor Safety: A Historical Review*. Oxford: ISBN 978-0-12-388446-6, ELSEVIER academic Press.
- Sehgal, B., Karbojian, A., Giri, A., O., K., Bonnet, J., & Wenz, T. (2005). Assessment of Reactor Vessel Integrity (ARVI). *Nuclear Engineering and Design*, 235(<https://doi.org/10.1016/j.nucengdes.2004.08.055>), 213-232.
- Shapiro, Z. M., & Moffette, T. R. (1957). Hydrogen Flammability Data and Application to PWR Loss-of-Coolant Accident. Pittsburgh, Pennsylvania: Report WAPD-SC-545, Bettis Plant.
- Slade, D. H. (1968). *Meteorology and atomic energy*. Washington DC: US AEC Report TID-24190.
- Sokolov, N., & Andreeva-Andrievskaya, L. (1993). Kinetics of Interaction between materials in Water-Cooled Power Reactor Core. Recommendations for Application within the Framework of the International Standard Problem for the CORA-W2 experiment. Moscow: Bochvar Institute of the Inorganic Materials the Inorganic Materials.
- Stakhanova, A., Gabrielli, F., Sanchez-Espinoza, V. H., Hoefler, A., & Pauli, E. (2022). Uncertainty and sensitivity analysis of the QUENCH-08 experiment using the FSTC tool. *Annals of Nuclear Energy*, 169(ISSN 0306-4549), 108968.
- Stakhanova, A., Gabrielli, F., Sanchez-Espinoza, V., Pauli, E., & Hoefler, A. (2022). Uncertainty and Sensitivity Analysis of the ASTEC simulations results of a MBLOCA scenario at a Generic KONVOI Plant using FSTC tool. The 10th European Review Meeting on Severe Accident Research (ERMSAR2022) (pp. 861-872). Karlsruhe: KITopen-ID: 1000151444, DOI: 10.5445/IR/1000151444.

- Stefanova, A., Gencheva, R., & Groudev, P. (2011). Simulation of VVER MCCI reactor test case with ASTEC-v2 / MEDICIS computer code. *Energy Forum* (pp. 108-113). Varna: INIS-BG--15766 INIS Vol. 44, INIS Issue: 18.
- Steinbrück, M., Große, M., Sepold, L., & Stuckert, J. (2010). Synopsis and Outcome of the QUENCH Experimental Program. *Nuclear Engineering and Design*, 240(<https://doi.org/10.1016/j.nucengdes.2010.03.021>), 1714-27.
- Strahlenschutzkommission (SSK). (2019). Operational intervention levels for measures to protect the population against incidents involving releases of radionuclides. Bonn: Geschäftsstelle der Strahlenschutzkommission.
- Stuckert, J., & Gerogiev, Y. G. (2012). Analysis of the QUENCH-12 bundle experiment with the ATHLET-CD2.2A code. Karlsruhe: KIT Scientific Publishing, Report-Nr. KIT-SR 7622.
- Stuckert, J., Gorbachev, A., Heck, M., Ivanova, I., Schanz, G., Stegmaie, U., & Steinbrück, M. (2008). Results of the QUENCH-12 experiment on reflood of a VVER-type bundle. Karlsruhe: Wissenschaftliche Berichte. FZKA, DOI: 10.5445/IR/270072587.
- Stuckert, J., Steinbrück, M., & Große, M. (2015). Experimental program QUENCH at KIT on core degradation during reflooding under LOCA conditions and in the early phase of a severe accident. *Modelling of Water Cooled Fuel Including Design Basis and Severe Accidents* (pp. 281-298). Chengdu, DOI: 10.5445/IR/1000078815: IAEA-TECDOC-CD-1775, ISBN: 978-92-0-158615-5.
- Studer, E., Magnaud, J., Dabbane, F., & Tkatschenko, I. (2006). International standart problem on containment thermal-hydraulics ISP47, Step 1-Results from the MISTRA exercise. *Nuclear Engineering and Design*, 237([10.1016/j.nucengdes.2006.08.008](https://doi.org/10.1016/j.nucengdes.2006.08.008) . cea-02355776), 536-551.
- Sun, J., Takle, E. S., & Acevedo, O. C. (2020). Understanding Physical Processes Represented by the Monin–Obukhov Bulk Formula for Momentum Transfer. *Boundary-Layer Meteorology*, 177(1573-1472, DOI: 10.1007/s10546-020-00546-5), 69-95.
- Thyker-Nielsen, S., Deme, S., & Mikkelsen, T. (1999). Description of the Atmospheric Dispersion Module RIMPUFF. RODOS(WG2)-TN(98)-02.
- Trellue, H. R. (1998). Development of Monteburns: A Code That Links MCNP and ORIGEN2 in an Automated Fashion for Bunrp Calculations. New Mexico: LA-13514-T, Los Alamos National Laboratory.
- Tusheva, P. (2012). Modelling and Analysis of Severe Accidents for VVER-1000 Reactors. Dresden: HZDR-025.
- U. S. NRC. (2016). State-of-the-Art Reactor Consequence Analyses Project: Uncertainty Analysis of the Unmitigated Long-Term Station Blackout of the Peach Bottom Atomic Power Station. Albuquerque: Office of Nuclear Regulatory Research.

- U.S. NRC. (2013). State-of-the-Art Reactor Consequence Analyses Project Volume 2: Surry Integrated Analysis. Sandia National Laboratories, Albuquerque, New Mexico, NUREG/CR-7110, Vol. 2,; Office of Nuclear Regulatory Research.
- U.S. NRC. (2017). State-of-the-Art Reactor Consequence Analysis (SOARCE) Project: Sequoyah Integrated Deterministic and Uncertainty Analyses. Albuquerque: NUREG/CR-7245, Office of Nuclear Regulatory Research.
- U.S. Nuclear Regulatory Commission (NRC). (2005). Kalinin VVER-1000 Nuclear Power Station Unit 1 PRA (Beta Project). Washington, DC 20555-0001: U.S. Nuclear Regulatory Commission.
- Urbanic, V., & Heidrich, T. (1978). High-Temperature Oxidation of Zircaloy-2 and Zircaloy-4 in Steam. *Journal of Nuclear Materials*, 75, 151-261.
- Van Dorsselaere, J.-P., Albiol, T., & Micaelli, J.-C. (2011). Research on Severe Accidents in Nuclear Power Plants. In P. V. Tsverkov, *Nuclear Power - Operation, Safety and Environment* (p. Chapter 8). RIjeka: IntechOpen, DOI: 10.5772/17552.
- Veteau, J.-M., & Wittmaack, R. (1996). CORINE Experiments and Theoretical Modelling. FISA 95 symposium on EU research on severe accidents (pp. 271-286). Luxembourg: EUR 16896 EN.
- WENRA. (2013). Safety of new NPP designs. 52 pages, Study by Reactor Harmonization Working Group RHWG March 2013: Reactor Harmonization Working Group RHWG.
- Wies, & H.W. (1998). Development and application of KORIGEN. Brennelementtechnik, Kernausslegung, Reaktorbetrieb : Fachtagung der KTG-Fachgruppen 'Brennelemente' und 'Reaktorphysik und Berechnungsmethoden' (pp. 155-160). Karlsruhe: 32.23.01; LK 01.
- Wilks, S. S. (1941). Determination of sample sizes for setting tolerance limits. *Annals of Mathematical Statistics*, 12, 91-96.
- Zannetti, P. (1990). Gaussian Models. In C. M. *Air Pollution Modeling: Theories*, Zannetti, P. (pp. 141-183). Boston, MA: Springer US, 10.1007/978-1-4757-4465-1_7, https://doi.org/10.1007/978-1-4757-4465-1_7.

Appendix A Further results of the ASTECV2.1 validation on the QUENCH-12 experiment

Chapter A was dedicated to the validation of the ASTEC code by QUENCH-12 experiment and comparison of key variables. In this section, additional comparison results are shown, and the following variables are investigated:

- Temperature comparison at several elevations
- Oxide scale growth on fuel rods

A.1 Temperature comparison at several elevation

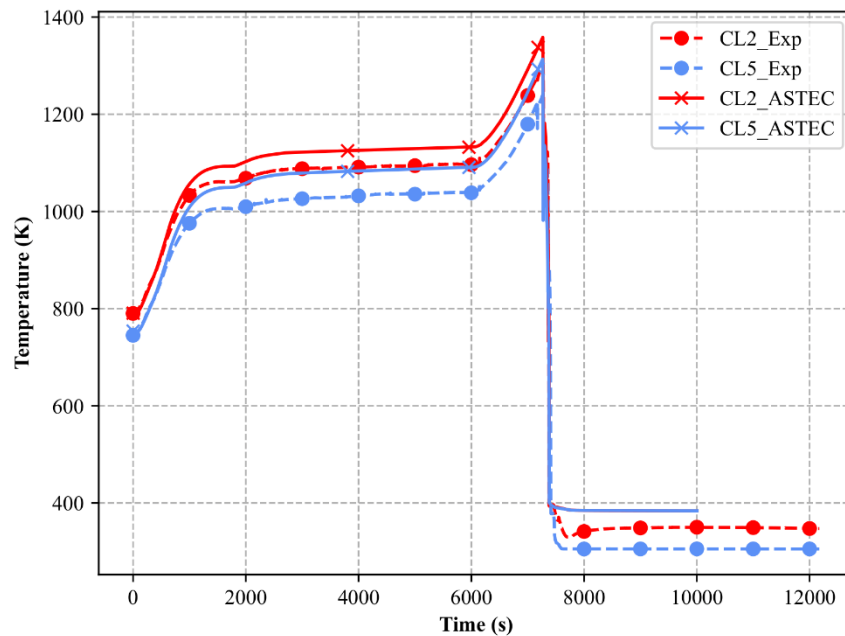


Figure A.1- 1: Comparison of predicted and experimental temperature results for heated rod at the axial elevation of 350 mm

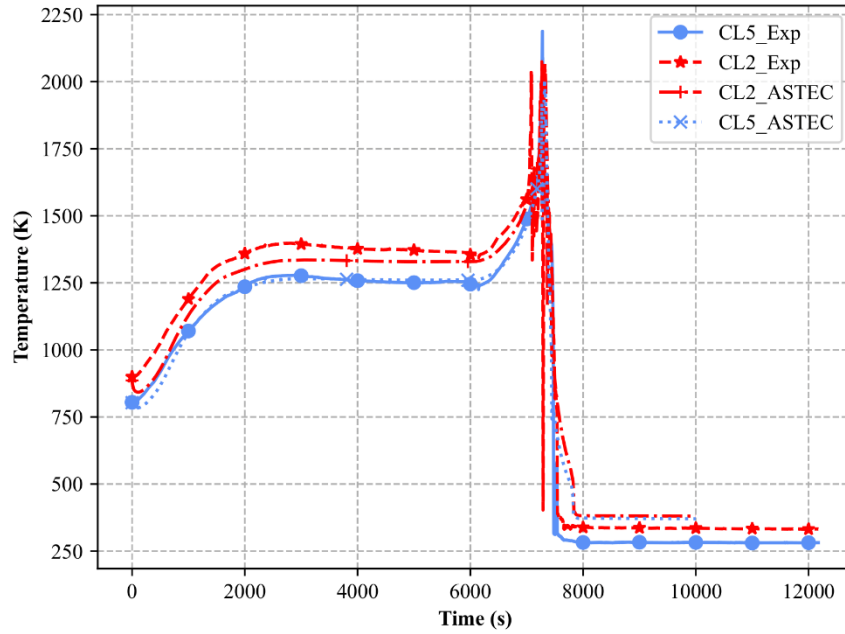


Figure A.1- 2: Comparison of predicted and experimental temperature results for heated rod at the axial elevation of 1050 mm

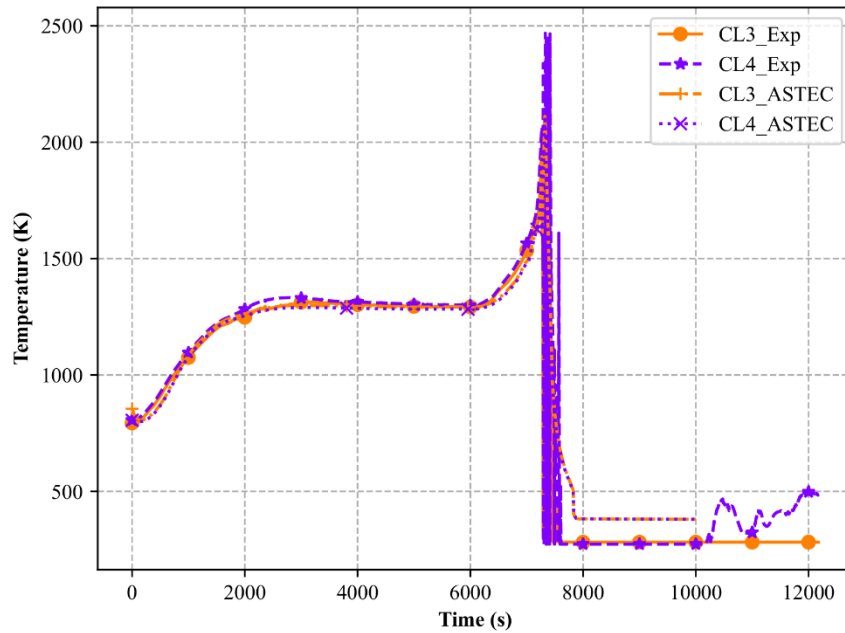


Figure A.1- 3: Comparison of predicted and experimental temperature results for unheated rod at the axial elevation of 1050 mm

A.2 Oxide scale growth on fuel rods

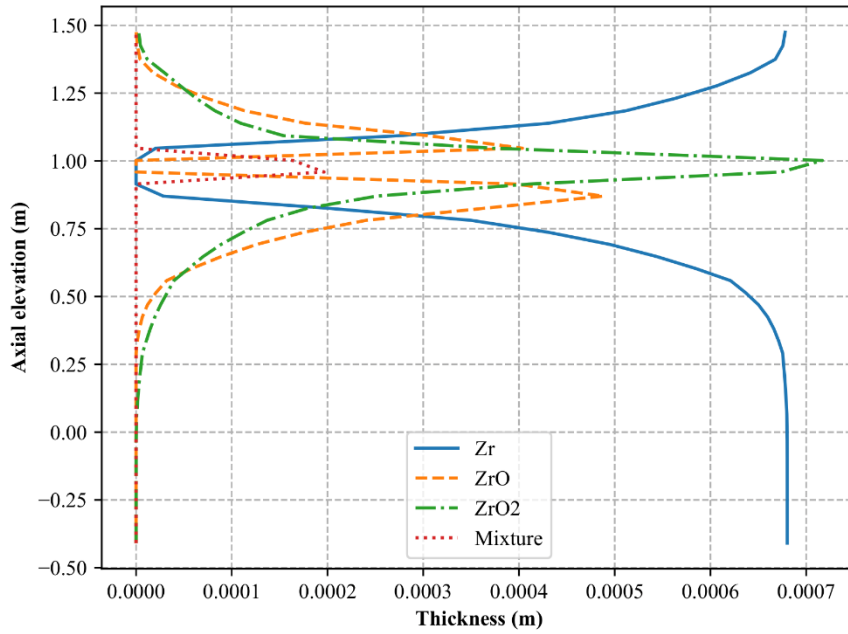


Figure A.2- 1: Oxide scale growth prediction for inner heated rod group (CLAD2) during the transient

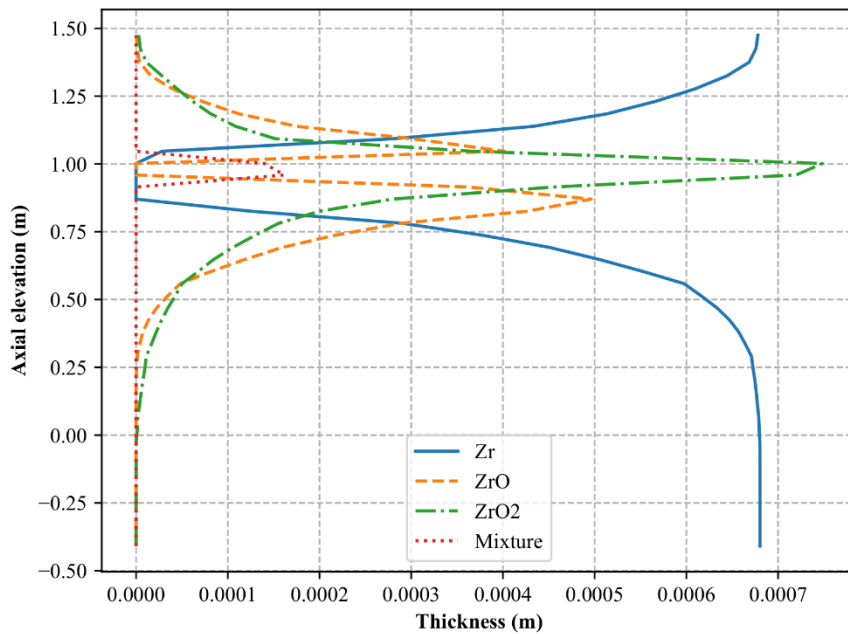


Figure A.2- 2: Oxide scale growth prediction for inner unheated rod group (CLAD3) during the transient

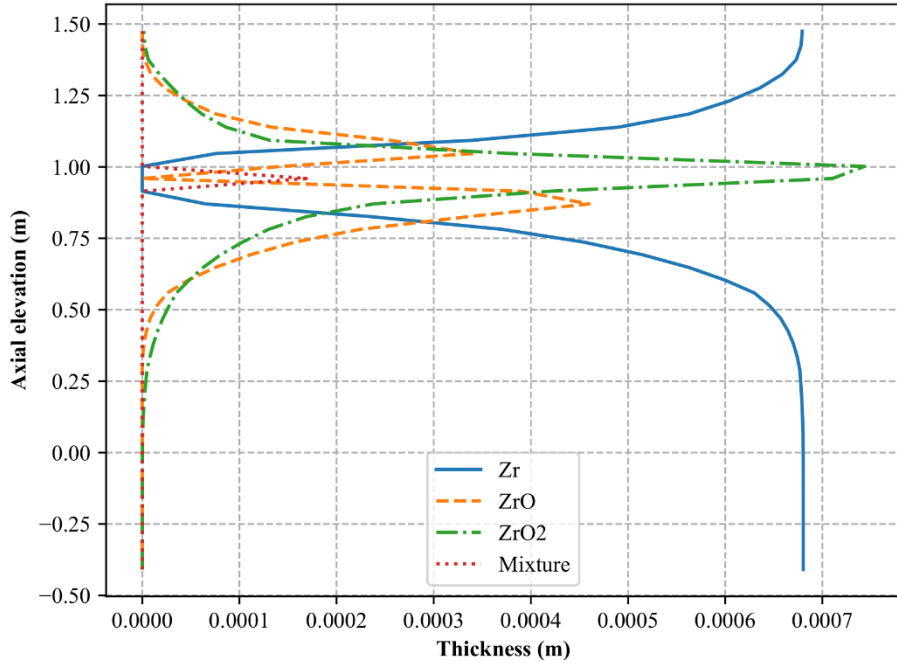


Figure A.2- 3: Oxide scale growth prediction for outer unheated rod group (CLAD4) during the transient

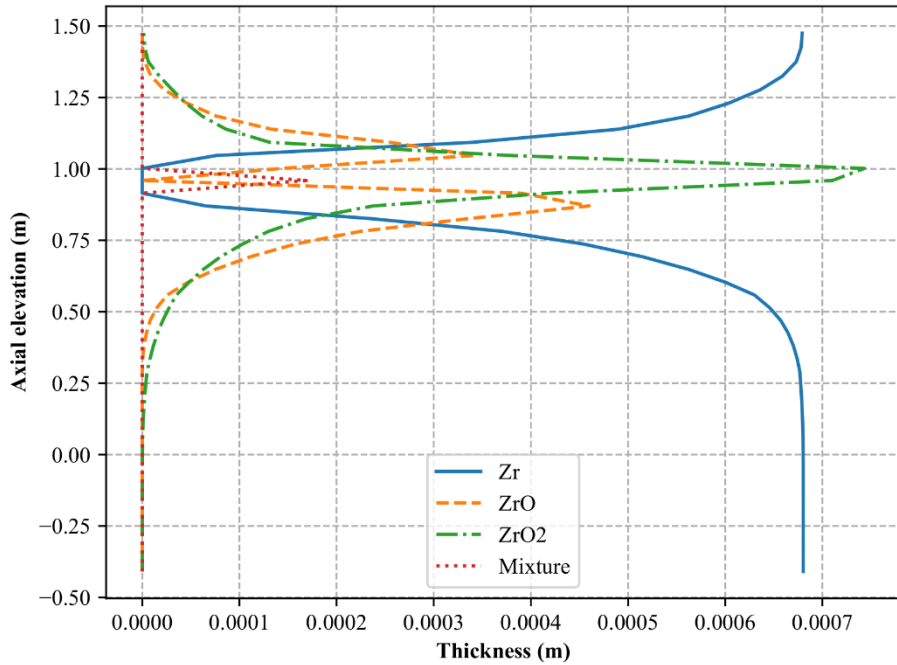


Figure A.2- 4: Oxide scale growth prediction for outer heated rod group (CLAD5) during the transient

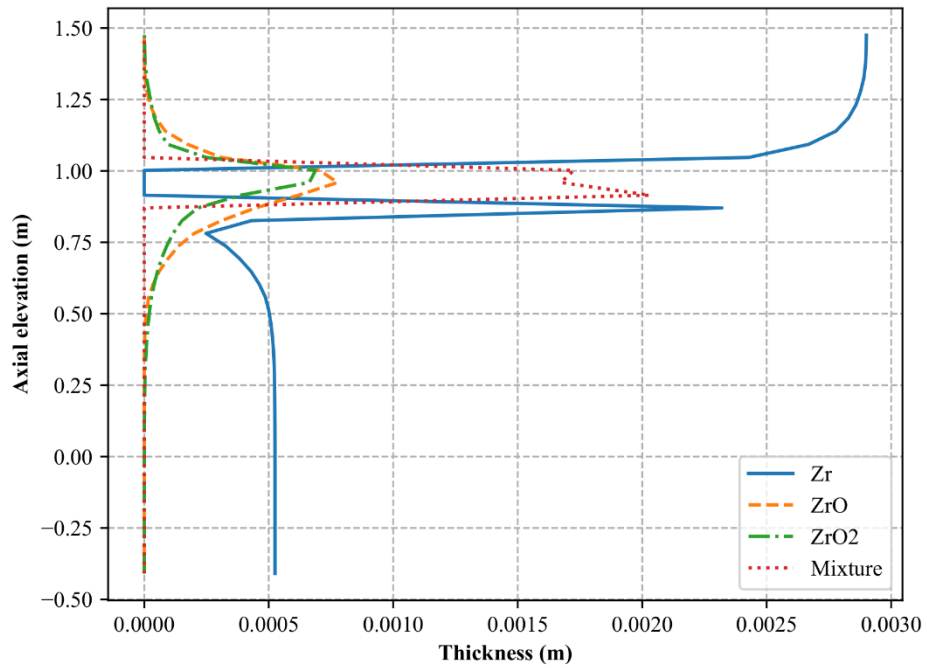


Figure A.2- 5: Oxide scale growth prediction for shroud (SHR) during the transient

Appendix B Further results of the performed sequences in a VVER-1000 using ASTEC V2.2

Appendix C presents key findings on the performed VVER-1000 accident sequences. The additional in-vessel and ex-vessel accident progression parameters as well as element and isotope base FP inventory distribution have been demonstrated in this section. Following findings have been shown:

- Pressure inside of the primary circuit and inside of the containment
- Water inventories change inside of the accumulators.
- Vessel water inventory change
- Molten material composition inside of the lower plenum
- Cavity erosion and molten material mass in the cavity
- Mass of the gas inventory inside of the containment

B.1 Further results of LBLOCA on the cold with SBO accident

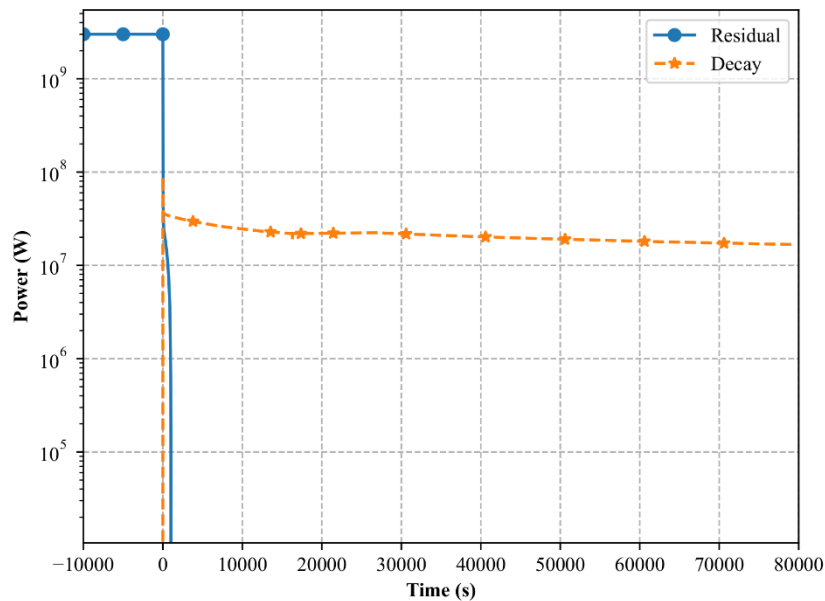


Figure B.1- 1: Power profile change in time in case of LBLOCA on the cold leg of the pressurizer loop along with the SBO

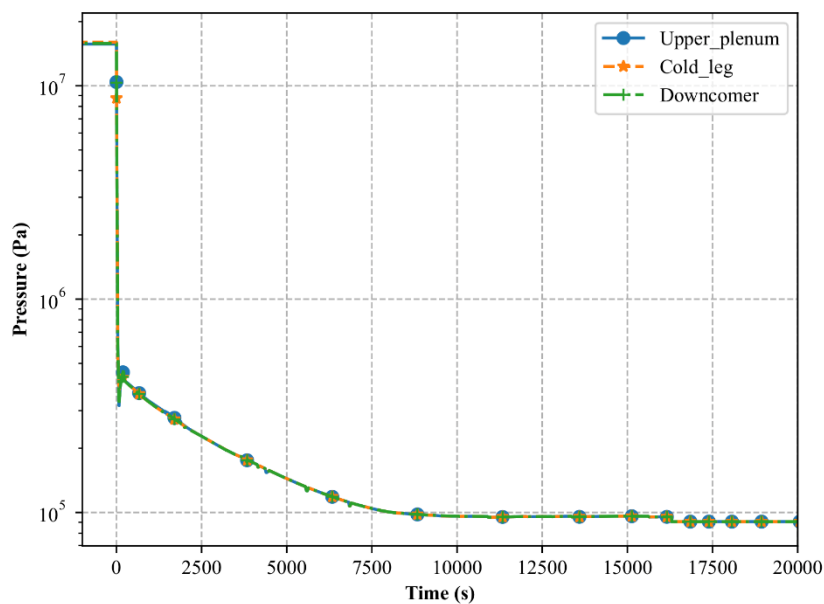


Figure B.1- 2: Calculated pressure change inside of the primary circuit in time in case of LBLOCA on the cold leg of the pressurizer loop along with the SBO

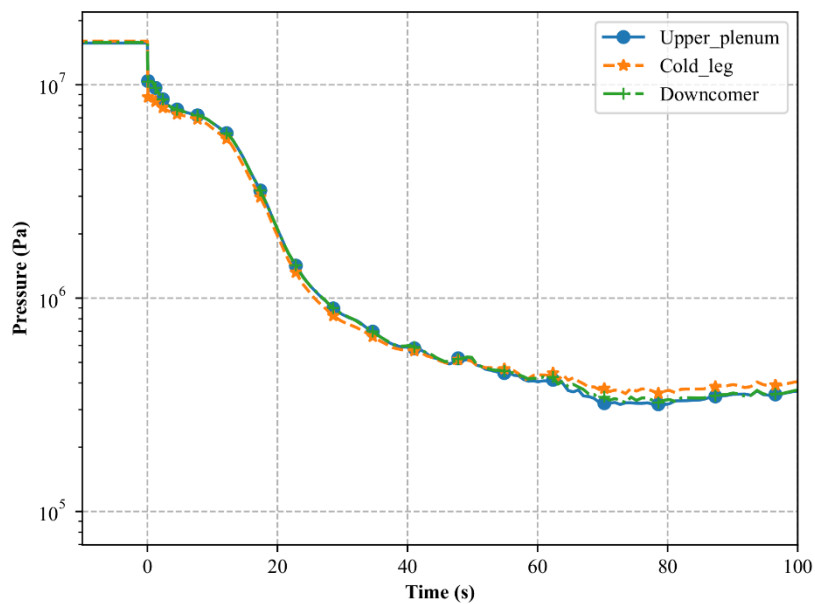


Figure B.1- 3: Calculated pressure change inside of the primary circuit in first 100 seconds in case of LBLOCA on the cold leg of the pressurizer loop along with the SBO

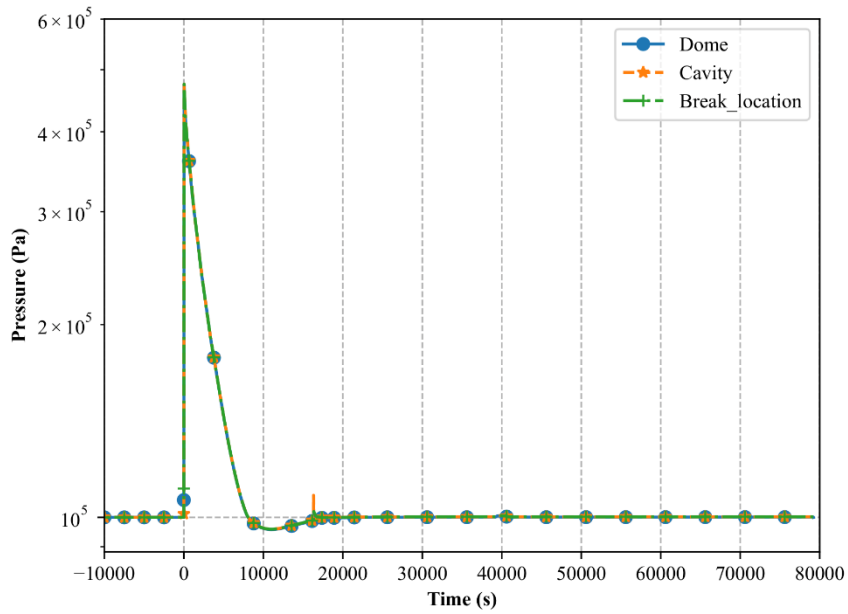


Figure B.1- 4: Calculated pressure change inside of the containment in time in case of LBLOCA on the cold leg of the pressurizer loop along with the SBO

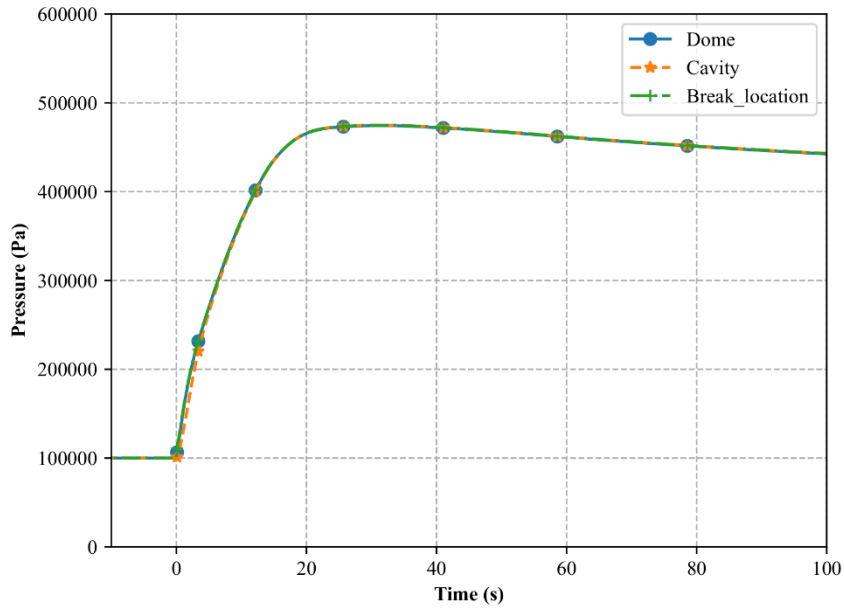


Figure B.1- 5: Calculated pressure change inside of the containment in first 100 seconds in case of LBLOCA on the hot leg of the pressurizer loop along with the SBO

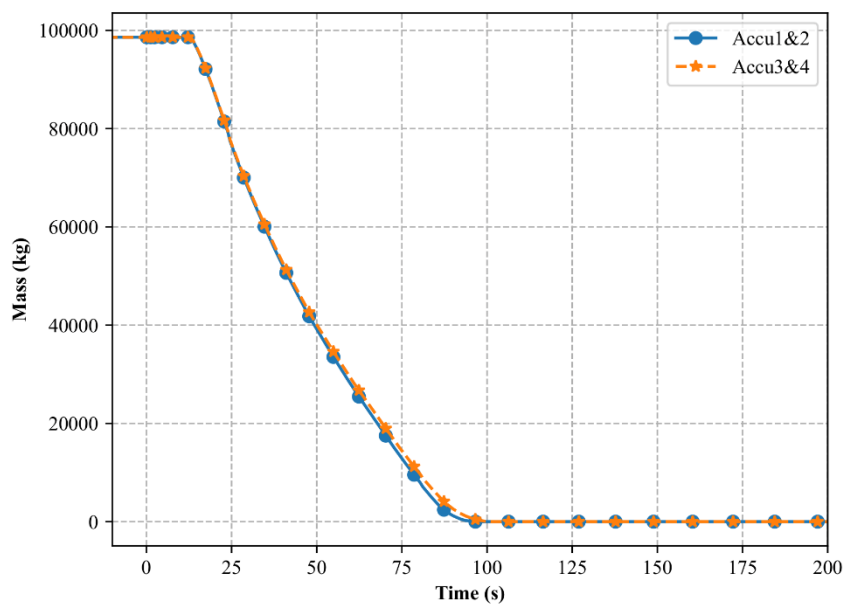


Figure B.1- 6: Calculated water inventory change in accumulators in time in case of LBLOCA on the cold leg of the pressurizer loop along with the SBO

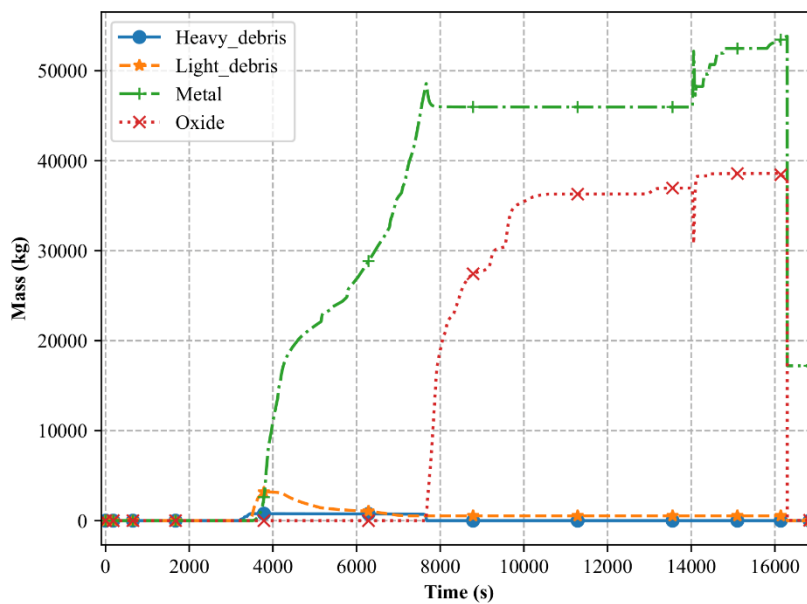


Figure B.1- 7: Calculated molten material distribution inside of the lower plenum in time in case of LBLOCA on the hot leg of the pressurizer loop along with the SBO

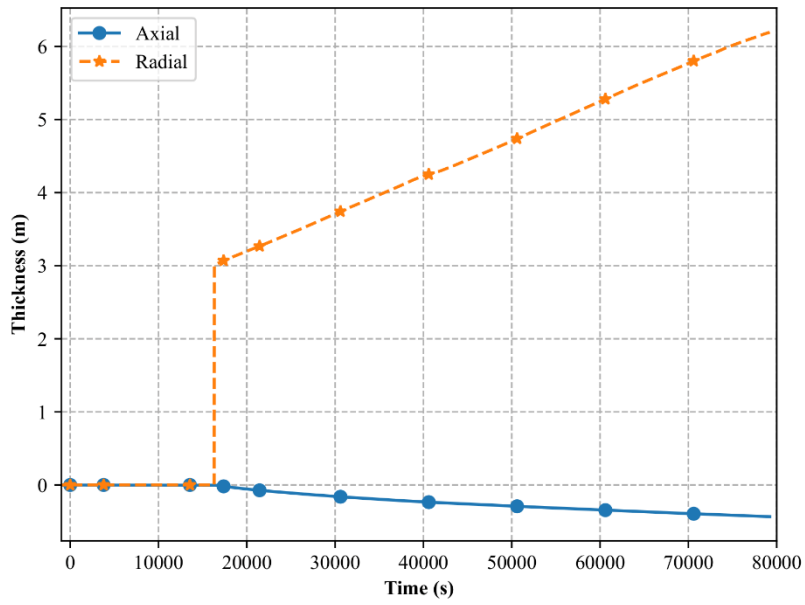


Figure B.1- 8: Calculated vertical and horizontal erosion inside of the cavity in time in case of LBLOCA on the cold leg of the pressurizer loop along with the SBO

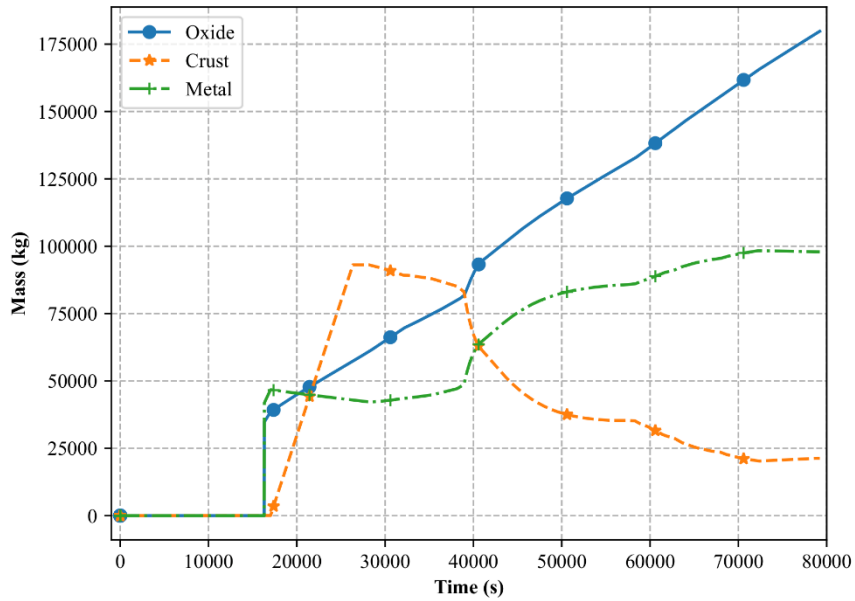


Figure B.1- 9: Mass change of layers inside of the cavity in case of LBLOCA on the cold leg of the pressurizer loop along with the SBO

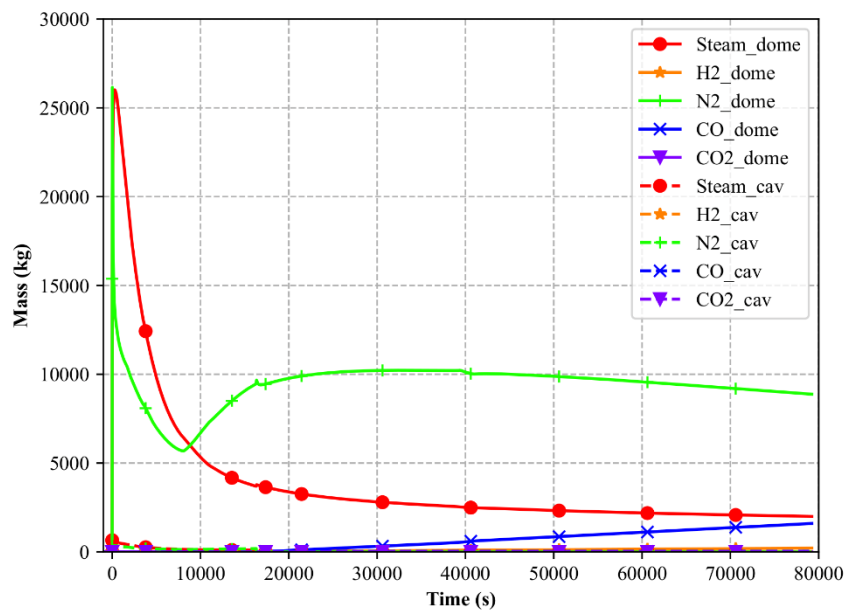


Figure B.1- 10: Calculated mass change of gases inside of the containment in case of LBLOCA on the hot leg of the pressurizer loop along with the SBO

B.2 Further results of LBLOCA on the hot leg with SBO accident

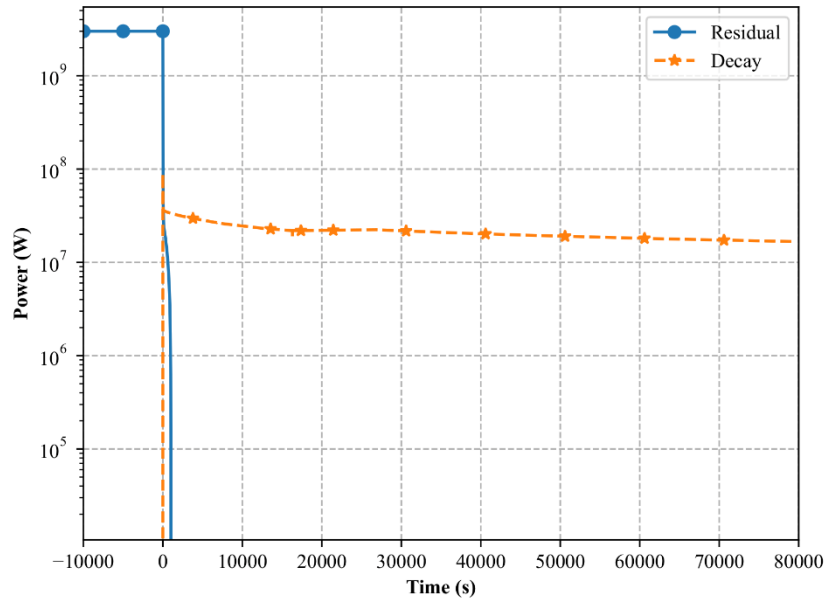


Figure B.2- 1: Power profile change in time in case of LBLOCA on the hot leg of the pressurizer loop along with the SBO

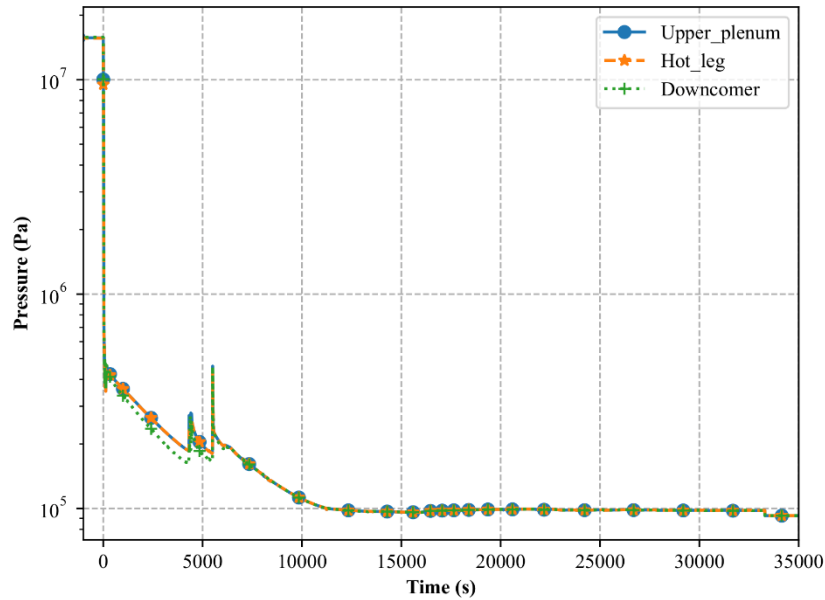


Figure B.2- 2: Pressure change inside of the primary circuit in time in case of LBLOCA on the hot leg of the pressurizer loop along with the SBO

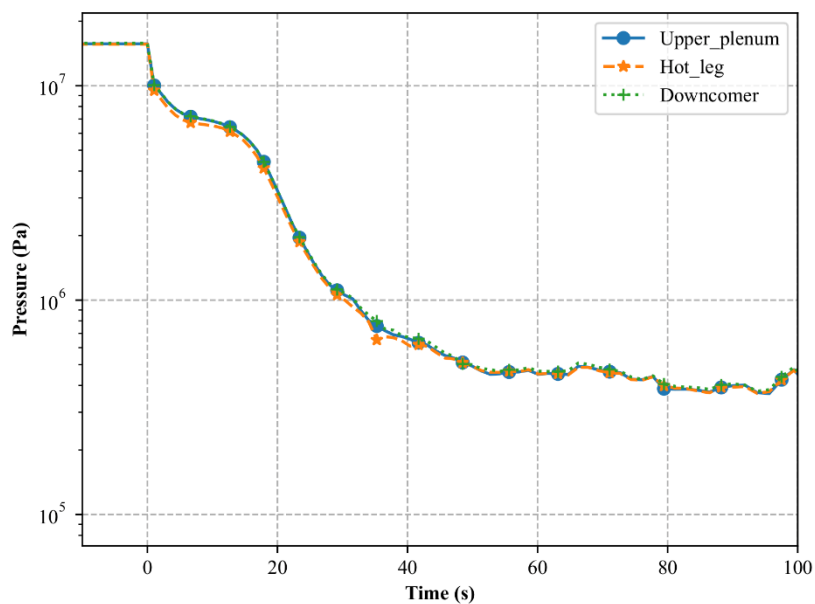


Figure B.2- 3: Pressure change inside of the primary circuit in first 100 seconds in case of LBLOCA on the hot leg of the pressurizer loop along with the SBO

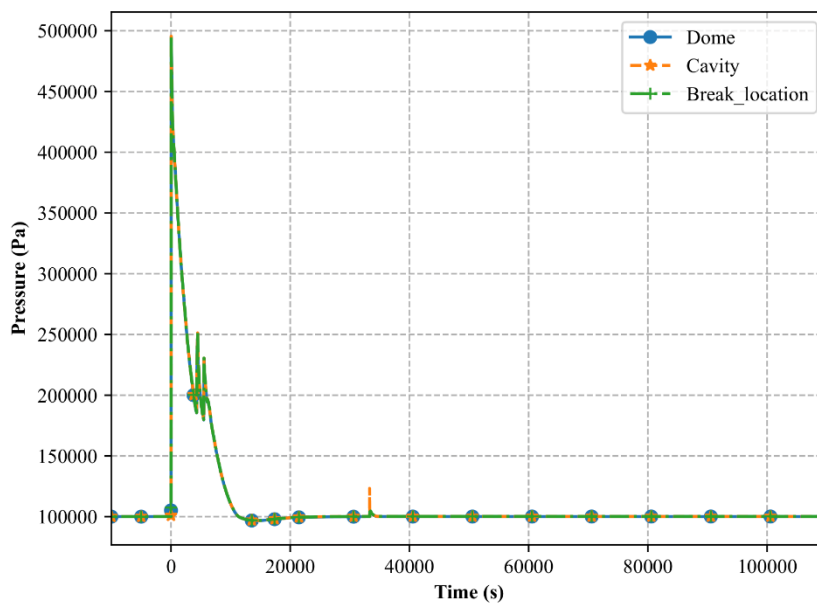


Figure B.2- 4: Pressure change inside of the containment in time in case of LBLOCA on the hot leg of the pressurizer loop along with the SBO

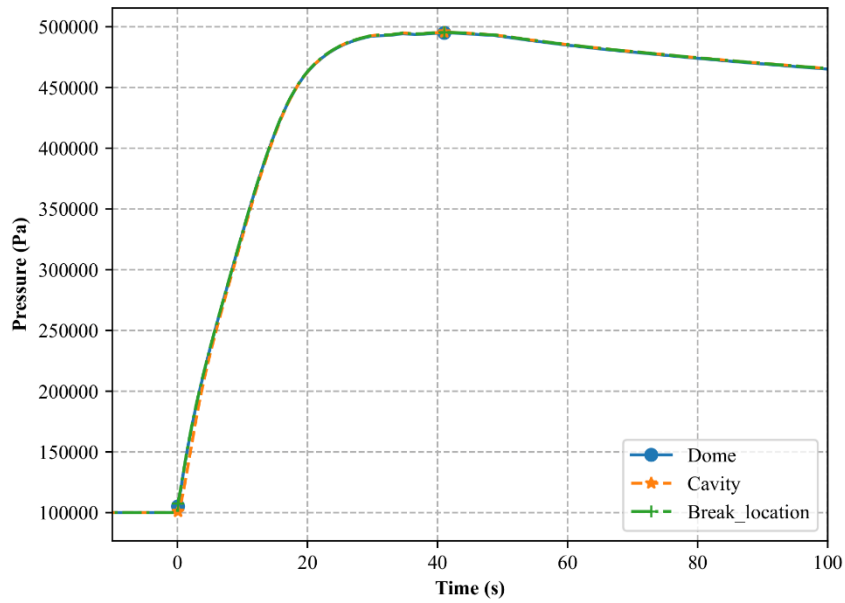


Figure B.2- 5: Pressure change inside of the containment in first 100 seconds in case of LBLOCA on the hot leg of the pressurizer loop along with the SBO

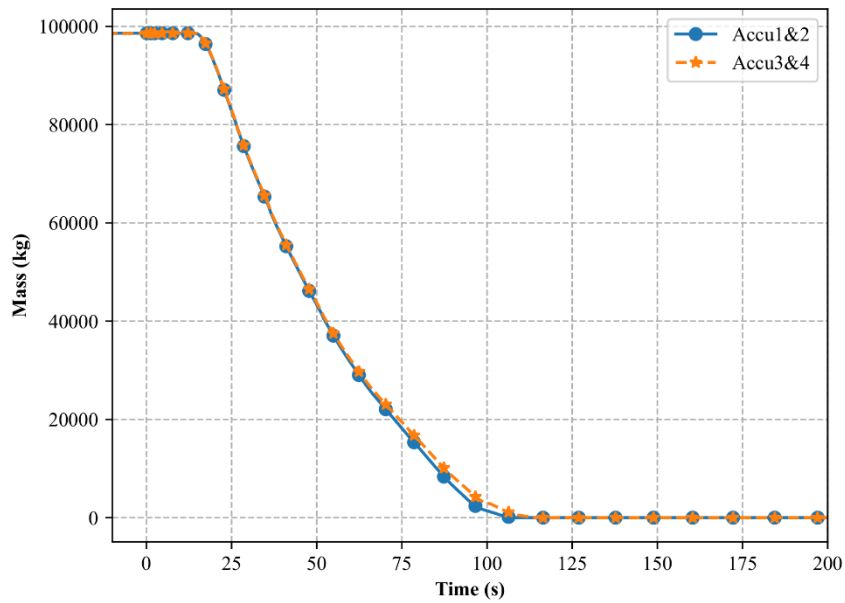


Figure B.2- 6: Water inventory change in accumulators in time in case of LBLOCA on the hot leg of the pressurizer loop along with the SBO

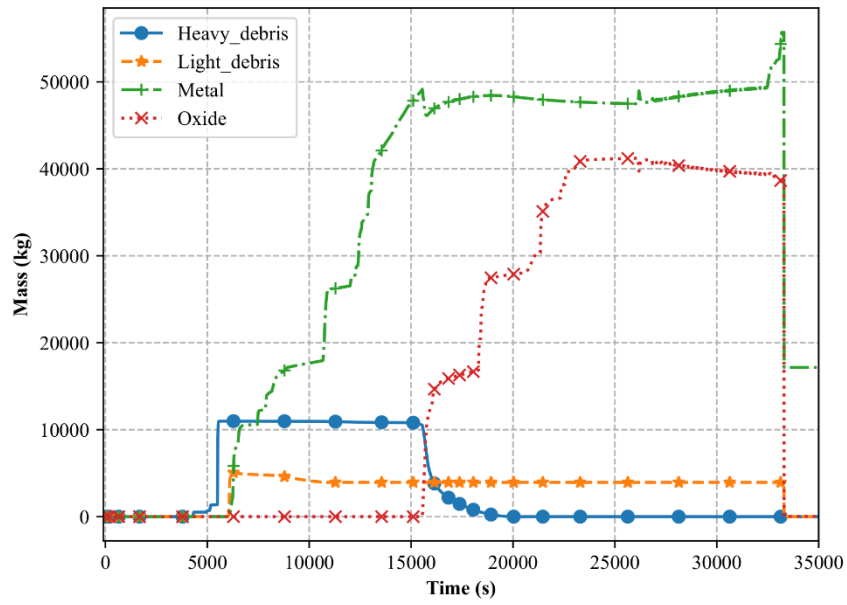


Figure B.2- 7: Molten material distribution inside of the lower plenum in time in case of LBLOCA on the hot leg of the pressurizer loop along with the SBO

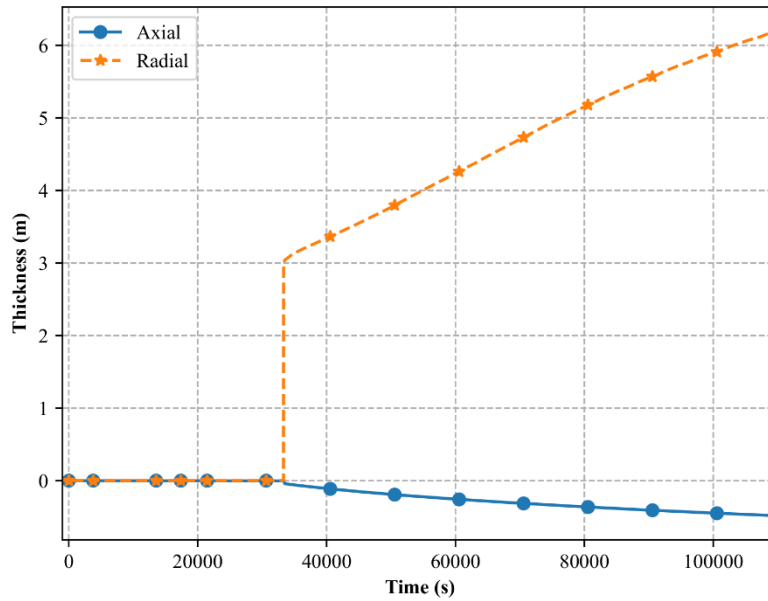


Figure B.2- 8: Vertical and horizontal erosion inside of the cavity in time in case of LBLOCA on the hot leg of the pressurizer loop along with the SBO

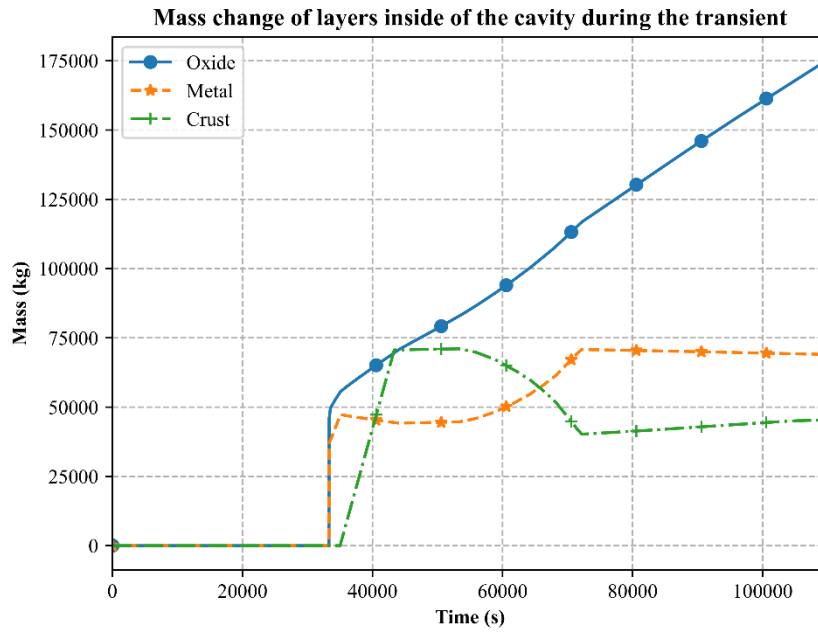


Figure B.2- 9: Mass change of layers inside of the cavity in case of LBLOCA on the hot leg of the pressurizer loop along with the SBO

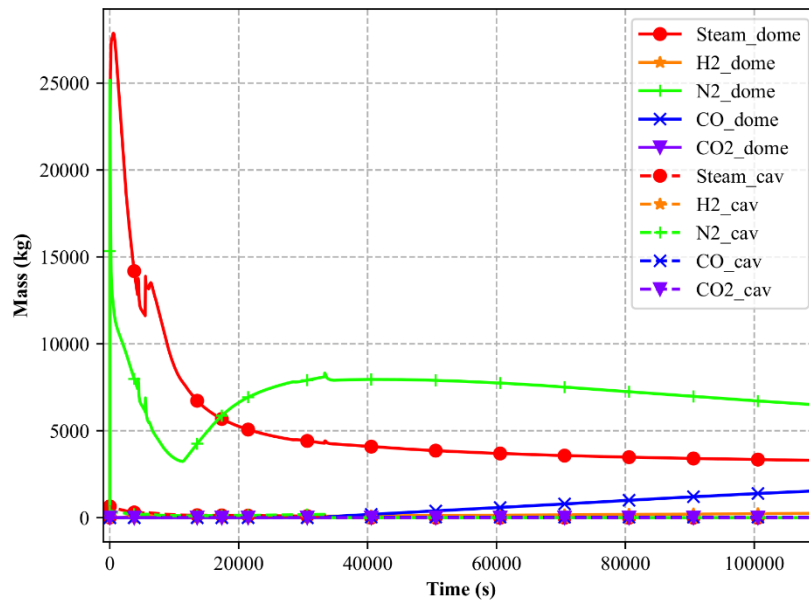


Figure B.2- 10: Mass change of gases inside of the containment in case of LBLOCA on the hot leg of the pressurizer loop along with the SBO

Appendix C Further results of radiological consequence analysis by JRODOS

Appendix C includes further results of performed JRODOS analysis for two different accident scenarios. These following results are shown in this section:

- Cloud arrival and departure times
- Deposition of Cs-137 isotope
- Deposition of iodine species
- Thyroid and effective dose from all pathways for an adult and for children after 1 year
- Lifetime thyroid and effective dose from all pathways for an adult and for children
- Activity concentration by cesium and by iodine species for grass and cow's milk
- Application of emergency response applications

C.1 Further results of the radiological consequence analysis in Kozloduy NPP with the ST estimations of the break on the cold leg with SBO

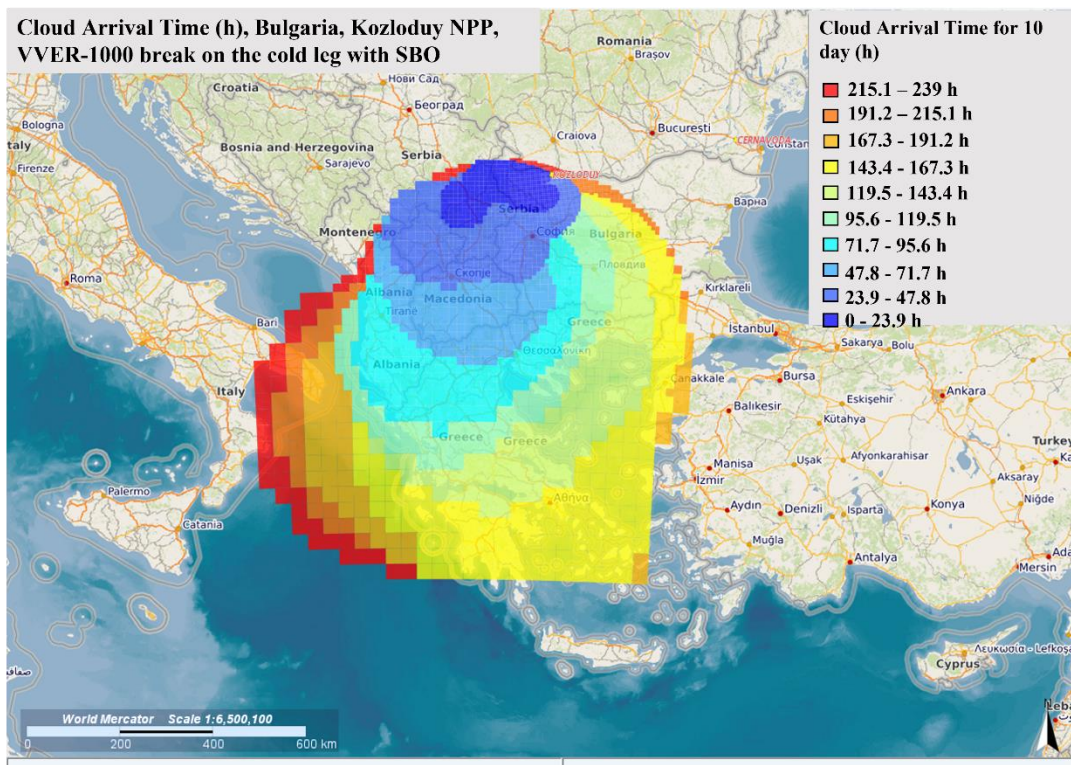


Figure C.1- 1: Simulated cloud arrival time of 10-day of dispersion on the Kozloduy NPP

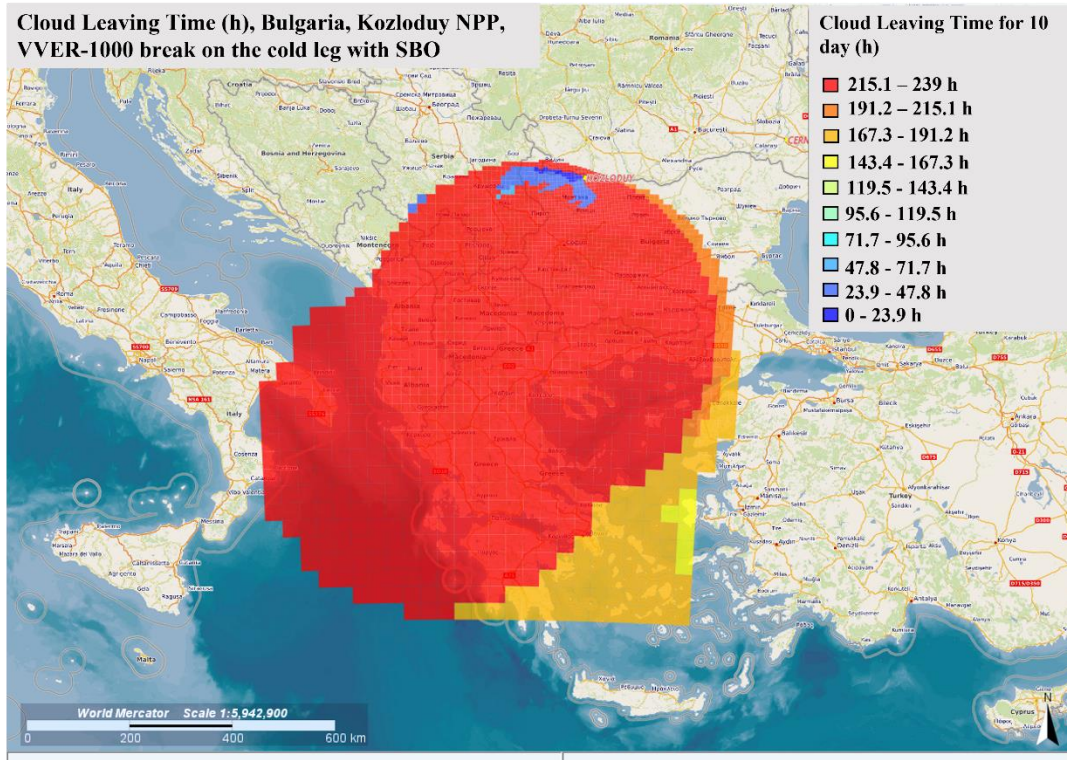


Figure C.1- 2: Simulated cloud departure time of 10-day of dispersion on the Kozloduy NPP

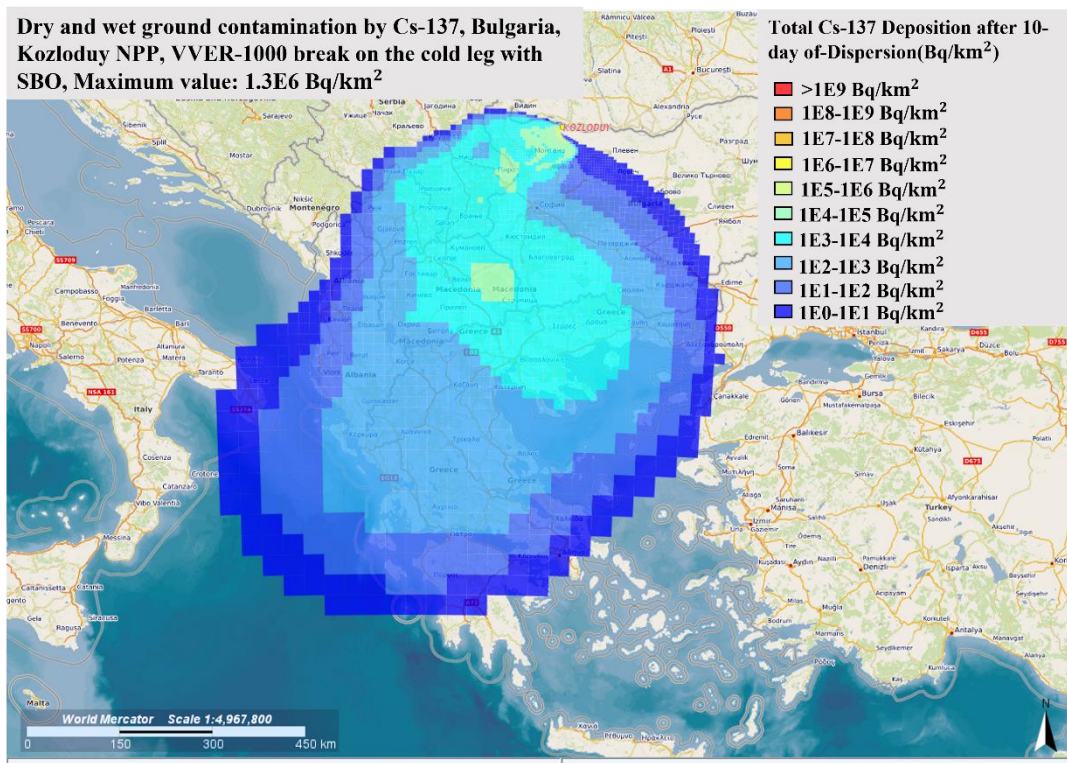


Figure C.1- 3: Simulated Cs-137 contamination over the calculation site at the end of the 10-day of radiological dispersion of ST calculated for the cold leg accident

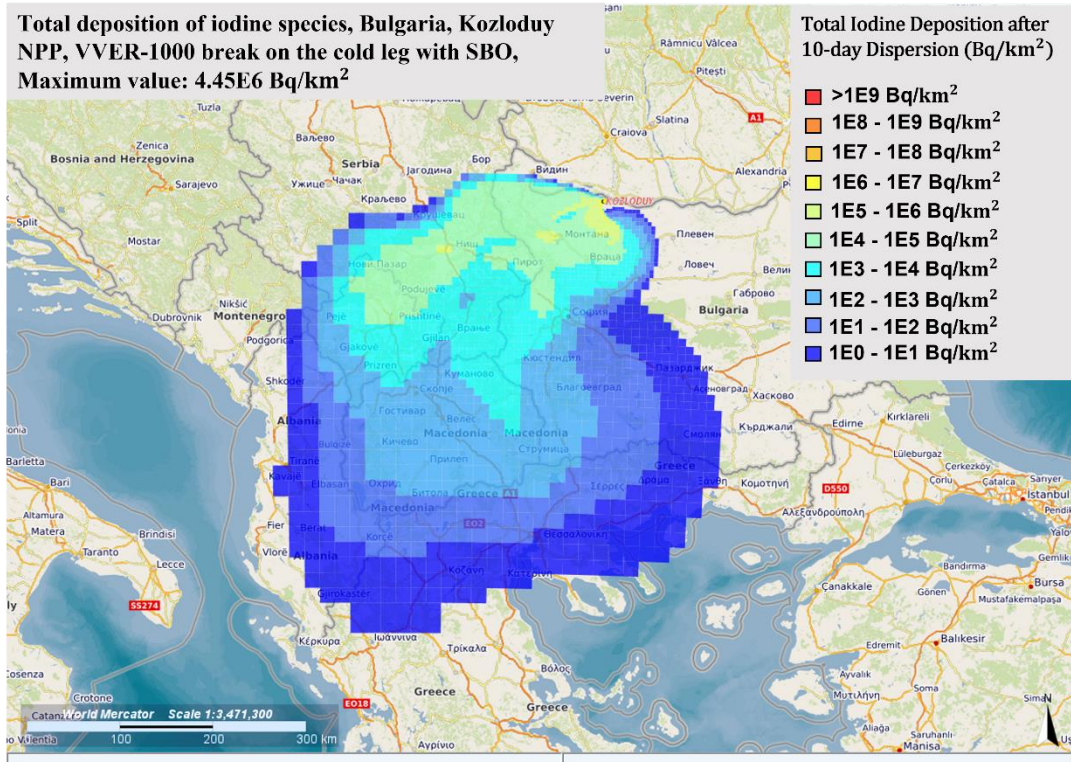


Figure C.1- 4: Simulated total iodine contamination over the calculation site at the end of the 10-day radiological dispersion of ST calculated for the cold leg accident

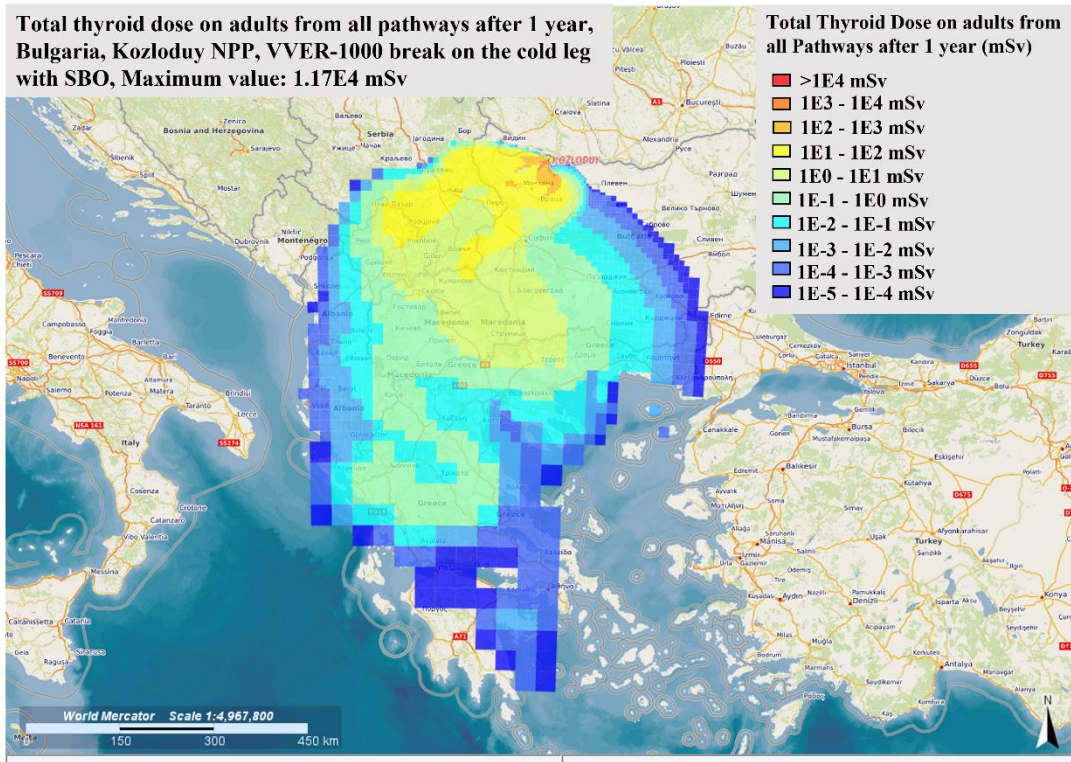


Figure C.1- 5: Simulated thyroid dose on adults by all pathways 1 year after 10-day of radiological distribution of ST calculated for a cold leg accident

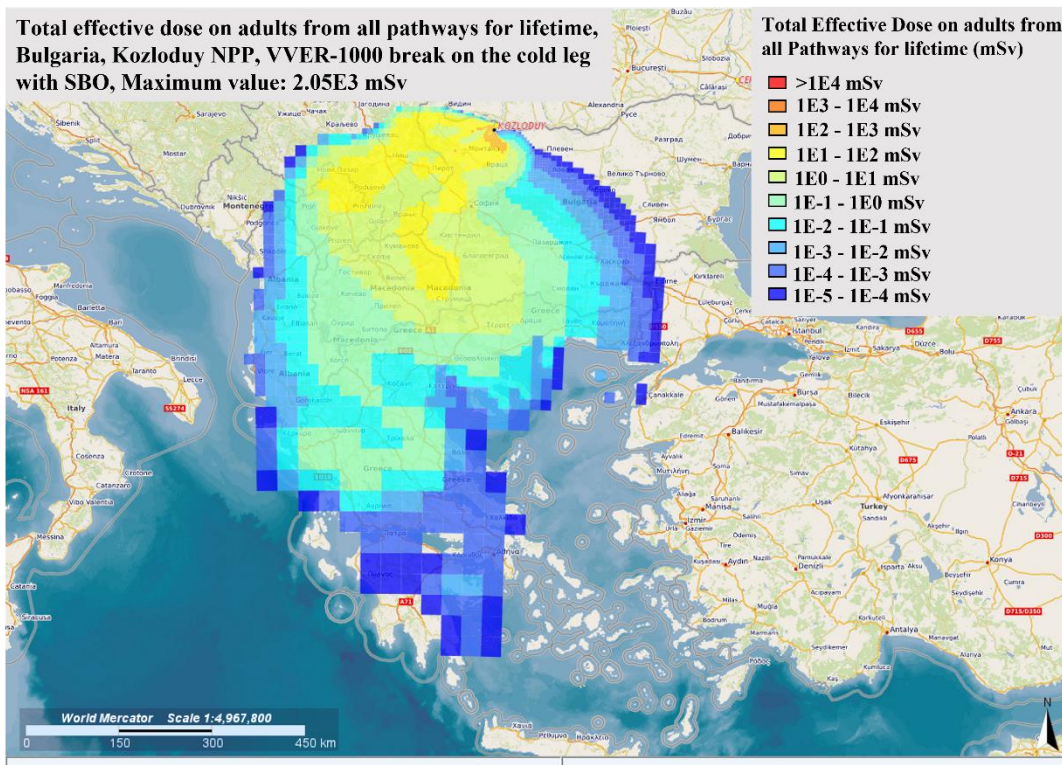


Figure C.1- 6: Calculated lifetime effective dose on adults by all pathways after 10-day of radiological distribution of ST calculated for a cold leg accident

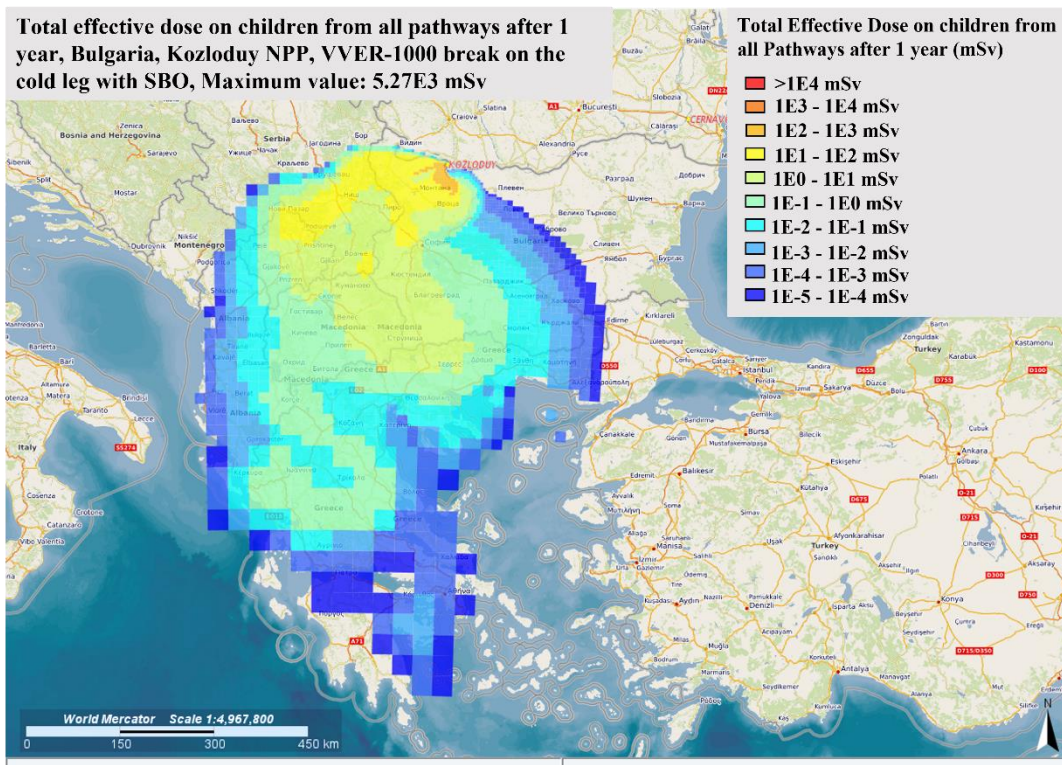


Figure C.1- 7: Simulated effective dose on children by all pathways 1 year after 10-day of radiological distribution of ST calculated for a cold leg accident

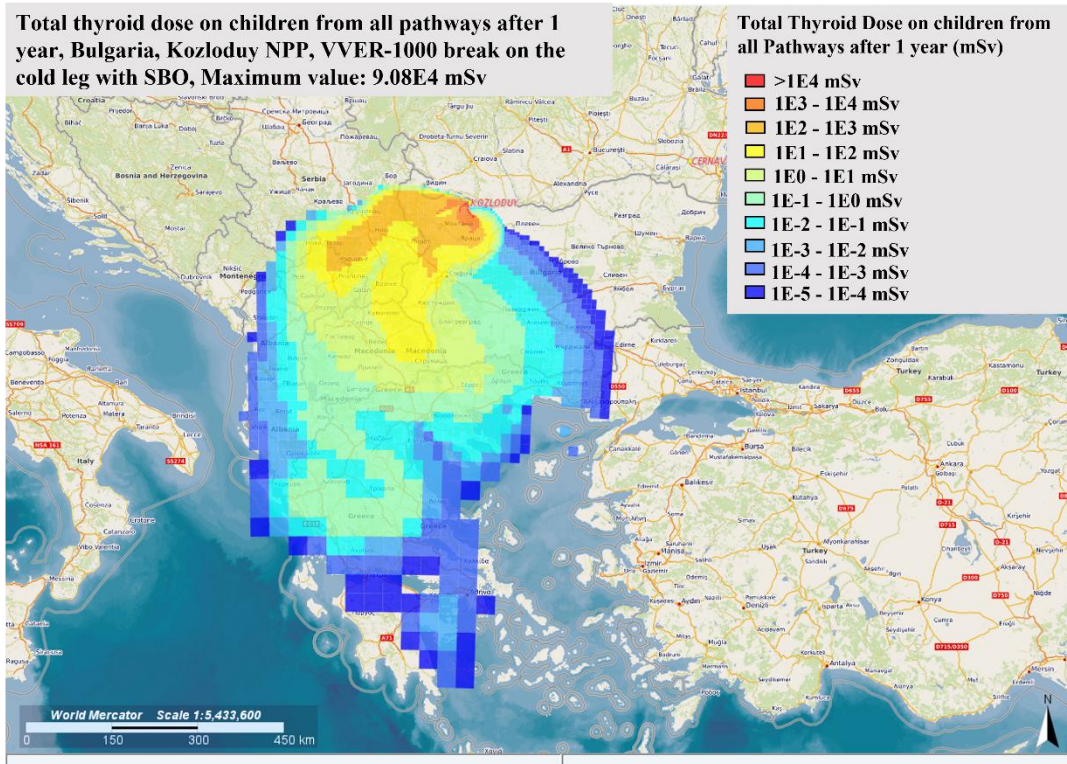


Figure C.1- 8: Simulated thyroid dose on children by all pathways 1 year after 10-day of radiological distribution of ST calculated for a cold leg accident

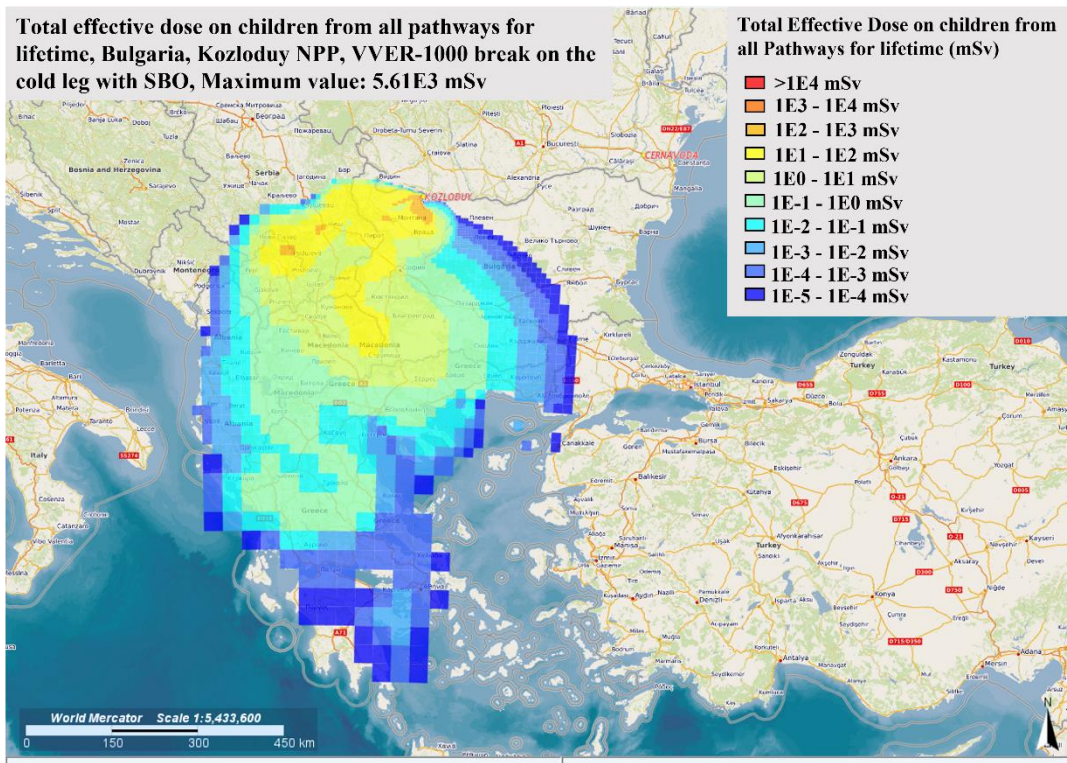


Figure C.1- 9: Simulated lifetime effective dose on children by all pathways after 10-day of radiological distribution of ST calculated for a cold leg accident

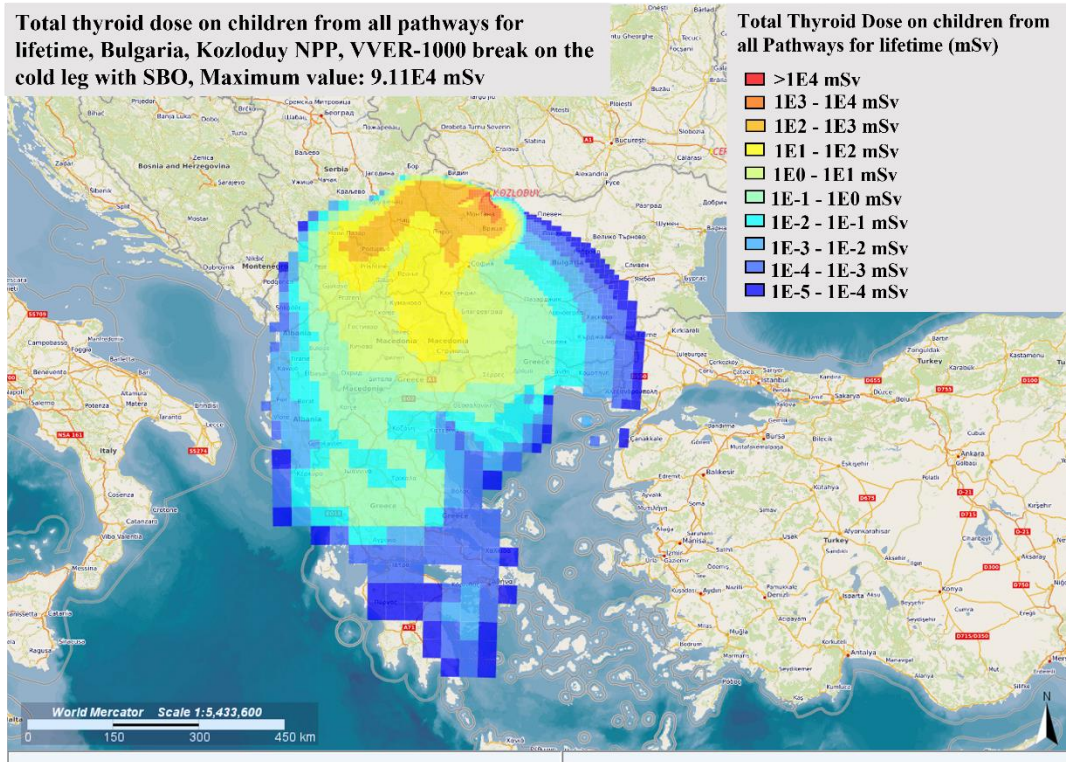


Figure C.1- 10: Simulated lifetime thyroid dose on children by all pathways after 10-day of radiological distribution of ST calculated for a cold leg accident

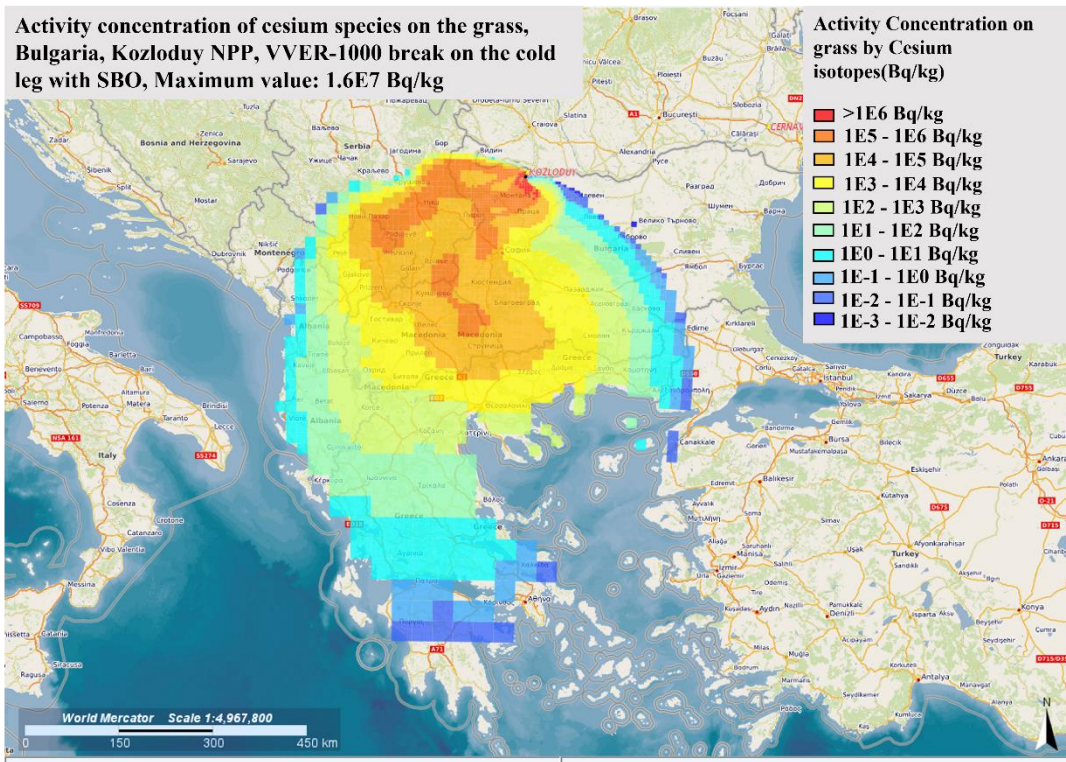


Figure C.1- 11: Simulated maximum activity of the cesium isotopes in the grass at the end of 10th day of radiological dispersion for the cold leg accident case

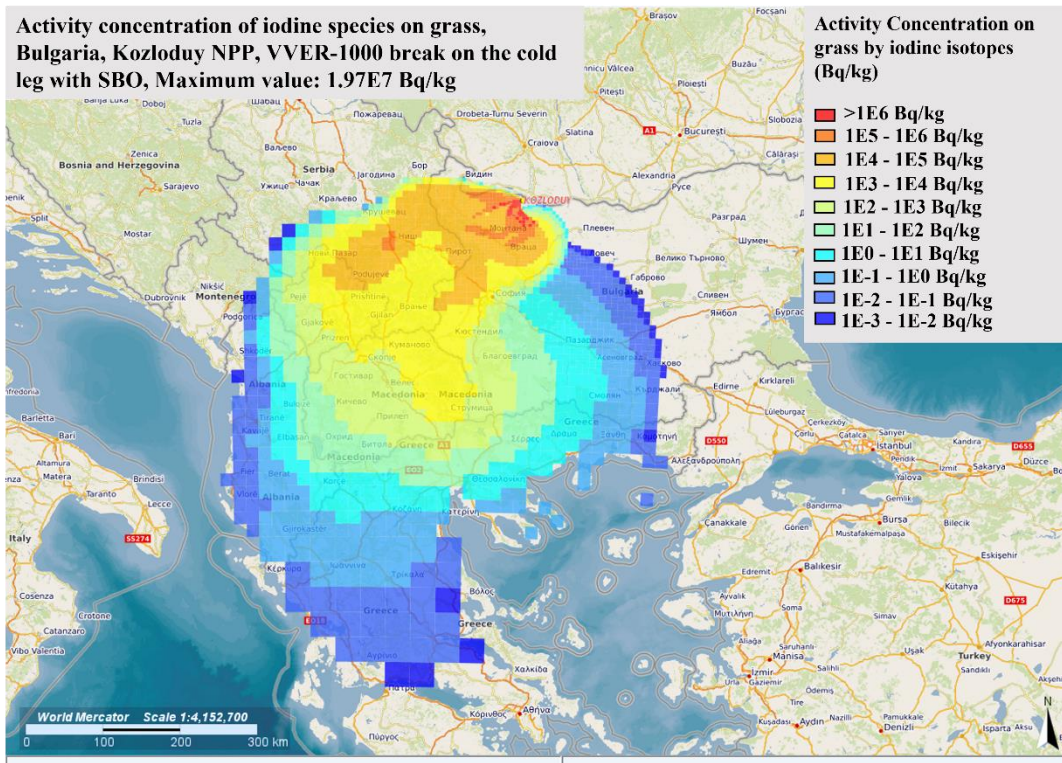


Figure C.1- 12: Simulated maximum activity of the iodine isotopes in the grass at the end of 10th day of radiological dispersion for the cold leg accident case

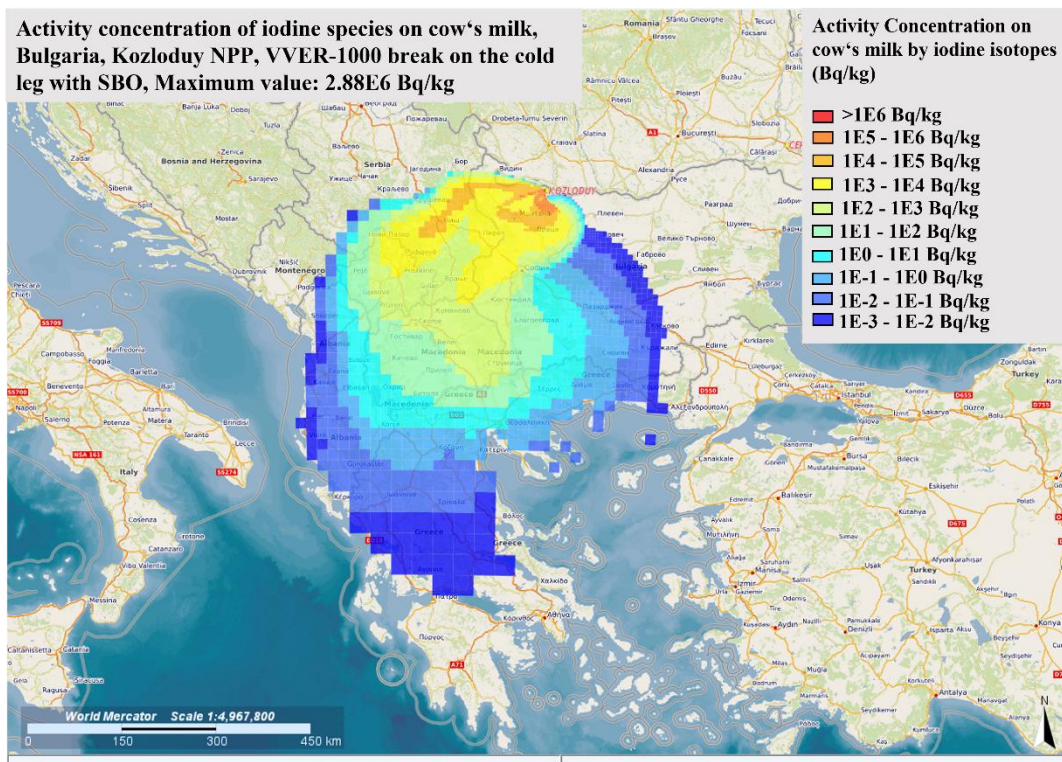


Figure C.1- 13: Simulated maximum activity of the iodine isotopes in the cow's milk at the end of 10th day of radiological dispersion for the cold leg accident case

C.2 Further results of the radiological consequence analysis in Akkuyu NNP with the ST estimations of the break on the hot leg with SBO

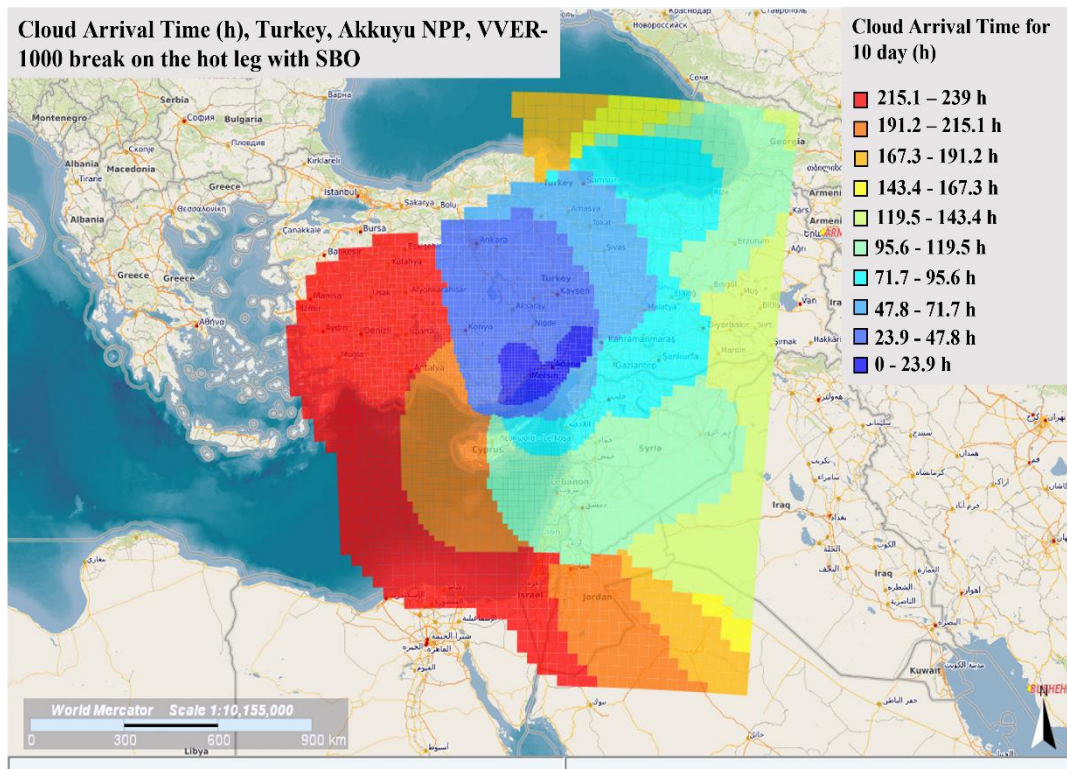


Figure C.2- 1: Cloud arrival time of 10-day of dispersion on the Akkuyu NPP

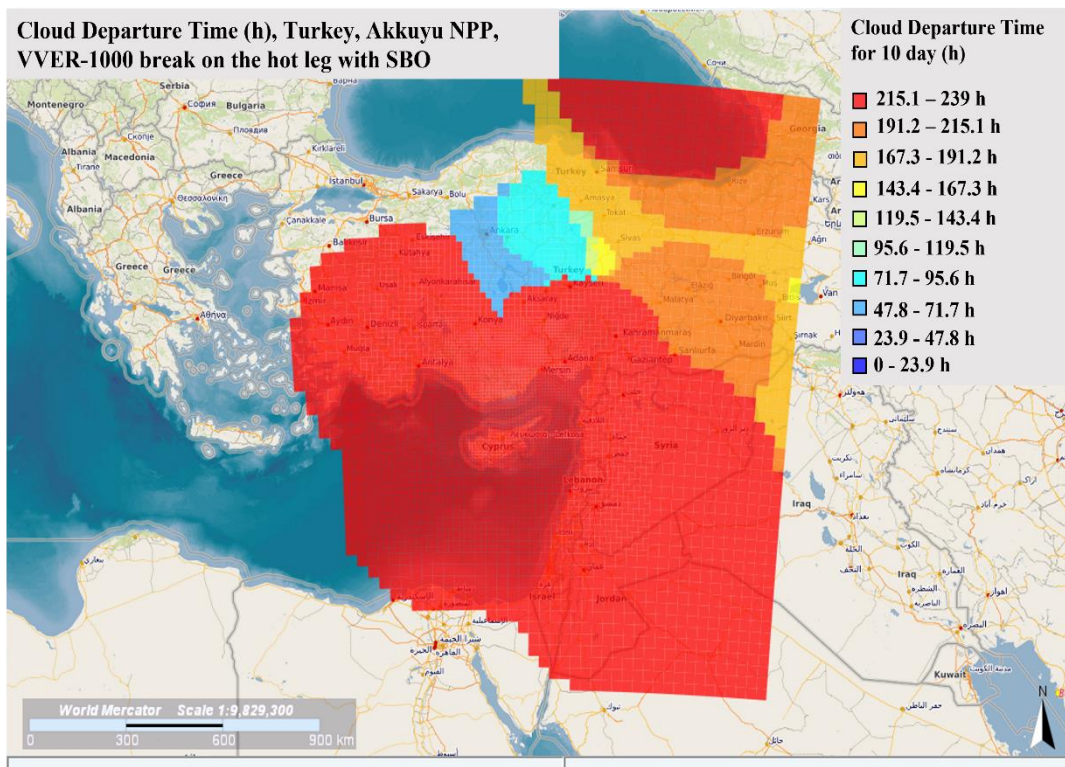


Figure C.2- 2: Cloud leaving time of 10-day of dispersion on the Akkuyu NPP

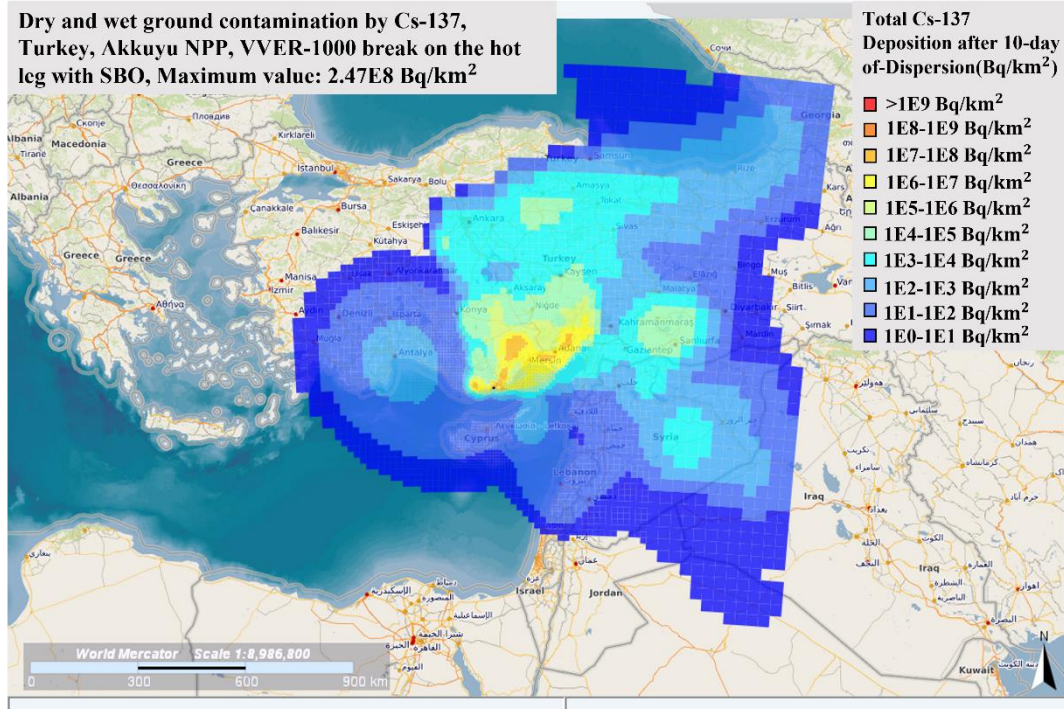


Figure C.2- 3: Simulated Cs-137 contamination over the calculation site at the end of the 10-day of radiological dispersion of ST calculated for the hot leg accident

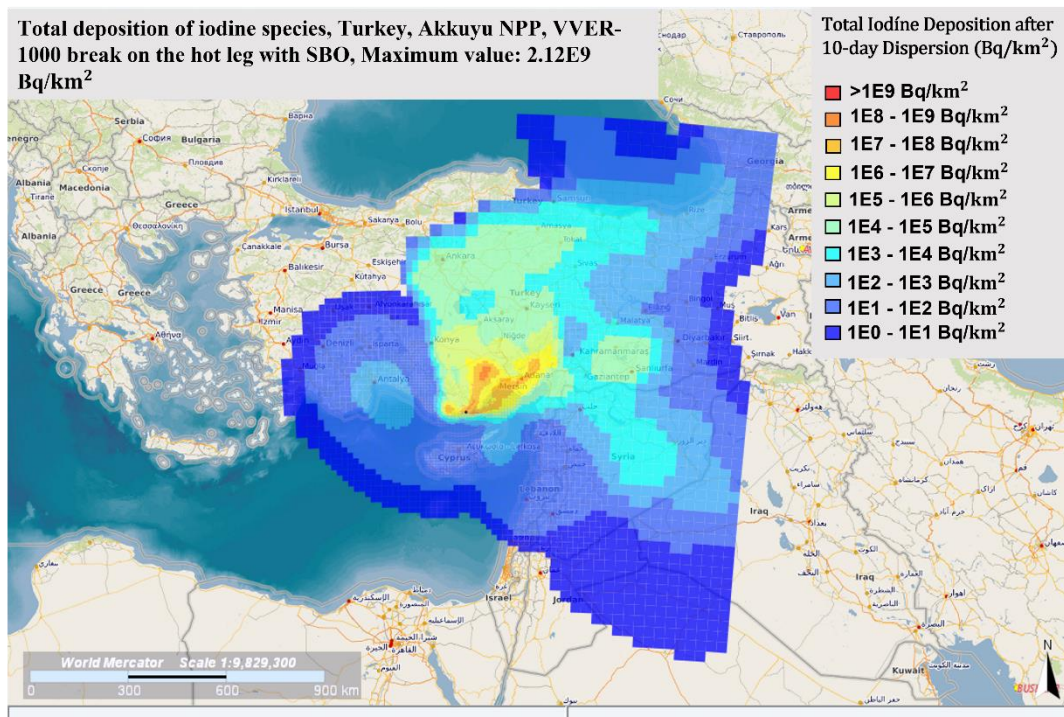


Figure C.2- 4: Simulated total iodine contamination over the calculation site at the end of the 10-day radiological dispersion of ST calculated for the hot leg accident

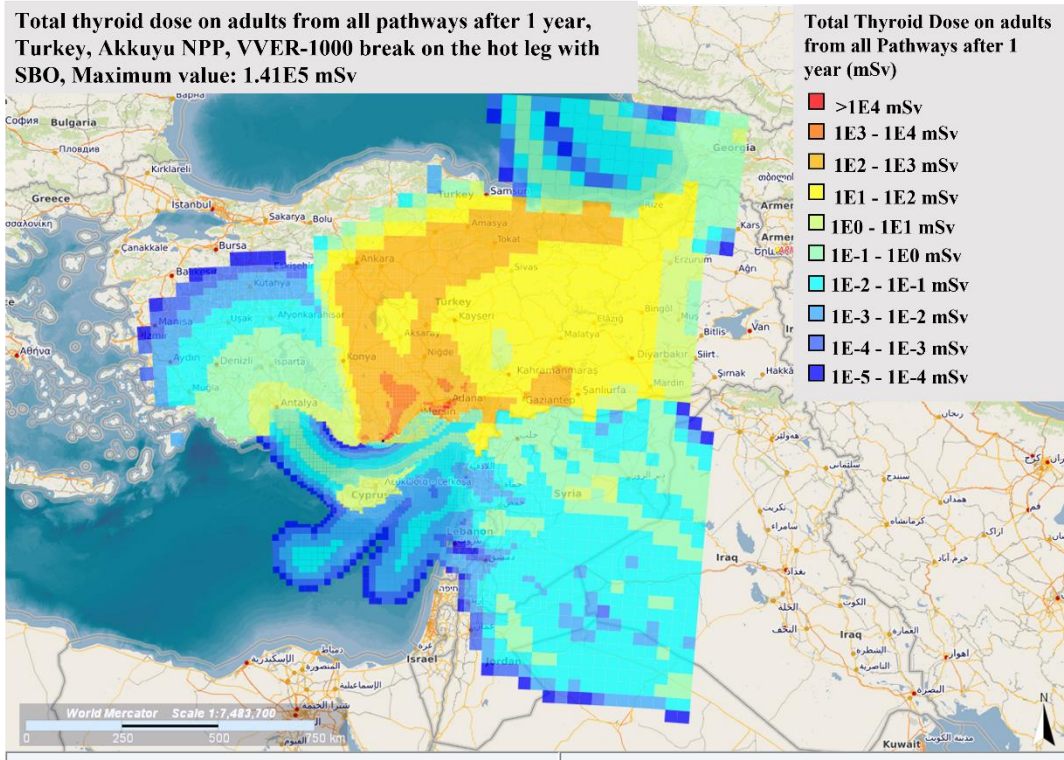


Figure C.2- 5: Simulated thyroid dose on adults by all pathways 1 year after 10-day of radiological distribution of ST calculated for a hot leg accident

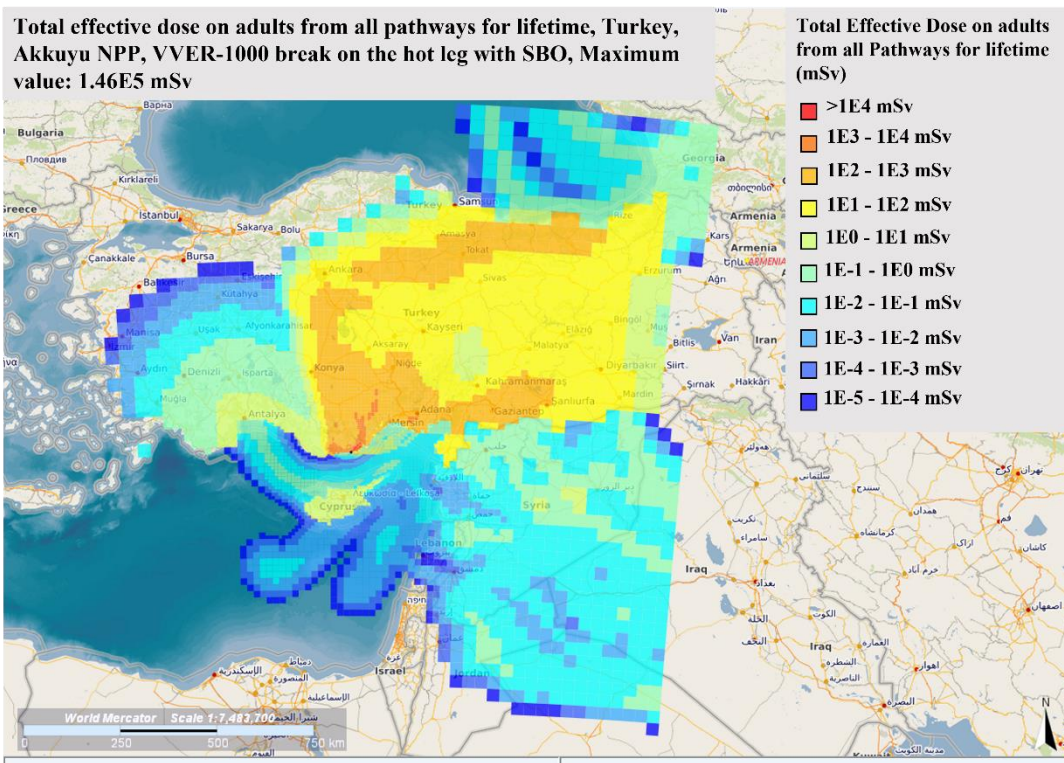


Figure C.2- 6: Simulated lifetime effective dose on adults by all pathways after 10-day of radiological distribution of ST calculated for a hot leg accident

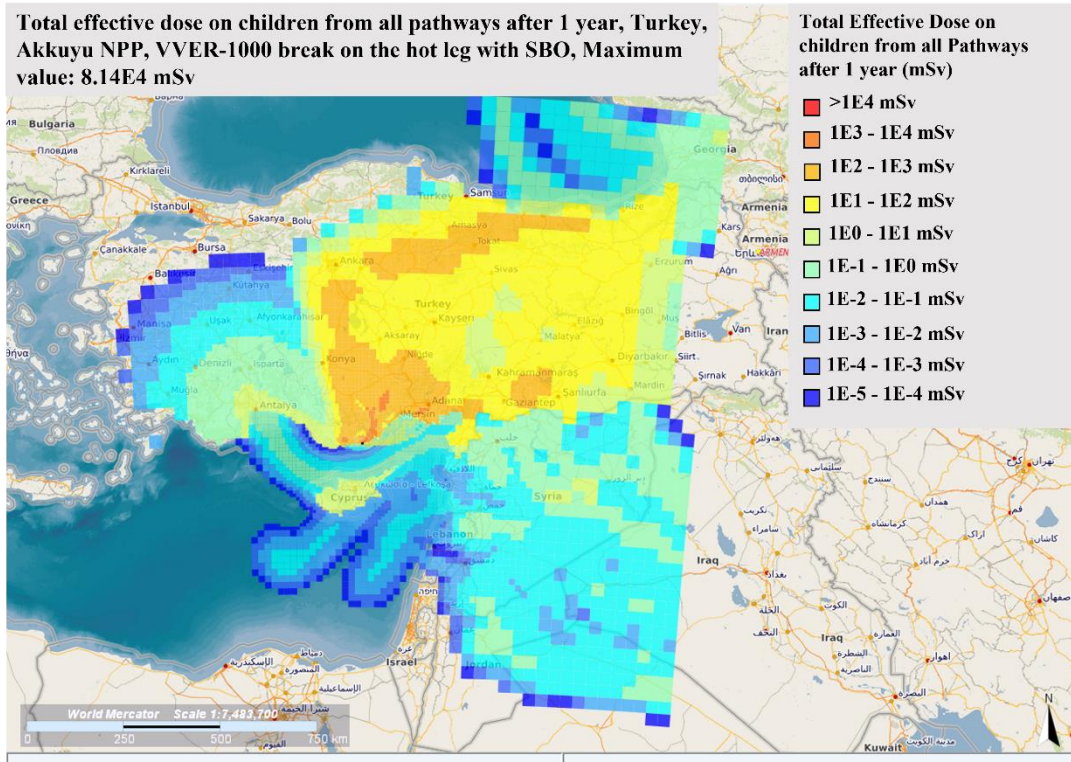


Figure C.2- 7: Simulated effective dose on children by all pathways 1 year after 10-day of radiological distribution of ST calculated for a hot leg accident

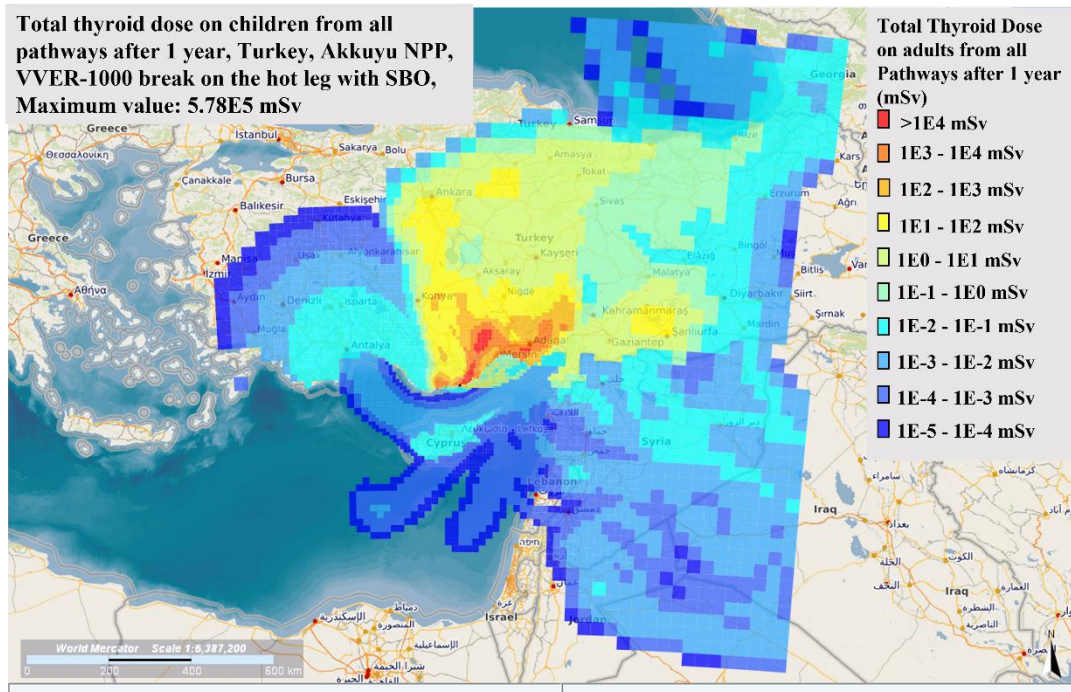


Figure C.2- 8: Simulated thyroid dose on children by all pathways 1 year after 10-day of radiological distribution of ST calculated for a hot leg accident

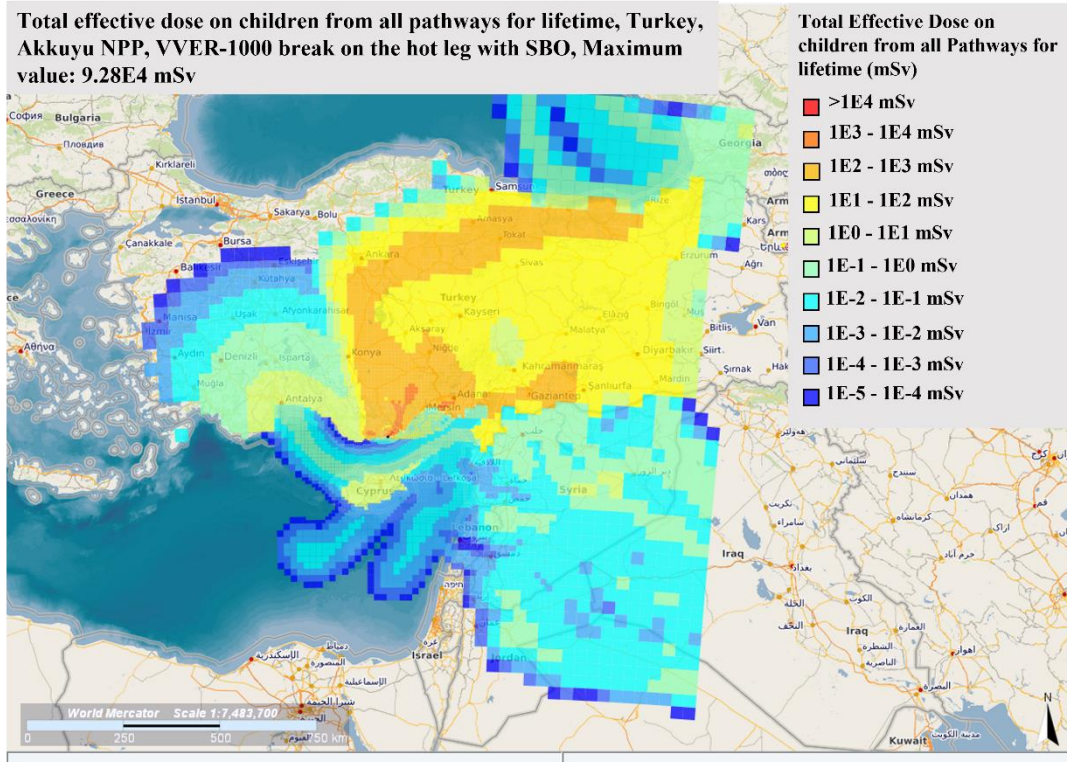


Figure C.2- 9: Simulated lifetime effective dose on children by all pathways after 10-day of radiological distribution of ST calculated for a hot leg accident

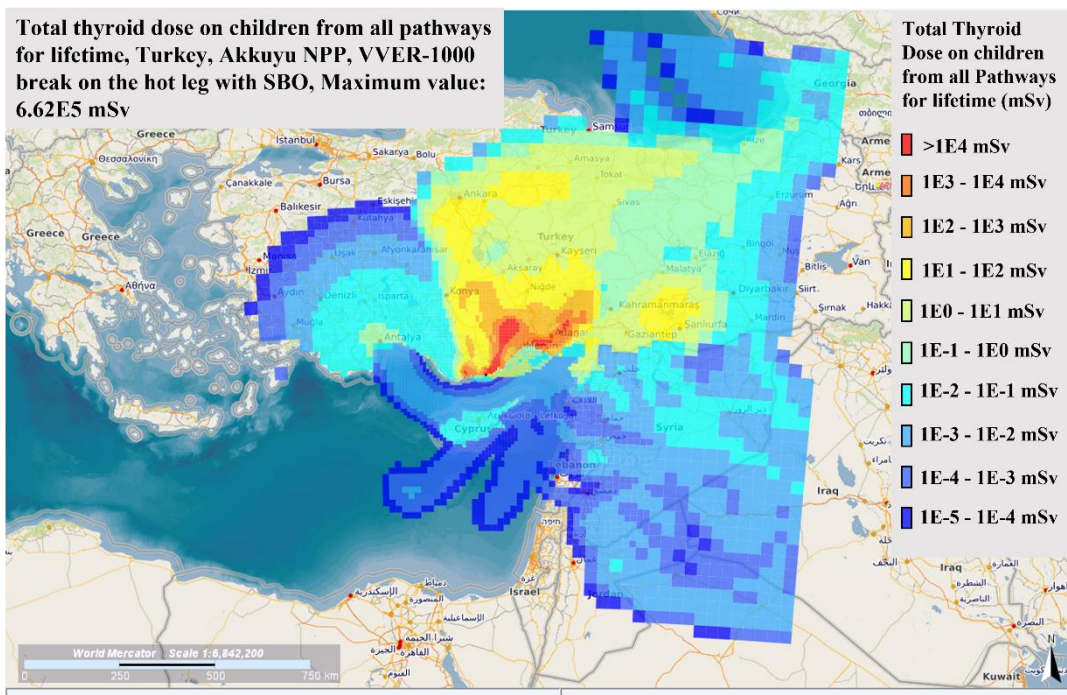


Figure C.2- 10: Simulated lifetime thyroid dose on children by all pathways after 10-day of radiological distribution of ST calculated for a hot leg accident

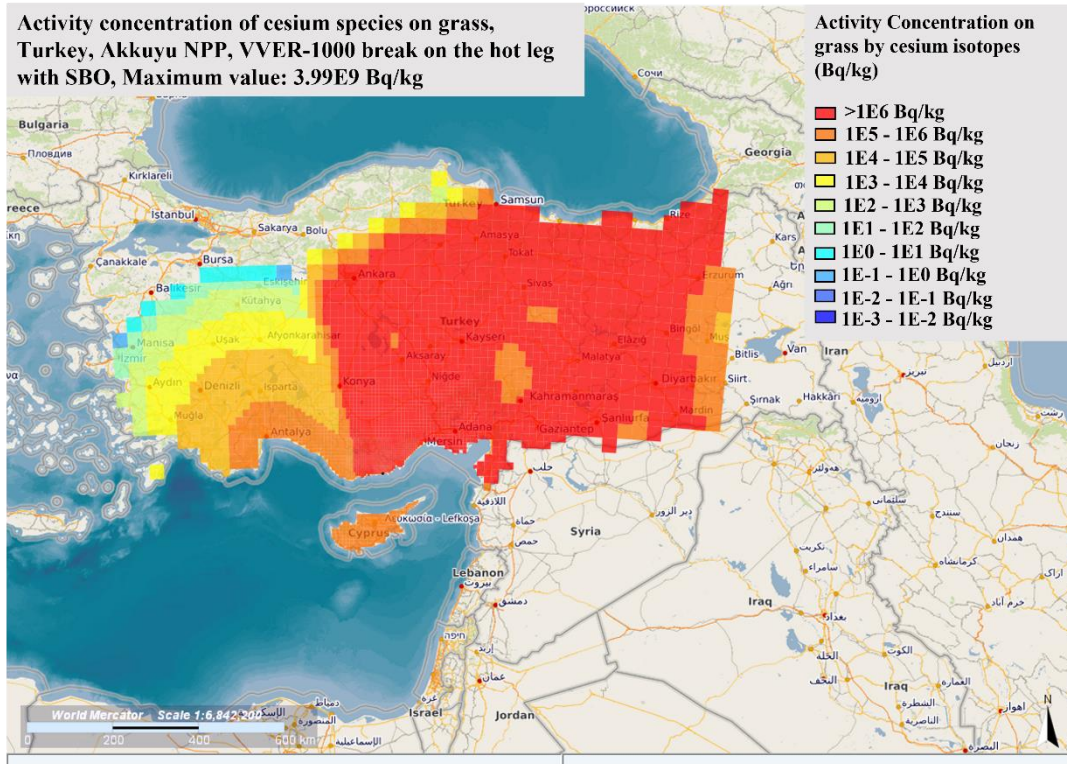


Figure C.2- 11: Simulated maximum activity of the cesium isotopes in the grass at the end of 10th day of radiological dispersion for the hot leg accident case

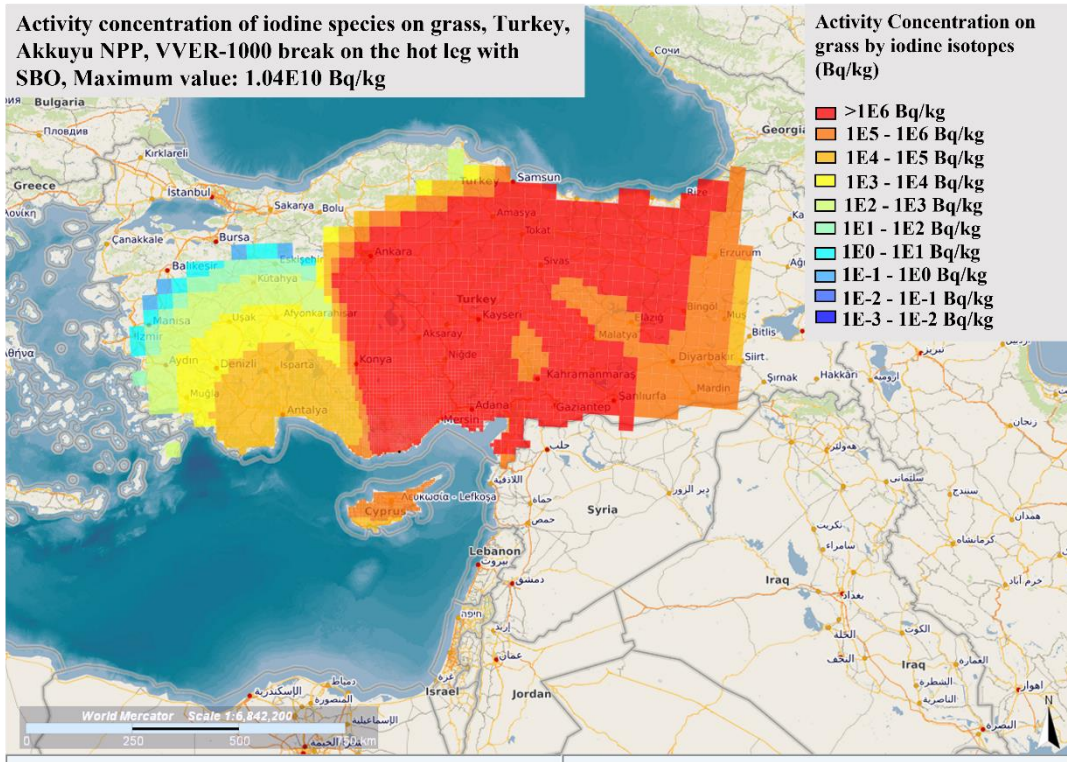


Figure C.2- 12: Maximum activity of the iodine isotopes in the grass at the end of 10th day of radiological dispersion for the hot leg accident case

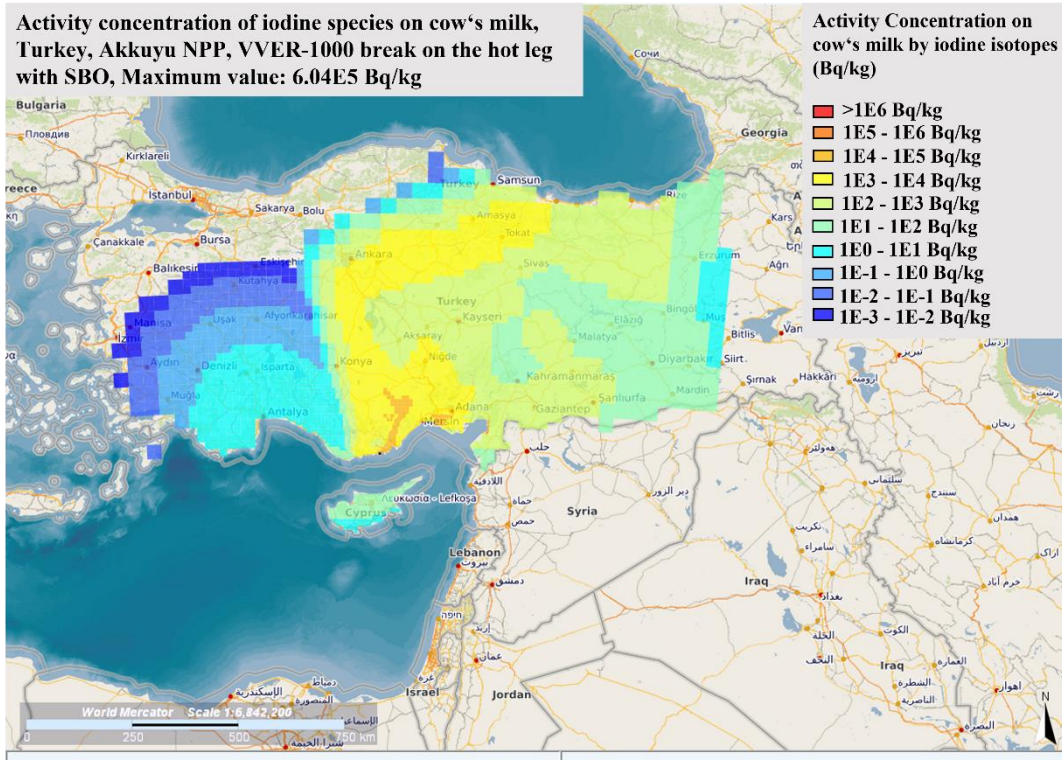


Figure C.2- 13: Simulated maximum activity of the iodine isotopes in the cow's milk at the end of 10th day of radiological dispersion for the hot leg accident case

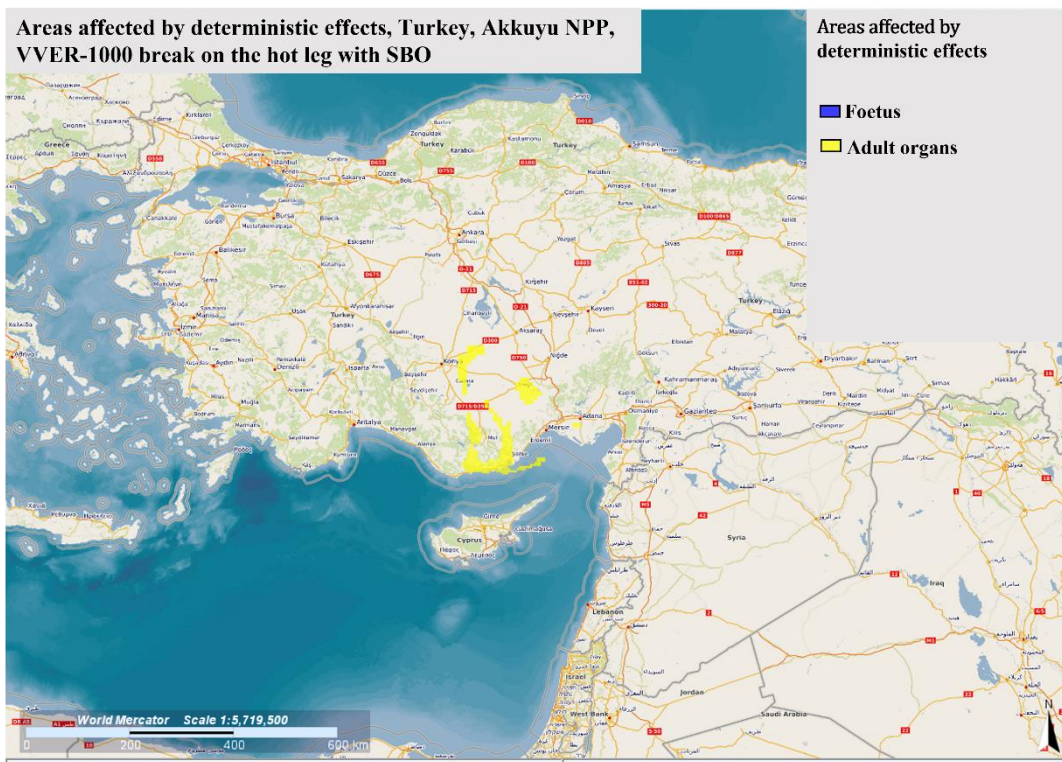


Figure C.2- 14: Simulated deterministic effect on foetus and adult organs at the end of 10th day of radiological dispersion for the hot leg accident case



Figure C.2- 15: Simulated sheltered regions as early emergency applications at the end of 10th day of radiological dispersion for the hot leg accident case



Figure C.2- 16: Simulated evacuated regions as early emergency applications at the end of 10th day of radiological dispersion for the hot leg accident case

Severe accident investigations for VVER-Reactors including Radiological Impact and the Quantification of Uncertainties



Figure C.2- 17: Simulated temporarily relocated regions as early emergency applications at the end of 10th day of radiological dispersion for the hot leg accident case

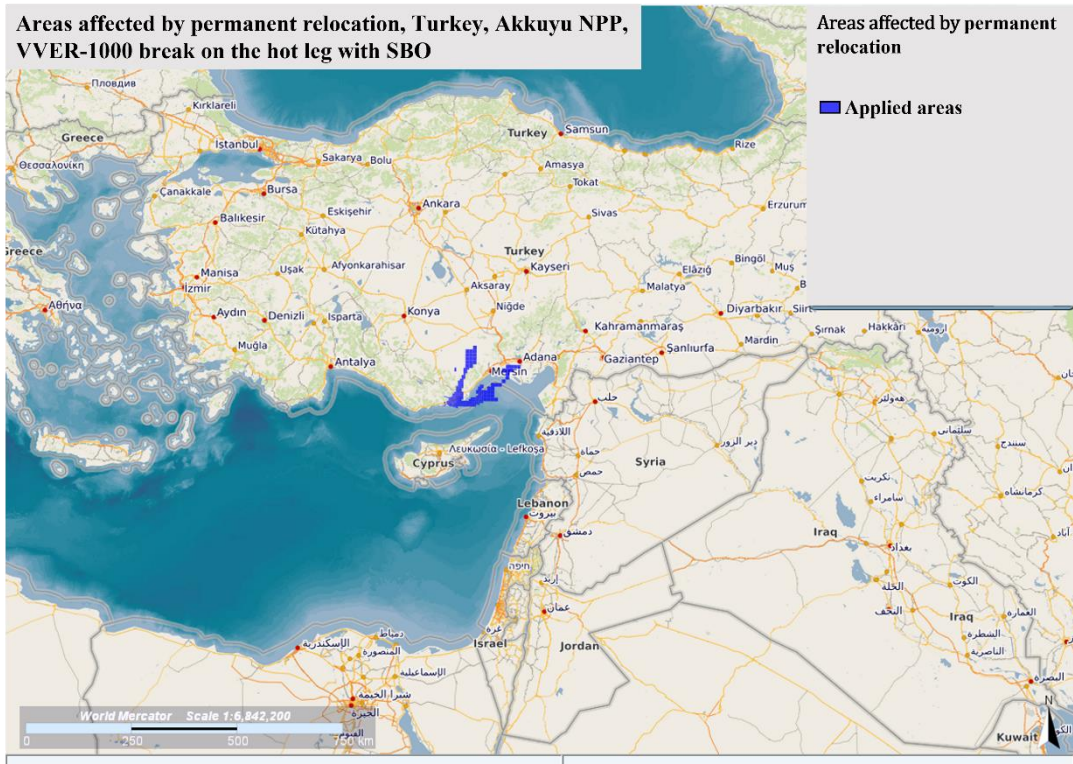


Figure C.2- 18: Simulated permanently relocated regions as early emergency applications at the end of 10th day of radiological dispersion for the hot leg accident case

Severe accident investigations for VVER-Reactors including Radiological Impact and the Quantification of Uncertainties

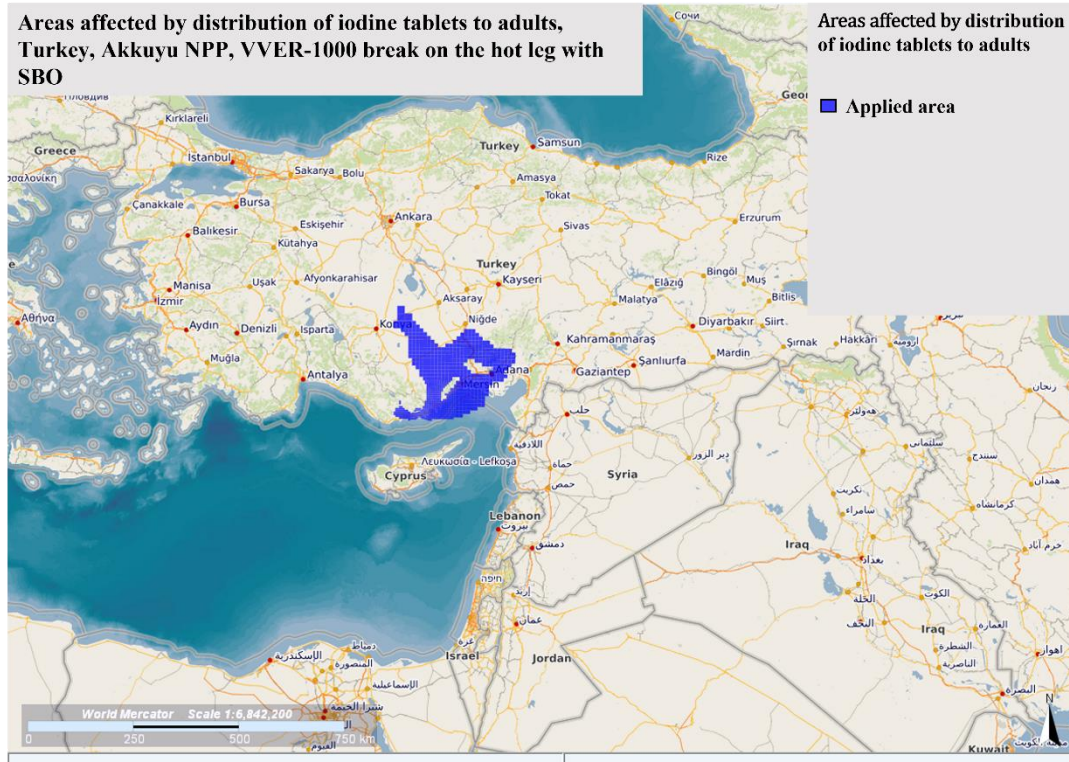


Figure C.2- 19: Simulated distribution of iodine tablets to the adults as early emergency applications at the end of 10th day of radiological dispersion for the hot leg accident case

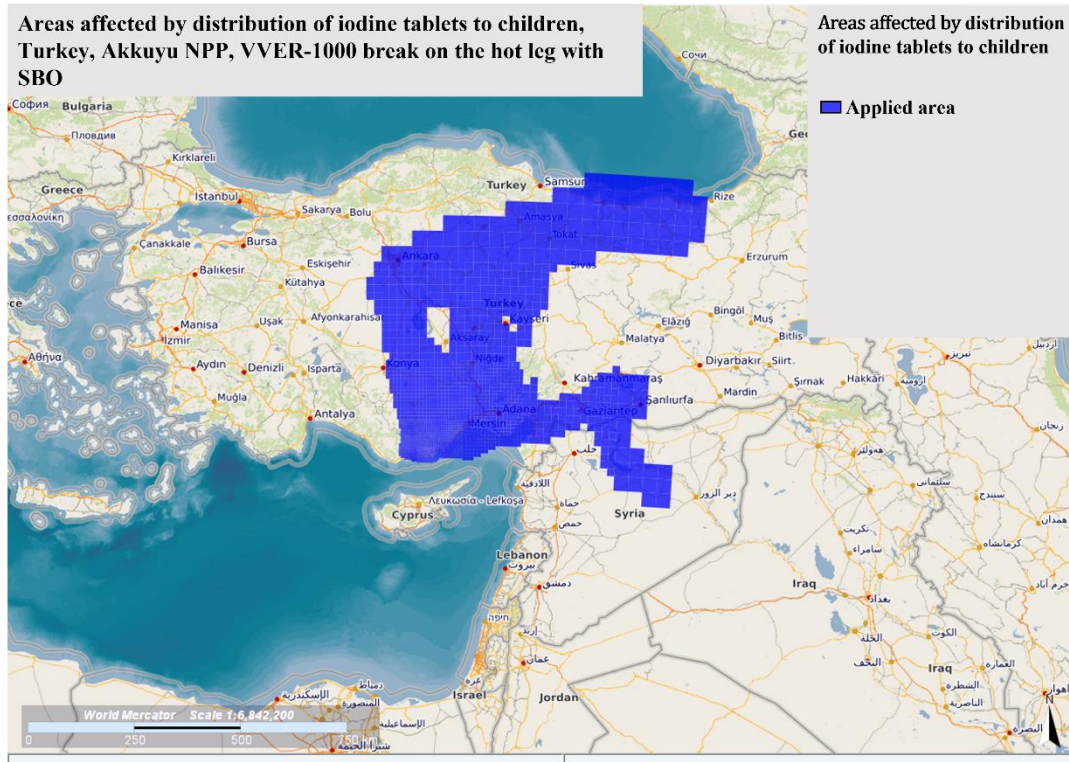


Figure C.2- 20: Simulated distribution of iodine tablets to the children as early emergency applications at the end of 10th day of radiological dispersion for the hot leg accident case

Appendix D Further results of the uncertainty quantification and sensitivity analysis by KATUSA and comparison of radiological consequences

Appendix D covers further results of the performed uncertainty quantification and sensitivity analysis. Additionally, additional results of the comparison of radiological consequences performed by using JRODOS with best-estimate and worst-case inventories is demonstrated. Following figures are shown:

- Uncertainty over the key results
- Sensitivity of selected uncertain parameters over the key results
- Acute effective dose comparison in Zaporizhzhia NPP
- Effective dose after 1 year comparison in Zaporizhzhia NPP

D.1 Further results of the uncertainty quantification and sensitivity analysis of the break on the cold leg with SBO

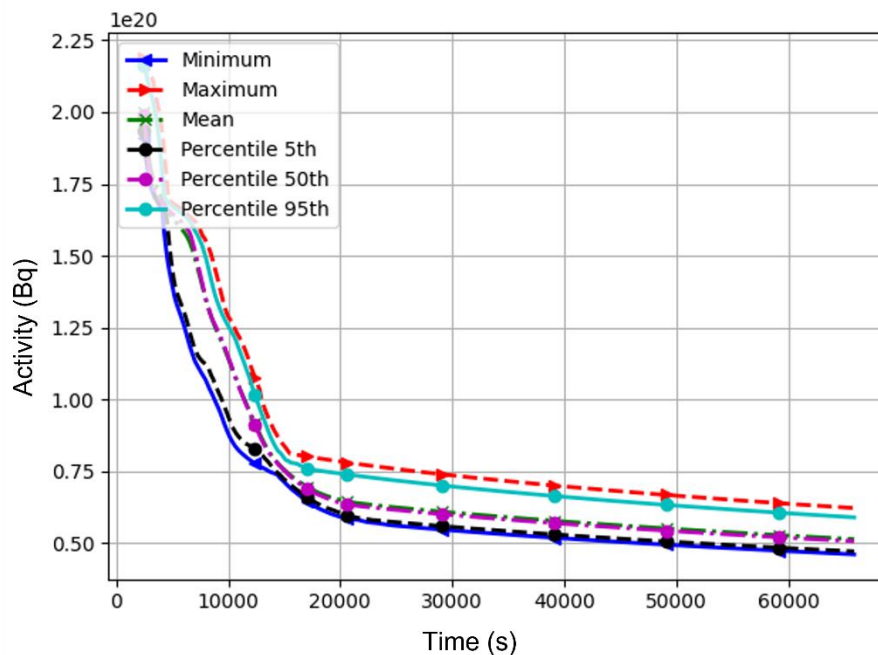


Figure D.1- 1_ Calculated minimum, maximum, mean and most probable values of activity released from the vessel in case of LBLOCA on the cold leg of the pressurizer loop along with the SBO

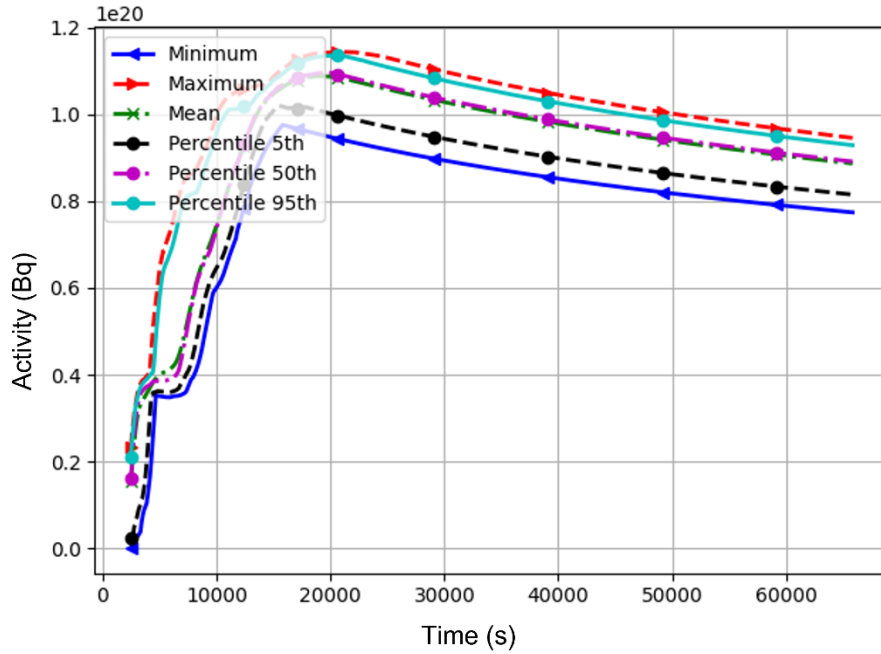


Figure D.1- 2: Calculated minimum, maximum, mean and most probable values of activity transported to the primary circuit in case of LBLOCA on the cold leg of the pressurizer loop along with the SBO.

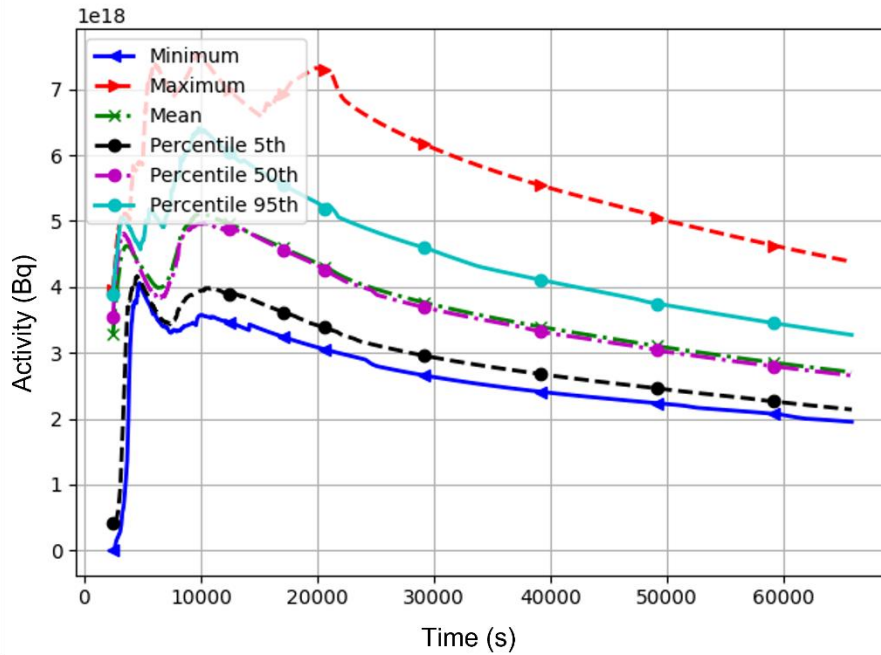


Figure D.1- 3: Calculated minimum, maximum, mean and most probable values of activity transported to the containment in case of LBLOCA on the cold leg of the pressurizer loop along with the SBO

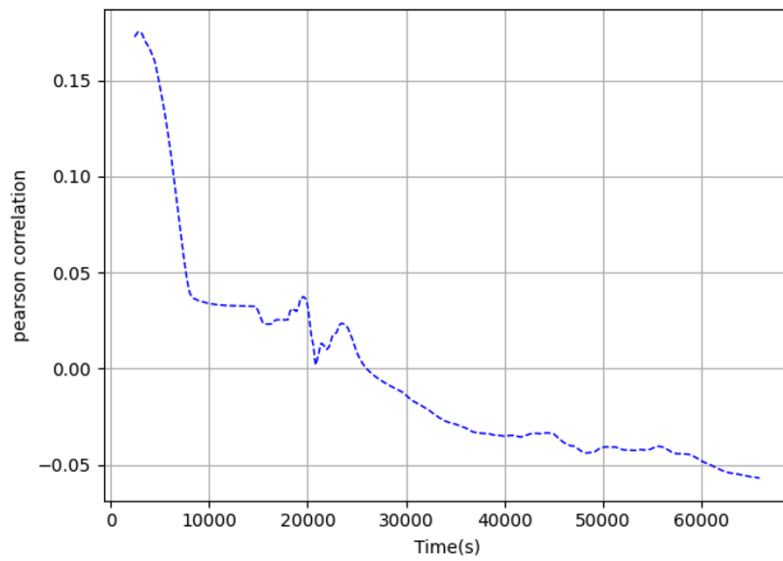


Figure D.1- 1: Pearson correlation coefficient between the activity released to the environment and leakage area inside of the containment (f_{leak}) in time in case of LBLOCA on the cold leg of the pressurizer loop along with the SBO

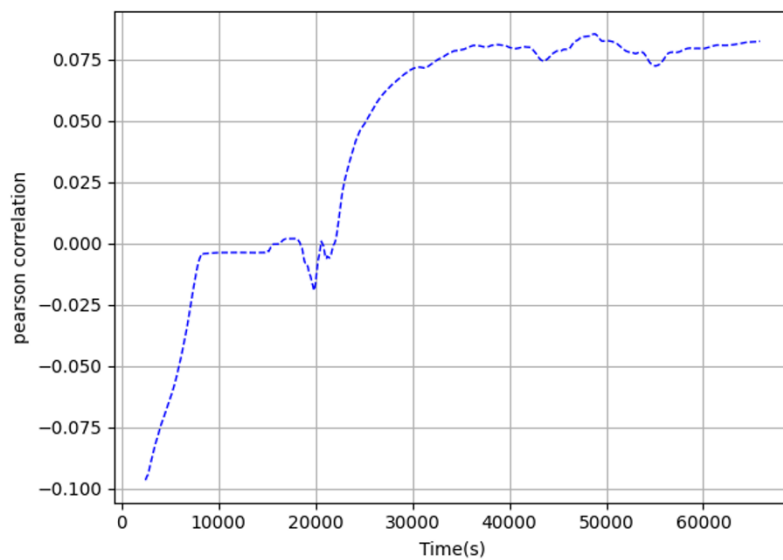


Figure D.1- 4: Pearson correlation coefficient between the activity released to the environment and maximum aerosol radius (fR_{max}) in time in case of LBLOCA on the cold leg of the pressurizer loop along with the SBO

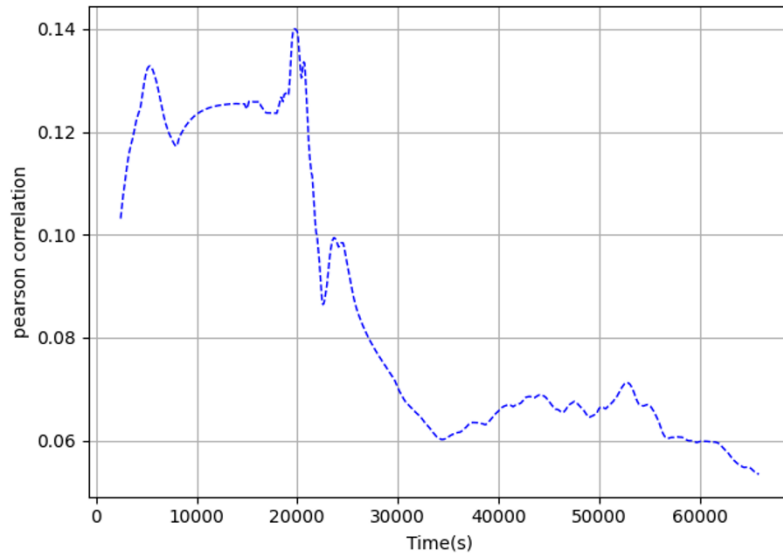


Figure D.1- 5: Pearson correlation coefficient between the activity released to the environment and minimum aerosol radius (fR_min) in time in case of LBLOCA on the cold leg of the pressurizer loop along with the SBO

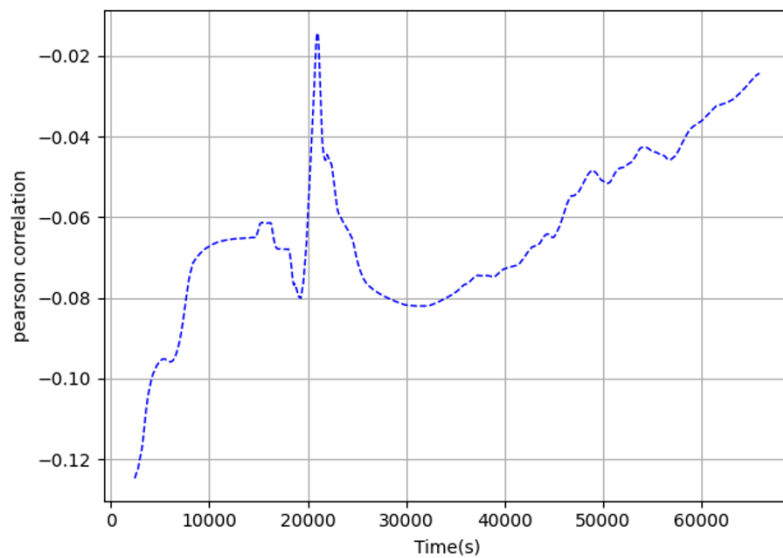


Figure D.1- 6: Pearson correlation coefficient between the activity released to the environment and aerosol density (frho) in time in case of LBLOCA on the cold leg of the pressurizer loop along with the SBO

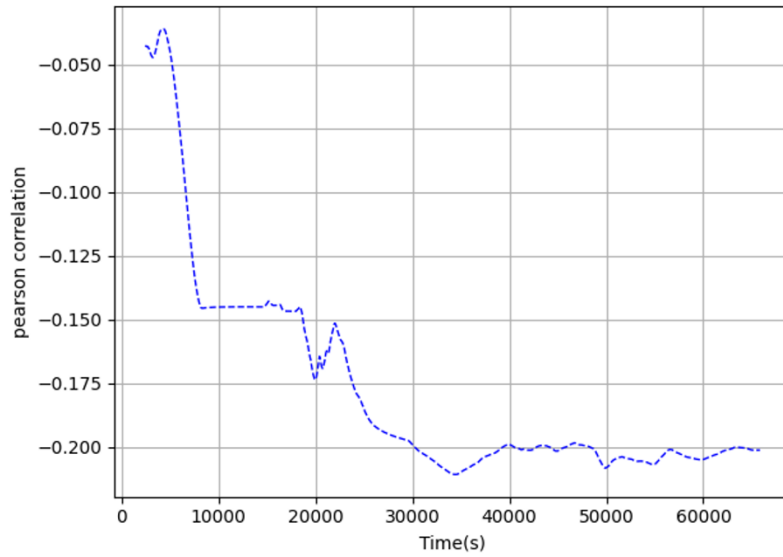


Figure D.1- 7: Pearson correlation coefficient between the activity released to the environment and aerosol specific heat (fspheat) in time in case of LBLOCA on the cold leg of the pressurizer loop along with the SBO

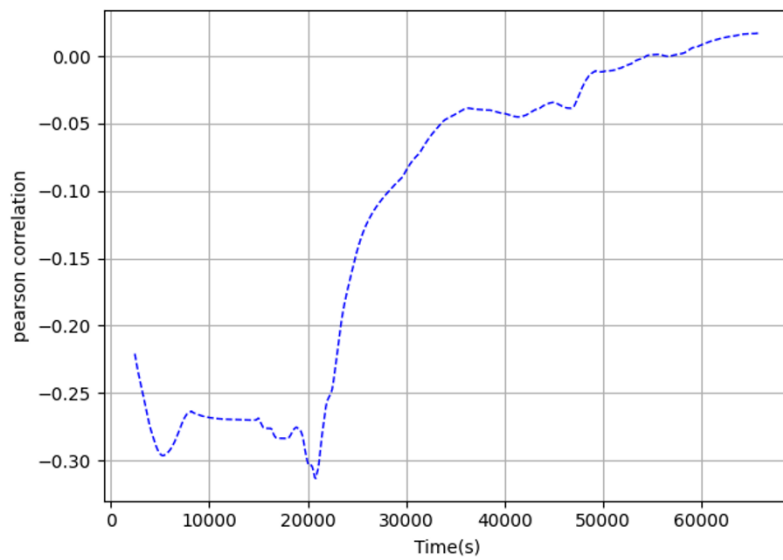


Figure D.1- 8: Pearson correlation coefficient between the activity released to the environment and Stokes velocity correction factor (fv_stks) in time in case of LBLOCA on the cold leg of the pressurizer loop along with the SBO

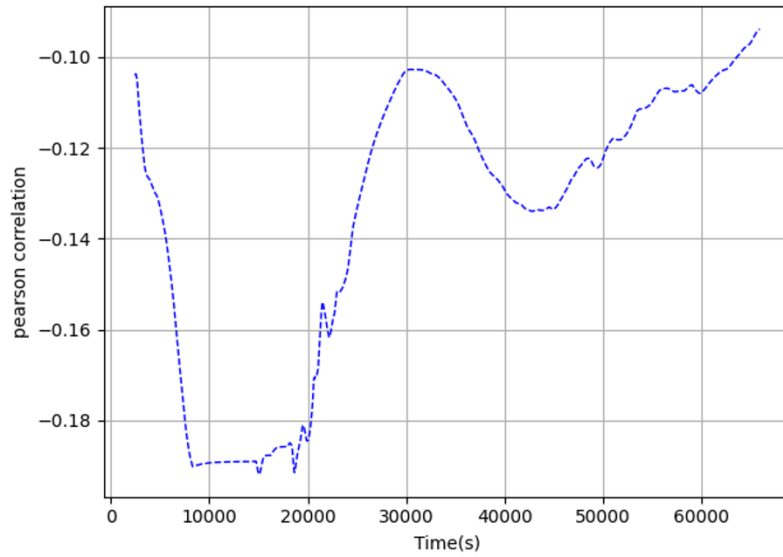


Figure D.1- 9: Pearson correlation coefficient between the activity released to the environment and cavity ablation temperature (fTABLA) in time in case of LBLOCA on the cold leg of the pressurizer loop along with the SBO

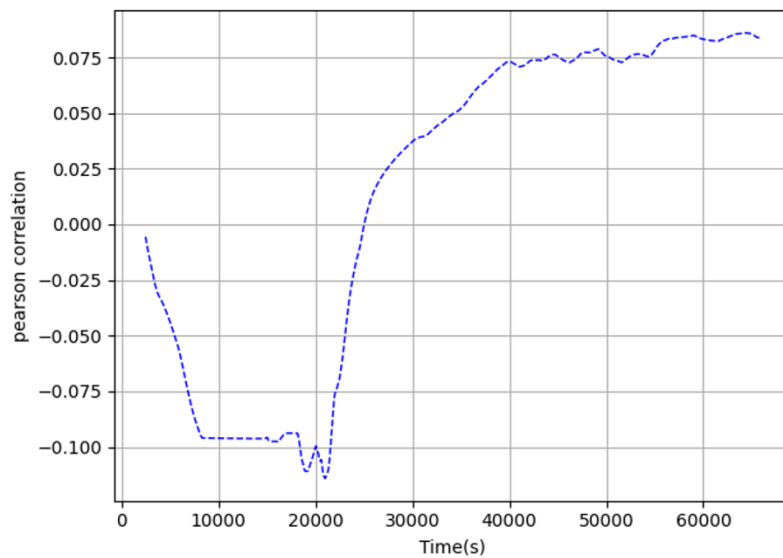


Figure D.1- 10: Pearson correlation coefficient between the activity released to the environment and oxidation onset temperature (fTBEG) in time in case of LBLOCA on the cold leg of the pressurizer loop along with the SBO

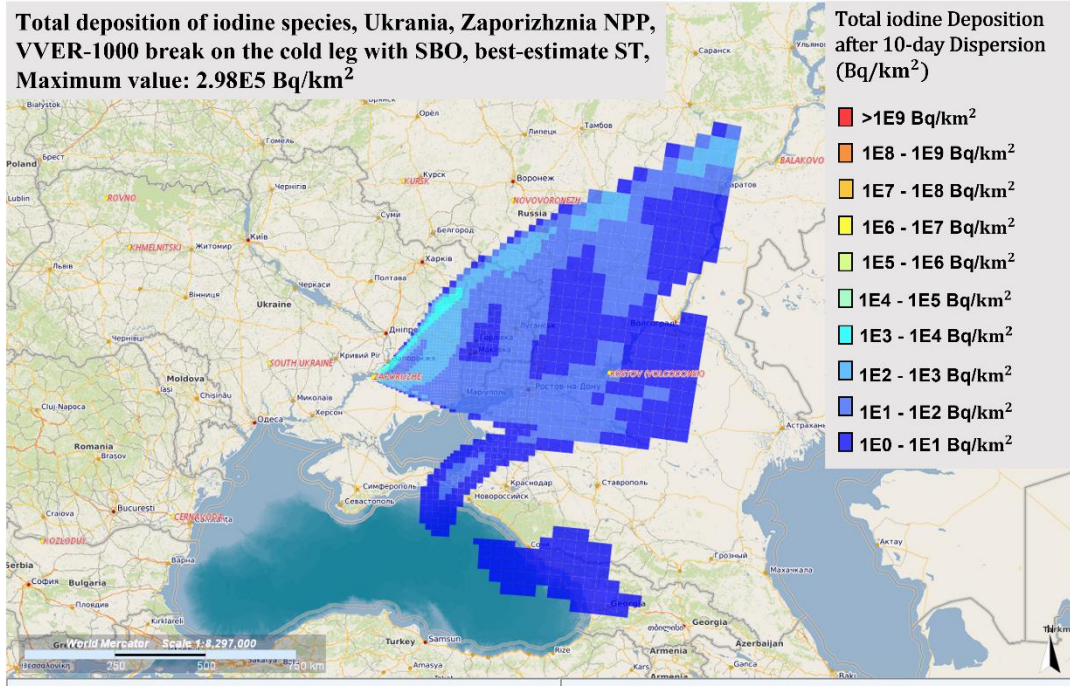


Figure D.1- 11: Simulated total deposition of iodine isotopes due to dispersion from Zaporizhzhia NPP in winter conditions with best-estimate ST inventory in case of LBLOCA on the cold leg of the pressurizer loop along with the SBO

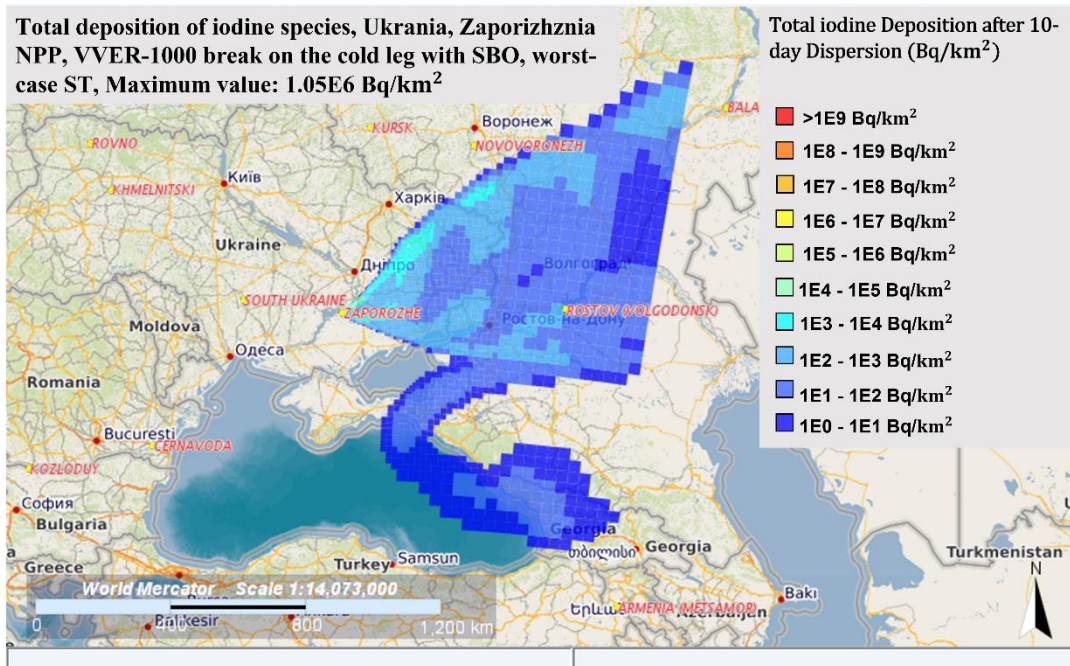


Figure D.1- 12: Simulated total deposition of iodine isotopes due to dispersion from Zaporizhzhia NPP in winter conditions with worst-case ST inventory in case of LBLOCA on the cold leg of the pressurizer loop along with the SBO

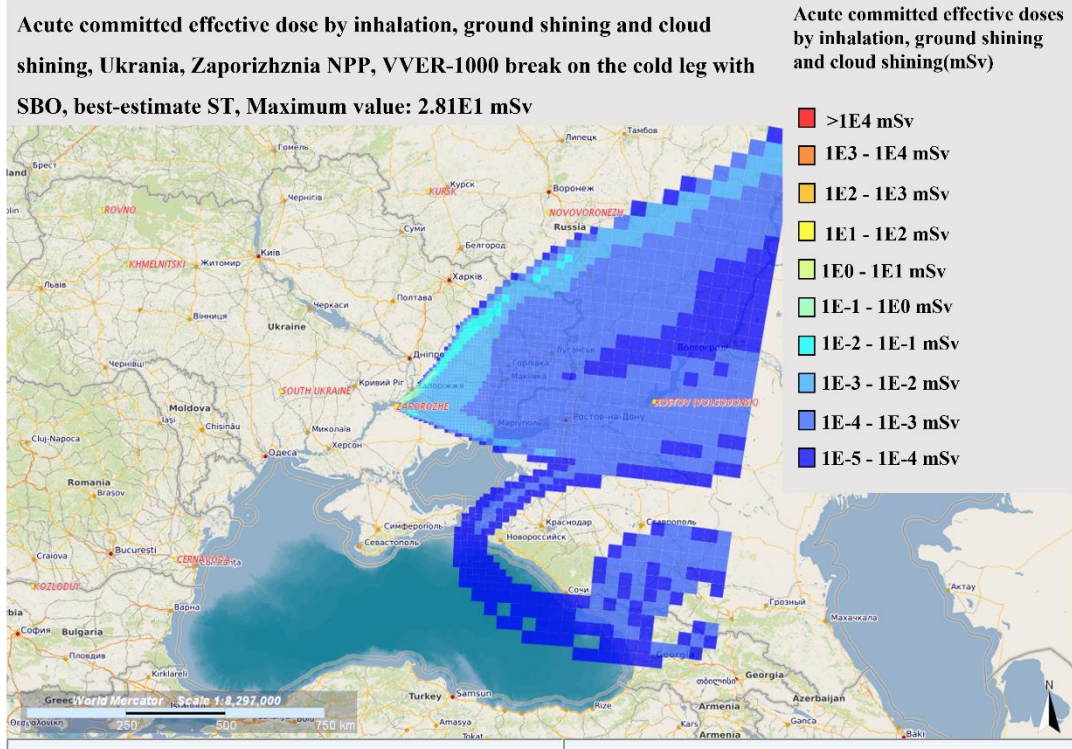


Figure D.1- 13: Simulated acute effective dose due to dispersion from Zaporizhzhia NPP in winter conditions with best-estimate ST inventory in case of LBLOCA on the cold leg of the pressurizer loop along with the SBO

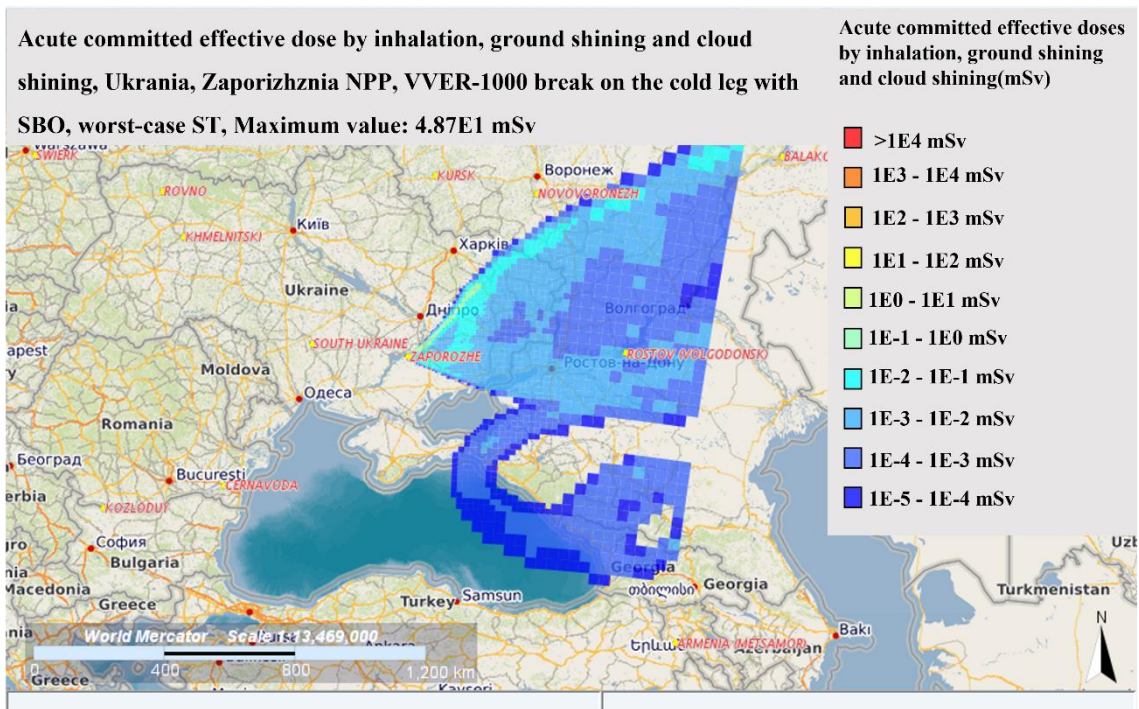


Figure D.1- 14: Simulated Acute effective dose due to dispersion from Zaporizhzhia NPP in winter conditions with worst-case ST inventory in case of LBLOCA on the cold leg of the pressurizer loop along with the SBO

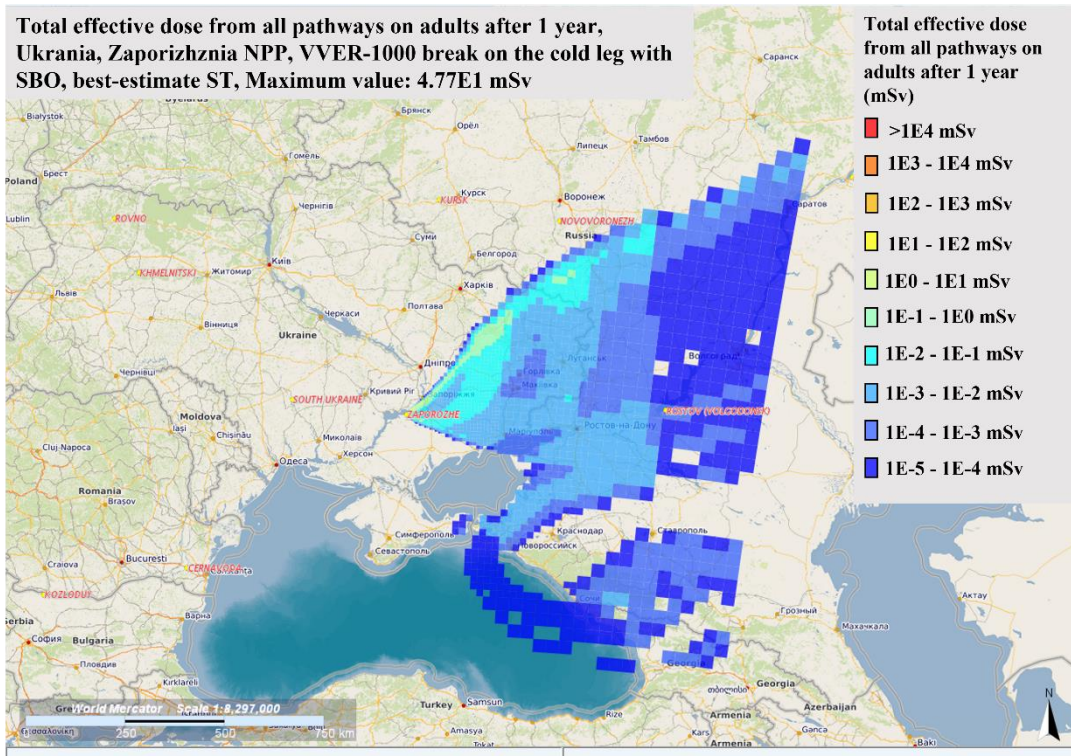


Figure D.1- 15: Simulated effective dose on adults after 1 year due to dispersion from Zaporizhzhia NPP in winter conditions with best-estimate ST inventory in case of LBLOCA on the cold leg of the pressurizer loop along with the SBO

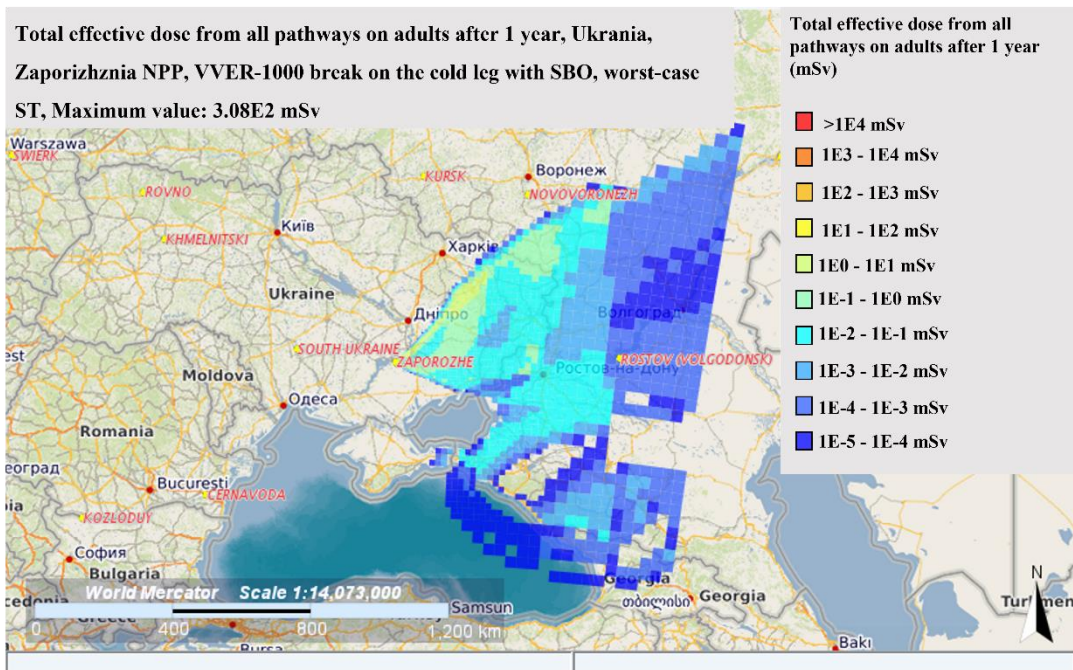


Figure D.1- 16: Simulated effective dose on adults after 1 year due to dispersion from Zaporizhzhia NPP in winter conditions with worst-case ST inventory in case of LBLOCA on the cold leg of the pressurizer loop along with the SBO

D.2 Further results of the uncertainty quantification and sensitivity analysis of the break on the cold leg with SBO

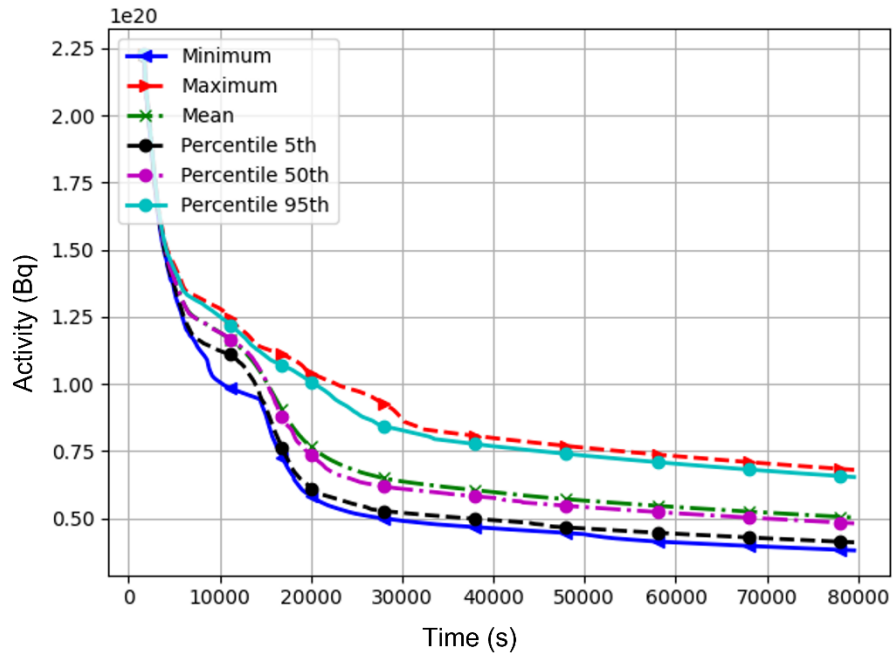


Figure D.2- 1: Calculated minimum, maximum, mean and most probable values of activity released from the vessel in case of LBLOCA on the hot leg of the pressurizer loop along with the SBO

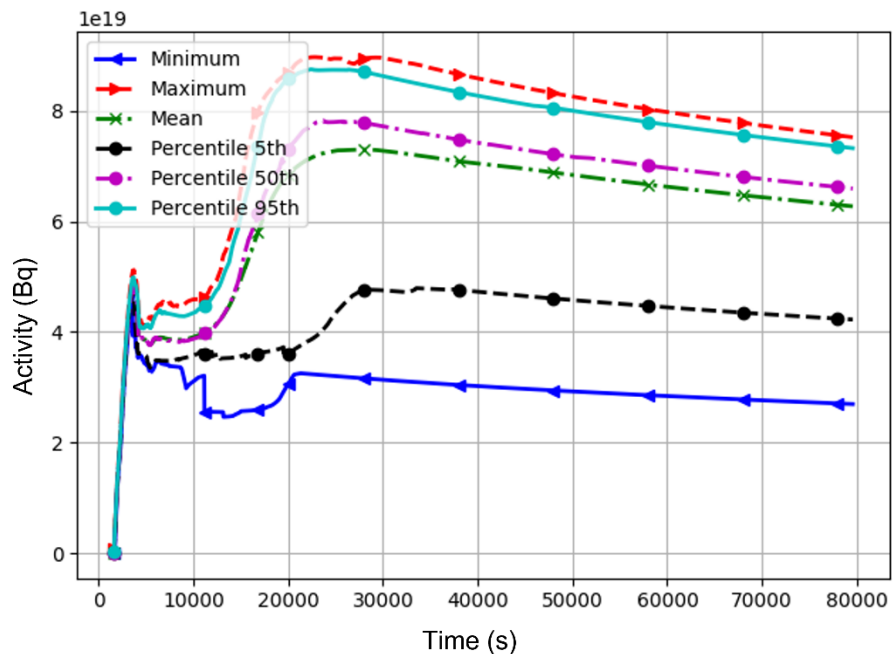


Figure D.2- 2: Calculated minimum, maximum, mean and most probable values of activity transported to the primary circuit in case of LBLOCA on the hot leg of the pressurizer loop along with the SBO

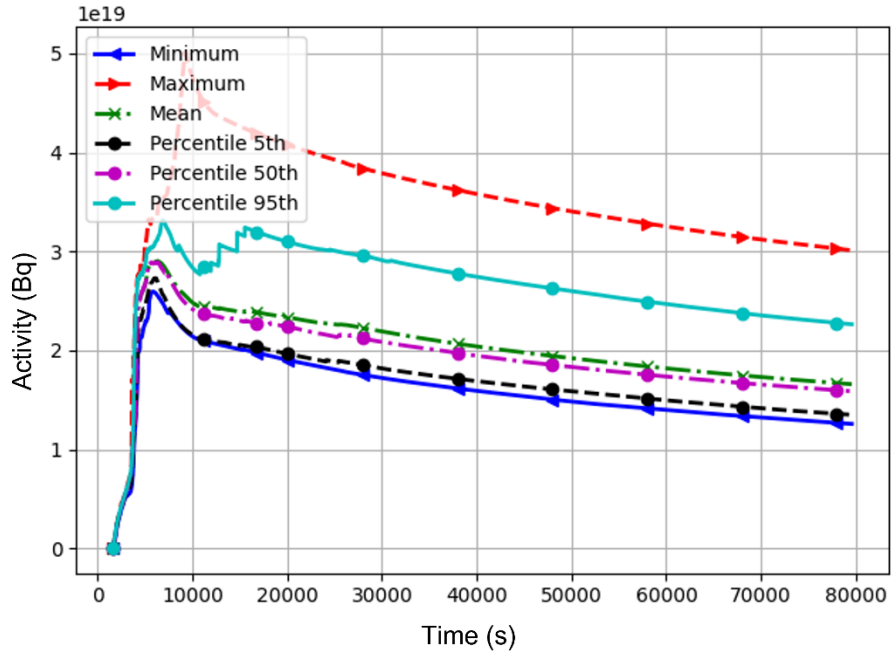


Figure D.2- 3: Calculated minimum, maximum, mean and most probable values of activity transported to the containment in case of LBLOCA on the hot leg of the pressurizer loop along with the SBO

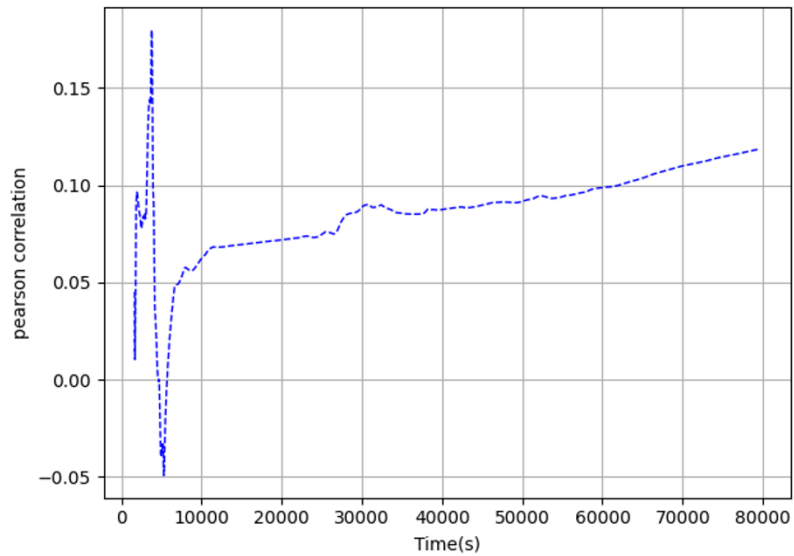


Figure D.2- 4: Pearson correlation coefficient between the activity released to the environment and leakage area inside of the containment (f_{leak}) in time in case of LBLOCA on the hot leg of the pressurizer loop along with the SBO

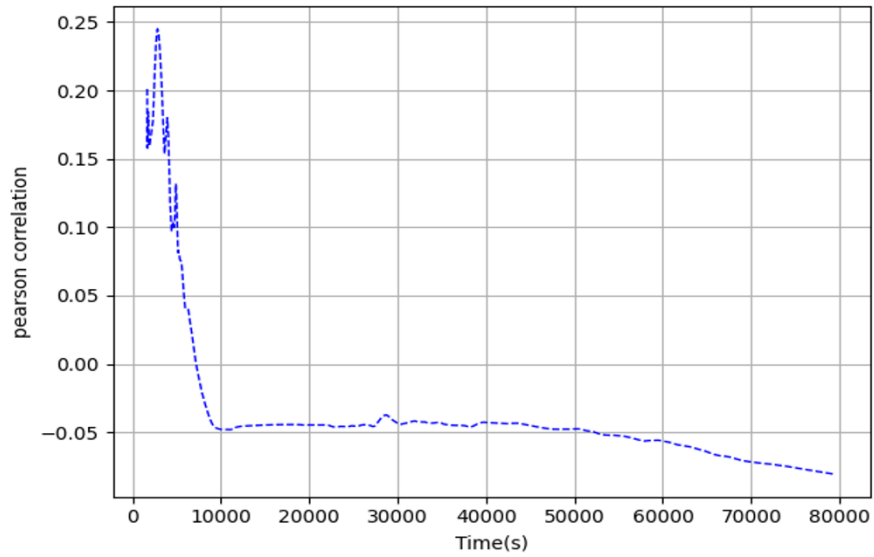


Figure D.2- 5: Pearson correlation coefficient between the activity released to the environment and maximum aerosol radius (fR_max) in time in case of LBLOCA on the hot leg of the pressurizer loop along with the SBO

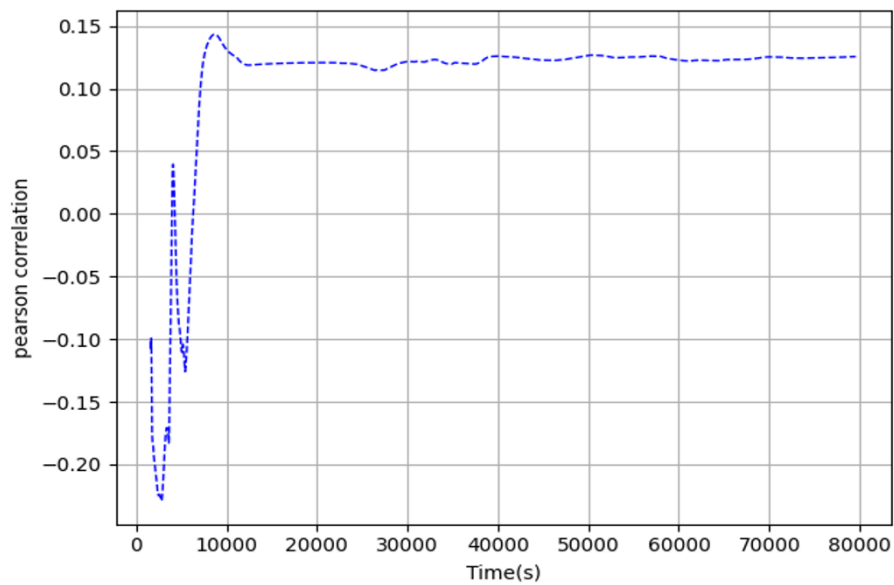


Figure D.2- 6: Pearson correlation coefficient between the activity released to the environment and minimum aerosol radius (fR_min) in time in case of LBLOCA on the hot leg of the pressurizer loop along with the SBO

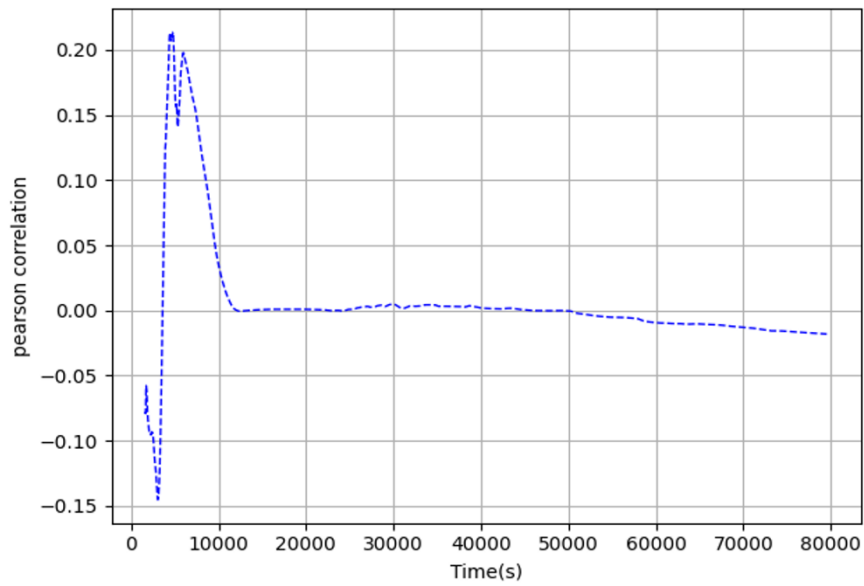


Figure D.2- 7: Pearson correlation coefficient between the activity released to the environment and aerosol density (frho) in time in case of LBLOCA on the hot leg of the pressurizer loop along with the SBO

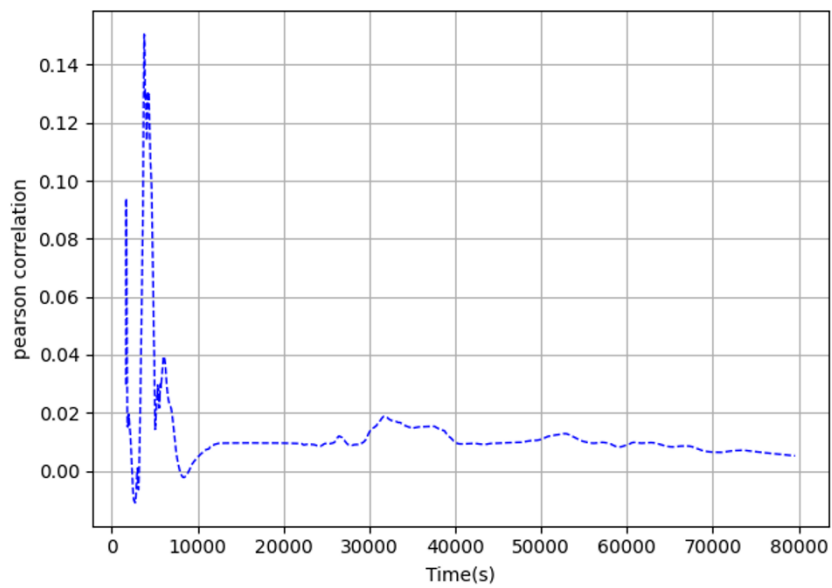


Figure D.2- 8: Pearson correlation coefficient between the activity released to the environment and aerosol specific heat (fspheat) in time in case of LBLOCA on the hot leg of the pressurizer loop along with the SBO

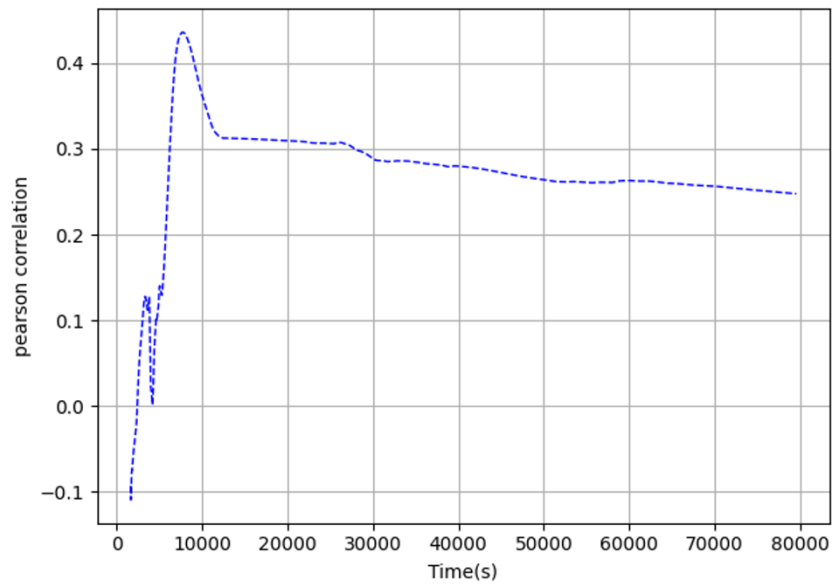


Figure D.2- 9: Pearson correlation coefficient between the activity released to the environment and Stokes velocity correction factor (fv_stks) in time in case of LBLOCA on the hot leg of the pressurizer loop along with the SBO

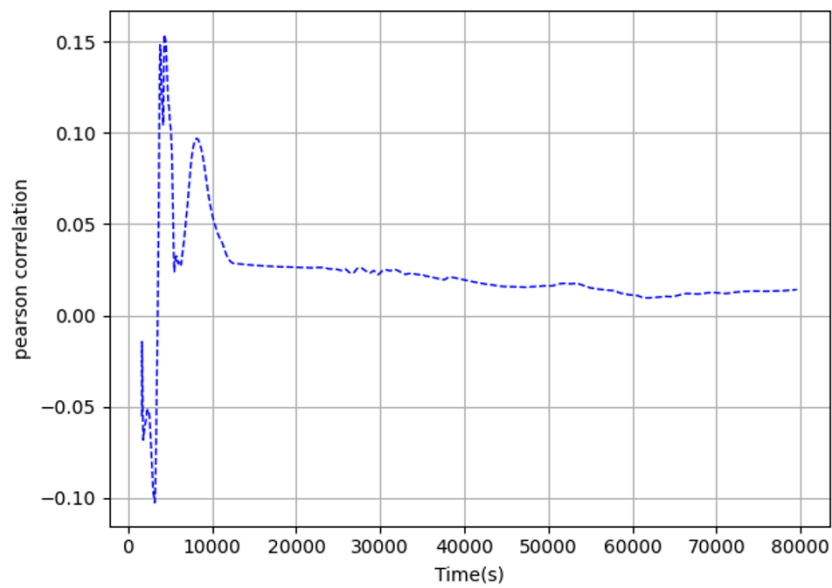


Figure D.2- 10: Pearson correlation coefficient between the activity released to the environment and cavity ablation temperature (fTABLA) in time in case of LBLOCA on the hot leg of the pressurizer loop along with the SBO

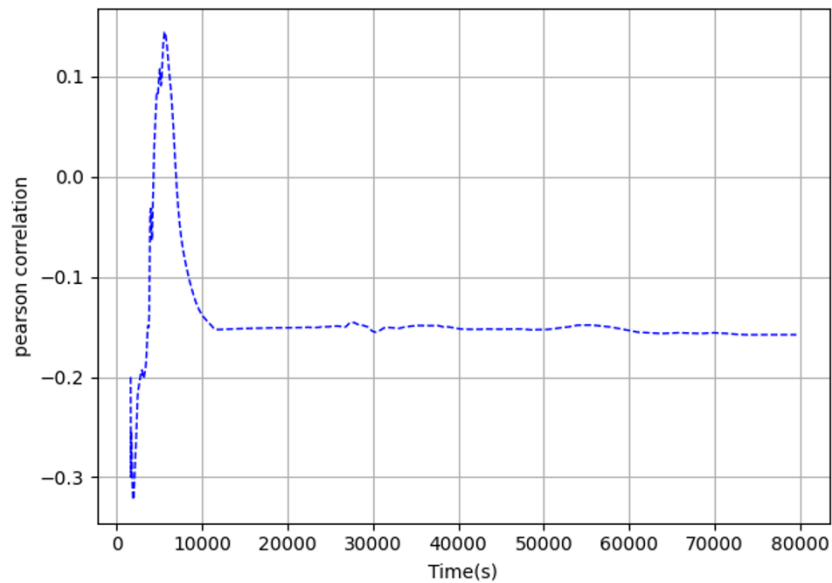


Figure D.2- 11: Pearson correlation coefficient between the activity released to the environment and oxidation onset temperature (ftBEG) in time in case of LBLOCA on the hot leg of the pressurizer loop along with the SBO

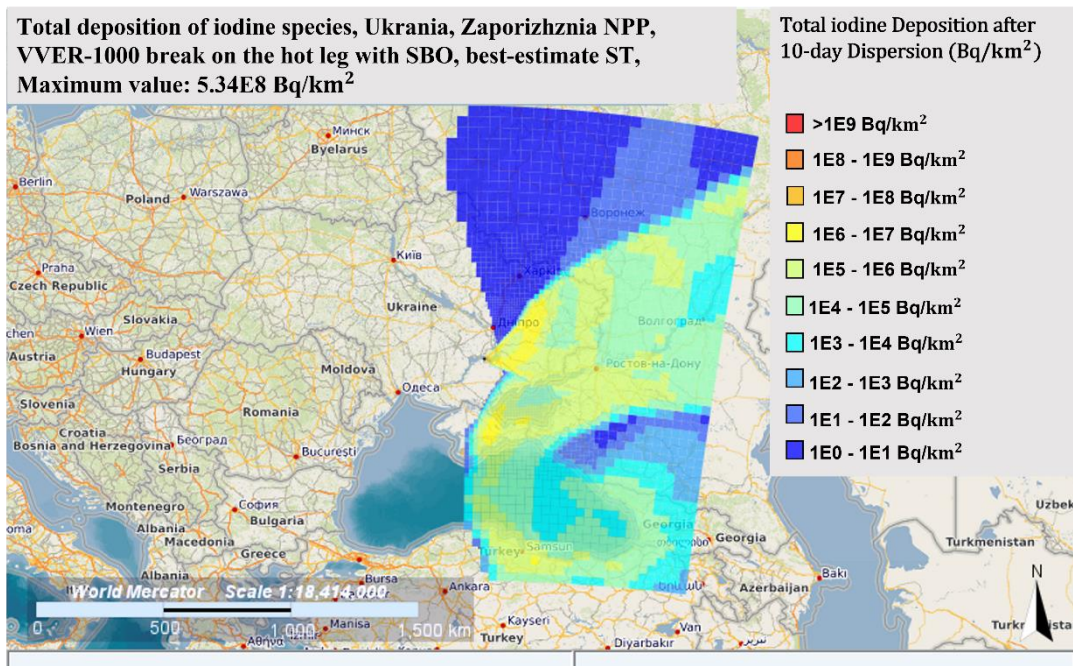


Figure D.2- 12: Simulated total deposition of iodine isotopes due to dispersion from Zaporizhzhia NPP in winter conditions with best-estimate ST inventory in case of LBLOCA on the hot leg of the pressurizer loop along with the SBO

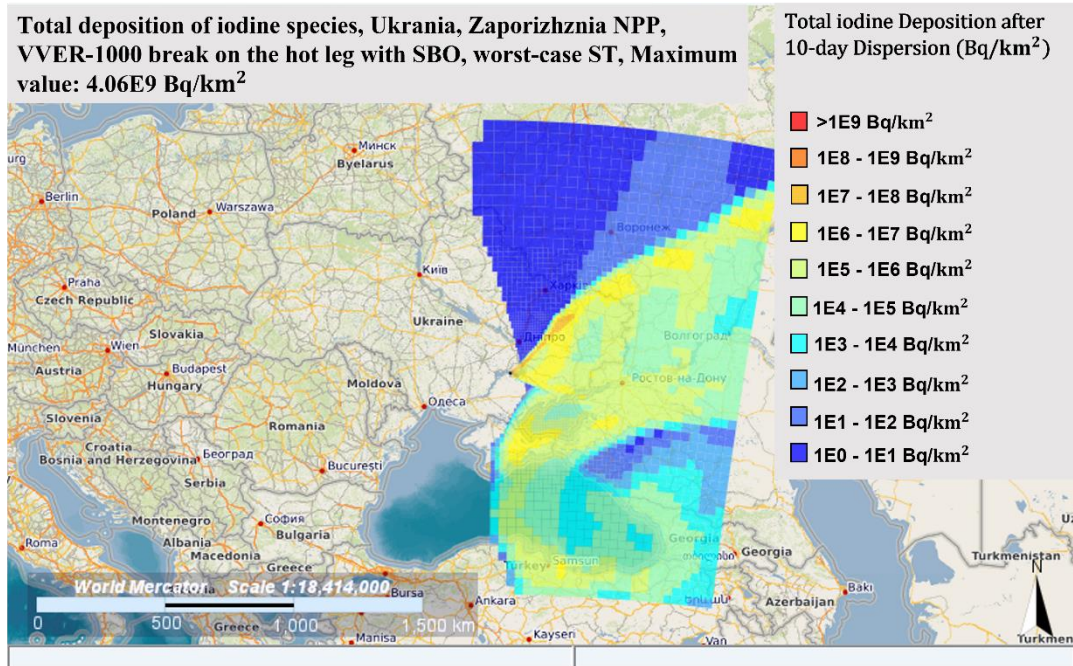


Figure D.2- 13: Total deposition of iodine isotopes due to dispersion from Zaporizhzhia NPP in winter conditions with worst-case ST inventory in case of LBLOCA on the hot leg of the pressurizer loop along with the SBO

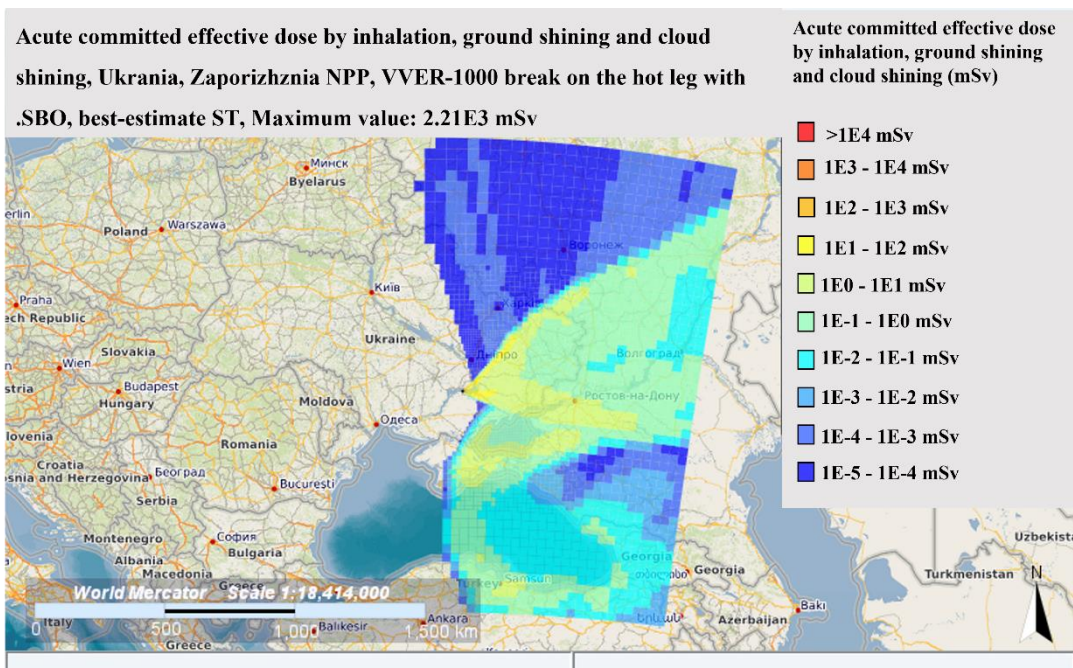


Figure D.2- 14: Acute effective dose due to dispersion from Zaporizhzhia NPP in winter conditions with best-estimate ST inventory in case of LBLOCA on the hot leg of the pressurizer loop along with the SBO

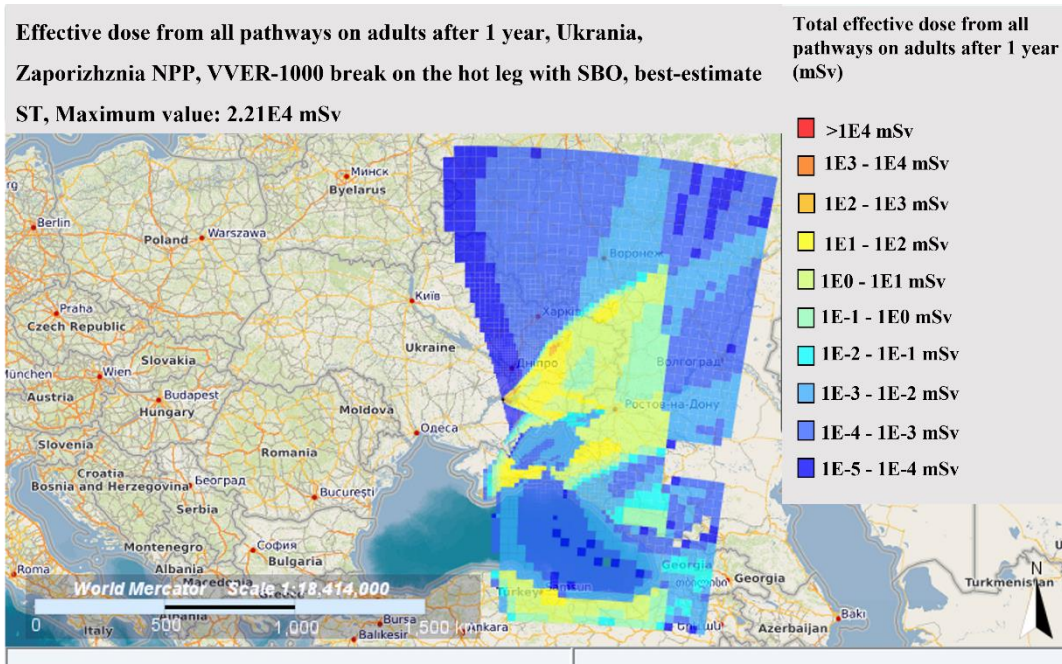


Figure D.2- 15: Simulated acute effective dose due to dispersion from Zaporizhzhia NPP in winter conditions with worst-case ST inventory in case of LBLOCA on the hot leg of the pressurizer loop along with the SBO

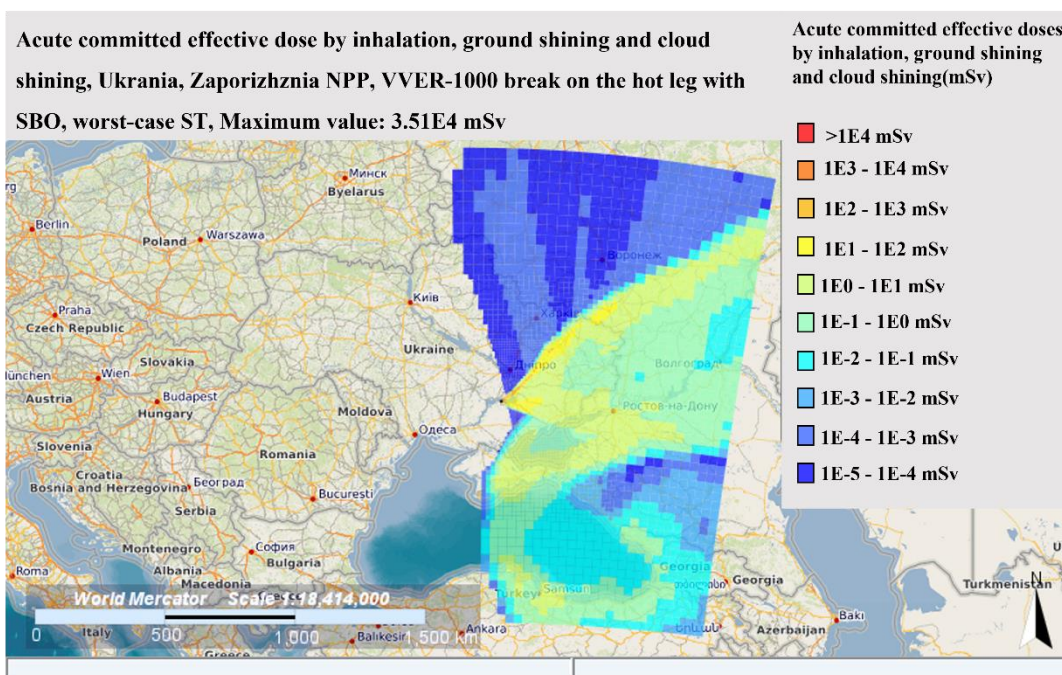


Figure D.2- 16: Simulated effective dose on adults after 1 year due to dispersion from Zaporizhzhia NPP in winter conditions with best-estimate ST inventory in case of LBLOCA on the hot leg of the pressurizer loop along with the SBO

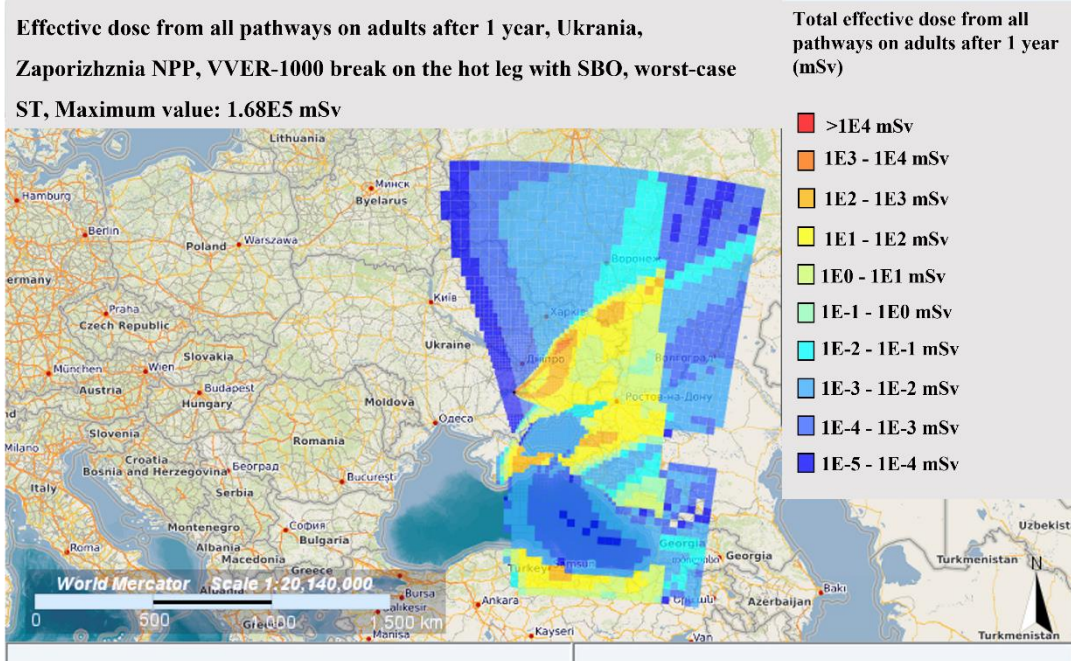


Figure D.2- 17: Simulated effective dose on adults after 1 year due to dispersion from Zaporizhzhia NPP in winter conditions with worst-case ST inventory in case of LBLOCA on the hot leg of the pressurizer loop along with the SBO